Paolo Marzullo
Giuliano Mariani
Editors

From Basic Cardiac Imaging to Image Fusion

Core Competencies Versus Technological Progress

Springer

From Basic Cardiac Imaging to Image Fusion

Paolo Marzullo · Giuliano Mariani
Editors

From Basic Cardiac Imaging to Image Fusion

Core Competencies Versus Technological Progress

Foreword by Philipp Kaufmann

Springer

Editors
Paolo Marzullo
CNR Institute of Clinical Physiology
and Fondazione Toscana Gabriele
Monasterio
Department of Nuclear Medicine
Pisa
Italy

Giuliano Mariani
Regional Center of Nuclear Medicine
University of Pisa
Pisa
Italy

ISBN 978-88-470-2759-6 ISBN 978-88-470-2760-2 (eBook)
DOI 10.1007/978-88-470-2760-2
Springer Milan Heidelberg New York Dordrecht London

Library of Congress Control Number: 2013932460

Printed on acid-free paper

Springer is part of Springer Science+Business Media (www.springer.com)

Foreword

Despite the impressive development in our understanding of cardiovascular diseases, such diseases are still responsible for about one-third of all deaths in Western societies. As an appropriate treatment can only be offered when an accurate diagnosis has been established, tremendous efforts have been made over the past two decades to further improve noninvasive imaging. As a result, a great variety of techniques is now available in daily clinical routine. Not only do clinicians sometimes feel confused by this vast array of choices; it is challenging even for the cardiac imager to take full advantage of all cardiac imaging modalities, including the latest developments of image fusion. It is in this context that *From Basic Cardiac Imaging to Image Fusion* comes as a very timely textbook that offers more than just a succinct overview of the current state-of-the-art, but is also witness to imaging as an emerging subspecialty in cardiology.

The book begins with a summary of cardiac anatomy and pathophysiology as the underlying basis that optimal cardiac imaging is best provided as an integral part of clinical cardiology. Nowadays, cardiac imaging means more than just taking a picture of the heart, as functional information can be obtained if appropriate stress protocols are used. Solid knowledge of the latter is provided in a specific chapter that provides the fundamental principles upon which the cardiologist can safely base the optimal stress protocol. This is followed by chapters explaining the different cross-sectional imaging modalities—comparing their relative benefits and merits—and chapters expanding on the advancements in radiation dose reduction for single photon emission computed tomography (SPECT) and CT imaging. This topic is receiving growing attention in view of the fact that we have experienced over the past three decades an impressive sixfold increase in radiation dose delivered per patient from medical imaging, a fact that raises concerns about potential carcinogenic effects.

The elegant combination of clinical insights and technical explanations throughout the book is complemented by a chapter that provides sound, relevant guidelines, and evidence-based diagnostic algorithms for evaluating patients with suspected coronary artery disease. This chapter rounds off the Editors' viewpoint that only interaction with and full integration of the fascinating array of possible imaging techniques with

the clinical context will determine the appropriate use of cardiac imaging.

Using this concept, it is highly likely that *From Basic Cardiac Imaging to Image Fusion* will become a helpful and important companion to trainees, cardiologist, and experts in cardiac imaging alike.

Philipp Kaufmann, MD
Professor and Director of Cardiac Imaging
University Hospital Zurich, Switzerland

Preface

The reason we are editing this book 10 years after one of us edited a similar publication is that the problem remains regarding how to integrate into optimized diagnostic protocols the vast amount of information that cardiac imaging can yield. At this time, even more so than 10 years ago, technological advances in cardiac imaging enable high-speed and high-resolution imaging of a wide spectrum of phenotypic manifestations related both to anatomy and function of the heart. However, in general, such imaging techniques involve high operational costs in terms of instrumentation/imaging agents and/or human resources/expertise. Furthermore, the process of integrating the wealth of information obtained by different 3D techniques is still far from allowing direct translation into clinical cardiology. Across countries, educational inequalities probably account for most of the difficulty in achieving meaningful merging of different approaches to cardiac imaging into diagnostic algorithms optimized in terms of clinical efficacy and cost effectiveness. In this regard, even if national rules often make imaging specialists and cardiologists equal in terms of years of training, the educational paths are frequently completely different in terms of clinical experience and crosstalk.

The solution to this problem is rather complex, and we believe that important steps forward will occur in this process thanks to growing interaction among the involved scientific medical societies. Great efforts in this direction have already been initiated—for instance, by implementing uniform processes of quality control in cardiology, radiology, and nuclear medicine and by updating guidelines. The unfavorable financial situation currently experienced worldwide will inevitably lead to strict control of the cost-benefit ratio of each technique and to definition of the more accurate, reliable, and reproducible prognostic parameters defining patient outcomes. Wise spending is already becoming a basic component of cardiac imaging, along with growing concerns regarding patient exposure to radiation.

Thus, despite towering technological progress and its growing everyday clinical use, the "circus" of cardiac imaging goes on setting new, increasingly advanced, goals and endpoints to enhance diagnostic accuracy and optimize merging of the imaging information spectrum. In order to reach these goals, we must expand our knowledge far beyond

our limited specialty areas and open our investigations to all available techniques. This is the rationale that guided us in collating this handbook. We asked a team of highly qualified experts from around the world to present and discuss the basic concepts of cardiac anatomy and pathophysiology of coronary circulation as a basis for cardiac imaging, focusing discussion on the integration of images and techniques to be used by the reader in clinical practice. Thus, each specialist contributing to this book compared data obtained within his/her subspecialty with the other contributing specialists. As a result, physicians ranging from cardiac surgeons, internal medicine specialists, and public health administrators can understand the key to hybrid cardiac imaging.

Chapter 1 of the book describes the anatomy of the heart and shows the link between imaging anatomy, function, and perfusion. To attain this information, stressors are needed, taking into consideration the variable degree of coronary vasodilation induced by physical or pharmacological stimulation. Chapter 2 describes all types of stressors and their contraindications and side effects. Perfusion is described in Chapter 3 without referring to a single technique but, rather, with an open perspective on all of them. The message is that perfusion itself is more valuable than the investigation technique being used, and differences among 3D methods should be well known by all specialists. Chapter 4 deals with myocardial innervation, an old but recently rediscovered method to assess adrenergic function, mostly relevant in heart failure. The value for clinical outcome of this evaluation is considerable, especially in high-risk populations. Beyond imaging, another important target is radiation dose reduction to patients both in multislice computed tomography and single photon emission computed tomographic imaging. In this regard, Chapters 5 and 6 describe the state-of-the-art of approaches that reduce exposure; the perspective of these approaches is to achieve better reproducibility in the future of low-dose procedures, combined with better quantitative management of cardiac patients, such as, for example, absolute left ventricular volume rather than ejection fraction; mass rather than wall thickness. The main issues for specialists who wrote Chapter 7 were to comment on the true role of 3D imaging in terms of standards (pathology) and available techniques or instrumentations to make image fusion applicable within imaging techniques. This chapter will probably make this book bewitching for clinicians, as with the last chapter, which compares current guidelines with evidence-based patterns of patient management. Of course, guidelines cannot be updated every month, but the common feeling is that some of them should include more cardiac imaging, particularly regarding myocardial innervation and stratification of high-risk patients, including those with diabetes.

Based on the above considerations, the best way to read this book is cover to cover, getting the best from each technique in an integrated perspective relative to the others, and attempting to avoid misadventures that frequently happen in this field.

Thank you for reading From Basic Cardiac Imaging to Image Fusion—Core Competencies versus Technological Progress. When you do, we will be honored to receive your comments by email:

marzullo@ftgm.it
giuliano.mariani@med.unipi.it

January 2013, Pisa, Italy

Paolo Marzullo
Giuliano Mariani

Contents

Contributors

Denis Agostini Nuclear Medicine, University Hospital CHU, Caen, France

Albert de Roos Radiology, LUMC, Leiden, The Netherlands

Berlinda J. de Wit-van der Veen Antoni van Leeuwenhoek Hospital, Nuclear Medicine, National Cancer Institute, Amsterdam, The Netherlands

Pasquale Perrone Filardi Department of Internal Medicine, Cardiovascular and Immunological Disorders, Federico II University of Naples, Naples, Italy

Elena Filidei Fondazione Toscana Gabriele Monasterio, Pisa, Italy

Josef Fox Department of Radiology, Section of Molecular Imaging and Therapy, Memorial Sloan Kettering Cancer Center, New York, USA

Dario Genovesi Department of Nuclear Medicine, Fondazione Toscana Gabriele Monasterio, Pisa, Italy

Alessia Gimelli Department of Nuclear Medicine, Fondazione Toscana Gabriele Monasterio, Pisa, Italy

Assuero Giorgetti Department of Nuclear Medicine, Fondazione Toscana Gabriele Monasterio, Pisa, Italy

Martina Marinelli Institute of Clinical Physiology, CNR, Pisa, Italy

Kenichi Nakajima Department of Nuclear Medicine, Kanazawa University Hospital, Kanazawa, Japan

Stephan G. Nekolla Nuklearmedizinische Klinik, Technische Universität München, Munich, Germany

Neeta Pandit-Taskar Department of Radiology, Section of Molecular Imaging and Therapy, Memorial Sloan Kettering Cancer Center, New York, USA

Stefania Paolillo Department of Internal Medicine, Cardiovascular and Immunological Disorders, Federico II University of Naples, Naples, Italy

Gianluca Pontone Centro Cardiologico Monzino, IRCCS, Milan, Italy

Eliana Reyes Nuclear Medicine Department, Royal Brompton Hospital, London, UK

Christoph Rischpler Nuklearmedizinische Klinik, Technische Universität München, Munich, Germany

Joanne D. Schuijf Toshiba Medical Systems Europe, Zoetermeer, The Netherlands

H. William Strauss Department of Radiology, Section of Molecular Imaging and Therapy, Memorial Sloan Kettering Cancer Center, New York, USA

Ernst E. van der Wall Cardiology, LUMC, Leiden, The Netherlands

Caroline E. Veltman Cardiology, LUMC, Leiden, The Netherlands

Hein Jan Verberne Department of Nuclear Medicine, Amsterdam Medical Center, University of Amsterdam, Amsterdam, The Netherlands

Cardiac Anatomy and Pathophysiology of Coronary Circulation as a Basis for Imaging

1

Josef Fox, Neeta Pandit-Taskar and H. William Strauss

1.1 Introduction

Cardiovascular disease is responsible for ~33% of all deaths in the USA (Heart Facts 2012) [1]. Approximately 28% (83 million people) of the US population has one or more forms of acquired heart or blood-vessel disease. Elevated blood pressure (hypertension) is present in 64 million adults, coronary artery disease in 16.3 million (9 million with angina or chest pain of cardiac origin), congestive heart failure (HF) in ~5.7 million, and stroke in 7 million. In 2008, coronary artery disease (CAD) caused ~405,000 deaths in the United States, making it the number one killer. About 1.2 million people will suffer a new or recurrent heart attack each year. In addition to CAD, HF (inability of the heart to pump sufficient blood to meet the demands of the body) is becoming more prevalent. About 550,000 new cases of HF occur each year, often as the final phase of hypertension, CAD, or cardiomyopathy. Cardiomyopathy, which is disease of the heart muscle, appears in two major forms: one is associated with abnormal increase in the size of cardiomyocytes (hypertrophic cardiomyopathy), and the second is associated with the inability of cardiomyocytes to contract effectively despite adequate blood supply, which results in muscle thinning and chamber dilation (dilated cardiomyopathy).

Hemodynamically significant CAD (coronary narrowing >50% of the lumen diameter) limits maximum perfusion to the myocardium. These narrowings may be the result of several lesions in a series or in a single vessel. Reduced myocardial perfusion leads to myocardial ischemia and infarction. Myocardial ischemia is a reversible condition caused by a temporary deficiency in the supply of oxygen to the myocardium. The usual cause is an increase in myocardial oxygen demand due to an increase in heart rate, blood pressure, or both. In the normal heart, the coronary artery dilates in response to the release of nitric oxide (caused by increased shear stress to the endothelial cells), allowing an increase in blood flow to deliver the additional oxygen. When coronary disease is present, and the vessel is narrowed and incremental, blood flow is limited (classic effort angina, as described by William Heberden [2]). A less common cause of decreased myocardial perfusion is spasm of a coronary artery (as described by Myron Prinzmetal [2]). A transient decrease in myocardial perfusion (lasting <10 min), which is myocardial ischemia, does not result in permanent damage to cardiac myocytes. On the other hand, protracted and more severe decreases in perfusion (>15 min duration), resulting in total loss of flow, results in cardiac myocyte death. This lack of blood supply usually occurs as a result of a combination of at least two

J. Fox · N. Pandit-Taskar · H. W. Strauss (✉)
Section of Molecular Imaging and Therapy
Department of Radiology, Memorial Sloan
Kettering Cancer Center, NY, USA
e-mail: straussh@mskcc.org

P. Marzullo and G. Mariani (eds.), *From Basic Cardiac Imaging to Image Fusion*,
DOI: 10.1007/978-88-470-2760-2_1, © Springer-Verlag Italia 2013

factors: (1) total or near-total occlusion of a coronary artery, and (2) insufficient flow through collateral vessels to meet the metabolic demands of tissue. Early identification of infarction is important, as restoring blood flow often results in preservation of at least some of the peripheral jeopardized myocardium and less impairment of ventricular function.

Although myocardial infarction can occur without warning and can cause sudden death, the underlying disease of the coronary arteries evolves over decades. Beginning around puberty, arterial lesions progress from small lipid deposits, called fatty streaks, in vessel walls to raised lesions that intrude on the arterial lumen over a period of ~30–50 years. Progression of coronary atheroma is accelerated in patients with diabetes, hypercholesterolemia, uremia, elevated homocysteine levels, and diets rich in saturated and trans fats. Atheromatous narrowings that occupy >50% of the lumen diameter restrict the maximum amount of blood that can flow through a vessel, but may not be accompanied by symptoms. Patients with coronary narrowings >70% of the lumen are often symptomatic during exertion. Clinical manifestation of myocardial ischemia is often dyspnea on exertion and, less frequently, chest pain. The vascular lumen must be narrowed by >90% to decrease myocardial perfusion at rest.

When coronary blood flow is not sufficient to meet the demands of the myocardium, the heart muscle becomes ischemic. Ischemia is associated with decreased tissue perfusion and contraction in the affected area. These changes can be readily detected by radionuclide imaging.

1.2 Anatomy

The adult heart weighs ~300 g and holds ~500 mL of blood: ~150 mL in the left (LV) and 160–170 mL in the right (RV) ventricle at end diastole and ~100 mL in each atrium at the end of atrial diastole. The right and left sides of the heart operate in parallel to eject the same amount of blood with each beat. The right side receives venous blood from the body and pumps this blood to the lungs, where it is oxygenated. The left side receives blood from the lungs and pumps it to the systemic circulation. The thin-walled atria serve as temporary reservoirs for blood returned to the heart, and the ventricles do the major work of pumping the blood away from the heart. The lungs are a low-resistance system (normal peak systolic pressure ~30 mmHg), whereas the systemic circulation is a higher-resistance system (normal peak systolic pressure ~120 mmHg). Hence, the left ventricle (LV) must work harder than the right. As a result the LV myocardium is thicker (~10–12 mm, compared with ~3–4 mm for the RV). Normal LV and RV myocardial perfusion ranges from 0.5–1 mL/min per gram of tissue at rest and may increase to 3–4 mL/min per gram at peak stress. However, as the RV myocardium is thinner, a gram of RV myocardium occupies a greater surface area than a gram of LV myocardium. As a result of the difference in work load, the LV myocardium receives the majority of coronary blood flow. In the basal state, the myocardium receives ~4% of cardiac output (~200 mL/min). At peak exercise, when cardiac output may increase to ~15 L/min, the heart muscle requires ~6% of cardiac output (~900 mL/min).

Right and left atria are separated by a thin, muscular wall—the interatrial septum; the RV and LV are separated by the thicker, muscular interventricular septum. Valves separate atria from ventricles and ventricles from arteries, and these valves prevent blood from flowing backward. The tricuspid valve (named for its three leaflets, or cusps) separates the right atrium from the RV, and the mitral valve separates the left atrium from the LV. The pulmonary valve separates the RV from the pulmonary artery, and the aortic valve separates the LV from the aorta. The left and right cusps of the tricuspid aortic valve give rise to the left main (MCA) and right (RCA) coronary arteries, respectively.

Blood supply to the myocardium comes from three major coronary arteries that originate from the aorta. The left MCA divides into two branches: the left anterior descending (LAD) and the left circumflex (LCx) arteries. The LAD supplies

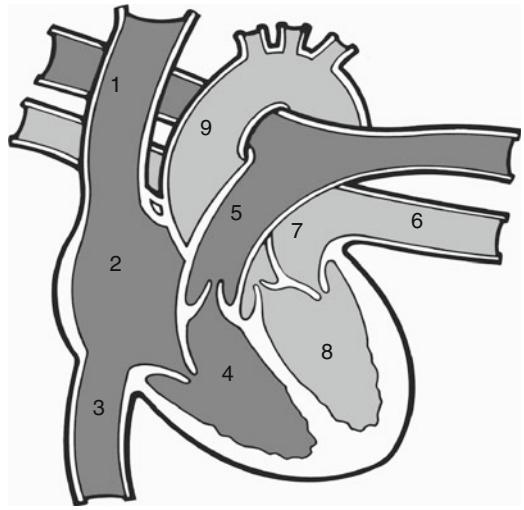

1. Superior vena cava
2. Right atrium
3. Inferior vena cava
4. Right ventricle
5. Pulmonary artery
6. Pulmonary vein
7. Left atrium
8. Left ventricle
9. Aorta

Fig. 1.1 Diagram of the adult human heart

oxygen and nutrition to the interventricular septum and the anterior wall of the LV; the LCx supplies the left atrium and the posterior and lateral walls of the LV. The RCA supplies the inferior wall of the LV, the free wall of the RV, and the right atrium. Blood drains from the myocardium to the coronary veins, which run alongside the coronary arteries and terminate in the coronary sinus of the right atrium, where this deoxygenated blood mixes with blood from the vena cava.

1.3 Physiology

1.3.1 Circulation

Venous blood returns from the systemic circulation to the heart via the superior and inferior vena cavae (Fig. 1.1). Although venous pressure is low, resistance to blood flow is also low, and blood flows through the large veins at 40 cm/s on its way to the right atrium at a pressure >5 mm. Blood traverses the tricuspid valve to enter the RV, which then pumps the blood through the pulmonic valve into the pulmonary artery and lungs for oxygenation. Blood is expelled from the RV at a pressure of 25–30 mmHg. In the enormous capillary bed of the lungs (~300 million alveolar capillaries), the velocity of blood slows to 1 mm/s to allow time for the exchange of carbon dioxide for oxygen in the capillaries. The oxygenated blood returns to the left atrium via the pulmonary veins at a pressure <5 mmHg. The blood then flows through the mitral valve to the LV, which expels blood through the aortic valve at a velocity of ~15 m/s into the aorta at a systolic pressure of ~120 mmHg. A significant increase in LV diastolic pressure causes an increase in pulmonary blood volume, increasing lung stiffness and breathing effort, resulting in dyspnea.

1.3.2 Mechanical Activity of the Heart

Each cardiac cycle (i.e., one beat) consists of systole—the period of ventricular contraction—and diastole—the period of ventricular relaxation. The right and left sides of the heart contract in unison. During diastole, both atria and ventricles are relaxed. Atrial pressure is slightly higher than ventricular pressure, the tricuspid and mitral valves are open, and blood passes from the atria into the ventricles; 80–90% of ventricular filling takes place in this passive fashion. Aortic and pulmonic valves are closed during this time because pulmonary artery and aortic pressures are higher than ventricular pressures. During diastole, coronary flow is

high. At the end of diastole, atria contract, adding 10–20% more volume to ventricles. Blood quantity in the ventricle at the end of diastole—end-diastolic volume—is ~150 mL in the LV and 170 mL in the RV in an average 70 kg body-weight adult.

During systole, myofibrils of the ventricular myocardium shorten, coronary blood flow is reduced, and ventricular pressure rises. In early systole, the mitral and tricuspid valves close. This is followed by the interval of isovolumetric (i.e., no change in volume) contraction, when continued shortening of the myofibrils causes ventricular pressure to exceed pulmonary artery and aortic pressure. The pulmonic and aortic valves then open, and ventricular ejection begins. Blood returning to atria during systole, when the tricuspid and mitral valves are closed, causes atrial volume and pressure to increase. At the conclusion of ventricular ejection, myofibrils rapidly relax, ventricular pressure falls, pulmonic and aortic valves close, tricuspid and mitral valves open, and ventricles start to fill with blood from the atria. Filling occurs rapidly during early diastole and slows as atrial pressure and volume decrease. This filling pattern ensures the heart's ability to function unimpaired during times of increased heart rate (as with exercise and emotional stress), when the length of diastole is shortened.

The amount of blood ejected from the LV over a 1 min interval is the cardiac output (usually expressed in liters per minute) and is typically normalized for body surface area (BSA), called the cardiac index). A normal 70 kg adult has a cardiac output of ~5–6 L/min at rest. The amount of blood ejected in a single beat is the stroke volume (usually expressed in milliliters). The normal adult stroke volume is ~80–100 mL. Cardiac output is distributed to the organs in proportion to their oxygen requirements, which change from rest to exertion (Table 1.1).

Table 1.1 Distribution of cardiac output in humans at rest and exercise (from McCardle et al. 1981)

Distribution of cardiac output		
Cardiac output	Rest (5 L/min) (%)	Exercise (15 L/min) (%)
Brain	15	4
Heart	4	6
Kidneys	20	5
Liver	10	1
Gastrointestinal track	15	1
Skeletal muscle	20	70
Skin	6	10
Other	10	4

1.3.3 Electrical Activity of the Heart

The myocardial muscle has an intrinsic rhythm of contraction. The sinoatrial node, a small mass of specialized cells embedded in the wall of the right atrium near the entrance of the superior vena cava, has the fastest inherent rhythm and serves as the impulse generator for the remainder of the heart. The wave of electrical depolarization spreads to the surrounding atrial muscle cells and stimulates mechanical contraction. There are no specialized conduction fibers within atria, and the impulse spreads from cell to cell to cover the entire atria within 0.08 s. Mechanical contraction requires approximately 0.1 s, longer than the spread of the electrical signal.

There is a delay in electrical signal transmission from atria to ventricles. As the signal enters the atrioventricular (AV) node, it is held for >0.1 s before entering the specialized conduction system (the bundle of His) in the interventricular septum. This delay allows atria to empty prior to ventricular systole onset. Propagation of the electrical signal from the AV node through the bundle of His to the ventricular myocardium is followed by mechanical systole onset, which requires ~0.3 s.

Electrocardiogram (ECG) reflects electrical activity (Fig. 1.2). It typically consists of a P wave, QRS complex, and T wave. The P wave is the electrical signal that starts atrial contraction, the QRS complex serves the same function in the ventricles (depolarization), and the T wave identifies an electrical reset of ventricles for the

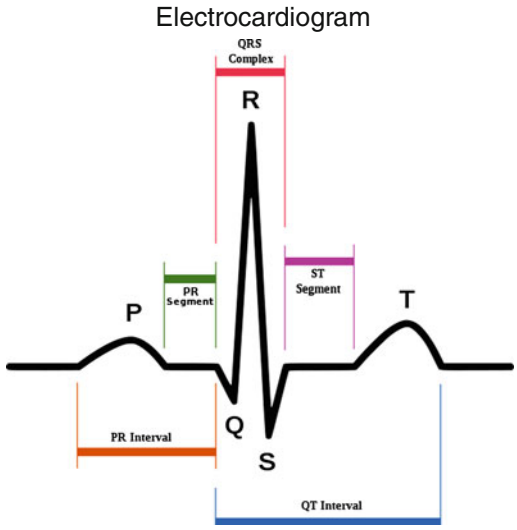

Fig. 1.2 Electrocardiogram depicting *P* wave, *QRS* complex, and *T* wave. (*Source* Wikipedia)

next cardiac cycle (repolarization). During much of diastole, the heart is electrically silent.

1.4 Radionuclide Imaging

The major clinical indications for radionuclide studies of the heart are to characterize the presence and severity of acquired heart diseases, such as the following:

1. Measure regional and global myocardial perfusion and perfusion reserve in patients with known or suspected coronary artery disease (CAD).
2. Determine the stability of regional and global RV and LV function in patients treated with cardiotoxic drugs and patients with congestive HF.
3. Quantify the relationship of myocardial perfusion to myocardial glucose utilization to detect viable ischemic myocardium.
4. Determine sympathetic innervation in patients with congestive HF.

Radionuclide images are recorded with either single-photon or positron-emitting radiopharmaceuticals. State-of-the-art instrumentation records both anatomic and emission information contemporaneously, which allows localization and attenuation correction of emission data. Combined radionuclide cameras and computed tomography (CT) devices, commonly known as hybrid camera instrumentation, are available for both single-photon-emission CT (SPECT) and annihilation radiation detection positron-emission tomographs (PET). PET has a much higher spatial resolution ($\sim$3 mm in reconstructed data) than do single-photon systems ($\sim$8 mm in the reconstructed data). The newest PET instruments comprise time-of-flight (TOF) information, allowing very high contrast and improved spatial resolution compared with earlier instrumentation. In addition to higher spatial resolution, PET perfusion tracers have the added capability of absolute quantitation; for example, they allow calculation of global and regional coronary flow reserve (e.g., expressing myocardial perfusion as milliliters per gram of myocardium).

1.5 Myocardial Perfusion Imaging

Normal coronary arteries are 3 mm in diameter at vessel origin. Coronary arteries (Fig. 1.3) are capable of supplying the myocardium with 0.6–1 mL/min per gram of LV muscle under basal conditions. When the myocardial oxygen demand increases (due to increases in heart rate, blood pressure, or both), arteries dilate, and blood flow typically increases by threefold (but may increase up to fivefold in physically well-trained individuals). If a coronary artery is narrowed by >50%, blood flow cannot increase sufficiently to meet the demand for oxygen. When myocardial oxygen demand exceeds oxygen supply, myocardial ischemia occurs. The underperfused myocardium zone stops contracting within a few seconds if the mismatch is severe, or contraction is reduced if the mismatch is less severe, causing a regional-wall-motion abnormality on gated perfusion images recorded during ischemia. If the area supplied by the stenosed coronary artery is extensive, overall ventricular function may be impaired, reducing the ejection fraction (EF).

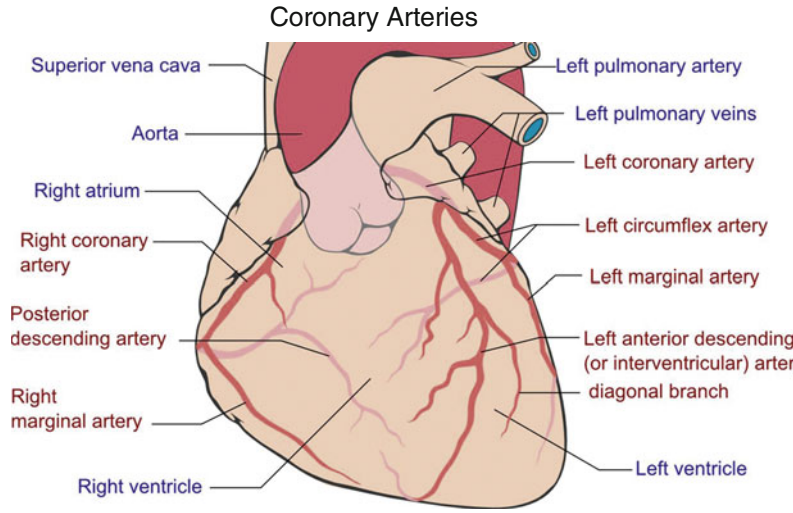

Fig. 1.3 Major coronary arteries, anterior view. (*Source* Wikipedia)

Perfusion imaging is primarily performed to detect the location and extent of reduced myocardial perfusion. To detect myocardial ischemia, two sets of perfusion images are recorded: one following injection at rest, and the second following injection at peak stress. The rest injection defines the distribution of myocardial perfusion when there is basal coronary blood flow. Regions of decreased perfusion at rest are usually caused by myocardial scar, typically due to prior infarction. The peak stress injection defines the distribution of myocardial perfusion when there is maximal coronary blood flow. A region of decreased perfusion seen on stress-injected images, which was not present at rest, signifies an area of myocardial ischemia. An unchanged region of diminished perfusion seen at rest and stress signifies myocardial scar.

1.5.1 Single-Photon Agents Used for Perfusion Imaging

A myocardial perfusion agent should have the following properties:

1. High first-pass myocardial extraction ($\geq$60%).
2. Linear relationship between myocardial uptake and coronary flow.
3. Myocardial uptake independent of metabolic state.
4. Stable myocardial distribution during imaging.

Thallium-201 is a monovalent cationic radiopharmaceutical with biological behavior similar to that of potassium. The agent has a first-pass myocardial extraction of 88%, a linear relationship to flow up to approximately 2.5 times basal flow rates, and myocardial uptake and initial retention independent of metabolic state. Approximately 3.5% of the injected activity localizes in the myocardium. Myocardial concentration of thallium-201 will decrease by 30–50% over the course of $\sim$4 h, with more rapid clearance from areas of normal perfusion than from regions of diminished perfusion. For diagnostic purposes, thallium-201 images must be recorded within $\sim$20 min of tracer administration to depict the distribution of myocardial perfusion at the time of injection. This property of redistribution makes it possible to detect areas of ischemia by comparing images recorded immediately after injection to delayed images recorded several hours later. This attribute of the tracer serves as a basis for viability imaging. The long effective half-life (and the high renal retention) limits the dose to be injected to $\sim$4 mCi.

Two technetium-99m (^{99m}Tc)-labeled tracers, sestamibi [methoxyisobutyl isonitrile (MIBI)] and tetrofosmin are now in wide clinical use. They have lower myocardial extraction ($\sim$60%

for MIBI and 55% for tetrofosmin versus 88% for thallium-201); therefore a smaller fraction of the injected activity localizes in the myocardium. However, tetrofosmin and MIBI have more favorable dosimetry (20 mCi of MIBI delivers 3.6 rad to the large bowel, and 20 mCi of tetrofosmin delivers only 1.5 rad), which permits administration of activities up to 30 mCi. The higher administered activity results in much greater photon flux from the myocardium and allows recording of high-quality, gated data after injection at rest and at stress. MIBI and tetrofosmin have biological half-lives >5 h in the myocardium, allowing images to be recorded up to 90 min after injection. Because technetium-99m agents do not redistribute, separate injections are required to depict perfusion at rest and under stress.

To detect ischemia, thallium-201 and technetium-99m agents perform equally well. The sensitivity of myocardial perfusion imaging for detecting CAD is >85% and the specificity of this test is 80–90%. Thallium-201 is preferred over technetium-99m tracers when there is a question of myocardial viability.

1.5.1.1 Exercise Stress Test

In patients who are able to exercise and achieve an adequate heart rate (defined as ≥85% of their age-predicted maximum heart rate), double product (defined as product of peak systolic blood pressure and heart rate ≥20,000) or workload (defined as ≥80% functional aerobic capacity), treadmill or bicycle exercise is the preferred form of stress because it provides the most information concerning patient symptoms, cardiovascular function, and hemodynamic response during usual forms of activity. The inability to perform an exercise test is a negative prognostic factor in patients with CAD.

To maximize detection of CAD with stress perfusion imaging, the radiopharmaceutical should be administered at the peak of exercise and the exercise should continue for an additional 1–2 min to permit the tracer to clear from the blood and localize in the myocardium in proportion to perfusion at the peak of exercise. Imaging should commence within 10 min of injection with thallium and within 15–45 min for MIBI and tetrofosmin. Imaging within a short time of the conclusion of stress increases the likelihood of detection of markers of severe ischemia, such as increased lung uptake on ^{201}Tl images and transient enlargement of the LV cavity and/or a drop in EF on either ^{201}Tl or ^{99m}Tc images. These markers of increased risk may be present even in the absence of disparities on the rest/stress perfusion images [3].

1.5.1.2 Pharmacological Stress Test

Some patients cannot exercise because of peripheral vascular disease, neurological problems, or musculoskeletal abnormalities. In these patients, myocardial blood flow can be increased by administering drugs that cause vasodilation of the coronary arteries. Vasodilators typically used are adenosine receptor agonists and include dipyridamole, adenosine, and regadenoson. Dipyridamole reduces the metabolism of endogenously produced adenosine by inhibiting adenosine deaminase, which results in increased tissue concentrations of adenosine. Exogenous adenosine, on the other hand, directly increases the tissue concentration of adenosine. Regadenoson is a newer agent that selectively occupies the adenosine A2 receptor sites and may cause fewer side effects. Dipyridamole lasts for hours after administration; adenosine has a biological half-life of only 10 s; regadenoson has a biologic half-life of approximately 30 min.

When these drugs are infused, coronary arteries dilate to increase myocardial blood flow uniformly to all areas of the myocardium. If tracer is administered at the time of the maximum effect of the drug, all areas of the myocardium show homogeneous uptake. If a vessel is markedly narrowed or fails to vasodilate appropriately (caused by endothelial dysfunction, a phenomenon that occurs in areas with underlying inflamed atheroma), flow distal to the narrowing does not increase to the same degree as that in myocardial territories supplied by normal coronary arteries, and areas of low uptake can be seen (Fig. 1.4). Although this

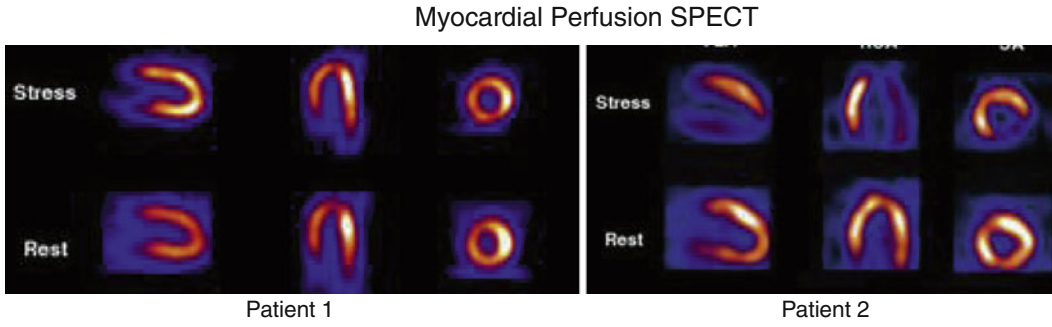

Fig. 1.4 Myocardial single-photon-emission computed tomography (SPECT) images at rest (*bottom row*) and during stress (*top row*) in two patients in the vertical long axis (*left*), horizontal long axis (*center*), and short axis (*right*). The patient on the *left* does not have myocardial ischemia or scar. The patient on the *right* has significant narrowing of the right coronary artery, which is not flow limiting at rest but is flow limiting after administration of vasodilator stress

phenomenon does not usually cause ischemia, as occurs in exercise tests, the underlying basis for detecting abnormalities (stenosis of a coronary artery) remains the same.

The effects of dipyridamole, adenosine, and regadenoson are counteracted by caffeine and xanthine-containing medications such as aminophylline. In the unlikely event that a patient develops serious complications, such as third-degree heart block or severe hypotension, aminophylline should be available for immediate intravenous administration. As adenosine is very short-lived, stopping the infusion usually will decrease symptoms within ~1 min. To avoid false-negative test results when these agents are used as a pharmacologic stress, patients should abstain from caffeine-containing products for at least 24 h prior and should discontinue all xanthine-containing medications 36 h before the study. Adenosine or regadenoson infusions are often combined with low-level exercise to minimize side effects and improve the image quality.

An alternative to vasodilator pharmacologic stress utilizes dobutamine, a sympathomimetic drug that increases heart rate and blood pressure. This agent increases myocardial work and hence the need for increased flow in coronary arteries. In contrast to other drugs in this category, dobutamine produces a low incidence of cardiac arrhythmia. The drug has a half-life of ~1–2 min, which limits the duration of effect. As with vasodilator agents, heart rate, electrocardiograph (ECG), and blood pressure must be monitored continuously during administration. Because the drug causes increased oxygen consumption, it can cause ischemia, similar to the effect of exercise.

Although pharmacological testing is useful in patients who cannot exercise, vasodilator agents cause a marked increase in blood flow to the liver, which can make it difficult to see lesions of the inferior wall. Neither the vasodilators nor dobutamine provide the breadth of information about cardiac performance that is available with an exercise study. Exercise testing offers information about the overall status of the patient's cardiovascular fitness, the exercise duration and severity that cause symptoms, and timing of symptoms versus. objective indicators of ischemia (ST segment changes on ECG or perfusion-scan abnormalities). This information frequently plays a key role in therapeutic planning.

1.5.2 Single-Photon Data Acquisition

Data can be recorded with planar or SPECT techniques. Planar imaging is rarely used, except in morbidly obese patients, in whom the quality of SPECT images is reduced. SPECT cardiac images are recorded at 3° to 6° steps in an arc spanning at least 180°, beginning at 30° right anterior oblique (RAO) and moving to 30° left

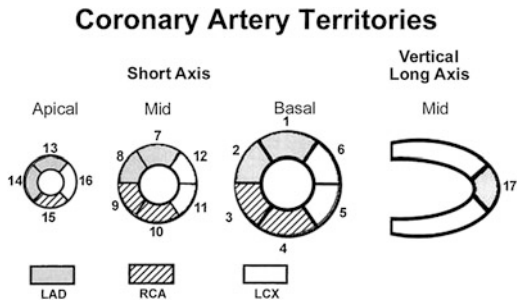

Fig. 1.5 The 17-segment model used to evaluate myocardial perfusion images and regional wall motion. Tracer uptake (for perfusion) or regional wall motion in each segment is scored using a five-point grading system: 0 = normal radiotracer uptake or regional function, 1 = mildly reduced, 2 = moderately reduced, 3 = severely reduced, and 4 = absence of radiotracer uptake. From [8]

posterior oblique (LPO). Images are usually recorded with a multidetector scintillation camera with extrinsic resolution better than 5 mm full width at half maximum (FWHM),with the two detectors positioned at 90° to each other. The individual projections are reconstructed into a series of transverse slices through the imaged volume. The transverse slices are reoriented along the long and short axes of the LV. The reoriented images are then reconstructed into three standard cardiac views: vertical long axis (corresponding to coronal images), horizontal long axis (corresponding to transverse sections), and short axis (corresponding to sagittal views). These reoriented images depict the myocardium or blood pool in a standard 17-segment presentation, which simplifies interpretation (Fig. 1.5). Short-axis images depict the myocardium from the apex to the base; vertical long-axis images slice the volume from the anterolateral wall to the inferior wall; horizontal long-axis images depict the RV, septum, and posterior wall. Transverse section images should provide six to eight slices through the heart (typical reconstructions are one to two pixels thick, with no spaces between slices). Before reconstruction, projection images should be reviewed as a cinematic display to detect patient motion, major changes in cardiac position during acquisition, and technical problems, such as missed or duplicated angles. Single episodes of motion less than two pixels can usually be tolerated. Although motion-correction software is available in many reconstruction software programs, corrections are often incomplete and may result in artefacts in reconstructed data.

To maximize spatial resolution, high- or ultrahigh-resolution collimation should be used, and detectors should be as close as possible to the surface of the patient when recording each image. Mechanically, it is easiest to rotate the detector through a circle when recording data for 15–60 s at each step.

New camera designs employing multi-pinhole collimation or multiple arrays of detectors with parallel-hole collimation and cadmium zinc telluride (CZT) detectors have a spatial resolution that is on par with PET imaging (3–5 mm). These systems permit data acquisition from the entire myocardium simultaneously, eliminating the need to move the detector during acquisition. Detectors are arranged in a semicircular arc, allowing data acquisition in 180°. As the entire heart is viewed simultaneously by the detectors, image acquisition time can be shortened without decreasing image quality. Alternatively, the administered activity can be reduced (as well as radiation burden to the patient) while imaging time is maintained. Preliminary studies comparing the performance of these ultrafast cameras with standard SPECT systems are encouraging [4, 5].

1.5.2.1 Gated Image Display

Data is usually recorded with synchronization to the patient's cardiac cycle (ECG gating). Gated acquisitions can be processed to show regional-wall motion and EF in addition to myocardial perfusion data (which is usually determined from the summed data due to the reduced noise). After data reconstruction, gated slices are usually displayed as multiple cine loops on the screen for visual assessment. Thereafter, endocardial borders of the midventricular horizontal and vertical long-axis slices are defined, and EF and ventricular volumes are calculated. These data can be appended to the evaluation of

myocardial perfusion and are particularly useful for determining the appearance of regional function in areas of diminished perfusion. Because the gated study is performed at rest, after the ischemic episode is over, zones of ischemia may have normal function (i.e., appear as areas of decreased intensity with normal thickening). Areas of scar, on the other hand, should have decreased perfusion and diminished function. Information about regional and global function adds diagnostic value to the overall procedure.

1.5.2.2 Attenuation Artifacts

Soft tissue of the chest, breast, and diaphragm are known to cause signal attenuation and lead to artifacts that resemble perfusion defects. Sometimes, the pattern is difficult to separate from real perfusion abnormalities. Generally attenuation is more pronounced for the lower-energy photons of ^{201}Tl and slightly less significant for ^{99m}Tc. Attenuation is typically accounted for by reviewing gated data in concert with perfusion images. Fixed defects attributable to attenuation should show normal function. Alternatively, prone imaging may mitigate certain attenuation artifacts. Attenuation correction can also be achieved by measuring attenuation coefficients using a transmission source, such as X-ray CT. The information is incorporated into reconstruction data to compensate for attenuation.

1.5.3 PET and Myocardial Perfusion

Positron-emitting radionuclides for assessing regional perfusion can be classified into two groups: tracers that are only partly extracted by myocardium: rubidium-82 (^{82}Rb) chloride and nitrogen-13 ([^{13}N] ammonia), and tracers that are freely diffusible: oxygen-15 [^{15}O]-water. ^{82}Rb chloride, a US Food and Drug Administration (FDA)-approved radiopharmaceutical, is available from a strontium-82 (^{82}Sr) generator (there is no need for a cyclotron on-site) and has a physical half-life of 75 s; ^{82}Rb behaves physiologically similarly to ^{201}Tl and is initially concentrated in the myocardium in proportion to regional myocardial perfusion, with an extraction of 65%. Retention of ^{82}Rb chloride depends at least partly on sodium–potassium adenosine triphosphatase (Na/K-ATPase) transport. Myocardial accumulation of ^{82}Rb chloride depends partly on the metabolic state of the myocardium. The short physical half-life of this tracer permits repeat measurements of myocardial perfusion with intervals as short as 10 min between measurements.

Nitrogen-13 ammonia, produced by deuteron bombardment of oxygen-16 (^{16}O) in a cyclotron, localizes in the myocardium in approximate proportion to regional myocardial perfusion, with the same practical limitations as ^{82}Rb chloride. Because of its 9.9 min physical half-life and favorable myocardial kinetics, image quality with [^{13}N]-ammonia is generally superior to that obtained with the shorter half-life ^{82}Rb. The 9.9 min physical half life and long myocardial retention require an interval of at least 45 min between rest and stress imaging.

Oxygen-15 is a cyclotron-produced radionuclide with a physical half-life of 122 s and can be used to label water ($H_2^{15}O$). Because water is virtually freely diffusible into myocytes, extraction of this tracer by myocardial tissue is nearly 100% and does not depend on the flow rate. In addition, this tracer is metabolically inert; therefore, its accumulation in the myocardium does not depend on the metabolic state of the tissue. However, because [^{15}O]-water resides in both the tissue and the blood pool, a second tracer (usually [^{15}O]-carbon monoxide, which is inhaled by the patient and subsequently binds avidly to erythrocytes) must be administered to permit correction for [^{15}O]-water activity emanating from the intravascular compartment.

As with single-photon myocardial perfusion imaging, separate rest and stress injections are required to detect myocardial ischemia and/or scar with PET radiopharmaceuticals. Stress images are usually produced by pharmacologically induced vasodilation with dipyridamole or adenosine. All these tracers yield accurate estimates of regional myocardial perfusion in

relative terms. Although quantification of myocardial perfusion in absolute terms can be most accurately performed with [^{15}O]-water, ^{82}Rb chloride and [^{13}N]-ammonia can also be used.

Most studies designed to assess accuracy of myocardial perfusion imaging with PET in detecting CAD used either ^{82}Rb chloride or [^{13}N]-ammonia. PET and SPECT have sensitivities ranging from 80 to 95%, depending on the patient population studied. However, because PET has higher energy of annihilation radiation and improved attenuation correction, its specificity tends to be ~10–15% higher than that of SPECT.

PET myocardial perfusion imaging has two advantages over single photon techniques: (1) it has a more robust attenuation correction, which reduces artifacts, and (2) absolute myocardial perfusion and flow reserve can be calculated. Flow reserve, the relative increase in myocardial perfusion from rest to stress, is a sensitive and specific indicator of coronary artery health. In patients with hyperlipidemia or diabetes and current smokers, perfusion reserve is diminished. Adding flow-reserve data to information on the regional distribution of myocardial perfusion enhances sensitivity of myocardial perfusion imaging. Flow reserve can be readily calculated from dynamic acquisitions at rest and at stress using commercially available software.

1.5.3.1 Myocardial Metabolism

Viability is typically assessed in a patient with a history of CAD and multiple infarcts, with a reduced EF and HF. In these patients, a combination of rest-injected perfusion imaging and an image recorded following injection of fluorine-18 fluorodeoxyglucose ([^{18}F]FDG) after preparation with glucose loading are compared. An area with decreased perfusion but relatively increased [^{18}F]FDG identifies ischemic but viable tissue. Patients with this outcome are often successfully treated with revascularization.

Fatty-acid tracers, such as [^{11}C]-palmitate and [^{11}C]-acetate are PET radiopharmaceuticals that are often employed in research studies. Myocardial uptake and clearance of palmitate reflects myocardial utilization of fatty acids; and acetate labeled with ^{11}C is a promising tracer of overall oxidative metabolism; [^{123}I]-beta-methyl-iodophenyl pentadecanoic acid (BMIPP) has been proposed as being able to identify ischemia at rest based on the ability to represent persistent metabolic alteration after recovery of ischemia, the so-called ischemic memory.

1.6 Radionuclide Evaluation of Ventricular Function

The heart's ability to function as a pump can be measured by recording data with ECG gating during myocardial perfusion imaging or by imaging a radiopharmaceutical that is retained in the blood pool. In perfusion imaging, the tracer allows visualization of wall motion, change in cavity size, and thickening of the myocardium from diastole to systole. An alternative approach labels the blood in the cardiac chambers. Blood-pool imaging allows assessment of both global and regional RV and LV function.

There are two approaches to evaluating ventricular function with tracers in the blood pool: first pass and equilibrium. Although recording techniques are different between the two measuring techniques, measurements are similar. These include chamber size and shape, wall motion during each beat, and ventricular EF assessment. An equilibrium-gated blood-pool study (GBP) is a preferred method over the first-pass method for assessing LV function due to technique and data processing simplicity.

1.6.1 MUGA

Because multiple points in the cardiac cycle are recorded, the technique is often called multiple-gated acquisition (MUGA). After the tracer has equilibrated in the blood pool (~5–10 min after administration of labeled red cells), data are recorded in synchrony with the patient's cardiac cycle. The R wave of the patient's ECG is used as a fiducial marker for the end of diastole. Heart rate is expressed in milliseconds per cycle. Cardiac cycle length is usually divided into 16

frames (or 32 or 64 frames to determine filling rates). The computer is programmed to record data from the first portion of the cardiac cycle into the first frame, the second portion of the cycle into the second frame, and so on until the last frame is reached or the next R wave is sensed, which resets the recording to the first frame to repeat the process. Data from ~500–1,000 cycles are added to obtain an "average" cardiac cycle. Equilibrium GBP imaging can be done as either planar or SPECT acquisition.

- Planar images are usually recorded in three views: (1) anterior (to examine right atrial and RV size and motion); (2) 45° left anterior oblique (LAO), optimized to separate the RV and LV and to determine timing and motion of the anterior and posterior wall, and motion and thickening of the septum of the LV); (3) either the left-lateral or left-posterior oblique view (to view inferior and posterior surfaces of the LV and size and motion of the left atrium). In planar imaging, the left atrium overlaps the LV posteriorly in the LAO view; the RV obscures the inferior wall of the LV in the RAO or anterior view. Because the left atrium and LV beat out of phase with each other (i.e., the atrium fills while the ventricle empties and vice versa), including the left atrium in the LV region of interest (ROI) reduces the calculated LVEF.
- Gated blood-pool SPECT images are acquired in a similar fashion to myocardial perfusion studies, with two detectors at 90° recording information from the 45°RAO to the 45° LPO positions. Data are reconstructed in similar fashion to perfusion images, with reorientation of blood-pool data to produce a standard cardiac orientation. Reconstructed and reoriented tomographic display permits more accurate assessment of right and left atrial and ventricular function and chamber size. The function of each myocardium segment can be assessed using the same 17-segment model employed for perfusion imaging.

If the patient has a markedly irregular heart rate (>10% variation in R–R interval in >10% of beats), as occurs in atrial fibrillation or with multiple premature contractions, heart filling and emptying rates change substantially from beat to beat. As a result, gating becomes difficult, and wall motion and EF cannot be optimally assessed.

1.6.2 Data Analysis

Planar LAO or best septal view is analyzed to calculate EF from total counts in the LV at end-systole and end-diastole (after background correction). ROIs can be drawn over the LV automatically (using either a second derivative or threshold algorithm) or manually. A background region is selected, located between the 3 o'clock and 6 o'clock positions from the LV away from the pulmonary artery, left atrium, and spleen. The background subtraction step is crucial to the subsequent EF calculation. Subtraction of too much background results in a falsely elevated EF, and subtraction of too little produces a falsely depressed EF. The total background-corrected counts in the LV on each frame are then normalized to the counts in the end-diastolic frame, and the time-activity curve from the LV ROI is displayed. The EF is calculated from the time-activity curve. Normal values for the LVEF range from 50 to 75%. Normal LVEF in women is generally ~5% higher than men, because female hearts are slightly smaller. In addition to EF, the time of filling and emptying and ejection and filling rates of ventricles can be readily computed from these curves. An alternative approach to calculating EF uses a single ROI, based on the end-diastolic frame, to measure the time-activity curve. The LVEF can also be calculated from the gated SPECT data, by counting the pixels in the left ventricular ROI at diastole and systole.

A major application of rest GBP images is evaluation of LV function in patients receiving potentially cardiotoxic chemotherapy. Patients frequently are evaluated before administration of these agents and at the conclusion of a course of therapy. Patients with a drop in LVEF ≥5% from a prior determination or whose LVEF are <50% are likely to be experiencing significant

cardiotoxicity from the therapy. Patients with antecedent heart disease are at particular risk.

Regional motion of the LV and RV can be readily appreciated from visual assessment of the cinematic display. One approach applies a qualitative assessment to specific segments in the LV. Each segment is evaluated as being either normal, mildly hypokinetic, moderately hypokinetic, severely hypokinetic, or akinetic/dyskinetic. An alternative approach to depicting regional function is the stroke-volume image, obtained by subtracting the end-systolic from the end-diastolic image. Similarly, a "dyskinesis" image can be recorded by subtracting the end-diastolic from the end-systolic image. Phase and amplitude images can also be generated. Phase analysis assumes that the heart contracts in a specific pattern that resembles the waveform of a cosine function. Each pixel in the image can be evaluated for the timing (phase) of these changes in activity and for its amount of change (amplitude) between maximum and minimum count values in the pixel. This information can be calculated and presented as a functional image in which specific colors or brightness represent information about amplitude or phase. A novel 3D GBP SPECT approach, from which a contraction homogeneity index is derived and compared with planar-phase analyses, is being assessed as a potential marker for evaluating patients in need of cardiac resynchronization therapy [6].

1.7 Imaging Cardiac Neurotransmission

Imaging of the regional myocardial distribution of adrenergic innervation has been used to assess certain cardiomyopathies and regional changes of myocardial innervation in ischemic heart disease. Catecholamine excesses are characteristic of the pump-failure state; however, myocardial norepinephrine stores are depleted due to reduced beta-adrenergic receptor density and decreased norepinephrine transport activity. Alterations in myocardial sympathetic activity may result in ventricular arrhythmias and even sudden cardiac death.

Iodine-123-metaiodobenzylguanidine ([^{123}I]-MIBG) is a guanethidine derivative known as a potent neuron-blocking agent acting selectively on sympathetic nerve endings. MIBG has a molecular structure similar to that of noradrenaline and therefore increased affinity for neuronal uptake. It also utilizes the same uptake and storage mechanism as noradrenaline. [^{123}I]-MIBG shows increased uptake in the healthy heart because of its dense sympathetic innervation. Myocardial [^{123}I]-MIBG uptake and retention is reduced in patients with congestive HF, indicating an alteration in sympathetic nervous system activity. Planar and SPECT images of the heart are typically acquired at 20 min and again 4 h after tracer administration. SPECT imaging is particularly helpful for separating overlapping lung and myocardial activity. A qualitative visual assessment is made using a point scale for detecting reduction in [^{123}I]-MIBG concentration in given myocardial segments. An accelerated myocardial washout rate is an indicator of sympathetic dysfunction. A semiquantitative measurement of myocardial [^{123}I]-MIBG uptake is also performed on the anterior planar view by placing ROIs over the LV myocardium and the noncardiac portion of the mediastinum; a heart-to-mediastinum ratio (HMR) is then calculated. An HMR <1.4 on delayed images is generally considered abnormal. The landmark multicenter AdreView Myocardial Imaging for Risk Evaluation in Heart Failure (ADMIRE-HF) trial prospectively validated the strong prognostic value of quantitative MIBG imaging in a large population of patients with HF. During a median follow-up of 17 months, 237 of 961 patients experienced 293 events, which were significantly more frequent in patients with a heart/mediastinum ratio (H/M) <1.6. Preserved neuronal uptake of [^{123}I]-MIBG (H/M >1.6) in this population was associated with $<1\%$ incidence of cardiac death per year; whereas, patients with an H/M <1.2 had a tenfold greater risk of cardiac death (9.6% annual rate) [7]. [^{123}I]-MIBG imaging is also under

evaluation as an adjunct biomarker for predicting response to resynchronization therapy in patients with cardiac dyssynchrony [8].

References

1. Roger VL, Go AS, Lloyd-James DM, Benjamin EJ, Berry JD, Borden WB (2012) Heart disease and stroke statistics—2012 update. Circulation 125:e12–e230
2. Prinzmetal M, Kennamer R, Merliss R, Wada T, Bor N (1959) Angina pectoris. I. A variant form of angina pectoris; preliminary report. Am J Med 27:375–388
3. van der Veen BJ, Kuperij N, Stokkel MPM (2010) Transient ischemic dilatation ratio derived from myocardial perfusion scintigraphy: What are we looking at? J Nucl Cardiol 17:207–215
4. Duvall DL, Sweeny JM, Croft LB et al (2011) Comparison of high efficiency CZT SPECT MPI to coronary angiography. J Nucl Cardiol 18:595–604
5. Gimelli A, Bottai M, Giorgetti A et al (2011) Comparison between ultrafast and standard single-photon emission CT in patients with coronary artery disease: a pilot study. Circ Cardiovasc Imaging 4:51–58
6. Harel F, Finnerty V, Grégoire J et al (2008) Comparison of left ventricular contraction homogeneity index using SPECT gated blood pool imaging and planar phase analysis. J Nucl Cardiol 15:80–85
7. Jacobson AF, Senior R, Cerqueira MD et al (2010) Myocardial iodine-123 meta-iodobenzylguanidine imaging and cardiac events in heart failure. Results of the prospective ADMIRE-HF (AdreView Myocardial Imaging for Risk Evaluation in Heart Failure) study. J Am Coll Cardiol 55:2212–2221
8. Tanaka H, Tatsumi K, Fujiwara S et al (2012) Effect of left ventricular dyssynchrony on cardiac sympathetic activity in heart failure patients with wide QRS duration. Circ J 76:382–389

Recommended Reading

9. Cerqueira MD, Weissman NJ et al (2002) Standardized myocardial segmentation and nomenclature for tomographic imaging of the heart: a statement for healthcare professionals from the cardiac imaging committee of the council on clinical cardiology of the American heart association. Circulation 105:539–542 (American Heart Association Writing Group on Myocardial Segmentation and Registration for Cardiac Imaging)
10. Lloyd-Jones D, Adams RJ, Brown TM et al (2010) Heart disease and stroke statistics–2010 update: a report from the American Heart Association. Circulation. 121:e46–e215
11. Bonow RO, Mann DL, Zipes DP, Libby P (2011) Braunwald's heart disease: a textbook of cardiovascular medicine, 9th edn. Elsevier, Philadelphia
12. McCardle WD, Katch FI, Katch VL (1981) Exercise, physiology, energy, nutrition and human performance. Lea & Febiger, Philadelphia
13. Zaret BL, Beller GA (2010) Clinical nuclear cardiology: state of the art and future directions, 4th edn. Elsevier, Philadelphia

How Should We Stress the Human Heart?

2

Eliana Reyes

2.1 Introduction

Cardiac stress testing, whether conducted alone [e.g., exercise electrocardiogram (ECG)] or combined with cardiac imaging, plays a major role in the diagnosis of coronary artery disease (CAD) by provoking myocardial ischemia and allowing the detection of myocardial perfusion abnormalities that arise from flow-limiting coronary stenosis. Most flow-limiting stenoses would otherwise go undetected, as compensatory dilation of the resistance vessels maintains resting myocardial blood flow within normal limits. During cardiac stress, hyperemic flow varies linearly with perfusion pressure, resulting in reduced myocardial perfusion as stenosis severity increases. This results in disparate distribution of myocardial blood flow and forms the basis for perfusion imaging. Depending on the severity of underlying stenosis and the magnitude of increase in oxygen demand, cardiac stress may induce myocardial ischemia, which would result in angina, ECG and hemodynamic changes, and myocardial contractile dysfunction in addition to perfusion abnormalities. Cardiac stress imaging therefore provides valuable diagnostic information to guide clinical decision making with regard to medical therapy and revascularization. Dynamic exercise and pharmacological stress agents are used for this purpose, with newly developed agents able to overcome some of the limitations of existing methods. How to stress the human heart is a question that can only be answered after a comprehensive understanding of the properties and mechanism of action of the various forms of stress currently available. This chapter is dedicated to the several modalities of cardiac stress used to assess patients with known or suspected CAD undergoing noninvasive cardiac imaging.

2.2 Dynamic Exercise

Isotonic or dynamic exercise is the most physiological form of cardiac stress and induces coronary hyperemia by increasing heart work and metabolic demand, hence provoking secondary coronary vasodilation. Maximal exercise can provoke a two to threefold increase in myocardial blood flow within a normal vascular territory. An optimal exercise test can add important diagnostic and prognostic information to imaging results by unveiling ischemic ECG and hemodynamic changes and allowing study of the relationship between symptoms and workload and assessment of exercise capacity, a well-recognized and independent predictor of adverse cardiac events.

E. Reyes (✉)
Nuclear Medicine Department,
Royal Brompton Hospital, London, UK
e-mail: e.reyes@rbht.nhs.uk

P. Marzullo and G. Mariani (eds.), *From Basic Cardiac Imaging to Image Fusion*,
DOI: 10.1007/978-88-470-2760-2_2,

Table 2.1 Contraindications to exercise testing

Absolute
• Recent acute or complicated myocardial infarction or unstable angina
• Known significant left-main-stem stenosis
• Acute or decompensated heart failure
• Untreated life-threatening arrhythmias
• Severe dynamic (e.g., HOCM) or fixed (e.g., aortic valve stenosis) LVOTO
• Poorly controlled and severe systemic hypertension
• Recent pulmonary embolism or infarction
• Severe pulmonary hypertension
• Acute systemic or cardiac inflammatory process or acute illness
Relative
• Reduced exercise capacity (e.g., orthopedic, musculoskeletal, or neurological condition that precludes dynamic exercise)
• Poor motivation or willingness to exercise

HOCM hypertrophic obstructive cardiomyopathy; *LVOTO* left ventricular outflow tract obstruction

2.2.1 Indications

Exercise is indicated in patients physically able and sufficiently motivated to reach an adequate level of cardiac work that would ensure a maximal or near-maximal coronary hyperemic response (Table 2.1). Preparation is similar to that of conventional exercise ECG with the exception that patients should be advised to refrain from methylxanthine-containing products, as vasodilator stress may be undertaken if the patient fails to complete the exercise test (see Sect. 2.3). Anti-ischemic drugs, especially beta-adrenergic blockers, may lead to a rise in ischemic threshold, which may reduce the sensitivity of diagnostic imaging [1]. Anti-ischemic drugs should therefore be discontinued for a minimum of five half-lives before the exercise test.

2.2.2 Contraindications

In addition to the well-known contraindications to exercise testing (Table 2.1), exercise should be avoided in patients with left bundle branch block (LBBB) and paced ventricular rhythm. This is particularly relevant to myocardial perfusion scintigraphy (MPS), as exercise is associated with a high incidence of septal defects on stress images in the absence of obstructive CAD (Fig. 2.1). The exact underlying mechanism remains unknown. Although it has been attributed to a true reduction in perfusion to the septum, recent evidence suggests that the temporal delay between left and right ventricular activation in LBBB may result in reduced septal thickening and decreased counts in the septum due to partial volume effect [2]. The rise in heart rate that occurs during exercise would increase the probability of septal defects arising from the conduction abnormality.

2.2.3 Protocols

Currently available protocols involve continuous exercise with incremental workloads between multiple stages, producing a progressive increase in myocardial oxygen demand. The choice of one protocol over the others depends on the patient's physical conditioning and familiarity with exercise (e.g., walking versus cycling). The treadmill Bruce protocol is the most commonly indicated test because it involves large increments in workload, allowing most patients to reach their maximal or near-maximal exercise capacity over a relatively

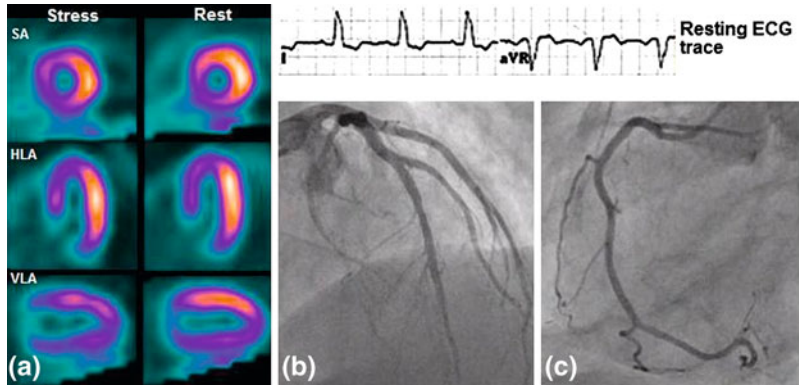

Fig. 2.1 Stress/rest myocardial perfusion scintigraphy (**a**) shows an extensive and partially reversible perfusion abnormality involving the septum and adjacent anteroseptal and inferoseptal regions in a patient with *LBBB* left bundle branch block on his resting *ECG* electrocardiogram, and normal left and right coronary arteries on subsequent coronary angiogram. (**b**, **c**) *SA* short axis, *HLA* horizontal long axis, *VLA* vertical long axis

short period. Regardless of the protocol used, an optimal exercise test should be symptom limited, with the patient achieving at least 85% of their age—and gender-adjusted maximum predicted heart rate unless cardiac symptoms and ischemic ECG changes develop (i.e., >1 mm ST-segment elevation in non-Q-wave leads or ≥2 mm horizontal or downsloping ST-segment depression at 60–80 ms after the J point in three or more consecutive beats on any ECG lead). At this point, the perfusion tracer is administered intravenously followed by a saline flush. After this, it is recommended that the patient continue exercising for at least 2 min to allow for adequate myocardial extraction of tracer (MPS protocol).

2.2.4 Diagnostic Performance and Accuracy

There is variation in the reported accuracy of exercise testing when combined with diagnostic imaging, partly because of differences in protocols and standards of interpretation. For instance, the sensitivity of exercise MPS for detecting coronary stenosis is in the region of 85%, whereas its specificity for ruling out disease is about 75% [3]. It is important to emphasize that the adequacy of the exercise test influences the diagnostic performance of cardiac imaging, as failure to increase myocardial oxygen demand may prevent detection of abnormal coronary vasodilator reserve. Hence, pharmacological stress must be considered in patients who fail to reach an exercise endpoint and in those expected to perform suboptimally.

2.2.5 Safety

Serious adverse events during exercise are uncommon, but the incidence increases in high-risk populations, such as those with severe multivessel CAD and impaired left ventricular function. In general, there is a 1 in 10,000 risk of cardiac death or fatal myocardial infarction (MI) and a 1 in 5,000 risk of nonfatal MI or life-threatening complications during exercise testing [4].

2.3 Pharmacological Agents

2.3.1 Vasodilators

These agents cause primary or direct coronary vasodilation independent of heart work and comprise two categories: (1) adenosine receptor agonists, which can be classified further

according to their selectivity for the adenosine receptor (nonselective agonists, adenosine; selective agonists, regadenoson, apadenoson, and binodenoson); (2) inhibitors of adenosine metabolism and breakdown (dipyridamole). In general, vasodilators cause a greater increase in blood flow, up to four to five times its resting level, than dynamic exercise. Importantly, these potent vasodilators may abolish coronary autoregulation; in the presence of significant epicardial stenosis, their administration may induce myocardial ischemia, especially in the subendocardium (see Sect. 3.1.1). Vasodilator stress has several practical advantages over exercise, including flexibility (as physical limitations would not affect test performance), high reproducibility, and the need for little or minimal motivation and cooperation from the patient. There are also a few disadvantages, such as inability to monitor adequacy of stress and the fact that it is not possible to assess the relationship between physical activity, metabolic stress, and symptoms.

2.3.1.1 Adenosine

Adenosine is a naturally occurring purine nucleoside composed of a molecule of adenine and ribose joined by a β-N_9-glycosidic bond. Over recent decades, it has become increasingly clear that adenosine plays a major role in the adaptation to inadequate oxygen supply by regulating several biological functions by activating adenosine receptors A_1, A_{2A}, A_{2B}, and A_3. In the cardiovascular system, adenosine reduces workload to the heart, slowing the heart rate by inhibiting sinus atrial (SA) node activity and delaying atrioventricular (AV) node conduction [5]. It also attenuates myocardial contractility that results from beta-adrenergic stimulation. However, the earliest response to a myocardial oxygen supply–demand imbalance is a rise in interstitial adenosine and a reduction in coronary vascular resistance [6]. Adenosine dilates the small resistance vessels by binding to adenosine A_{2A} receptors located on the surface of arteriolar smooth muscle cells [5]. Activation of this receptor subtype increases cellular cyclic adenosine monophosphate (cAMP), which in turn mediates the opening of potassium adenosine triphosphate (K_{ATP}) channels and decreases calcium (Ca^{2+}) uptake, causing smooth muscle relaxation [7]. Adenosine can also dilate the large conductance vessels by an endothelium-dependent flow-mediated mechanism, but this effect is rather modest and does not relate to the severity of coronary stenosis [8].

Adenosine has a rapid onset of action, with average time from infusion initiation to maximal coronary vasodilator response being achieved in little more than 80 s [9]. It is rapidly taken up by erythrocytes and endothelial cells following its intravenous administration, which explains the very short half-life (<10 s) and thus the need for continuous administration [10].

At the recommended dose for perfusion imaging (i.e., 140 mcg/kg/min), adenosine provokes maximal coronary vasodilation with a peak blood-flow velocity similar to that observed after intracoronary papaverine [9]. This leads to a fourfold increase in myocardial perfusion, with absolute values in the region of 4.5 mL/min/g [11, 12]. No further increase in coronary blood flow occurs at higher infusion rates. Smaller doses of adenosine can provoke maximal hyperemia but are associated with wide fluctuations in coronary vascular resistance [9]. In the presence of flow-limiting coronary stenosis, myocardial perfusion abnormality is primarily the result of heterogeneous distribution of blood flow. However, adenosine may induce myocardial ischemia through coronary steal. This phenomenon is characterized by a fall in driving pressure for collateral flow from normal to stenotic coronary territories as a result of the greater vasodilator response of the normal vascular bed to adenosine (intercoronary steal) [13]. Intercoronary steal is rare but relatively more prevalent among elderly patients with severe multivessel CAD. Blood-flow diversion from subendocardium to subepicardium may also occur (intracoronary steal) [14].

The peripheral hemodynamic response to 140 μg/kg/min of adenosine is rather modest, with an average decrease in both systolic and diastolic blood pressure of approximately

Table 2.2 Side effects during adenosine stress

Side effect	Adenosine only $n = 9{,}256$[a] (%)	Adenosine and exercise $n = 1{,}261$[b] (%)
Any symptom	81	56
Chest pain	35	17
Dyspnea	35	30
Flushing	37	7
Headache	14	5
Nausea	15	2
Dizziness	10	1

[a] Frequency ≥5%. Modified from [15]
[b] Reyes et al. [57]

10 mmHg and a heart rate increase in the region of 10 bpm, and this is an important advantage over other equally potent coronary vasodilators that can have a profound effect on peripheral resistance and blood pressure [9, 15]. Importantly, the systemic response to adenosine bears no predictable relationship to its coronary effect, and hence positive image findings may be seen in patients with a blunted hemodynamic response to adenosine [16]. This phenomenon has been attributed to differing receptor-affinity thresholds, variations in tissue-receptor reserve, cardiac output, and adrenergic and vagal tone, which might influence delivery and response to adenosine by the heart and other tissues and organs [17, 18].

Activation of receptors other than the coronary A_{2A} subtype occurs at vasodilator doses of adenosine. This nonselective activation is responsible for most adenosine-related side effects (Table 2.2). Although side effects are fairly common, they are usually mild and well-tolerated, although occasionally more significant [15].

2.3.1.2 Regadenoson

Regadenoson is among the newly developed selective adenosine A_{2A} receptor agonists and the only one commercially available. Regadenoson is a 2-[N-1-(4-N-methylcarboxamidopyrazolyl)]-adenosine derivative. Early receptor binding and tissue response experiments, as well as ex vivo isolated heart models, show a high binding and functional selectivity of regadenoson for the adenosine A_{2A} receptor, with minimal or no activity or binding for other adenosine receptors [19, 20]. These studies also show that regadenoson is more potent than adenosine at inducing coronary arteriolar vasodilation, with a half maximal effective concentration (EC_{50}) of 6.4 nM versus 59 nM for adenosine [19, 20].

The effect of regadenoson on the coronary circulation is concentration dependent, with single doses of 100, 300, 400, and 500 mcg causing a threefold increase in peak coronary blood-flow velocity [21]. Unlike lower doses, 400 and 500 mcg doses showed a sustained effect that lasted for at least 2 min, providing sufficient time for adequate myocardial extraction of tracer. Fewer side effects were reported with the 400 mcg dose. Subsequent studies demonstrate that body weight and body mass index (BMI) have no effect on the volume of distribution or total body clearance of regadenoson and do not appear to alter its efficacy for detecting inducible myocardial perfusion abnormality [22–24]. This evidence supports the use of a single dose of 400 mcg, which is characterized by a rapid onset of action, with peak coronary vasodilation by 30 s following intravenous administration and a short-lasting effect (<5 min). Importantly, there is no need for dose adjustment in patients with renal or hepatic failure [25, 26].

There is a modest decrease in both systolic and diastolic blood pressure of approximately 10 mmHg and an average increase in heart rate

of 25 bpm following an intravenous injection of 400 mcg [27]. The magnitude of increase in heart rate is out of proportion to the decrease in blood pressure, and this has been attributed to direct stimulation of adenosine A_{2A} receptors on the sympathetic nerve endings [28].

Clinical trials show that regadenoson has a side-effect profile similar to that of adenosine, although there are some variations between agents with regard to type, quality, and duration of side effects [27]. In general, most side effects are short lived, mild, and well tolerated. When compared with adenosine, test tolerability is better after regadenoson [22, 23].

2.3.1.3 Dipyridamole

Dipyridamole was the first vasodilator agent used for diagnostic imaging. It has a lipophilic pyrimidine base that inhibits cellular reuptake of endogenous adenosine and its breakdown, hence increasing its interstitial concentration [29]. The maximal coronary vasodilator response to dipyridamole is similar to that of exogenous adenosine, but adenosine is often preferred over dipyridamole because of its rapid onset of action and shorter half-life (10 s versus 30 min for dipyridamole) [30]. Dipyridamole causes fewer side effects than adenosine but they tend to last longer; administration of an adenosine receptor antagonist such as aminophylline is often required [31]. Despite this, the safety profile of dipyridamole is comparable with that of adenosine, but prolonged action and side effects can be seen in patients with liver failure owing to its hepatic metabolism [31].

2.3.2 Indications

Vasodilator stress is commonly indicated in patients with a contraindication to exercise or when it is not possible to obtain an adequate exercise test (Table 2.1). Vasodilators should be considered the first-line test in patients with LBBB or paced rhythm on their resting ECG because of the lower incidence of tachycardia-related artefacts on diagnostic imaging. Preparation for vasodilator stress includes abstention from methylxanthine-containing products, including coffee, tea, chocolate, caffeinated drinks and food, aminophylline, and theophylline for a minimum of 24 h prior to the test. Methylxanthines are competitive antagonists to the adenosine receptors and at concentrations commonly encountered in daily life may prevent the action of adenosine agonists (Fig. 2.2). Dipyridamole should be withheld for 48 h because it blocks adenosine transport and may prolong its effects. Discontinuation of antianginal drugs before vasodilator stress remains controversial, with limited evidence suggesting that beta-blockade may attenuate blood-flow heterogeneity induced by primary vasodilators (Fig. 2.3) [32–34].

2.3.3 Contraindications

In general, vasodilator stress should be avoided in patients with a history of severe obstructive airways disease or ongoing bronchospasm, advanced degree of atrioventricular block without a functioning pacemaker, symptomatic hypotension, and recent methylxanthine or dipyridamole use [35, 36].

Bronchospasm represents the commonest noncardiac adverse event caused by vasodilators and occurs almost exclusively in patients with obstructive airway disease. Adenosine and dipyridamole are therefore contraindicated in patients at high risk for or with ongoing bronchospasm. Regadenoson is not contraindicated in obstructive airway disease but should be administered with caution in these patients. Vasodilators should be avoided in patients with hypotension (i.e., blood pressure <90/60 mmHg) because of the potential for exacerbation owing to a reduction in vascular resistance, and in advanced degrees of AV block without a functioning pacemaker or with sick sinus syndrome because of the increased risk of rhythm disturbances. Further evidence is needed regarding safety and tolerability of regadenoson in patients with severe forms of obstructive airways disease and in patients with advanced

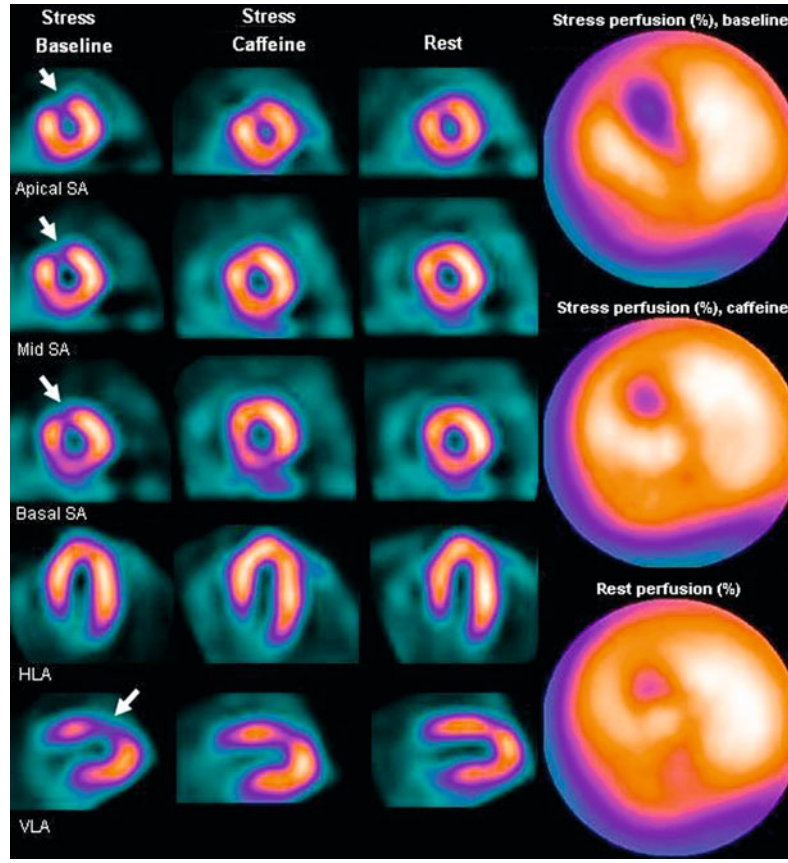

Fig. 2.2 Caffeine (serum caffeine level = 4.1 mg/L) attenuates the extent and depth of inducible perfusion abnormality (*arrows*) after 140 mcg/kg/min of adenosine in a patient with previous *CABG* (coronary artery bypass graft) [*LIMA*, left internal mammary artery to *LAD*, left anterior descending artery, vein grafts to *LCx*, left circumflex artery, and *RCA*, right coronary artery] and recurrent symptoms. *SA* short axis, *HLA* horizontal long axis, *VLA* vertical long axis

degrees of AV block. Although recent caffeine consumption is a contraindication to regadenoson stress, a study in healthy volunteers suggests that at the recommended dose of 400 mcg, regadenoson may overcome the antagonism mediated by caffeine on the adenosine receptors [37]. Further evidence is forthcoming in patients undergoing regadenoson MPS before and after caffeine intake [38].

2.3.4 Protocols

2.3.4.1 Adenosine

Standard protocol consists of an intravenous infusion of 140 mcg/kg/min of adenosine for 6 min, with tracer injection after 3 min of infusion (Fig. 2.4). Because of its rapid onset of action, several studies investigated the effectiveness of shorter adenosine protocols, observing a similar accuracy for detecting coronary stenosis with a 4- and 5- versus 6-min infusion [39]. Shorter infusion times (<4 min) were associated with smaller perfusion abnormalities on stress images; this may compromise diagnostic performance and should therefore be avoided [40, 41]. Coronary blood flow would return to baseline 1–2 min after termination of adenosine infusion. Adenosine may be coupled with dynamic or isometric exercise to reduce the incidence and severity of untoward effects (Table 2.2). Exercise is particularly effective in reducing the incidence of cardiac conduction abnormalities and intensity and frequency of side effects that result from the peripheral vasodilator effect of adenosine (e.g., headache, flushing, hypotension), hence improving test tolerability [42]. When combined with MPS, supplemental exercise is associated with better

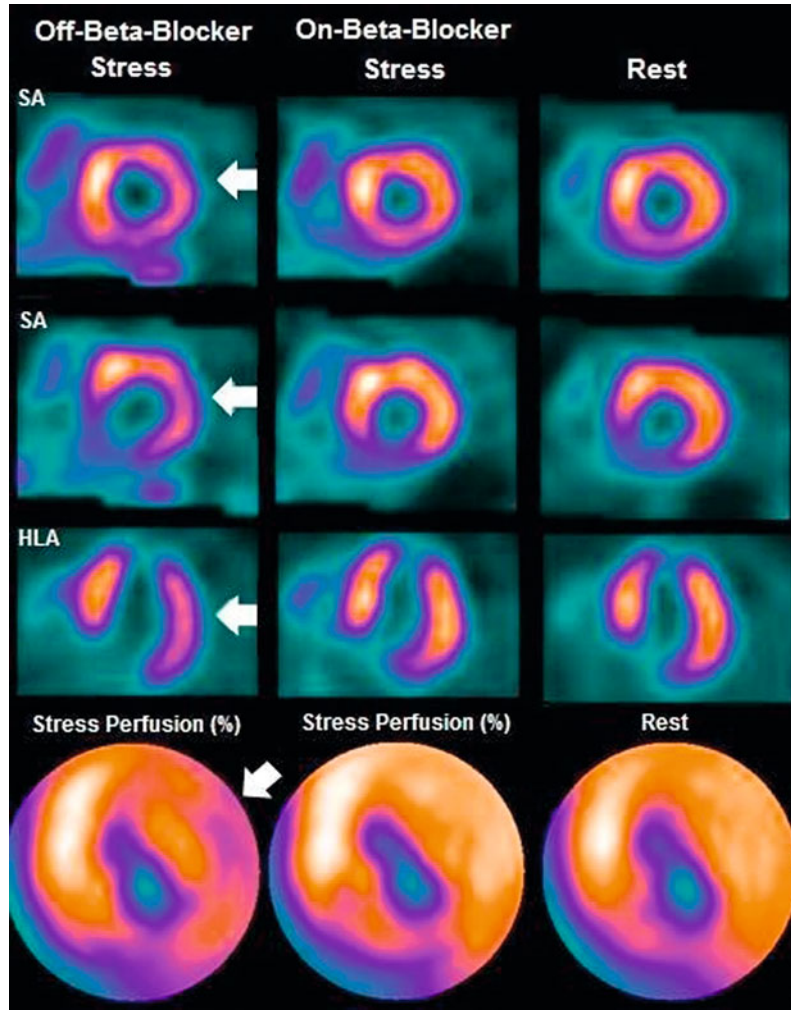

Fig. 2.3 Tomograms (*upper panel*) and polar maps (*lower panel*) show a mild but extensive adenosine-induced perfusion abnormality in the lateral wall (*arrows*) that is no longer present after beta-blockade. *SA* short axis, *HLA* horizontal long axis

image quality. Exercise enhances image quality by provoking splanchnic vasoconstriction, which reduces the extracardiac accumulation of tracer, thus increasing heart-to-background tracer-activity ratio [43]. Exercise may also enhance the detection of inducible myocardial perfusion abnormality, and this seems to be independent of its effect on image quality. Nearly 60% of all vasodilator stress tests are combined with exercise [44].

In patients with well-controlled or mild asthma or chronic obstructive pulmonary disease (COPD), adenosine can be given as a titrated protocol starting at a low dose of 70–100 mcg/kg/min for 1 min and increasing if tolerated up to 140 mcg/kg/min, with tracer injection 2 min after the maximal dose of 140 mcg/kg/min [45, 46]. A beta-2 adrenergic agonist inhaler, such as salbutamol, can be given prior to starting the adenosine infusion. In patients reporting recent caffeine consumption (<12 h) there is evidence that a 50% increase in adenosine dose (210 mcg/kg/min) may overcome the attenuating effect of caffeine contained in beverages such as coffee and tea [47].

2.3.4.2 Regadenoson

Regadenoson is administered intravenously as a single dose of 400 mcg over 10 s, followed immediately by a 10-mL saline flush with tracer injection 10–20 s after saline injection. No dose

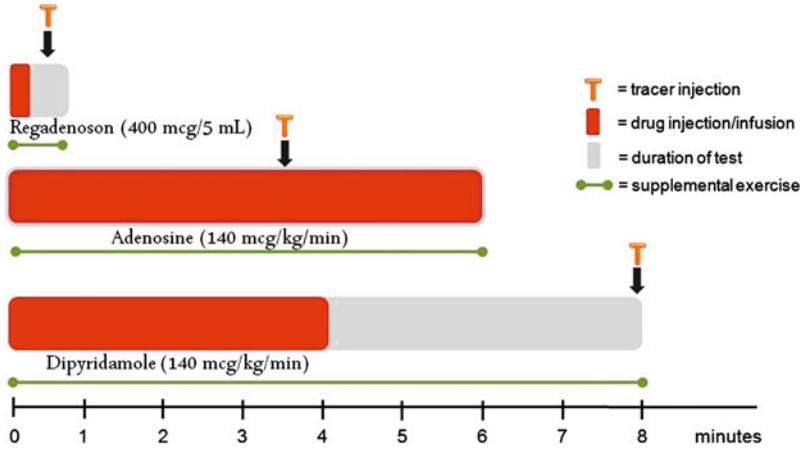

Fig. 2.4 Protocols for vasodilator stress myocardial perfusion imaging according to pharmacological agent. Heart rate, blood pressure, and *ECG* electrocardiogram should be monitored throughout. All vasodilators can be coupled with submaximal isotonic (dynamic) or isometric exercise

adjustment for patient weight or renal or hepatic function is required. Regadenoson is well tolerated, and most side effects are mild and short lived, but some symptoms may last up to 30 min. Aminophylline may be used to counteract persistent or intolerable symptoms. As with the other vasodilators, the addition of exercise may help reduce the incidence and severity of side effects and improve test tolerability [48].

2.3.4.3 Dipyridamole

Dipyridamole is given intravenously at 140 mcg/kg/min for 4 min (Fig. 2.4). As with the other vasodilators, it can be combined with exercise to minimize side effects and improve image quality when performed with MPS. Coronary hyperemia reaches a peak 3–4 min after completion of the infusion, at which point the tracer should be injected. As would be expected, hyperemic response to dipyridamole is equivalent in magnitude to that provoked by adenosine [30].

2.3.5 Diagnostic Performance and Accuracy

High accuracy for CAD detection is documented for vasodilator stress when combined with diagnostic imaging. The sensitivity of adenosine MPS for detecting angiographically significant epicardial coronary stenosis (≥70% luminal diameter reduction) is in the region of 90%, with a specificity ranging from 75 to 100% [3]. Diagnostic accuracy of dipyridamole MPS is similar to that of adenosine [3]. With regard to regadenoson, data from two large randomized clinical trials demonstrate that regadenoson MPS is not inferior to adenosine MPS for detecting inducible perfusion abnormality [27]. Indeed, good agreement between regadenoson and adenosine MPS has been found for several imaging variables [22, 27]. Furthermore, quantitative assessment of myocardial perfusion using a normal database suggests that the scintigraphic information obtained after regadenoson administration is almost identical to that following adenosine stress [49].

2.3.6 Safety

Adenosine stress has an excellent safety profile, with an estimated risk for death or nonfatal MI of less than 1 in 10,000 cases [15]. A similar low event rate is documented when adenosine is administered as early as 48–72 h after an uncomplicated acute coronary syndrome [50]. The safety profile of dipyridamole is similar to

that of adenosine, and pooled data so far suggest that regadenoson is equally as safe [31, 51]. Vasodilator stress should be stopped if symptomatic hypotension, bronchospasm, persistent and/or symptomatic arrhythmia, or signs and symptoms suggestive of severe myocardial ischemia occur.

2.4 Inotropic Agents

2.4.1 Dobutamine

Dobutamine is the only inotropic drug used for pharmacological stress testing. The value of dobutamine stress for perfusion imaging has not been documented as extensively as for the primary vasodilators, and estimates of its diagnostic accuracy vary significantly across publications. The latter is attributed to inadequate protocols, lack of standardized endpoints, and concomitant use of beta-adrenergic receptor blockers. In addition, the hyperemic effect of dobutamine is less predictable than that of primary vasodilators, and individual responses are highly variable and, in some cases, suboptimal. As a result, dobutamine is recommended only in patients in whom other forms of stress are not possible or are contraindicated.

Dobutamine is a sympathomimetic agent and a synthetic analog of dopamine. It exerts a potent β_1-adrenergic receptor-agonist action and a less profound β_2- and α_1-adrenergic receptor-agonist effect. At low doses (<20 mcg/kg/min), dobutamine exerts a predominant inotropic effect, increasing myocardial oxygen demand and provoking secondary coronary vasodilation and hyperemia. At higher doses, further activation of β_1-adrenoceptors results in a predominant chronotropic effect. The net effect is an increase in heart rate, myocardial contractility, cardiac output, and a small increase in blood pressure [52]. In some patients, vigorous myocardial contraction may activate intramyocardial mechanoreceptors, which cause sympathetic withdrawal and enhance parasympathetic activity. This is known as the vasodepressor Bezold–Jarisch reflex. As a result, paradoxical sinus deceleration and marked hypotension develop. This paradoxical response has also been associated with angiographically significant coronary stenosis and significant underlying ischemia [53].

The onset of action of dobutamine occurs 2 min after intravenous infusion initiation and reaches a peak 5–10 min later. The increase in myocardial perfusion is dose dependent; at doses ≥20 mcg/kg/min, dobutamine increases myocardial perfusion two to three times its resting value [54]. Dobutamine has a half-life of approximately 2 min owing to its rapid hepatic metabolism.

2.4.2 Indications

Contrary to its primary role in assessing myocardial contractile function and detecting ischemia-induced wall-motion abnormality, dobutamine is regarded as a third-line agent for perfusion imaging. It is mainly indicated when exercise is not possible and vasodilator stress is contraindicated. Preparation for dobutamine stress includes discontinuation of beta-adrenergic receptor antagonists for a minimum of five half-lives.

2.4.3 Contraindications

Because of its sympathomimetic effect, contraindication to dobutamine stress is similar to that of dynamic exercise, including recent acute coronary syndrome, untreated severe arrhythmias, and severe or uncontrolled hypertension. Dobutamine should also be avoided in patients with severe dynamic or fixed left ventricular outflow-tract obstruction. As for exercise, dobutamine is not ideal in patients with LBBB and ventricular paced rhythm, as these may cause artefactual perfusion abnormalities of the septum on stress MPS.

2.4.4 Protocol

Dobutamine is infused intravenously starting at 5 or 10 mcg/kg/min and increasing to 15, 20, 30,

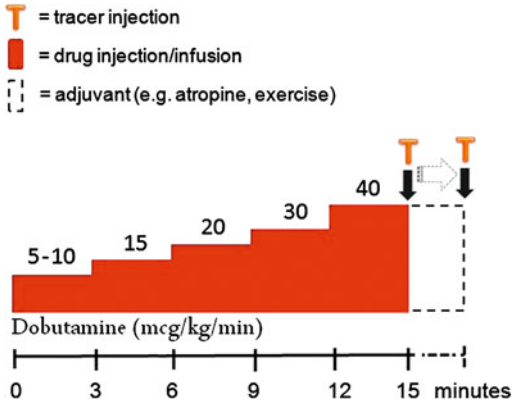

Fig. 2.5 Protocol for dobutamine myocardial perfusion scintigraphy (MPS). Protocol varies from center to center, but it normally consists of a stepwise IV injection of dobutamine starting at 5–10 mcg/kg/min and increasing by 5 or 10 mcg/kg/min every 3 or 5 min up to the maximal dose of 40 mcg/kg/min. The tracer is injected after 3–5 min on the maximal dose. In some centers, an adjuvant such as atropine is administered if ≥85% of maximal predicted heart rate is not achieved at the maximal dose. Heart rate, blood pressure, and electrocardiogram (ECG) should be monitored throughout the test

and 40 mcg/kg/min at 3–5 min intervals (Fig. 2.5). The tracer is injected after 3–5 min on the maximal dose of 40 μg/kg/min unless myocardial ischemia develops or age—and gender-adjusted maximal predicted heart rate is reached. In patients unable to reach maximal or near-maximal predicted heart rate, 0.25–2.0 mg of atropine, a competitive antagonist of muscarinic cholinergic receptors, can be administered intravenously. Atropine increases heart rate through blockade of vagal effects on M_2 receptors in the sinoatrial (SA) node. Side effects are rare, but atropine intoxication at relatively low doses (<1 mg) have been documented in the elderly.

Dobutamine can also be coupled with supplemental low-level exercise to prevent hypotension and improve test tolerability. Exercise may enhance image quality by reducing background liver and gut activity and may provide additional chronotropic and inotropic stimulation, with a further increase in myocardial oxygen demand [55].

2.4.5 Diagnostic Performance and Accuracy

Stress imaging with dobutamine has a diagnostic accuracy similar to that of exercise and vasodilators. The reported sensitivity of dobutamine MPS for detecting coronary stenosis is in the region of 80–90%, with a specificity ranging between 64 and 100% [52]. Sensitivity increases when atropine is added (from 82 to 90%) without compromising specificity [52].

2.4.6 Safety

The commonest side effects during dobutamine infusion are symptomatic hypotension, tachyarrhythmias, chest pain, and dyspnea, which usually respond to appropriate medical care. The safety profile of dobutamine is similar to that of other modalities of stress, but complications may arise in high-risk populations. In nuclear cardiology practice, the reported incidence of sustained ventricular tachyarrhythmias, nonfatal myocardial infarction, and cardiac death during dobutamine stress is low [52, 56].

2.5 Conclusion

Cardiac stress is an essential part of diagnostic imaging, and current practice relies on a number of methods that are effective at characterizing the hemodynamic significance of coronary obstruction and its impact on myocardial perfusion. A large body of evidence supported by expert consensus and anecdotal experience indicate that all existing methods are safe when performed appropriately, and their diagnostic accuracies are comparable. It is important to bear in mind that inadequate patient preparation and inappropriate use of any of these forms of stress may lead to a significant reduction in diagnostic accuracy of stress imaging. Moreover, it is advised that each imaging center regularly monitors local competence, diagnostic

accuracy, and safety according to the different modalities of stress used.

References

1. Muller-Suur R, Eriksson SV, Strandberg LE, Mesko L (2001) Comparison of adenosine and exercise stress test for quantitative perfusion imaging in patients on beta-blocker therapy. Cardiology 95:112–118
2. Hayat SA, Dwivedi G, Jacobsen A, Lim TK, Kinsey C, Senior R (2008) Effects of left bundle-branch block on cardiac structure, function, perfusion, and perfusion reserve: implications for myocardial contrast echocardiography versus radionuclide perfusion imaging for the detection of coronary artery disease. Circulation 11:1832–1841
3. Loong CY, Anagnostopoulos C (2004) Diagnosis of coronary artery disease by radionuclide myocardial perfusion imaging. Heart 90:v2–v9
4. Gibbons RJ, Balady GJ, Bricker JT et al (2002) ACC/AHA 2002 guideline update for exercise testing: summary article: a report of the American College of Cardiology/American heart association task force on practice guidelines (committee to update the 1997 exercise testing guidelines). Circulation 106:1883–1892
5. Fredholm BB, IJzerman AP, Jacobson KA, Klotz KN, Linden J (2001) International Union of Pharmacology. XXV. Nomenclature and classification of adenosine receptors. Pharmacol Rev 53: 527–552
6. Mubagwa K, Flameng W (2001) Adenosine, adenosine receptors and myocardial protection: an updated overview. Cardiovasc Res 52:25–39
7. Sato A, Terata K, Miura H et al (2005) Mechanism of vasodilation to adenosine in coronary arterioles from patients with heart disease. Am J Physiol Heart Circ Physiol 288:H1633–H1640
8. Lupi A, Buffon A, Finocchiaro ML, Conti E, Maseri A, Crea F (1997) Mechanisms of adenosine-induced epicardial coronary artery dilatation. Eur Heart J 18:614–617
9. Wilson RF, Wyche K, Christensen BV, Zimmer S, Laxson DD (1990) Effects of adenosine on human coronary arterial circulation. Circulation 82:1595–1606
10. Moser GH, Schrader J, Deussen A (1989) Turnover of adenosine in plasma of human and dog blood. Am J Physiol 256(4 Pt 1):C799–C806
11. Kaufmann PA, Gnecchi-Ruscone T, Di TM, Schafers KP, Luscher TF, Camici PG (2000) Coronary heart disease in smokers: vitamin C restores coronary microcirculatory function. Circulation 102:1233–1238
12. De BB, Pijls NH, Barbato E et al (2003) Intracoronary and intravenous adenosine 5′-triphosphate, adenosine, papaverine, and contrast medium to assess fractional flow reserve in humans. Circulation 107:1877–1883
13. Akinboboye OO, Idris O, Chou RL, Sciacca RR, Cannon PJ, Bergmann SR (2001) Absolute quantitation of coronary steal induced by intravenous dipyridamole. J Am Coll Cardiol 37:109–116
14. Werner GS, Fritzenwanger M, Prochnau D et al (2006) Determinants of coronary steal in chronic total coronary occlusions donor artery, collateral, and microvascular resistance. J Am Coll Cardiol 48:51–58
15. Cerqueira MD, Verani MS, Schwaiger M, Heo J, Iskandrian AS (1994) Safety profile of adenosine stress perfusion imaging: results from the Adenoscan Multicenter Trial Registry. J Am Coll Cardiol 23:384–389
16. Mishra RK, Dorbala S, Logsetty G et al (2005) Quantitative relation between hemodynamic changes during intravenous adenosine infusion and the magnitude of coronary hyperemia: implications for myocardial perfusion imaging. J Am Coll Cardiol 45:553–558
17. Fredholm BB, Irenius E, Kull B, Schulte G (2001) Comparison of the potency of adenosine as an agonist at human adenosine receptors expressed in Chinese hamster ovary cells. Biochem Pharmacol 61:443–448
18. Shryock JC, Snowdy S, Baraldi PG et al (1998) A2A-Adenosine receptor reserve for coronary vasodilation. Circulation 98:711–718
19. Gao Z, Li Z, Baker SP et al (2001) Novel short-acting A2A adenosine receptor agonists for coronary vasodilation: inverse relationship between affinity and duration of action of A2A agonists. J Pharmacol Exp Ther 298:209–218
20. Zablocki J, Palle V, Blackburn B et al (2001) 2-substituted pi system derivatives of adenosine that are coronary vasodilators acting via the A2A adenosine receptor. Nucleosides, Nucleotides Nucleic Acids 20:343–360
21. Lieu HD, Shryock JC, von Mering GO et al (2007) Regadenoson, a selective A2A adenosine receptor agonist, causes dose-dependent increases in coronary blood flow velocity in humans. J Nucl Cardiol 14:514–520
22. Reyes E, Staehr P, Olmsted A et al (2011) Effect of body mass index on the efficacy, side effect profile, and plasma concentration of fixed-dose regadenoson for myocardial perfusion imaging. J Nucl Cardiol 18:620–627
23. Cerqueira MD, Nguyen P, Staehr P, Underwood SR, Iskandrian AE, On behalf of the ADVANCE-MPI Trial Investigators (2008) Effects of age, gender, obesity, and diabetes on the efficacy and safety of the selective A2A agonist regadenoson Versus adenosine in myocardial perfusion imaging: integrated ADVANCE-MPI trial results. J Am Coll Cardiol Img 1:307-316

24. Dibella EV, Fluckiger JU, Chen L et al (2012) The effect of obesity on regadenoson-induced myocardial hyperemia: a quantitative magnetic resonance imaging study. Int J Cardiovasc Imaging 28:1435–1444
25. Gordi T, Blackburn B, Lieu H (2007) Regadenoson pharmacokinetics and tolerability in subjects with impaired renal function. J Clin Pharmacol 47:825–833
26. Gordi T, Frohna P, Sun HL, Wolff A, Belardinelli L, Lieu H (2006) A population pharmacokinetic/pharmacodynamic analysis of regadenoson, an adenosine A2A-receptor agonist, in healthy male volunteers. Clin Pharmacokinet 45:1201–1212
27. Iskandrian AE, Bateman TM, Belardinelli L et al (2007) Adenosine versus regadenoson comparative evaluation in myocardial perfusion imaging: results of the ADVANCE phase 3 multicenter international trial. J Nucl Cardiol 14:645–658
28. Dhalla AK, Wong MY, Wang WQ, Biaggioni I, Belardinelli L (2006) Tachycardia caused by A2A adenosine receptor agonists is mediated by direct sympathoexcitation in awake rats. J Pharmacol Exp Ther 316:695–702
29. Botvinick EH, Dae MW (1991) Dipyridamole perfusion scintigraphy. Semin Nucl Med 21:242–265
30. Rossen JD, Quillen JE, Lopez AG, Stenberg RG, Talman CL, Winniford MD (1991) Comparison of coronary vasodilation with intravenous dipyridamole and adenosine. J Am Coll Cardiol 18:485–491
31. Ranhosky A, Kempthorne-Rawson J (1990) The safety of intravenous dipyridamole thallium myocardial perfusion imaging. Intravenous dipyridamole thallium imaging study group. Circulation 81:1205–1209
32. Reyes E, Stirrup J, Roughton M, D'Souza S, Underwood SR, Anagnostopoulos C (2010) Attenuation of adenosine-induced myocardial perfusion heterogeneity by atenolol and other cardioselective beta-adrenoceptor blockers: a crossover myocardial perfusion imaging study. J Nucl Med 51:1036–1043
33. Taillefer R, Ahlberg AW, Masood Y et al (2003) Acute beta-blockade reduces the extent and severity of myocardial perfusion defects with dipyridamole Tc-99 m sestamibi SPECT imaging. J Am Coll Cardiol 42:1475–1483
34. Sharir T, Rabinowitz B, Livschitz S et al (1998) Underestimation of extent and severity of coronary artery disease by dipyridamole stress thallium-201 single-photon emission computed tomographic myocardial perfusion imaging in patients taking antianginal drugs. J Am Coll Cardiol 31:1540–1546
35. Anagnostopoulos C, Harbinson M, Kelion A et al (2004) Procedure guidelines for radionuclide myocardial perfusion imaging. Heart 90(Suppl 1):i1–10
36. Henzlova M, Cerqueira MD, Hansen C, Taileffer R, Siu-Sun Y (2009) ASNC imaging guidelines for nuclear cardiology procedures: stress protocols and tracers. In: American society of nuclear cardiology (ASNC) 2009 at http://www.asnc.org/section_73.cfm . 01/02/2010
37. Gaemperli O, Schepis T, Koepfli P et al (2008) Interaction of caffeine with regadenoson-induced hyperemic myocardial blood flow as measured by positron emission tomography: a randomized, double-blind, placebo-controlled crossover trial. J Am Coll Cardiol 51:328–329
38. Tejani FH, Thompson RC, Iskandrian AE, McNutt BE, Franks B (2011) Effect of caffeine on SPECT myocardial perfusion imaging during regadenoson pharmacologic stress: rationale and design of a prospective, randomized, multicenter study. J Nucl Cardiol 18:73–81
39. O'Keefe JH Jr, Bateman TM, Handlin LR, Barnhart CS (1995) Four- versus 6-minute infusion protocol for adenosine thallium-201 single photon emission computed tomography imaging. Am Heart J 129:482–487
40. Villegas BJ, Hendel RC, Dahlberg ST, McSherry BA, Leppo JA (1993) Comparison of 3- versus 6-minute infusions of adenosine in thallium-201 myocardial perfusion imaging. Am Heart J 126:103–107
41. Treuth MG, Reyes GA, He ZX, Cwajg E, Mahmarian JJ, Verani MS (2001) Tolerance and diagnostic accuracy of an abbreviated adenosine infusion for myocardial scintigraphy: a randomized, prospective study. J Nucl Cardiol 8:548–554
42. Pennell DJ, Mavrogeni SI, Forbat SM, Karwatowski SP, Underwood SR (1995) Adenosine combined with dynamic exercise for myocardial perfusion imaging. J Am Coll Cardiol 25:1300–1309
43. Thomas GS, Prill NV, Majmundar H et al (2000) Treadmill exercise during adenosine infusion is safe, results in fewer adverse reactions, and improves myocardial perfusion image quality. J Nucl Cardiol 7:439–446
44. Reyes E, Wiener S, Underwood SR (2012) Myocardial perfusion scintigraphy in Europe 2007: a survey of the European council of nuclear cardiology. Eur J Nucl Med Mol Imaging 39:160–164
45. Reyes E, Loong CY, Wechalekar K, Latus K, Anagnostopoulos C, Underwood SR (2007) Side effect profile and tolerability of adenosine myocardial perfusion scintigraphy in patients with mild asthma or chronic obstructive pulmonary disease. J Nucl Cardiol 14:827–834
46. Sundram F, Notghi A, Smith NB (2009) Pharmacological stress myocardial perfusion scintigraphy: use of a modified adenosine protocol in patients with asthma. Nucl Med Commun 30:217–225
47. Reyes E, Loong CY, Harbinson M, Donovan J, Anagnostopoulos C, Underwood SR (2008) High-dose adenosine overcomes the attenuation of myocardial perfusion reserve caused by caffeine. J Am Coll Cardiol 52:2008–2016

48. Thomas GS, Thompson RC, Miyamoto MI et al (2009) The RegEx trial: a randomized, double-blind, placebo- and active-controlled pilot study combining regadenoson, a selective A(2A) adenosine agonist, with low-level exercise, in patients undergoing myocardial perfusion imaging. J Nucl Cardiol 16:63–72
49. Mahmarian JJ, Cerqueira MD, Iskandrian AE et al (2009) Regadenoson induces comparable left ventricular perfusion defects as adenosine: a quantitative analysis from the ADVANCE MPI 2 trial. JACC Cardiovasc Imaging 2:959–968
50. Bouvier F, Hojer J, Hulting J, Ruiz H, Samad B, Jensen-Urstad M (1998) Myocardial perfusion scintigraphy (SPECT) during adenosine stress can be performed safely early on after thrombolytic therapy in acute myocardial infarction. Clin Physiol 18:97–101
51. Heller GV, Brown KA, Landin RJ, Haber SB (1997) Safety of early intravenous dipyridamole technetium 99 m sestamibi SPECT myocardial perfusion imaging after uncomplicated first myocardial infarction. Early Post MI IV Dipyridamole Study (EPIDS). Am Heart J 134:105–111
52. Geleijnse ML, Elhendy A, Fioretti PM, Roelandt JR (2000) Dobutamine stress myocardial perfusion imaging. J Am Coll Cardiol 36:2017–2027
53. Attenhofer CH, Pellikka PA, McCully RB, Roger VL, Seward JB (1997) Paradoxical sinus deceleration during dobutamine stress echocardiography: description and angiographic correlation. J Am Coll Cardiol 29:994–999
54. Jagathesan R, Kaufmann PA, Rosen SD et al (2005) Assessment of the long-term reproducibility of baseline and dobutamine-induced myocardial blood flow in patients with stable coronary artery disease. J Nucl Med 46:212–219
55. Aydin M, Caner B, Yildirir A, Sari O, Tokgozoglu L (2000) Dobutamine combined with low-level exercise for myocardial perfusion scintigraphy. Nucl Med Commun 21:1015–1020
56. Pennell DJ, Underwood SR, Ell PJ (1993) Safety of dobutamine stress for thallium-201 myocardial perfusion tomography in patients with asthma. Am J Cardiol 71:1346–1350
57. Reyes E, Rahman S, Loong CY, Anagnostopoulos C, Underwood SR. Comparison of nurse and doctor supervised stress testing in the setting of radionuclide myocardial perfusion imaging (abstract). Nucl Med Commun 2002; 23:380

Myocardial Perfusion Imaging: The Role of SPECT, PET and CMR

3

Caroline E. Veltman, Berlinda J. de Wit-van der Veen, Albert de Roos, Joanne D. Schuijf and Ernst E. van der Wall

3.1 Introduction

A large number of noninvasive cardiovascular imaging techniques can be employed for the diagnostic and prognostic evaluation of patients with chest pain. Noninvasive myocardial perfusion imaging is increasingly being applied for the detection and risk stratification of obstructive coronary artery disease (CAD). The main principle of myocardial perfusion imaging is the visualization of ischemia. The ischemic cascade may escalate from early perfusion abnormalities and metabolic changes to wall-motion abnormalities, systolic and diastolic dysfunction, and myocardial infarction. Therefore, early detection of ischemia is important and may contribute to lowering the morbidity and mortality rates in patients with ischemic heart disease. Detecting ischemia is an important part of the diagnostic strategy in clinical guidelines [1]. In this chapter, we focus on the role of single-photon emission computed tomography (SPECT), cardiac magnetic resonance (CMR), and positron emission tomography (PET) perfusion imaging for detecting CAD. The basic principles and interpretation, as well as the diagnostic performance, of these three most commonly used modalities for myocardial perfusion imaging are discussed. In addition, an overview of the benefits and drawbacks of each technique is provided. Finally, future technical developments and combined functional and anatomical imaging is briefly addressed.

C. E. Veltman (✉) · E. E. van der Wall
Department of Cardiology, LUMC, Leiden, The Netherlands
e-mail: c.e.veltman@lumc.nl

E. E. van der Wall
e-mail: E.E.van_der_Wall@lumc.nl

B. J. de Wit-van der Veen
Department of Nuclear Medicine, National Cancer Institute, Antoni van Leeuwenhoek Hospital, Amsterdam, The Netherlands
e-mail: lindavdveen@gmail.com

A. de Roos
Department of Radiology, LUMC, Leiden, The Netherlands
e-mail: A.de_Roos@lumc.nl

J. D. Schuijf
Toshiba Medical Systems Europe, Zoetermeer, The Netherlands

3.2 Single Photon Emission Computed Tomography

Perfusion imaging using SPECT is a predominant nuclear imaging technique used in ischemic heart disease. As with all radionuclide-based technologies, SPECT relies on the so-called tracer principle. This implies that a radioactive-labelled compound (radiopharmaceutical or radiotracer), which has the same properties as its biological nonradioactive analog, is administered to the patient by intravenous injection. Radiopharmaceutical distribution throughout the body can be traced by detecting the gamma rays (photons) emitted during its radioactive decay.

P. Marzullo and G. Mariani (eds.), *From Basic Cardiac Imaging to Image Fusion*,
DOI: 10.1007/978-88-470-2760-2_3,

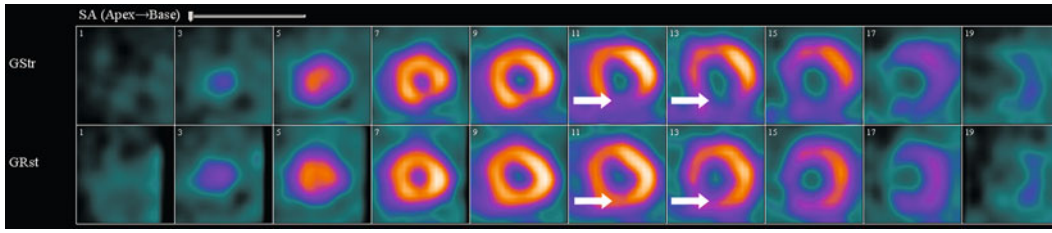

Fig. 3.1 Short-axis (oblique tomogram) images after stress (*upper*) and at rest (*lower*). Uptake in *left ventricle* is predominantly visible due to the higher perfusion rates and cardiomyocyte density within this wall. Overall, homogenous tracer accumulation can be seen, with the exception of a small area in the inferior wall of stress images (*arrows*). At rest, this small perfusion defect returns to normal, suggesting the presence of ischemia in that specific region

By applying this principle in cardiac imaging, it is possible to evaluate myocardial perfusion, function, viability, and innervation using various radiopharmaceuticals.

3.2.1 Principles of Myocardial Perfusion Imaging

Distribution and accumulation of radioactive perfusion tracers in the myocardium are related to coronary blood flow. Coronary autoregulation provides an efficient mechanism for maintaining adequate myocardial blood flow (MBF) during resting conditions in the presence of a flow-limiting coronary stenosis. However, during stress, myocardial perfusion is inadequate in the setting of flow-limiting coronary artery stenoses. Therefore, in areas with lowered or absent blood flow due to coronary artery stenosis, tracer accumulation is reduced compared with the surrounding myocardial areas with normal perfusion. Accordingly, local abnormalities in myocardial tracer uptake provide information on location and severity of a functionally significant coronary obstruction (Fig. 3.1). Furthermore, in the case of a previous myocardial infarction, due to the absence of blood flow in the fibrous scar tissue no tracer accumulation is observed in the infarcted area, resulting in a persistent perfusion defect in both rest and stress perfusion images. To differentiate between perfused, ischemic, and infarcted regions, a combined imaging protocol with acquisitions at rest and after stress is used in myocardial perfusion SPECT (MPS).

3.2.1.1 SPECT Perfusion Tracers

An ideal nuclear perfusion tracer should have a high first-pass extraction rate, a linear extraction ratio over a range of flow rates (normal mean flow at rest is between 0.7 and 1.3 mL/min/g), and a long retention time within the myocardium (i.e., biological half-life). For SPECT perfusion imaging, several radiopharmaceuticals can be used, most of which are either thallium-201 (^{201}Tl) or technetium-99m (^{99m}Tc) derivates. The characteristics of these compounds differ with respect to pharmacokinetics and physical properties [2].

Thallium-201

Thallium-201, supplied as thallous chloride, is an ionic tracer that demonstrates properties similar to potassium. As with potassium, ^{201}Tl is actively extracted by sodium/potassium (Na/K) pumps (first-pass extraction rate of ~85%) of myocytes. Immediately after intravenous injection, ^{201}Tl uptake depends on blood flow and ability of the myocardium to extract ^{201}Tl. ^{201}Tl distribution over time involves a constant redistribution of the tracer until equilibrium within cells is reached. ^{201}Tl retention in the cell relies mostly on the membrane intactness and cell viability. As ^{201}Tl is rapidly cleared from the blood and exchanges between inter- and

intracellular spaces, proper timing of the stress and rest images are important. After only 10 min, myocardial concentration reaches its peak, so stress imaging should commence shortly after stress induction. Rest images can be acquired the same day and are typically performed after 2–4 h postinjection.

Technetium-99m Sestamibi and Tetrofosmin

These lipophilic cations are passively transported across vascular and myocardial cell membranes. Due to their relatively positive charge, sestamibi and tetrofosmin are trapped within the mitochondria of cardiomyocytes by electrostatic interactions. Actual uptake is not only dependent on blood flow but also on intracellular pH, the electrochemical gradient of the mitochondrial membrane, and the presence of an active energy-production pathway. The initial extraction of both sestamibi (first-pass extraction rate ~65%) and tetrofosmin (first-pass extraction rate ~55%) is much lower than that of ^{201}Tl, which is an important drawback of the ^{99m}Tc tracers. Following intravenous administration, most activity is initially distributed within the gallbladder, liver, heart, spleen, and lungs. Both compounds have almost no redistribution over time. Over time, accumulations in the lungs and spleen will decrease, but those in the hepatobiliary system and intestines remain, as these are the main pathways for excretion. The ^{99m}Tc-labelled radiopharmaceuticals are nowadays commonly used as an alternative to ^{201}T1 chloride. Their advantages include a widespread availability from an onsite molybdenum generator, shorter physical half-life (6 h), and an energy peak of 140 kV, which is considered ideal for scintigraphic imaging. Unlike ^{201}Tl, ^{99m}Tc tracers are trapped within cardiomyocytes, resulting in a long retention time, thus allowing for imaging flexibility.

Although PET is considered superior for viability assessment, SPECT using ^{201}Tl and ^{99m}Tc tracers can also be used. In rest–redistribution, ^{201}Tl acquisitions hypoperfuse; however, still-viable areas appear as defects on rest images, although show reversibility in the subsequent redistribution images. Administration of ^{99m}Tc tracers following nitroglycerin infusion also enables evaluation of viability. These nitroglycerin-augmented studies are performed a few hours after a normal rest acquisition [3]. As the ^{99m}Tc perfusion tracers are more widely available compared with PET, post nitrate viability imaging has great potential for clinical practice (see Sect. 3.3.3 for more information).

3.2.1.2 Imaging Protocols

Different types of protocols (e.g., 2-day stress/rest, 1-day dual-isotope stress/rest, 1-day split-dose stress/rest) are described in the guidelines [4]. Though the exact protocols are usually institution specific, the basic elements of the MPS protocol are discussed.

Stress Induction

Stress is preferably induced by exercising the patient on a treadmill or bicycle. In addition to the information acquired regarding exercise tolerance, physical stress allows for a more accurate representation of cardiac function. During stress induction, electrocardiogram (ECG) recordings are performed to check for signs of myocardial ischemia and/or ventricular arrhythmias. In case of insufficient exercise capacity or contra-indications to physical stress, pharmacological stress agents such as dobutamine, adenosine, regadenoson, or dipyridamole can be used. Prior to stress induction, patients are generally instructed to stop β-blockers and calcium-channel antagonists, as these medications reduce the response to physical exercise or dobutamine. Moreover, patients are also instructed to abstain from caffeine-containing products, as caffeine is an important adenosine-receptor antagonist.

Tracer Administration

At the moment of peak stress, a small amount of radiotracer is intravenously injected. The activity depends on the radiotracer and the imaging protocol (^{201}Tl 75–110 MBq; ^{99m}Tc tracers 250–900 MBq). As these tracers rapidly accumulate within the myocardium, stress only needs to be continued for a few minutes following

injection. Depending on the type of radiotracer used, images are acquired immediately after stress induction or approximately 30 min to 2 h after injection.

SPECT Image Acquisition

This step relies on gamma rays (i.e., photons) emitted during radioactive decay being detected by a rotating gamma camera. This camera comprises a large number of detectors (i.e., scintillation crystals) mounted at one or multiple heads with a collimator placed in front of each camera head. The collimator is basically a lead plate with narrow holes, which only allows rays traveling perpendicular to a hole to be detected by the gamma camera. Consequently, acquired image resolution is better. At set angles along a 180 or 360° arc around the patient, multiple projection images are acquired. Duration of a single projection typically varies between 10 and 25 s, depending on the type of camera. The total set of projection images is converted using mathematical reconstruction algorithms into a 3D representation of radiotracer distribution within the body. To obtain oblique images of the heart, the 3D perfusion dataset also needs to be reoriented.

Modern SPECT cameras commonly incorporate a low-dose computed tomography (CT) scanner, images from which are used to estimate the degree in which gamma rays are affected by the body itself. Various tissue types affect the path and intensity of gamma rays differently, a process known as attenuation. Low-dose CT images are used to create an attenuation map, thus enabling mathematical correction for this effect (further detailed in Sect. 3.3.1.2).

At present, myocardial perfusion SPECT is mostly performed using ECG-gated SPECT. ECG gating refers to the process in which detected counts are related to specific time intervals within the cardiac cycle. The addition of an ECG to SPECT data allows evaluation of cardiac function (discussed in "Evaluation of Myocardial Function"). SPECT acquisition starts with the R-peak on the ECG, and all detected counts during this cardiac cycle (R–R interval) are allocated to specific intervals, or frames. In most clinical protocols, eight or 16 frames are used to describe one cardiac cycle. Higher frame rates result in better temporal resolution but at the cost of the number of detected counts. Thus, when gating is used, each projection image spans multiple heart cycles, and, at each camera angle, a number of projection images are acquired depending on the frame rate. Accordingly, a summation of projection images over all frames at one angle produces a conventional ungated projection image. Generally, perfusion patterns are evaluated on these static, ungated SPECT images.

3.2.2 Identifying CAD Using SPECT

In accordance with the professional guidelines for cardiovascular image interpretation, cardiac images are visually assessed in the three standard oblique views: short-axis, vertical long-axis, and horizontal long-axis [4]. Myocardial perfusion shown by the amount of tracer accumulation is reported based on a 17-segment model of the left ventricle (LV). Defects in regional perfusion are described with respect to the maximal tracer uptake within the entire myocardium. This implies that MPS visualizes perfusion relative to other myocardial areas and not as an absolute measure.

A homogeneous myocardial tracer uptake generally indicates a normal perfusion and hence the absence of a significant coronary stenosis or previous myocardial infarction (Fig. 3.2). To distinguish between normal, ischemic, and infarcted myocardium, stress and rest images are compared side by side. When tracer distribution is abnormal after stress and restores to normal at rest, myocardial ischemia is present (also known as reversible perfusion defect). Defects that remain unchanged in the stress and at-rest images represent areas of severe myocardial ischemia, acute myocardial infarction, or scarring of the myocardium due to previous infarctions (also known as persistent or fixed perfusion defects). Figure 3.3 shows a patient with myocardial scaring in the inferolateral region of the LV.

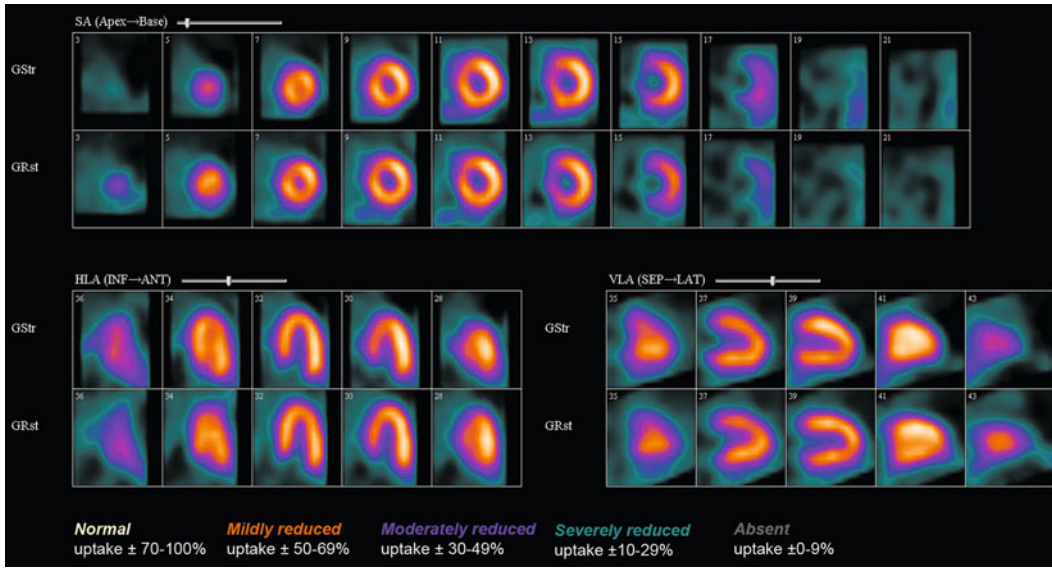

Fig. 3.2 Standard short-axis (*SA*), horizontal long-axis (*HLA*), and vertical long-axis (*VLA*) views of stress (*upper*) and rest (*lower*) acquisitions of a patient with normal perfusion. In all segments, a homogenous tracer accumulation is present. In normal myocardial perfusion images, the point of maximum tracer uptake is located in the lateral wall and of lowest uptake is in the septal wall. Also, the septal wall generally seems shorter compared with the lateral wall due to oblique placement of the basal plane and presence of a fibrous septum

3.2.2.1 Important Pitfalls and Artifacts

Though assessing perfusion seems straight forward, it is important to recognize artifacts and understand the effects they might have on image interpretation. The main image artifacts can roughly be divided into two categories: equipment-related and patient-related factors. Equipment-related artifacts have the property to simulate perfusion defects or create image irregularities throughout the entire field of view. They can be the result of various problems, including damaged camera parts, faulty electronics, improper tracer administration, or incorrect image reconstruction. The presence of these artifacts will usually be detected during the daily quality-control tests performed on the camera system.

Patient-related artifacts, on the other hand, are much more difficult to identify. Patient motion, soft-tissue attenuation, extracardiac tracer accumulation, anatomical variations, and irregular heart rate are all factors that can induce artifacts (Fig. 3.4). The fact that these artifacts are not stationary and change over time make detection difficult. To reduce artifacts due to motion and soft-tissue attenuation, modern cameras are implemented with attenuation- and motion-correction techniques.

In addition, another important pitfall of MPS imaging is related to the relative nature of SPECT perfusion imaging instead of measuring absolute myocardial perfusion. In patients with three-vessel disease, balanced ischemia can be present. In such patients, the extent of perfusion defects may be severely underestimated, as tracer accumulation is decreased in all myocardial segments. The occurrence of balanced ischemia in patients with three-vessel CAD might partly explain the discrepancies that at times arise between MPS and invasive coronary angiography [5].

Novel gamma-camera technology recently introduced combines cadmium zinc telluride (CZT) crystals with new collimator designs and cardiocentric acquisition. This new technology provides fast acquisitions (<10 min) and might also have a higher sensitivity in detecting CAD, especially in multivessel disease [6].

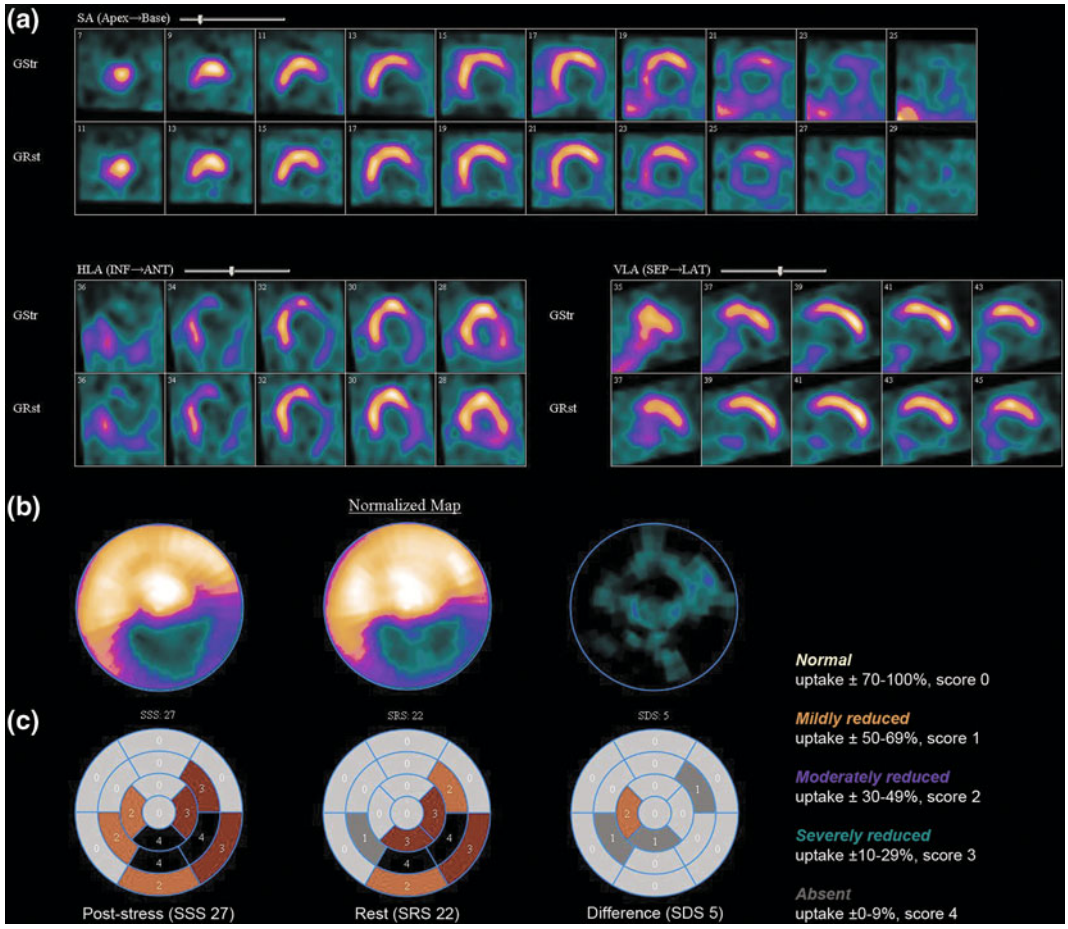

Fig. 3.3 A patient with scarring as a result of coronary artery disease (CAD) in the inferolateral wall of the left ventricle. **a** Standard views show severely reduced and absent tracer uptake in the inferolateral wall. Perfusion defects are present in both stress (*upper series*) and rest (*lower series*) images, representing extensive scar after myocardial infarction. **b** Polar maps confirm the presence of perfusion defects in the inferolateral region. In general, for both visual and polar-map assessment, a five-point scoring system is used to report perfusion abnormalities, ranging from normal to absent perfusion. **c** Summed perfusion scores at rest (*SRS*), stress (*SSS*), and difference (*SDS*) scores are automatically calculated in the standardized 17-segment left ventricular model. Again, polar maps confirm the presence of severe persistent perfusion abnormalities, with some reversibility in the border zone of the infarcted area

3.2.3 Quantifying Relative Perfusion and Function

The emphasis of perfusion imaging has shifted in the last decade from visual assessment alone toward an integrated evaluation of both myocardial perfusion and function. Moreover, the addition of automated evaluations improved diagnostic accuracy for detecting ischemia, which can be ascribed to a more effective distinction between true perfusion defects and image artifacts. Different automated approaches are available for quantitative image analyses, which use predefined information on shape, continuity, and wall thickness to model endocardial and epicardial contours for delineating the myocardium [7].

3.2.3.1 Perfusion Polar Maps

For perfusion quantification, images are displayed in so called polar maps (Fig. 3.3). This is

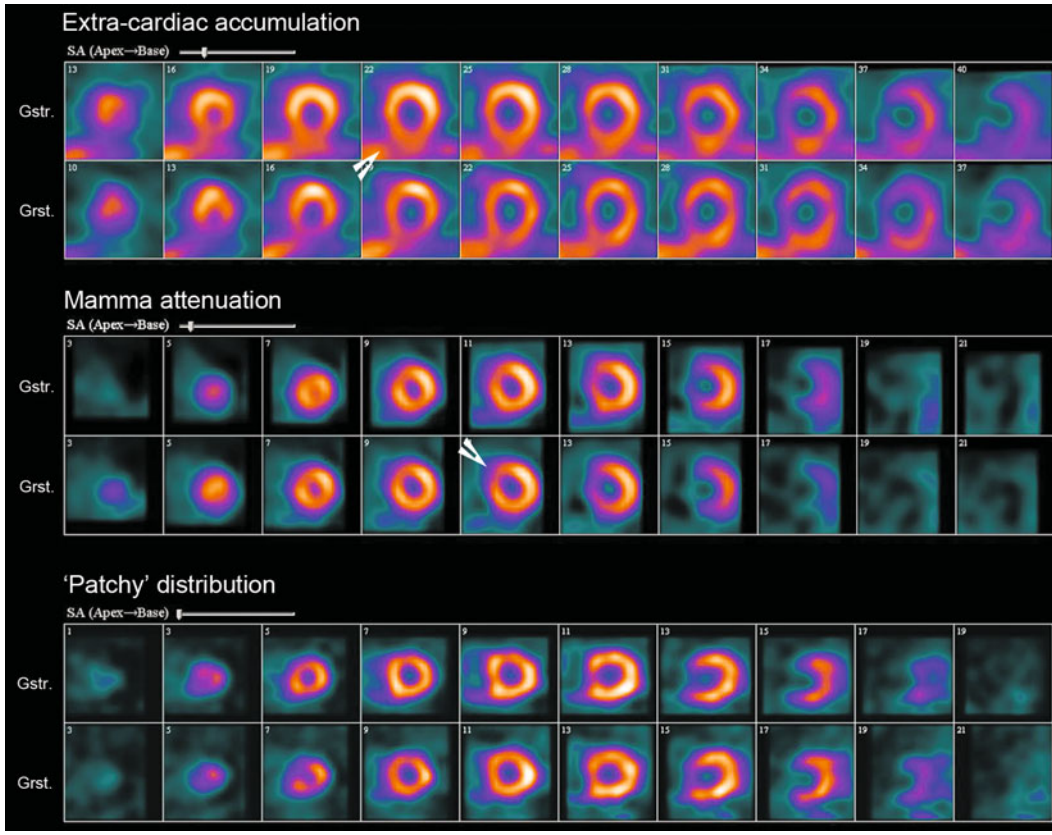

Fig. 3.4 Examples of important pitfalls of perfusion single-photon emission computed tomography (SPECT). Extra-cardiac accumulation of the radiopharmaceutical in the liver during stress and rest acquisition hampers assessment of the entire inferior wall. Mamma attenuation is known to mimic perfusion defects in the anteroseptal regions of the myocardium. These defects can be either fixed or reversible, depending of the position of the breast during acquisition. Soft-tissue attenuation will decrease in severity when attenuation correction using low-dose computed tomography is applied. A patchy distribution (i.e., irregular uptake pattern with many small insignificant defects) is often seen in obese patients both in stress and rest acquisitions due to extreme soft-tissue attenuation. However, this irregular pattern can also be seen in patients with diabetes mellitus, where it could also be related to the presence of microvascular disease, which is frequently observed in diabetic patients

a simple 2D representation of tracer distribution, which is unaffected by anatomical variations or size of the LV. The global spatial orientation of the myocardial regions in a polar map is equal to the short-axis view. In accordance with the 17-segment model, the outermost ring of the polar map matches the basal plane, the middle ring matches the midventricular regions, and the center of the polar map is the apical region. By relating a patient's polar map to an averaged polar map comprising data from a number of normal MPS studies, perfusion defects can automatically be identified. These defects are scored using a five-point scoring system in each of the 17 segments, with 0 indicating normal perfusion and 4 indicating complete absence of tracer uptake. The total defect score is a summation of all segments and is referred to as either summed stress score (SSS) or summed rest score (SRS), depending on the image series being used. Generally, a SSS or SRS ≤ 3 is considered normal or equivocal, 4–8 is mildly abnormal, 9–13 is moderately abnormal, and >13 is severely abnormal. The difference

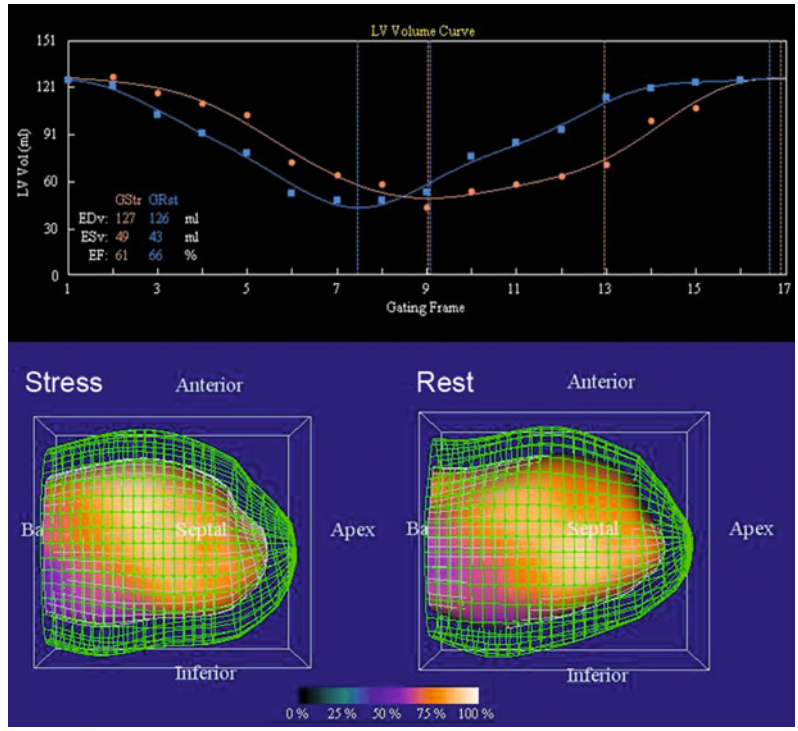

Fig. 3.5 Time-volume curves of stress (*red*) and rest (*blue*) acquisitions with the appropriate 3D left-ventricular mesh models. Based on the time–volume curve, functional indices can be estimated for both systolic and diastolic phases. Moving 3D models are used to evaluate regional-wall motion patterns in conjunction with the projected perfusion data

between stress and rest polar maps is referred to as summed difference score (SDS) and provides information on the amount of ischemia (Fig. 3.3). These automated measures are often used as a generalized and operator-independent method for reporting perfusion defects. Still, all perfusion defects described with this automated approach should also be visually evaluated in the three standard oblique views.

3.2.3.2 Functional Measures

Based on the automated delineation of the LV in all frames of the gated images, ventricle volume can be calculated over time (Fig. 3.5). The time–volume curve, the result of this operation, offers valuable information on both diastolic and systolic function. Parameters that can be determined based upon this curve include cardiac volumes, LV ejection fraction, and filling and emptying rates. The LV can also be displayed as a 3D model to evaluate regional left-ventricular wall motion and wall thickening during the cardiac cycle. Though the additive value of these functional measures has primarily been described in patients with heart failure, a functional evaluation may also be of added value in patients with CAD. The addition of functional information to perfusion images enables better identification of balanced ischemia and improves overall MPS diagnostic accuracy.

3.2.4 Clinical Value of Gated MPS

Myocardial perfusion SPECT is generally considered an accurate, safe, and cost-effective method for noninvasive identification of functionally significant CAD. Many studies have validated the use of MPS for the risk stratification of patients with suspected or proven CAD [8, 9]. Accordingly, MPS is included in the guidelines for assessing localization, severity, and extent of CAD [10]. Additionally, MPS provides important prognostic information and can therefore be used for risk stratification of future severe cardiac events in patients with stable ischemic heart disease [11]. Patients with normal, or near-normal, MPS have an annual risk for severe cardiac events of ~1%, which is

comparable with that of the general population [12]. On the other hand, event rates are significantly higher in patients with abnormal MPS (SSS $\geq$ 4) [13]. Importantly, the reliability of MPS depends on the indications for the scan. For detecting CAD in a non acute setting, MPS is best applied in patients with an intermediate pretest probability for CAD or with acute chest pain without ECG changes [14]. MPS overall diagnostic performance in detecting CAD on a patient basis expressed in sensitivity and specificity is ~88 and 61% respectively, using the acquisition protocols described previously [15]. When novel technologies, such as attenuation correction and/or new camera designs, are applied, higher sensitivity values can be achieved.

Furthermore, myocardial perfusion SPECT is commonly performed for cardiovascular screening in asymptomatic patients. In patients with type 2 diabetes mellitus, a high prevalence of abnormal stress myocardial perfusion studies is observed despite the absence of symptoms [16]. In conclusion, myocardial perfusion SPECT can be used for diagnostic purposes, to guide therapeutic management, and for risk stratification in different patients population.

3.3 Positron Emission Tomography

Though gated perfusion SPECT is the mainstay nuclear imaging technique for diagnosing CAD, PET has undergone rapid advances. The ability of PET to combine high-resolution perfusion imaging with absolute quantification of MBF and mathematical modelling of the kinetics of tracer distribution has great potential in a clinical setting. In addition, the combined assessment of perfusion and metabolic imaging makes it is possible to detect ischemic regions that are most likely to benefit from revascularization.

3.3.1 Principles of Perfusion PET

As with perfusion SPECT, PET relies on the tracer principle, meaning that a radiopharmaceutical is injected in order to visualize a specific biological process. Again, tracer distribution and accumulation are highly related to local blood flow, enabling identification of perfusion patterns. Radionuclides used in PET decay by emitting positrons (a positively charged electron). If this positron collides with an electron nearby, a process called annihilation occurs. During annihilation, the combined energy of the electron and positron is converted into two 511-KeV gamma rays that are emitted in opposite directions (at a 180° angle). These two gamma rays are detected by opposing detectors in the ring of the PET scanner.

3.3.1.1 PET Tracers

A number of tracers are commonly used for PET-based perfusion imaging. Each of these tracers has specific radiokinetic and physiological properties [17].

Oxygen-15 Water

With respect to its physiological properties, this is considered the ideal tracer for MBF quantification. It rapidly diffuses across cell membranes (first-pass extraction rate 95%) and has a near-linear uptake over a wide range of MBF rates (Fig. 3.6). However, [^{15}O]-water does not remain trapped within myocytes but constantly diffuses between the intra- and extracellular space. This constant redistribution, combined with its short physical half-life of 2.4 min, makes it difficult to create the high quality static images that are needed for the assessment of regional perfusion defects.

Nitrogen-13 Ammonia

On the other hand, [^{13}N]-ammonia has favorable radiokinetics, including a relatively high first-pass extraction of approximately 80%, an almost linear uptake, and relatively slow washout. These properties, combined with a longer physical half-life (9.8 min), ensure that [^{13}N]-ammonia is suitable for both MBF quantification and perfusion defect evaluation in static rest and stress images. However, the main disadvantage of both [^{13}N]-ammonia and radiolabeled water is the need for an onsite cyclotron for production of these radiolabeled imaging agents.

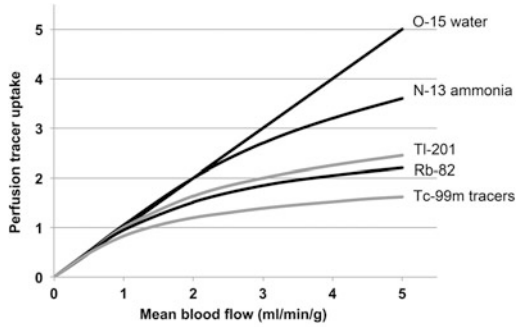

Fig. 3.6 Relationship between mean extraction rate and myocardial blood flow of the most commonly used single photon emission computed tomography (SPECT) and positron emission tomography (PET) perfusion tracers. The radiokinetics of [^{15}O]-water are considered ideal for absolute quantification, as extraction is proportional to blood flow. The other tracers show a flattened response at increasing flow rates, which is especially profound in the thallium-201, rubidium-82, and technetium-99m tracers, making them less suitable for absolute quantification

Rubidium-82

As an alternative, rubidium-82 (^{82}Rb) is being used increasingly in the clinical setting. ^{82}Rb is produced in an onsite generator instead of a cyclotron and has relatively simple radiokinetics. As with ^{201}Tl, ^{82}Rb is a potassium analog that is actively extracted by Na/K pumps (first-pass extraction rate ~85%). The drawbacks of ^{82}Rb include a very short physical half-life of 78 s and a nonlinear extraction at high blood flow rates. Recent studies suggest that with the use of proper correction models for the flow-extraction mismatch at higher flow rates, ^{82}Rb can accurately estimate MBF.

All aforementioned tracers have limitations that might hamper the widespread applicability of perfusion PET in a clinical setting. Accordingly, focus is placed on the development of new PET perfusion tracers. At present, fluorine-18 (^{18}F) and copper-62 (^{62}Cu)-labelled tracers are suggested as possible substitutes. The novel PET tracer ^{18}F-flurpiridaz has great potential, as it demonstrates high extraction rates even at high blood flows in combination with a slow washout. The phase 2 study demonstrated its clinical safety and superior imaging quality in poststress PET images when compared with poststress SPECT. A phase 3 multicenter study is assessing the diagnostic efficacy of ^{18}F-flurpiridaz imaging for CAD detection.

3.3.1.2 PET Imaging Protocols

At present, ^{82}Rb (activity 1.10–2.22 GBq) or [^{13}N]-ammonia (activity 0.35–1.2 GBq) are still the most frequently used tracers in clinical practice. Although this paragraph focuses on these two tracers, the general principles described also apply for ^{18}F- and ^{62}Cu-based tracers.

Tracer Administration

Tracer administration is commonly performed at rest and during stress. ^{82}Rb is typically used in combination with pharmacological stress induction using adenosine. Though [^{13}N]-ammonia, having a longer biological half-life than ^{82}Rb, can also be used in combination with physical stress, pharmacological protocols are generally used. Both tracers are injected as a single bolus or short infusion (<30 s). Immediately after tracer injection, image acquisition is initiated. When ^{82}Rb is used, image acquisition will continue for ~10 min. If [^{13}N]-ammonia is used gating may also be applied, and imaging continues for ~20 min.

Positron Emission Imaging

This technique relies on detection by the ring of detectors of two gamma rays that originate from the same annihilation event. An annihilation event is only registered if a detector pair identifies the gamma rays almost simultaneously (e.g., coincidence detection). This method of count detection enables accurate localization of the annihilation event along the line between two detectors. Inherently, this method of locating nuclear events has a better spatial resolution than detecting single-event emissions, thus explaining the superior resolution of PET (~5 mm) compared with SPECT imaging (~10 mm). The ideal method to store this data, although requiring substantial computing power, is in so-called list mode. List-mode acquisition detects all counts independently without combining counts into specific time frames. ECG gating can still be used, but counts are not

Fig. 3.7 Quantification model generally used for [^{13}N]-ammonia positron emission tomography (PET) studies. This model assumes that the tracer will diffuse freely from the blood vessel to the interstitial space. Once the intracellular space is reached, the [^{13}N]-ammonia is metabolized into [^{13}N]-glutamine within the myocytes; thereafter, it cannot return to the interstitial space and will be trapped in the cell

allocated to specific frames, and each count is individually stored in the database. After acquisition, it is possible to reconstruct this image data for a specific goal, such as quantifying MBF and assessing cardiac function or static regional flow patterns.

Low-Dose Computed Tomography Scans

These scans an important part of the PET-imaging protocol, as this data is used to model the distribution of attenuators throughout the body. When nuclear rays pass through tissue, attenuation occurs. The attenuation coefficient characterizes the degree to which radiation is absorbed or scattered within the tissue. Bone, for example, has a high coefficient and will absorb many of the rays, whereas fat has a very low coefficient. This heterogeneous distribution of attenuators makes it difficult to estimate the trajectory of the rays and hence the location of an annihilation event. As the X-ray tube of the CT scanner produces a homogenous amount of rays with a fixed energy, acquired images can be used to map attenuation coefficients of the body in 3D. This attenuation map is used to correct annihilation events detected by the PET scanner.

3.3.2 CAD Identification Using PET

Interpreting static PET perfusion images is almost similar to assessing SPECT perfusion images. First, image data needs to be reoriented in the standard short- and long-axis directions. Subsequently, perfusion patterns are visually described by comparing stress–rest images to discriminate between ischemic and infarcted regions. The additive value of PET over SPECT is related to its superior spatial resolution, increased tracer uptake at high possibility of absolute flow quantification.

3.3.2.1 Absolute Flow Quantification

Flow quantification involves imaging of tracer uptake and clearance from the myocardial tissue over time. A simple quantification model describes these processes using two compartments: arterial circulation and myocardial tissue (Fig. 3.7). Depending on the tracer being used, different pharmacokinetic characteristics can also be included into this model. The time–activity relationship for the arterial compartment, also known as the input function, can be acquired from either arterial blood sampling, a reference database, or sampling an arterial signal in PET images (i.e., LV blood cavity). Myocardial tissue activity concentration is directly derived from PET images. Assuming that the relationship between blood flow and extraction rate is proportional, MBF can then be quantified over time [18]. These flow quantification techniques are applied to both rest and stress images. Stress flow in particular, which is in fact an absolute measure of the hyperemic response of coronary arteries, can be helpful in assessing the significance of a stenosis. The difference between hyperemic response and rest perfusion, also known as the myocardial flow reserve, can provide additional information on functional abnormalities in the coronary circulation. Both measures are at present particularly useful in

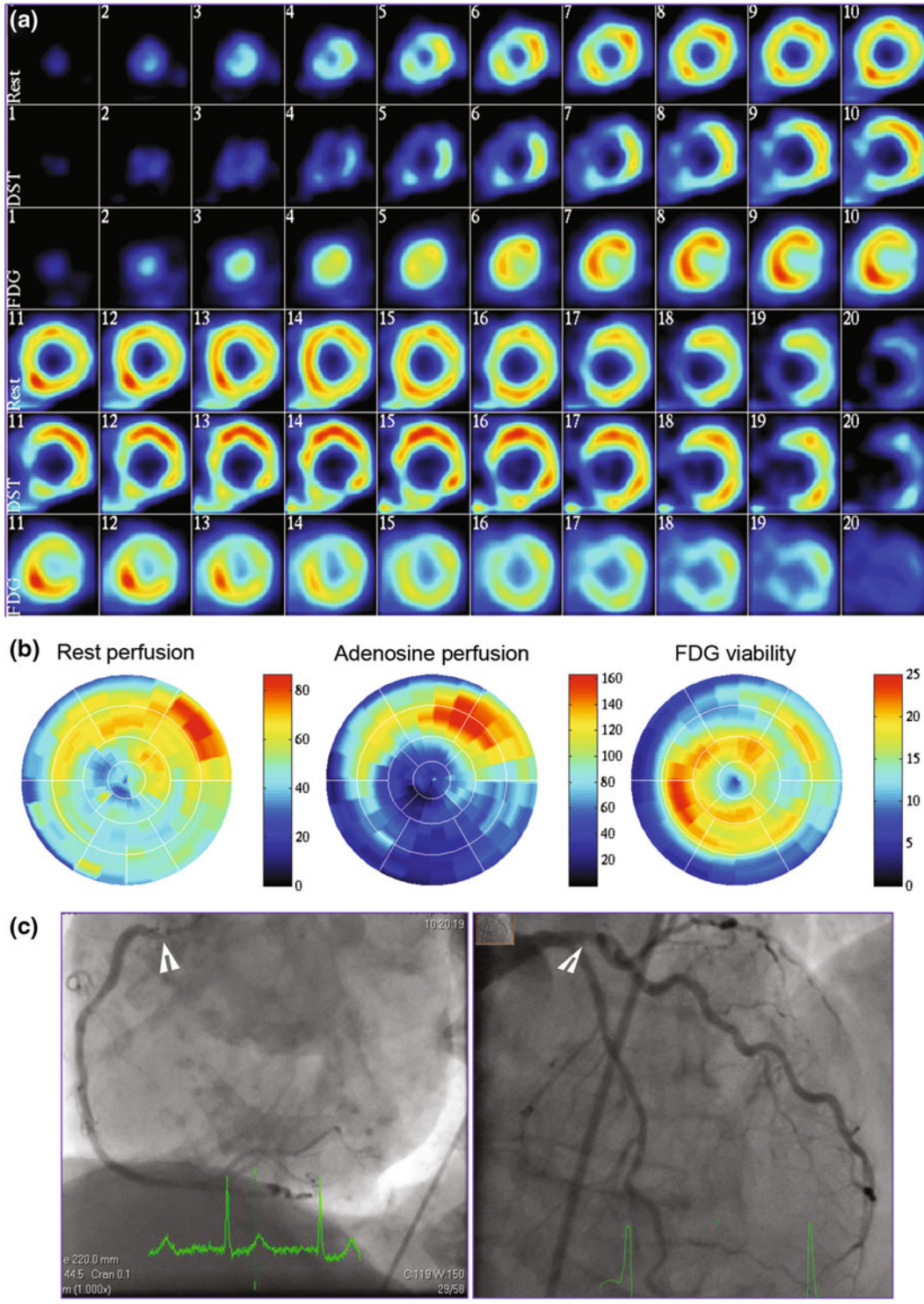

Case provided by R. Slart MD, PhD. Dept. of Nucleair Medicine and Molecular Imaging, University Medical Center Groningen

◀ **Fig. 3.8** In this asymptomatic male patient with increased risk profile for coronary artery disease (CAD) (hypertension, diabetes mellitus, severe obesity), rest–stress [^{13}N]-ammonia scan was combined with an [^{18}F]-fluorodeoxyglucose ([^{18}F]FDG) scan. **a** Short-axis images of rest (*upper row*) and stress (*middle row*) show severe perfusion defects in the anteroseptal, septal, and inferior regions over the entire wall that are in part reversible. The [^{18}F]FDG scan (*lower row*) shows intense uptake in these regions, thus suggesting the presence of viable myocardium. **b** On the quantitative myocardial blood flow (MBF) polar maps, mean blood flow at rest and stress were, respectively, 52 mL/min/100 g and 68 mL/min/100 g. These results indicate that blood flow in the entire myocardium is reduced. **c** Angiographic images showing the very proximally located stenoses in the right coronary artery and the left anterior descending artery (*arrows*). These ostial stenoses can easily be missed on invasive coronary angiography]

patients suspected with triple vessel disease. However, these parameters can also be used for early detection of nonsignificant stenosis (diameter occlusion <70%).

3.3.3 Myocardial Viability Imaging

PET perfusion imaging, especially in patients with severe CAD or ischemic cardiomyopathy, is regularly combined with metabolic imaging to detect hibernating myocardium. Hibernation refers to local cardiac dysfunction in areas with decreased perfusion, and also in which myocytes are still viable. The fact that these myocytes are still viable implies that these ischemic regions will likely benefit from revascularization therapies. Using tracer fluorine-18 fluorodeoxyglucose ([^{18}F]FDG), a radioactive glucose analogue, the extent of myocyte viability can be assessed. As the glucose metabolism is an adenosine triphosphate (ATP)-dependent process, it requires viable myocytes. Alternatively, the myocardium can utilize fatty-acid metabolism to obtain its energy. Therefore, the patient will fast 6–12 h prior to [^{18}F]FDG administration, after which a standardized glucose dose is administered. This preparation ensures that glucose metabolism will become the predominant process within the myocardium. When evaluating [^{18}F]FDG scans, comparison is made between its uptake and local perfusion patterns (Fig. 3.8). Identifying a mismatch within the perfusion–metabolism relationship is suggestive for hibernating myocardium. The areas in which both perfusion and [^{18}F]FDG uptake are decreased are generally scarred and have irreversible loss of cardiac function.

As described previously, viability can also be assessed using SPECT-based tracers. The visual agreement between [^{18}F]FDG PET and post nitrate ^{99m}Tc-sestamibi or tetrofosmin SPECT images is excellent, and diagnostic impact is also considered comparable [3]. Considering the high costs associated with PET and its limited availability, post-nitrate ^{99m}Tc-agents SPECT imaging will have great potential for use in clinical practice.

3.3.4 Clinical Utility of Perfusion PET in Assessing CAD

PET is considered to have a high diagnostic accuracy for detecting CAD due to its high count sensitivity, good spatial resolution, and sophisticated flow quantification techniques. There are a number of single-center studies comparing either [^{13}N]-ammonia or ^{82}Rb imaging with invasive coronary angiography. The pooled sensitivity and specificity of these PET imaging protocols in diagnosing CAD is 84 and 81%, respectively [15]. However, due to relatively high costs and a limited number of large multicenter studies indicating its additive value, the role of PET in risk stratification of patients with suspected CAD remains limited. The first studies to evaluate the clinical utility of myocardial perfusion PET demonstrate an excellent prognostic value [19]. However, costs associated with perfusion PET are substantial, and for many tracers currently used, an online cyclotron or generator is needed. These limitations led to the development of ^{18}F-labelled tracers, which may hold promise for better implementation of PET in the clinical routine.

3.4 Perfusion Cardiovascular Magnetic Resonance

CMR is a promising, noninvasive, ionizing-radiation-free imaging modality to evaluate ischemic heart disease. CMR is the reference standard technique for assessing cardiac structure and function. In recent years, tissue characterization by CMR has shown strong association with patient prognosis. Likewise, ischemia assessment by perfusion CMR has undergone considerable technical advancement and is extensively validated for routine clinical application for detecting myocardial ischemia. The general approach for CMR perfusion imaging relies on the visualization of contrast medium flowing through the myocardium. This is done using an MR pulse sequence to create images, thus increasing myocardial SI during the first passage of the contrast agent through the coronary bed, resulting in myocardium brightening. As a result, the relative level and extent of perfusion between adjacent myocardial segments as well as a determination of the absolute perfusion of a particular myocardial segment, can be visualized.

3.4.1 Basic Principles of CMR Perfusion

CMR images are acquired using MR sequences comprising a combination of radiofrequency pulses, magnetic gradient-field switches in the presence of a strong external magnetic field, and timed data acquisitions. CMR is mainly performed at a magnetic field strength of 1.5 Tesla, although 3-Tesla systems are now also being used. The benefit from higher field strengths is the increase in signal-to-noise ratio (SNR). However, there are problems related to artifacts due to field inhomogeneities and other technical issues that make high-field CMR less appealing for clinical use.

Actual perfusion of the myocardium is visualized by infusing gadolinium-based contrast agents. This exogenous contrast agent has high SI on the standard T1-weighted image sequences due to the presence of seven unpaired electrons in its molecule. Furthermore, the safety profile of gadolinium in patients with normal or mildly impaired renal function ensures that gadolinium is an attractive contrast agent. The preferred gadolinium dose ranges from 0.05 to 0.10 mmol/kg bodyweight to avoid artifacts due to saturation effects [20]. In first-pass perfusion CMR, the dynamic passage of gadolinium contrast is followed through the cardiac chambers and the myocardium under vasodilator stress using adenosine (140 μg kg^{-1} min^{-1}). During pharmacologic vasodilatation, myocardial areas subtended by normal coronary arteries show a three- to fivefold increase in blood flow compared with no (or only minimal) change in blood flow observed downstream of severely diseased arteries. Such areas therefore show lower peak enhancement, with delayed contrast uptake and appear hypointense (dark) compared with adjacent normal myocardium (Fig. 3.9). The same sequence is repeated at rest after approximately 10 min to allow sufficient contrast washout. CMR perfusion imaging has high spatial resolution (typically <3 mm), allowing identification of even small perfusion defects confined to the subendocardium [21].

3.4.2 Image Interpretation

The majority of clinical scans are analyzed qualitatively by visually comparing stress and rest scans in parallel. Typically, three short-axis slices are acquired per cardiac cycle: at the basal, mid papillary, and apical levels of the LV. High temporal resolution (every or every other heart beat) is required to capture transient ischemia in the myocardium under pharmacological stress and to distinguish artifacts (e.g., dark-rim artifacts during a few frames at peak enhancement). Rest and stress CMR perfusion are generally performed in combination to improve the differentiation between artifacts and true perfusion abnormalities. Various modifications of T1-weighted, ECG gated, multislice acquisitions have been proposed for assessing first-pass myocardial SI changes in cine mode.

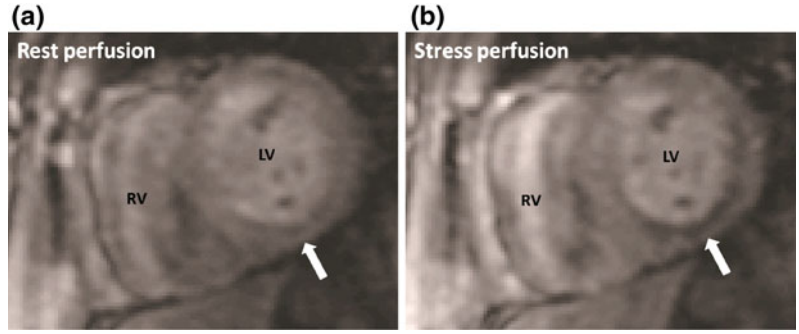

Fig. 3.9 Cardiac magnetic resonance (CMR) perfusion scan at (**a**) rest and (**b**) adenosine stress. Patients had significant stenosis of the right coronary artery. Note the hypoenhancement in the inferior wall during stress (*arrow*), which is not present at rest (*arrow*). Therefore, this hypoenhanced area represents a perfusion defect in the inferior wall

Commonly, an inversion recovery MR pulse sequence is used in conjunction with gadolinium first-pass contrast enhancement to evaluate a number of perfusion parameters, both qualitatively and quantitatively. Time versus intensity curves, where the first pass of gadolinium through the myocardium is plotted as SI versus time, allows quantitative analysis by deriving parameter values from the time series of intensity values. The SI curve for each sector should be compared with the wash-in curve of the LV blood pool, looking for the characteristic upslope and delayed and reduced peak signal amplitude. However, for routine clinical application, perfusion image interpretation is most commonly visual, and the extra processing time for quantitative analysis must be weighed against the speed of visual analysis. The potential added value of quantitative over qualitative perfusion analysis is under investigation.

3.4.3 Additional Imaging Protocols in Cardiovascular Magnetic Resonance Imaging

Visualizing irreversible myocardial injury using late gadolinium enhancement (LGE) or delayed enhancement was a major breakthrough that advanced the role of CMR in ischemic heart disease. The rationale behind LGE is an increase in the gadolinium-based contrast agent distribution within areas of fibrosis and an abnormally prolonged washout due to a decreased functional capillary density in the irreversibly injured myocardium. The regional increase in extracellular volume of gadolinium distribution manifests as hyper enhancement (high signal) in areas of myocardial injury compared with the black normal myocardium on LGE images.

Furthermore, the addition of edema imaging may provide useful insights into patients with acute coronary syndromes (ACS) or suspected myocarditis. Regional increases in myocardial water content can be detected with T2-weighted CMR imaging. However, further improvements in pulse-sequence techniques are required for this type of CMR imaging.

In conclusion, the optimal CMR protocol in patients with ischemic heart disease should exist of multiplanar cine imaging [horizontal long-axis, vertical long-axis, and LV outflow views, and contiguous short-axis view covering the right (RV) and LV], LGE acquisitions in the same planes, and perfusion imaging (basal, mid, and apical short-axis slices) under vasodilator stress. Edema imaging may be added in patients with ACS or suspected myocarditis. Furthermore, the indication for MR coronary angiography is only appropriate for identifying coronary anomalies or aneurysms [22].

3.4.4 Diagnostic Value and Clinical Advantages of CMR Perfusion Imaging

Diagnostic performance of stress CMR perfusion for detecting CAD is good, with a sensitivity of 89% and a specificity of 76% at the patient level [15]. There are a number of variations in clinical practice when performing CMR myocardial perfusion, such as variations in contrast dose. CMR accuracy increases when a combined analysis of perfusion, wall motion, and delayed-enhancement CMR techniques is performed. Furthermore, adenosine is superior to and safer than dipyridamole as a stress agent [23]. Finally, visual assessment of CMR perfusion images results in a higher sensitivity but lower specificity compared with semiquantitative analysis, which is more time consuming [23]. Overall, it seems that greater standardization of CMR techniques and protocols is required.

In a prospective trial comparing CMR myocardial perfusion diagnostic value versus SPECT for diagnosing CAD [24], >750 patients with suspected angina pectoris underwent CMR perfusion, SPECT, and invasive X-ray angiography. The authors used a combined analysis of CMR data (including perfusion, wall motion, and LGE whole-heart MR angiography) as a multiparametric test to identify CAD. Sensitivity and negative predictive value (NPV) of the combined CMR evaluation was significantly superior to SPECT but not for specificity and positive predictive value (PPV) data. It is expected that higher CMR field strengths and myocardial perfusion quantification may further improve CMR perfusion imaging results. For example, 3-Tesla CMR provides a wider dynamic range for T1 changes induced by gadolinium administration compared with lower field strengths. This may result in improved image quality to better visualize and quantify perfusion abnormalities. An experimental study has shown the feasibility and improved analysis over lower field strengths of measuring absolute MBF (expressed as milliliters per minute per gram) at 3-Tesla CMR [25].

Perfusion CMR has several advantages over existing tests, including an excellent safety profile, high sensitivity, relative absence of artifacts induced by unfavorable body habitus, and superior spatial resolution. These technical factors permit ischemia assessment in patients who may be challenging for other modalities. Moreover, the multicomponent examination in CMR imaging is mostly performed in clinical practice because it detects CAD even more accurately. Furthermore, because of the absence of harmful ionizing radiation, serial CMR perfusion examinations can be performed that may be clinically useful to reassess disease progression or evaluate response to therapy.

In conclusion, CMR myocardial perfusion imaging is now established as a reliable noninvasive tool for detecting CAD. However, availability and expertise varies among sites. Therefore, further standardization of techniques and postprocessing is required. In particular, the integrated CMR approach of multiparametric assessment of ischemic heart disease appears to offer improved diagnostic accuracy.

3.5 Future Perspectives

In the last three decades, myocardial perfusion imaging has established itself as an excellent noninvasive method diagnosing CAD with flow-limiting lesions. Additionally, myocardial perfusion imaging has proved to be highly useful for risk stratification in different clinical settings, such as stable CAD, prior to noncardiac surgery, after coronary revascularization, and in acute coronary syndromes. Importantly, in stable patients, a normal perfusion scan is associated with an excellent midterm prognosis, with a risk of death or nonfatal myocardial infarction of approximately 1% per year [12]. Nonetheless, myocardial perfusion imaging can only detect coronary lesions that induce perfusion defects; it does not exclude the presence of subclinical, nonobstructive coronary atherosclerosis. With the knowledge that approximately 70% of plaque ruptures leading to myocardial infarctions

occur in lesions that are nonobstructive plaques [26], the inability to diagnose nonobstructive CAD can be considered an important limitation of myocardial perfusion imaging. Therefore, combined functional and anatomical imaging, assessing both the presence of coronary lesions and their hemodynamic relevance, could better guide clinical discussion, leading to the most appropriate treatment strategy in patients with known or suspected CAD.

3.5.1 Cardiac Hybrid Imaging

The principle of multimodality imaging is to combine the strengths of different imaging modalities or imaging agents. This can be achieved by post acquisition fusion of two image data sets (i.e., software-based co registration) or by acquiring images using a true hybrid scanner. Modern PET and SPECT scanners are commonly integrated with either a low-dose or high-resolution CT system. Nonetheless, only the combination of a nuclear scanner with high-resolution CT is considered true hybrid imaging. Also, the first commercial hybrid PET-MRI systems are now available.

In the setting of CAD, visualizing coronary anatomy combined with molecular or physiological information may be of great diagnostic and prognostic value. The combination of high-resolution CT with nuclear imaging allows for better identification of the flow-limiting or culprit lesions that would benefit from revascularization therapies. Especially in low-risk populations or in patients with severe multivessel disease, this form of hybrid imaging can be of added clinical value [27]. Furthermore, with the development of new agents for specific atherosclerotic pathways, hybrid imaging will probably become even more important. Still, the routine clinical use of hybrid imaging remains controversial due to the increase in radiation exposure and the medical costs associated with excessive imaging. Therefore, large multicentre trails should provide more insight of the clinical value and effectiveness of hybrid cardiac imaging over the side-by-side evaluation of these images in specific patient populations [28].

3.5.2 Myocardial Computed Tomography Perfusion

Multidetector-row computed tomography (MDCT) is increasingly used for noninvasive anatomical evaluation of coronary artery stenoses. However, a major critique of this technique is the fact that no information on the physiological relevance of the detected lesions is provided when looking at the noninvasive angiographic images. As a result, when a significant lesion is detected on MDCT, noninvasive assessment of ischemia is still necessary in a substantial number of patients. Not surprisingly, therefore, recent advancements in scanner technology, such as wide-area coverage and faster rotation times, have rekindled the development of myocardial CT perfusion (CTP) protocols.

The principles of CTP are similar to those of CMR perfusion. Briefly, the technique relies on the fact that using iodinated contrast material, X-ray attenuation is proportional to contrast-agent concentration. Accordingly, myocardial regions with reduced perfusion are identified based on decreased attenuation. Correct timing of acquisition is crucial, and imaging should be performed during the early portion of first-pass circulation of the contrast bolus.

There are several approaches for myocardial CTP. During dynamic CTP, serial imaging over time is performed in order to obtain the kinetics of the contrast agent in the arterial blood pool and myocardium. The major advantage of this approach is that it allows absolute quantification of myocardial blood flow. Ho et al. show good agreement of CT-derived MBF and nuclear imaging [29]. So far, the widespread application of dynamic imaging protocols has been limited for several reasons. As multiple acquisitions are performed, the resulting radiation dose is relatively high. In addition, previous generations of CT scanners provided only limited coverage in the z-axis, thus failing to visualize the entire

heart during a dynamic imaging sequence. This problem has been overcome by the introduction of wide-area detectors or, to some extent, by imaging using a shuttle mode.

A more practical approach, therefore, may be helical CTP. During helical CTP, the heart is imaged during the upslope or the peak of contrast bolus. Whereas no absolute quantification of MBF can be performed, the helical approach can still provide qualitative and semiquantitative assessment of perfusion defects. Several single-center studies have been performed comparing helical CTP to either nuclear imaging or fractional flow reserve (FFR). Using FFR as the gold standard, Ko and colleagues demonstrated that, particularly in territories with concordant computed tomography angiography (CTA) and CTP results, the combination of CTA and CTP has a high accuracy to detect or exclude ischemia [30]. Recently, a meta-analysis was published, revealing a sensitivity, specificity, PPV, and NPV of 81, 93, 87, and 88% for CTA in combination with CTP using conventional coronary angiography and FFR as the gold standard [31].

It is conceivable that CTP may particularly enhance the diagnostic accuracy of CT in patients with abnormal or uncertain CTA studies. In these patients, further imaging is frequently needed to confirm the presence of a hemodynamically relevant stenosis requiring intervention. The addition of CTP in such patients may facilitate clinical management decisions (Fig. 3.10). On the other hand, in patients with normal coronary arteries on CTA, additional CTP may not be required. Indeed, several studies have indicated that the increased diagnostic accuracy of combined CTA and CTP compared with CTA alone can be largely attributed to an increase in PPV as well as improved reader confidence.

In conclusion, the combination of CTA and CTP may provide an attractive approach for comprehensive evaluation of both anatomy and function in a single examination. However, at present, several uncertainties remain: from the optimal acquisition method for CTP to its precise position within clinical practice. Also, the associated radiation dose remains a cause of concern. Nevertheless, recent studies suggest that a combined CTA and CTP protocol can be performed with a radiation dose in the range of 10–15 mSv, which is comparable with nuclear imaging [32]. Continuing advancements in dose-reduction techniques, such as iterative reconstruction, are expected to reduce X-ray exposure even further. Finally, available data remain restricted to relatively small, single-center studies. In this regard, results from the international multicenter trial Combined Non-invasive Coronary Angiography and Myocardial Perfusion Imaging Using 320 Detector Computed Tomography (Core320), comparing CTA in combination with CTP with invasive angiography and SPECT, will provide important data to consolidate the value of CTP in clinical practice.

3.6 Discussion

Noninvasive imaging is crucial in order to understand the pathophysiological mechanisms that underlie cardiac diseases. Moreover, the use of noninvasive imaging allows patients who might benefit from different therapies to be selected. Furthermore, it is frequently used to guide therapeutic interventions. Rest and stress myocardial perfusion imaging is used to diagnose CAD and identify patients at risk of future cardiac events. In addition, the combination of anatomical, morphological, and functional data obtained with different imaging modalities, such as radionuclide techniques, MDCT, and CMR, increases diagnostic accuracy and improves the efficacy of therapeutic interventions and clinical outcomes.

Achievements in the field of myocardial perfusion imaging are considerable, and new technical developments are ongoing. Yet, it remains a challenge to define which modality provides the best and most useful clinical information. All noninvasive tests have their limitations, such that alternative investigative options are needed. The relatively low specificity is the main limitation of myocardial perfusion SPECT. CMR and PET have significantly higher diagnostic accuracy than SPECT [15].

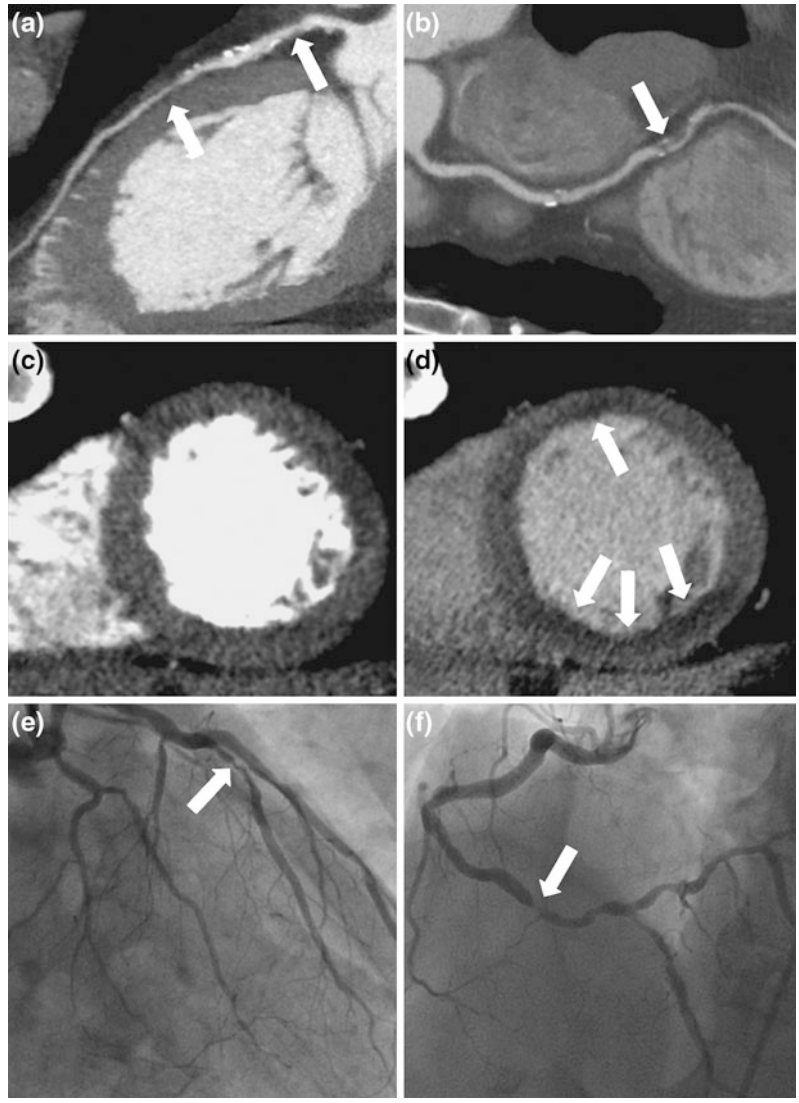

Fig. 3.10 Combined assessment of anatomy and function with computed tomography (CT). **a**, **b** Coronary computed tomography angiography (CTA obtained at rest. Atherosclerosis resulting in significant coronary stenoses can be seen on curved multiplanar reconstructions of the left anterior coronary artery (LAD) (**a**), and right coronary artery (RCA) (**b**), respectively. **c** Short-axis reconstruction of rest CTA scan shows normal myocardial perfusion. **d** However, during adenosine stress, hypoperfusion is identified in both anterior and inferior walls, indicating the presence of ischemia. **e**, **f** Invasive coronary angiography in combination with fractional flow reserve confirmed the presence of hemodynamically significant stenoses in both the LAD (**e**) and RCA (**f**). Image courtesy of Dr. K. F. Kofoed, Rigshospitalet, University of Copenhagen, Denmarkf

Moreover, with the use of CMR and PET, absolute measurements of myocardial perfusion can be obtained. However, the main limitation of PET is its limited availability and high costs, hampering its widespread clinical. SPECT is the most widely used and validated imaging technique, and advances in attenuation correction lead to an increased specificity of SPECT, with fewer false positives. In addition, novel techniques such as new dedicated ultrafast (UF)

cameras with pinhole collimation design and multiple CZT crystal arrays have been developed, which increase spatial resolution of myocardial perfusion SPECT. The short acquisition time and reduced radiation exposure, because of the smaller doses of radioisotope that are needed, with maintained image quality, are the main advantages of UF SPECT. The relatively low dose and excellent clinical accuracy open new perspectives in UF SPECT in ischemic patients [33].

In comparison with nuclear techniques, CMR perfusion imaging does not suffer from attenuation artifacts and provides the highest spatial resolution. In addition, it is often performed in combination with other imaging protocols, such as delayed gadolinium enhancement for detecting the presence and extent of myocardial scar, to identify CAD even more accurately. Nonetheless, the use of CMR perfusion imaging is less appropriate for patients with a pacemaker, who are claustrophobia, or have a wide abdominal girth.

In conclusion, SPECT, PET, and CMR each have their own respective merits and technical limitations. However, future technical developments are likely to improve the diagnostic performance and reduce the limitations for all three modalities by combined imaging of myocardial perfusion, prior myocardial infarction, and coronary anatomy. Finally, the choice of imaging modality in current clinical practice depends on a number of factors, such as local availability and operator expertise, the individual patient and—most importantly—the clinical question, which has to be answered.

References

1. Wijns W, Kolh P, Danchin N et al (2010) Guidelines on myocardial revascularization. Eur Heart J 31:2501–2555
2. Baggish AL, Boucher CA (2008) Radiopharmaceutical agents for myocardial perfusion imaging. Circulation 118:1668–1674
3. Giorgetti A, Marzullo P, Sambuceti G et al (2004) Baseline/post-nitrate Tc-99m tetrofosmin mismatch for the assessment of myocardial viability in patients with severe left ventricular dysfunction: comparison with baseline Tc-99m tetrofosmin scintigraphy/FDG PET imaging. J Nucl Cardiol 11:142–151
4. Hesse B, Tägil K, Cuocolo A et al (2005) EANM/ESC procedural guidelines for myocardial perfusion imaging in nuclear cardiology. Eur J Nucl Med Mol Imaging 32:855–897
5. Ibrahim DY, DiFilippo FP, Steed JE, Cerqueira MD (2006) Optimal SPECT processing and display: making bad studies look good to get the right answer. J Nucl Cardiol 13:855–866
6. Gimelli A, Bottai M, Giorgetti A et al (2011) Comparison between ultrafast and standard single-photon emission CT in patients with coronary artery disease: a pilot study. Circ Cardiovasc Imaging 4:51–58
7. Slomka P, Xu Y, Berman D, Germano G (2012) Quantitative analysis of perfusion studies: strengths and pitfalls. J Nucl Cardiol 19:338–346
8. Underwood SR, Anagnostopoulos C, Cerqueira M et al (2004) Myocardial perfusion scintigraphy: the evidence. Eur J Nucl Med Mol Imaging 31:261–291
9. Marcassa C, Bax JJ, Bengel F et al (2008) Clinical value, cost-effectiveness, and safety of myocardial perfusion scintigraphy: a position statement. Eur Heart J 29:557–563
10. Perrone-Filardi P, Achenbach S, Möhlenkamp S et al (2011) Cardiac computed tomography and myocardial perfusion scintigraphy for risk stratification in asymptomatic individuals without known cardiovascular disease: a position statement of the working group on nuclear cardiology and cardiac CT of the European society of cardiology. Eur Heart J 32:1986–1993
11. Gimelli A, Rossi G, Landi P et al (2009) Stress/rest myocardial perfusion abnormalities by gated SPECT: still the best predictor of cardiac events in stable ischemic heart disease. J Nucl Med 50:546–553
12. van Werkhoven JM, Schuijf JD, Gaemperli O et al (2009) Prognostic value of multislice computed tomography and gated single-photon emission computed tomography in patients with suspected coronary artery disease. J Am Coll Cardiol 53:623–632
13. Shaw LJ, Iskandrian AE (2004) Prognostic value of gated myocardial perfusion SPECT. J Nucl Cardiol 11:171–185
14. Hendel RC, Berman DS, Di Carli MF et al (2009) ACCF/ASNC/ACR/AHA/ASE/SCCT/SCMR/SNM 2009 appropriate use criteria for cardiac radionuclide imaging. J Am Coll Cardiol 53:2201–2229
15. Jaarsma C, Leiner T, Bekkers SC et al (2012) Diagnostic performance of noninvasive myocardial perfusion imaging using single-photon emission computed tomography, cardiac magnetic resonance, and positron emission tomography imaging for the detection of obstructive coronary artery disease: a meta-analysis. J Am Coll Cardiol 59:1719–1728
16. Scholte AJ, Schuijf JD, Kharagjitsingh AV et al (2009) Prevalence and predictors of an abnormal stress myocardial perfusion study in asymptomatic

patients with type 2 diabetes mellitus. Eur J Nucl Med Mol Imaging 36:567–575
17. Knuuti J, Bengel FM (2008) Positron emission tomography and molecular imaging. Heart 94:360–367
18. Klein R, Beanlands RS, deKemp RA (2010) Quantification of myocardial blood flow and flow reserve: Technical aspects. J Nucl Cardiol 17:555–570
19. Schindler TH, Schelbert HR, Quercioli A, Dilsizian V (2010) Cardiac PET imaging for the detection and monitoring of coronary artery disease and microvascular health. JACC Cardiovasc Imaging 3:623–640
20. Wolff SD, Schwitter J, Coulden R et al (2004) Myocardial first-pass perfusion magnetic resonance imaging: a multicenter dose-ranging study. Circulation 110:732–737
21. Karamitsos TD, Dall'Armellina E, Choudhury RP, Neubauer S (2011) Ischemic heart disease: comprehensive evaluation by cardiovascular magnetic resonance. Am Heart J 162:16–30
22. Hendel RC, Patel MR, Kramer CM et al (2006) ACCF/ACR/SCCT/SCMR/ASNC/NASCI/SCAI/SIR 2006 appropriateness criteria for cardiac computed tomography and cardiac magnetic resonance imaging: a report of the American college of cardiology foundation quality strategic directions committee appropriateness criteria working group, American college of radiology, society of cardiovascular computed tomography, society for cardiovascular magnetic resonance, American society of nuclear cardiology, North American society for cardiac imaging, society for cardiovascular angiography and interventions, and society of interventional radiology. J Am Coll Cardiol 48:1475–1497
23. Hamon M, Fau G, Née G et al (2010) Meta-analysis of the diagnostic performance of stress perfusion cardiovascular magnetic resonance for detection of coronary artery disease. J Cardiovasc Magn Reson 12:29
24. Greenwood JP, Maredia N, Younger JF et al (2012) Cardiovascular magnetic resonance and single-photon emission computed tomography for diagnosis of coronary heart disease (CE-MARC): a prospective trial. Lancet 379:453–460
25. Christian TF, Bell SP, Whitesell L, Jerosch-Herold M (2009) Accuracy of cardiac magnetic resonance of absolute myocardial blood flow with a high-field system: comparison with conventional field strength. JACC Cardiovasc Imaging 2:1103–1110
26. Falk E, Shah PK, Fuster V (1995) Coronary plaque disruption. Circulation 92:657–671
27. Pazhenkottil AP, Nkoulou RN, Ghadri JR et al (2011) Impact of cardiac hybrid single-photon emission computed tomography/computed tomography imaging on choice of treatment strategy in coronary artery disease. Eur Heart J 32:2824–2829
28. Flotats A, Knuuti J, Gutberlet M et al (2011) Hybrid cardiac imaging: SPECT/CT and PET/CT. A joint position statement by the European Association of Nuclear Medicine (EANM), the European Society of Cardiac Radiology (ESCR) and the European Council of Nuclear Cardiology (ECNC). Eur J Nucl Med Mol Imaging 38:201–212
29. Ho KT, Chua KC, Klotz E, Panknin C (2010) Stress and rest dynamic myocardial perfusion imaging by evaluation of complete time-attenuation curves with dual-source CT. JACC Cardiovasc Imaging 3:811–820
30. Ko BS, Cameron JD, Meredith IT et al (2012) Computed tomography stress myocardial perfusion imaging in patients considered for revascularization: a comparison with fractional flow reserve. Eur Heart J 33:67–77
31. Tashakkor AY, Nicolaou S, Leipsic J, Mancini GB (2012) The emerging role of cardiac computed tomography for the assessment of coronary perfusion: a systematic review and meta-analysis. Can J Cardiol 28:413–422
32. George RT, Arbab-Zadeh A, Miller JM et al (2012) Computed tomography myocardial perfusion imaging with 320-row detector computed tomography accurately detects myocardial ischemia in patients with obstructive coronary artery disease. Circ Cardiovasc Imaging 5:333–340
33. Gimelli A, Bottai M, Genovesi D et al (2012) High diagnostic accuracy of low-dose gated-SPECT with solid-state ultrafast detectors: preliminary clinical results. Eur J Nucl Med Mol Imaging 39:83–90

Innervation of the Heart: Imaging Findings Using [^{123}I]-MIBG Scintigraphy in Different Pathologies

4

Denis Agostini, Kenichi Nakajima and Hein Jan Verberne

4.1 Introduction

The heart is innervated by the autonomic nervous system (ANS). The ANS provides innervation through fibers originating from autonomic ganglia located outside the central nervous system (CNS) in response to the preganglionic cholinergic stimulation coming from the CNS. The ANS has great influence on cardiovascular physiology by controlling the cardiac performance (contractility, conduction, and heart rate) to respond quickly and effectively to changing demands. The sympathetic nervous system (SNS) is dominant in the heart, principally in the ventricles.

4.1.1 Sympathetic Innervation

The SNS is one of the neurohormonal compensation mechanisms that play key roles in the pathogenesis of heart failure (HF). The SNS, together with the hypothalamic–pituitary–adrenal axis, was thought to play an important supportive role in the flight, fright, and fight reaction of humans and animals in response to stressful situations. The cardiac autonomic nervous system (ANS) consists of two distinct and counteracting forms: sympathetic and parasympathetic innervation. They differ in their major neurotransmitters, norepinephrine and acetylcholine, and exert stimulating or inhibitory effects on target tissues via adrenergic and muscarinic receptors. Both are responsible for electrophysiologic and hemodynamic adaptation of the cardiovascular system to changing demands.

4.1.1.1 Anatomy and Physiology of the SNS in the Myocardium

Whereas parasympathetic fibers are mainly present in the atria and less abundant in ventricular myocardium, the SNS is the predominant autonomic component in the ventricles. Sympathetic fibers travel along epicardial vascular structures and penetrate into underlying myocardium similar to coronary vessels. On the basis of tissue norepinephrine content, the heart is characterized by dense sympathetic innervation with a gradient from the atria to the base of the heart and from the base to the apex of the ventricles [1, 2].

D. Agostini (✉)
Nuclear Medicine, University Hospital CHU, Caen, France
e-mail: agostini-de@chu-caen.fr

K. Nakajima
Department of Nuclear Medicine, Kanazawa University Hospital, Kanazawa, Japan
e-mail: nakajima@med.kanazawa-u.ac.jp

H. J. Verberne
Department of Nuclear Medicine, Amsterdam Medical Center, University of Amsterdam, Amsterdam, The Netherlands
e-mail: h.j.verberne@amc.uva.nl

P. Marzullo and G. Mariani (eds.), *From Basic Cardiac Imaging to Image Fusion*,
DOI: 10.1007/978-88-470-2760-2_4, © Springer-Verlag Italia 2013

4.1.1.2 SNS Neurotransmitters

The dominant sympathetic transmitter, norepinephrine, is synthesized within neurons by an enzymatic cascade. Dihydroxyphenylalanine (DOPA) is generated from tyrosine and subsequently converted to dopamine by DOPA decarboxylase. Dopamine is transported into storage vesicles by the energy-requiring vesicular monoamine transporter. Norepinephrine is synthesized by dopamine β-hydroxylase within these vesicles. Neuronal stimulation leads to norepinephrine release through fusion of vesicles with the neuronal membrane (exocytosis). Apart from neuronal stimulation, release is also regulated by a number of presynaptic receptor systems, including α_2-adrenergic receptors, which provide negative feedback for exocytosis. Apart from norepinephrine, sympathetic varicosities store neuropeptide Y (NPY), methionine enkephalin, leucine enkephalin, β-endorphin, and adenosine triphosphate (ATP) in small and large vesicles. These neurotransmitters are co-released. It is important to realize that norepinephrine and ATP are locally recycled, whereas peptide neurotransmitters are transported along the sympathetic axon to the nerve terminal. At a high stimulation frequency over a longer period of time, the sympathetic nerve terminal is devoid of peptide neurotransmitters in relation to norepinephrine and ATP. The marked preferential increase in the release of cardiac norepinephrine probably contributes to the eventual depletion of norepinephrine in the failing heart. The heart is also thought to be functionally denervated, with reduction of tyrosine hydroxylase activity to account for the loss of norepinephrine.

In the synaptic cleft, only a small amount of released norepinephrine is actually available to activate postsynaptic receptors on the myocyte surface. Most norepinephrine undergoes reuptake into nerve terminals by the presynaptic norepinephrine transporter (uptake 1 mechanism) and recycles into vesicles or is metabolized in cytosol by monoamine oxidase (MAO). Small fractions of the released norepinephrine diffuse into vascular space, where it can be measured as norepinephrine spillover in coronary sinus or will be taken up by extraneuronal cells via the uptake 2 mechanism and followed by degradation to norepinephrine metabolites by catechol O-methyltransferase (COMT).

Sympathetic neurotransmission is achieved by norepinephrine-mediated activation of postsynaptic adrenoceptors. These are membrane-bound proteins on target tissue and are classified in subtypes according to their molecular biological and pharmacological characteristics. β-adrenoceptors are highly abundant in the myocardium and exert chronotropic, dromotropic, and inotropic effects. Both β_1- and β_2-subtypes are present at a ratio of $\sim$5:1 in the healthy human heart. β_1-adrenoreceptor activation leads to a much higher degree of adenyl cyclase stimulation compared with β_2-adrenoreceptor activation. However, the degree of stimulation of muscle contraction is similar for β_1- and β_2-adrenoreceptors and is directly related to their relative densities. The α-adrenoceptors are mainly present in the vascular wall but are also present in myocardium, where they account for approximately 15% of cardiac adrenergic receptors. Two classes of α- adrenergic receptors have been identified: α_1 and α_2. The α_1-adrenergic receptors can be further characterized into various subtypes, which are the result of separate gene products differing in structure, G-protein coupling, tissue distribution, signaling, regulation, and functions. Major arteries (including aorta, pulmonary arteries, mesenteric vessels, and coronary arteries) are heavily populated with α_1-receptors, and activation of these receptors by endogenous agonists of α-adrenergic receptors, epinephrine, and norepinephrine has been demonstrated to be a major contributor in the regulation of blood flow by vasoconstriction. The α_2-adrenergic receptors play a prominent role in SNS regulation. Activation of α_2-adrenergic receptors in the brainstem leads to reduced sympathetic tone, with a resultant decrease in heart rate and blood pressure. This effect is augmented by stimulation of α_2-adrenergic receptors on sympathetic nerve terminals. These presynaptic α_2-adrenergic

receptors serve as autoreceptors regulating catecholamine release. There are three α_2-adrenergic receptors subtypes (α_{2A}, α_{2B}, and α_{2C}), and studies using gene-targeting strategies indicate independent functions for each.

In conclusion, α_2-adrenergic receptors play an important role in regulating the SNS both centrally, by regulating sympathetic tone, and peripherally, by regulating transmitter release from presynaptic nerve terminals.

4.1.1.3 Uptake 1 and Uptake 2

Reuptake of catecholamines from the synaptic cleft is mediated by high-affinity, low-capacity, sodium-chloride-dependent transporters present in the outer membrane of the presynaptic nerve endings. This transport system is also known as the uptake 1 mechanism and consists of the norepinephrine transporter (NET) and the dopamine transporter (DAT). In addition to uptake 1, catecholamines are removed from the circulation by a second transport system. This second transport system consists of sodium-chloride-independent, corticosterone-sensitive, high-capacity extraneuronal monoamine transporters (EMT) originally discovered as a transport mechanism in rat heart and designated as uptake 2 mechanism. Molecular cloning has shown that uptake 1 and uptake 2 belong to two different families of transporters. The presynaptic neuronal uptake 1 transporters for norepinephrine and dopamine are both members of the solute carrier family of transporters (SLC6A2 and SLC6A3, respectively). Uptake-2 belongs to another subgroup of the SLC transporters (SLC22) and can be placed in the family of organic cation transporters (OCT), which has several members (OCT1, OCT2, and OCT3, or SLC22A1, SLC22A2, and SLC22A, respectively). The classical uptake 2 or EMT is most likely to be represented by OCT3 and is expressed in different organs (i.e., heart, liver, skeletal muscle, placenta, and kidney). OCTs are involved in absorption, distribution, and elimination of endogenous compounds (i.e., amines) as well as of drugs, toxins, and other xenobiotics.

Neuronal reuptake by uptake 1 is quantitatively most important for the clearance of released catecholamines, accounting for ~90% of their removal at the presynaptic nerve endings. Although OCT3 has been proposed to be the classical EMT, the three OCTs together are thought to be responsible for the extra-neuronal clearance of catecholamines that have escaped from reuptake by uptake 1. In general, uptake 1 and uptake 2 mechanisms are thought to have similar functions between species. However, small differences in the relative expression of these mechanisms between species have been reported. Due to these differences in distribution (i.e., expression) of uptake mechanisms, results found in experimental animal studies may not exactly reflect the situation in humans.

4.1.1.4 The SNS and Heart Failure

The SNS is one of the neurohormonal compensation mechanisms that play key roles in the pathogenesis of cardiac heart failure (CHF). Neurohormonal activation and a hyperadrenergic state cause desensitization and down-regulation of cardiac β-adrenoceptors and alterations in the postsynaptic signal transduction, which further impair myocardial performance. In the failing heart, not only are postsynaptic changes observed but so are presynaptic changes. An impaired cardiac uptake 1 mechanism has been observed. Although the pathogenetic mechanisms for altered presynaptic innervation are not fully elucidated, it is likely that it is by these mechanisms that the high concentration of catecholamines in the synaptic cleft is maintained. These effects probably further sustain and exacerbate the remodeling process [3].

4.1.2 From Guanethidine to Meta-Iodobenzylguanidine

4.1.2.1 Guanethidine

In the 1960s, guanethidine, a false neurotransmitter, was found to be a sympathetic selective and potent neuron blocking agent and was

developed as an antihypertensive drug. Guanethidine acts on the presynaptic sympathetic nerve ending by inhibiting or interfering with the release and/or distribution of norepinephrine rather than acting on the postsynaptic (i.e. effector) cell by inhibiting the association of norepinephrine with its receptors. In contrast to ganglionic blocking agents, guanethidine suppresses responses mediated by α- and β-adrenergic receptors equally, but does not produce parasympathetic blockade. Side effects are related to its neuron-blocking properties and include orthostatic and exercise hypotension, sexual dysfunction, and diarrhea. Guanethidine is no longer available in the USA due to its side effects and because there are substantially better drugs available. It is still licensed in some countries, i.e., the UK, for rapid control of blood pressure in a hypertensive emergency.

4.1.2.2 [^{123}I]-Meta-Iodobenzylguanidine

The modification of guanethidine into meta-iodobenzylguanidine (MIBG) increased the affinity for the presynaptic sympathetic nerve endings. MIBG labeling with radioactive iodine enabled scintigraphic visualization of presynaptic sympathetic nerve endings in humans. The first clinical application of the radiolabeled [^{131}I]-MIBG was visualization of the adrenal medulla and different neural-crest-derived tumors, such as pheochromocytomas and neuroblastomas. The striking myocardial uptake, however, prompted Wieland et al. to suggest the potential use of the radiolabeled MIBG for myocardial imaging [4]. However, due to the suboptimal imaging characteristics of ^{131}I and a less favorable radiation burden, radiolabeling of MIBG with ^{123}I for diagnostic scintigraphic purposes was to be preferred. In 1981, Kline et al. [5] were one of the first to report on the use of myocardial scintigraphy with [^{123}I]-MIBG in five healthy individuals. They concluded that [^{123}I]-MIBG had the potential to provide (semi-) quantitative information on myocardial catecholamine content.

Much work has been done to elucidate the uptake mechanisms of MIBG in the presynaptic sympathetic nerve endings. MIBG localizes in adrenergic nerve terminals primarily via the uptake 1 mechanism (see "Uptake 1 and Uptake 2"). The affinity (K_m: affinity constant) and capacity (V_m: capacity constant) of the uptake 1 mechanism for MIBG is similar to those for norepinephrine (K_m of 1.22 ± 0.12 μM for MIBG and 1.41 ± 0.12 μM for norepinephrine; V_m of 64.3 ± 3.3 pmol/10^6 cells/10 min for MIBG and 36.6 ± 7.2 pmol/10^6 cells/10 min for norepinephrine). Uptake 1 predominates at low concentrations of both catecholamines and MIBG, whereas uptake 2 predominates at higher concentrations. It is therefore to be expected that MIBG administered in tracer amounts will primarily reflect uptake 1. Blocking experiments,

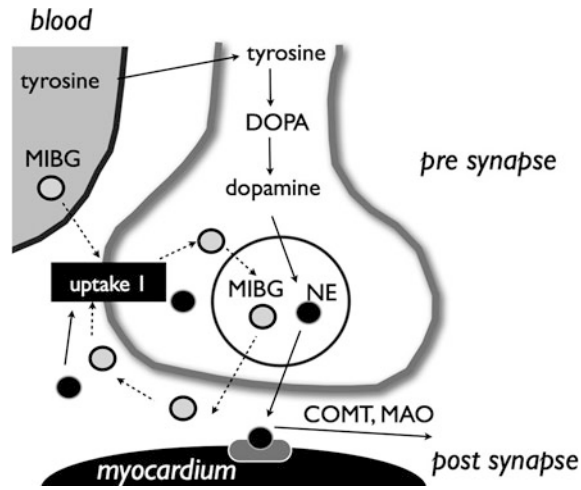

Fig. 4.1 Sympathetic nerve terminal. Dihydroxyphenylalanine (*DOPA*); monoamine oxidase (*MAO*); catechol O-methyltransferase (*COMT*)

however, have shown that uptake 2 is responsible for up to 61% of cardiac MIBG uptake.

4.1.3 [^{123}I]-MIBG Myocardial Scintigraphy

In the past two decades, a large number of investigators have demonstrated decreased myocardial [^{123}I]-MIBG uptake in chronic HF patients and have shown that those with the lowest uptake tend to have the poorest prognosis [6–8]. There have also been findings suggesting that abnormalities of myocardial [^{123}I]-MIBG uptake may be predictive of increased risk for ventricular arrhythmia and sudden cardiac death (SCD) and implant cardiac defibrillator (ICD) discharge [9–11]. One factor that has constrained acceptance of cardiac [^{123}I]-MIBG imaging as a clinical management tool in HF has been the variability of technical aspects of the procedure. Although most publications include the heart-to-mediastinum (H/M) ratio as the measure of myocardial uptake, the methods used to obtain this parameter show considerable variation (Fig. 4.1).

4.1.3.1 General Procedure for Planar [^{123}I]-MIBG Scintigraphy

In order to block thyroid uptake of free radioactive iodide, either 500 mg potassium perchlorate or 200 mg potassium iodide (10% solution) is orally administered. Thirty minutes later, ~185–370 MBq [^{123}I]-MIBG is administered intravenously. [^{123}I]-MIBG is internalized by presynaptic nerve endings of postganglionic neuronal cells through the energy-dependent uptake 1 system. A 15% energy window is usually used, centered on the 159 keV ^{123}I photopeak. Anterior planar scintigraphic images are obtained 15 min (early) and 4 h (late) after injection and stored in a 128 × 128 matrix.

4.1.3.2 Semiquantitative Parameters

The commonly used myocardial [^{123}I]-MIBG indices are the H/M ratio and myocardial washout. On anterior planar images, regions of interest (ROIs) are drawn over the heart and the mediastinum. The mean count density in each ROI is obtained, and the H/M ratio (specific activity/nonspecific activity) is calculated. Myocardial [^{123}I]-MIBG washout is calculated as the difference between the early and late H/M and expressed as a percentage of the early H/M:

$$\text{washout rate (WR)} = \left\{\frac{(\text{earlyH/M} - \text{lateH/M})}{\text{earlyH/M}}\right\} \times 100\,\%$$

The early H/M probably reflects the integrity of presynaptic nerve terminals and uptake 1 function. The late H/M combines information on neuronal function from uptake to release through the storage vesicle at the nerve terminals. Myocardial [^{123}I]-MIBG washout is an index of the degree of sympathetic drive. This implies that increased sympathetic activity is associated with high myocardial [^{123}I]-MIBG washout and low myocardial [^{123}I]-MIBG delayed uptake.

4.1.3.3 Impact of ROI Definition

For [^{123}I]-MIBG, there are several ways to define the mediastinal (size and placement) and myocardial ROIs [i.e., myocardium, including the left ventricular (LV) cavity, versus myocardium excluding the LV cavity]. However, there are limited data on the impact of ROI definition on H/M ratios and myocardial washout. Somsen et al. [12] demonstrated in 25 healthy volunteers that [^{123}I]-MIBG semiquantitative parameters using an ROI of the myocardium including the LV showed the lowest interindividual and within-individual variability. In a large retrospective study, a uniform analysis with clear definition of the myocardial ROI (variable in size, including the LV cavity) and the mediastinal ROI (fixed size) showed remarkable consistency in interpretation between three blinded image evaluators. These findings suggest that rigorous and uniform analysis of cardiac [^{123}I]-MIBG semiquantitative parameters minimizes inter- and intra-individual variation.

4.1.3.4 Influence of Collimation

The most well-validated influence on the measured late H/M is collimator type. In addition to the prime emission of 159-keV photons, ^{123}I emits high-energy photons of >400 keV [~2.87%, main contributor 529 keV (1.28%)]. These high-energy photons lead to penetration of the collimator septa and cause scatter detected in the 159-KeV energy window. Septal penetration affects estimation of the H/M ratio in [^{123}I]-MIBG imaging with a low-energy (LE) collimator. Regardless, LE collimators are frequently used for imaging [^{123}I]-MIBG. Medium-energy (ME) collimators have been shown to improve quantitative accuracy in ^{123}I studies. Therefore, to minimize the effects of septal penetration, the ME collimator is preferred. However, the use of ME collimation provides relatively low spatial resolution, which may hamper accurate estimation of activity in small regions through a partial volume effect. In brain single-photon-emission computed tomography (SPECT) imaging with [^{123}I]-labelled agents, collimation with low energy, high resolution (LEHR) is preferred, because high spatial resolution is required, head and brain tissue lead to a more or less homogeneous scatter, and the regions are mostly equidistant from the gamma camera. In cardiac scintigraphy with ^{123}I labelled agents, however, H/M ratios are assessed from counts in relatively large regions, the thorax and abdomen lead to an inhomogeneous scatter, and the myocardium is not equidistant from the gamma camera, especially for SPECT imaging. In cardiac scintigraphy with [^{123}I]-labelled agents, the tradeoff between spatial resolution and septal penetration is therefore in favor of low septal penetration. Moreover, in a checker phantom, the use of ME collimation in cardiac scintigraphy with ^{123}I showed contrast accuracy similar to technetium-99 m (^{99m}Tc).

Whereas these results would suggest that semiquantitative cardiac [^{123}I]-MIBG imaging might be best performed using ME collimators, there are practical limitations to such a recommendation. Almost all nuclear medicine procedures are now performed on a multihead gamma camera, and many dedicated dual-head cardiac cameras are not supplied with ME collimators. Despite these considerations, the use of ME collimation in cardiac scintigraphy with ^{123}I is advocated.

4.1.4 Normal Databases of Cardiac MIBG

The quantitative approach played an important role in [^{123}I]-MIBG studies for estimating disease severity and prognosis, as discussed in other sections of this chapter. Most [^{123}I]-MIBG studies examining HF use the H/M ratio. It is unanimously reported that a low H/M ratio is a predictor of serious cardiac events, including cardiac death and lethal arrhythmia. The diagnostic thresholds of an H/M ratio of 1.2–1.7 are generally used for determining poor prognosis. Understanding normal [^{123}I]-MIBG databases is thus essential for properly applying MIBG studies in clinical practice. In this section, standardized [^{123}I]-MIBG parameters, normal values of the H/M ratio and WR, three-dimensional distribution of SPECT imaging, and the need for standardization are discussed [13].

4.1.4.1 Definition of WR for Normal Databases

To calculate [^{123}I]-MIBG WR from the heart, most Japanese [^{123}I]-MIBG studies used the following formula:

$$\mathrm{WR} = \left(\left(\mathrm{H_{early}} - \mathrm{M_{early}}\right) - \left(\mathrm{H_{late}} - \mathrm{M_{late}}\right) \times \mathrm{k}\right) \Big/ \left(\mathrm{H_{early}} - \mathrm{M_{early}}\right),$$

where H_{early} and H_{late} are the average heart count in early and late imaging, and M_{early} and M_{late} are the average mediastinal count in early and late imaging. The coefficient k is the decay correction factor calculated as 1/(0.5^(t/13)), where t is time (h) between early and late imaging. The k value is 1.173 and 1.238 for 3 and 4 h, respectively.

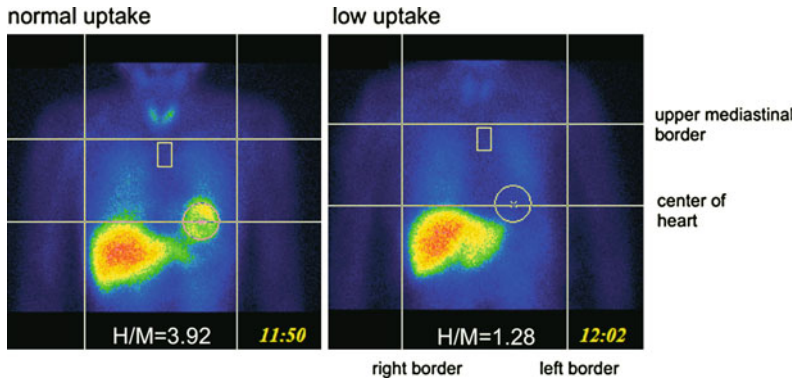

Fig. 4.2 Semiautomatic region of interest (*ROI*) setting in individuals with normal and low [^{123}I] metaiodobenzylguanidine (*MIBG*) uptake. *Horizontal* and *vertical lines* are automatic guides for defining chest region

4.1.4.2 Semiautomatic Calculation of H/M Ratio (Smart MIBG Software)

Despite the recommendation for ROI location, ROI size and location are not fixed and can be a cause of variation among operators and institutions. A semiautomated method was developed for placing the mediastinal ROI after placing a circular ROI on the heart. The cardiac circular ROI is manually set in the center of the heart so as not to overlap lung activity, as some patients show very low uptake in the heart. Then, the following steps are utilized as an automatic algorithm:

- detection of the right border of the body
- detection of the midline of the mediastinum
- determination of the left border of the body
- determination of the upper border of the mediastinum
- setting the rectangular mediastinal ROI in the area of the lowest count; namely, 1/10 width of the body and 30% height of the mediastinum.

The algorithm of this semiautomatic algorithm is available in Japan using Smart [^{123}I]-MIBG Software (Fig. 4.2). The intraclass correlation coefficient from the semiautomated method showed excellent reproducibility for early ($r = 0.99$) and late ($r = 0.99$) imaging. The Bland–Altman plots demonstrated better agreement using the semiautomated method (95% limits from −0.11 to 0.10) compared with that in the manual method (−0.34 to 0.27).

4.1.4.3 Normal Values of H/M Ratio and WR

It is well known that differences in data acquisition, particularly collimator type, affect H/M ratios, and these differences are obstacles for unifying multicenter data [13]. Standardization of [^{123}I]-MIBG cardiac sympathetic imaging proposed by the European Association of Nuclear Medicine (EANM) Cardiovascular Committee and the European Council of Nuclear Cardiology (ECNC) dealt with this issue.

Table 4.1 Heart-to-mediastinum (H/M) ratio and washout rate (WR)

Mean and normal ranges		
H/M ratio[a]		
	LE collimators	ME or LME collimators
Early	2.39 ± 0.21 (1.97–2.81)	2.76 ± 0.31 (2.14–3.38)
Late	2.49 ± 0.25 (1.99–2.99)	3.01 ± 0.35 (2.31–3.71)
Washout rate[b]		
	Decay and BG correction:	13% (3–22%)
	Decay correction without BG:	16% (9–23%)

LE low energy, *ME* medium energy, *LME* low-to-medium energy, *BG* background
[a] Mean and standard deviation
[b] Median and 10–90 percentile

Although LE high-resolution collimators are extensively available for common use, ME collimators are shown to provide superior semi-quantitative accuracy in [^{123}I]-MIBG studies [13]. Normal values of the H/M ratio were also significantly different when the Japanese Society of Nuclear Medicine (JSNM) Working Group MIBG databases were observed (Table 4.1). Although LE and ME types are two major groups, strictly speaking, LE general-purpose and LE HR collimators show slightly different characteristics for ^{123}I for septal penetration from 529-KeV energy. Although the low-medium-energy (LME) collimator (Toshiba/Siemens, Japan) and ME collimator provide an identical H/M ratio, similar LME types from other venders may show different characteristics. Considering variations of collimator types among camera vendors, the JSNM proposed a calibration method based on specific phantoms designed for measuring H/M ratio. This type of calibration among institutions and camera types provides ME-collimator-comparable H/M values, even when using LE collimators, and results in distribution of normal H/M values from multiple institutions to a normal distribution. Deconvolution of a septal penetration method seems to be a promising method for correcting both two- and three-dimensional heart-to-calibration ratios.

Normal H/M ratio and WR values are shown in Table 4.1. Although WR is not largely influenced by collimator choice, factors of background correction, time-decay correction, and time between early and late imaging should be standardized. As WR reflects physiological dynamic changes, both background and decay corrections are recommended.

4.1.4.4 Regional MIBG Distribution in SPECT Study

SPECT images are acquired by a single pass of 60 steps at 30 s per step (64 × 64 matrix), starting at a 45° right anterior oblique projection and proceeding counterclockwise to the 45° left posterior oblique projection. Data are reconstructed in short-, horizontal long-, and vertical long-axis tomograms, and scatter or attenuation correction may be applied.

When regional [^{123}I]-MIBG distribution is observed, factors of physical characteristics of ^{123}I, pharmaceutical dynamics and relative count distribution in liver, heart, and lungs are related. [^{123}I]-MIBG distribution in the SPECT study is similar to that of perfusion imaging tracers, but the inferior accumulation is relatively lower in an [^{123}I]-MIBG study, in particular, for aged persons. The JSNM working group accumulated [^{123}I]-MIBG databases (both 360° and 180° rotations separately) from near-normal individuals who had no history of cardiac diseases and were not taking medications due to diabetes, hypertension, or dyslipidemia. The average and mean deviation of distribution patterns using a polar-map display is shown in Fig. 4.3. In late imaging, the inferior wall shows lower activity and a relatively large deviation, which is in agreement with our impression of clinical [^{123}I]-MIBG imaging. Heterogeneity of [^{123}I]-MIBG distribution is not artifacts but physiological phenomenon and correlate with sympathetic and vagal activities in normal individuals. To evaluate ischemic myocardial diseases, in which [^{123}I]-MIBG shows regional denervation in the ischemic or infarcted area, comparison between [^{123}I]-MIBG distribution in patients and optimal [^{123}I]-MIBG normal databases is essential. In the meantime, gated SPECT perfusion data should be interpreted in patients with ischemic cardiomyopathy to obtain information on a potential infarcted area and wall-motion kinetic. SPECT images can be scored using a point scale for visual evaluation of [^{123}I]-MIBG concentration in given cardiac segments, comparable with a myocardial perfusion imaging scoring approach. Careful interpretation should be performed, with knowledge of normal variants and potential artifacts.

4.1.4.5 Applying [^{123}I]-MIBG to Multicenter Studies

To apply [^{123}I]-MIBG in multicenter studies, the following steps are required. First, the acquisition method for [^{123}I]-MIBG should be standardized, and guidelines as given by EANM

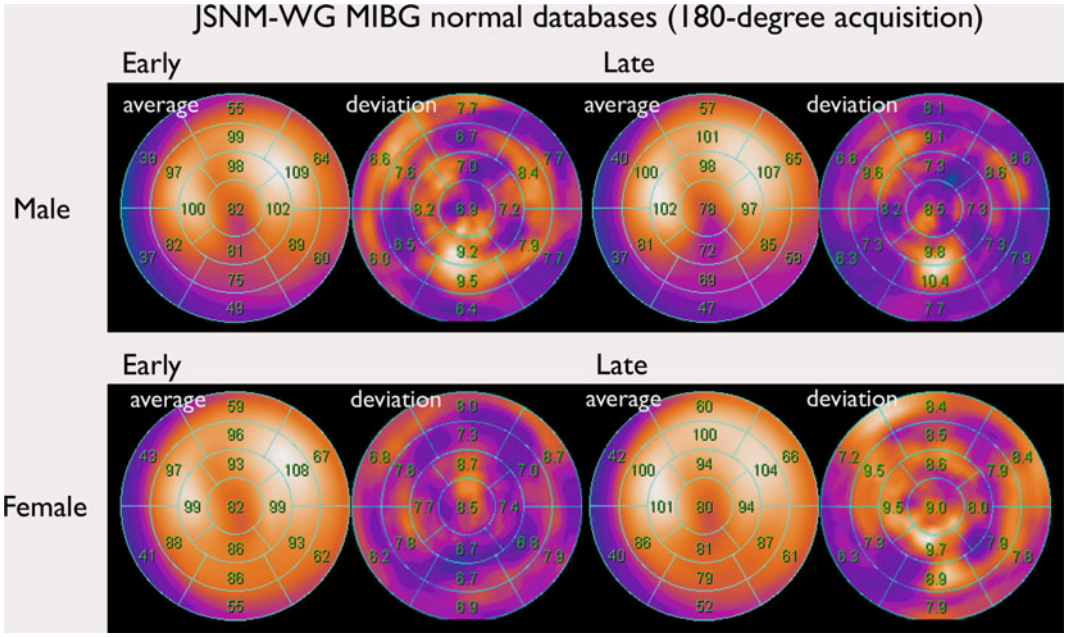

Fig. 4.3 Standard databases from the Japanese society of nuclear medicine (*JSNM*) working group in male and female patients. Polar maps from 180° rotation acquisition, with averages and mean deviations

would be helpful [14]. Steps should include collimator types, matrix, acquisition time, camera rotation, and parameter calculation method. Second, the ROI setting for the H/M ratio should be standardized, and common software based on an automatic algorithm is important. Third, interinstitutional calibration is desirable, because various camera types from various venders each have their own characteristics for ^{123}I imaging. Finally, normal databases and normal values should be provided to compare and follow-up patients over the long clinical course.

4.1.4.6 Potential Pitfalls of Cardiac [^{123}I]-MIBG Imaging

Some potential technical pitfalls of [^{123}I]-MIBG scintigraphy can be identified. First, evaluation of SPECT images may be hampered by severely reduced myocardial uptake of the tracer in patients with severe HF (H/M ratio <1.2). Furthermore, the readers should be aware of the fact that [^{123}I]-MIBG shows reduced uptake in the inferior wall under normal conditions and particularly in elderly patients. Additionally, [^{123}I]-MIBG is taken by peripheral tissues supplied by sympathetic nerves, including tissue in liver, lungs, and thyroid gland [14]. In patients with excessive extracardiac (gastrointestinal or liver) [^{123}I]-MIBG uptake, evaluation of cardiac SPECT images may be difficult.

4.1.5 [^{123}I]-MIBG Imaging in Cardiac Pathologies

4.1.5.1 In Ischemic Cardiomyopathy

Sympathetic nervous tissue is more sensitive to the effects of ischemia than is myocardial tissue. Uptake of [^{123}I]-MIBG is significantly reduced in areas of myocardial infarction (MI) and adjacent noninfarcted regions, as well as in areas with acute and chronic ischemia. It is likely that ischemia induces damage to sympathetic neurons, which may take a long time to regenerate, and that episodes of ischemia result in decreased [^{123}I]-MIBG uptake.

Matsunari et al. [15] report a dissociation between recovery of myocardial perfusion after an ischemic event and myocardial innervation,

as determined with [^{123}I]-MIBG SPECT. Despite considerable myocardial salvage following coronary artery reperfusion, [^{123}I]-MIBG images obtained a mean of 11 days after MI and reperfusion demonstrated a persistent area of myocardial denervation within the LV. This area was comparable with the area of ischemic myocardium at risk, as determined by myocardial perfusion SPECT during the acute ischemic event. Such modifications of cardiac neuronal function may have an important role in the pathophysiology of HF and arrhythmias, but further studies are warranted to determine the clinical value of innervation imaging in ischemic heart disease.

4.1.5.2 In Arrhythmogenesis

Cardiovascular disease is the single most common cause of natural death in developed countries. SCD accounts for 50% of all cardiovascular deaths. The most common primary electrical event at the time of SCD is ventricular tachycardia (VT), which degenerates first to ventricular fibrillation (VF) and later to asystole.

SCD is usually attributed to structural heart disease, principally in the setting of acute or chronic MI. Ventricular tachyarrhythmias can be provoked in these patients with heterogeneous remodeling of sympathetic innervation, attributable to nerve growth and degeneration by physical or mental stress or by catecholamine application. On the other hand, adrenergic denervation of viable myocardium may also result in denervation supersensitivity, with exaggerated response of myocardium to sympathetic stimulation and increased vulnerability to ventricular arrhythmias. Therefore, when assessing the arrhythmogenic potential, variables such as presence of denervated but viable myocardium, severity of denervation, underlying level of sympathetic tone, and subsequent influences on local ventricular repolarization should be taken into account.

Whereas preventing arrhythmic deaths is generally ineffective with pharmacologic treatment, ICDs reduce the mortality rate in subgroups of patients thought to be at risk. However, identifying patients who most benefit from these devices remains difficult, and device implantation in patients who will not benefit leads to unnecessary morbidity, with increased medical costs. Arora et al. [9] evaluated the use of [^{123}I]-MIBG cardiac imaging (as means of local myocardial sympathetic innervation) and spectral analysis of heart-rate volume (HRV) (as means of central autonomic tone) in patients with ICDs. They studied 17 patients who had ICDs for various indications. The combined use of [^{123}I]-MIBG scintigraphy and HRV analysis correlated with the occurrence of an appropriate ICD discharge. Patients with ICD discharges had lower early H/M ratio, more extensive [^{123}I]-MIBG defects, and more [^{123}I]-MIBG/^{99m}Tc-sestamibi mismatch segments (denervation in areas of myocardial viability) compared with patients without previous ICD discharge. In addition, the ICD discharge group had reduced HRV values; suggesting abnormally increased sympathetic tone when compared with patients without previous ICD discharge. Therefore, the combined noninvasive evaluation of local cardiac autonomic innervation and systemic autonomic function by means of [^{123}I]-MIBG and HRV allowed identification of patients at risk for potentially fatal arrhythmias and SCD, who were most likely to benefit from an ICD.

In a phase 2, open-label, multicenter study that enrolled 50 patients with LV dysfunction and previous MI, Bax et al. [16] found that late [^{123}I]-MIBG SPECT defect score was the only variable that showed a significant difference between patients with and without positive electrophysiological studies. Further studies should demonstrate clinically relevant risk stratification of [^{123}I]-MIBG imaging, such as high negative predictive value (NPV) for life-threatening ventricular arrhythmias, especially in patients with ischemic heart disease and depressed LVEF. Boogers et al. [11] demonstrated in patients with severe (LVEF $< 35\%$) cardiomyopathy and ICD that late MIBG SPECT imaging was a better prognostic indicator of arrhythmias and cardiac death than perfusion and innervation mismatch SPECT imaging. One hundred and sixteen HF patients

referred for ICD therapy were enrolled. During a mean follow-up of 23 ± 15 months, appropriate ICD therapy (primary end point) was documented in 24 (21%) patients and appropriate ICD therapy or cardiac death (secondary end point) in 32 (28%) patients. Late [^{123}I]-MIBG SPECT defect score was an independent predictor for both end points. Patients with a large late [^{123}I]-MIBG SPECT defect (summed score >26) showed significantly more appropriate ICD therapy (52% versus 5%, $p < 0.01$) and appropriate ICD therapy or cardiac death (57% versus 10%, $p < 0.01$) than in patients with a small defect (summed score ≤26) at 3-year follow-up. Then, they concluded that cardiac sympathetic denervation predicts ventricular arrhythmias causing appropriate ICD therapy as well as the composite of appropriate ICD therapy or cardiac death.

4.1.5.3 In Atrial Fibrillation

Akutsu et al. [17] investigated whether cardiac SNS activity measured by [^{123}I]-MIBG imaging would be associated with both the occurrence of HF and the transit to permanent atrial fibrillation in patients with paroxysmal atrial fibrillation. They evaluated 98 consecutive patients with idiopathic atrial fibrillation and preserved LVEF (>50%) during 4 ± 3.6 years. Lower late H/M ratio and lower LVEF were the independent predictors of transit to permanent atrial fibrillation, with adjusted hazard ratios of 3.44 [95% confidence interval (CI) 1.9–6.2, $p < 0.0001$] and 1.04 (95% CI 1.01–1.08, $p = 0.014$). They concluded that [^{123}I]-MIBG imaging may be a useful modality for predicting the development of atrial fibrillation.

4.1.5.4 Risk Stratification of Patients with Heart Failure

Long-term prognosis of patients with HF remains poor, with a 5-year mortality rate of 59% for men and 45% for women. Furthermore, prognosis in HF can be determined reliably only in populations and not in individuals. To improve survival, adequate risk stratification is needed. The most significant predictors of survival in clinical management include decreasing LVEF, worsening New York Heart Association (NYHA) functional status, degree of hyponatremia, decreasing peak exercise oxygen uptake ($V0_2$), decreasing hematocrit, resting tachycardia, renal insufficiency, intolerance to conventional therapy, and refractory volume overload. Impaired cardiac adrenergic innervation as assessed by [^{123}I]-MIBG imaging is strongly related to mortality in patients with HF, independently of its cause. Merlet et al. [6] studied the prognostic value of [^{123}I]-MIBG scintigraphy compared with that of other noninvasive cardiac imaging indices in 90 patients with either ischemic ($n = 24$) or idiopathic ($n = 66$) cardiomyopathy. During a follow-up period of 1–27 months, ten patients underwent cardiac transplantation, and 22 died. Among all clinical and imaging variables (cardiac [^{123}I]-MIBG uptake, radionuclide LVEF, X-ray cardiothoracic ratio, and echographic end-diastolic diameter), the late H/M ratio was the best predictor of event-free survival. The same authors [7] subsequently evaluated 112 patients with HF and dilated cardiomyopathy (DCM) (NYHA classes II–IV, LVEF < 40%, LV end-diastolic diameter 70 ± 8 mm, and pulmonary capillary wedge pressure 19 ± 8 mmHg). Among all variables (cardiac [^{123}I]-MIBG uptake, circulating NE concentration, LVEF, peak $V0_2$, X-ray cardiothoracic ratio, M-mode echographic end-diastolic diameter, and right-sided heart catheterization parameters), only late H/M ratio and LVEF were independent predictors for mortality (mean follow-up 27 ± 20 months). In addition, [^{123}I]-MIBG uptake and circulating NE concentration were the only independent predictors for life duration. In both studies by those authors, a late H/M ratio of 1.2 was used to identify reduced [^{123}I]-MIBG uptake. The low value of H/M ratio (1.2) was due to the absence or nonrecommendation of certain treatment in HF, such as beta-blockers, angiotensin receptor blockers, and aldosterone antagonists within the (1988–1990) period.

Cohen-Solal et al. [18] showed in a study of 93 HF patients and LV dysfunction that late H/M ratio was reduced and correlated with other predictors of prognosis, such as LVEF, cardiac index, pulmonary wedge pressure, and peak $V0_2$. Moreover, a late H/M ratio $\leq$1.2 and peak $V0_2$ were predictive of death or cardiac transplantation over 10 $\pm$ 8 months of follow-up, whereas early H/M ratio and WR were not. Wakabayashi et al. studied 414 patients (42% with symptomatic HF) with [^{123}I]-MIBG scintigraphy. Over a mean follow-up of 22 $\pm$ 7 months, 37 cardiac deaths occurred. Late H/M ratio was the most powerful predictor of cardiac mortality among the variables. A late H/M ratio $\leq$1.74, age >60 years, history of MI, and NYHA class III or IV strongly indicated poor clinical outcomes. Wakabayashi et al. [19] reported [^{123}I]-MIBG imaging as the most powerful independent long-term prognostic value for both ischemic ($n = 76$) and idiopathic ($n = 56$) cardiomyopathy patients, which hints at cardiac autonomic dysfunction as a common end point leading to cardiac death, regardless of the underlying etiology of the cardiac disease. Late H/M ratio was the most powerful independent predictor of cardiac mortality in both groups of patients (superior to early H/M ratio and WR) and had an identical threshold (1.82) for both groups for identifying patients at risk of cardiac death. Nevertheless, when analyzing patients with LVEF <40%, the upper cutoff value of late H/M ratio was 1.50 for ischemic patients and 2.02 for idiopathic patients, which may suggest that the underlying etiology of HF relates to the threshold of the late H/M ratio for differentiation of high-risk patients. This study was designed, however, before optimal up-to-date HF treatment, and derived results may not translate to current cohorts of HF patients.

All these results suggest that the late H/M ratio may be the best prognostic parameter that can be obtained from planar [^{123}I]-MIBG imaging. Agostini et al. [20] showed in a European retrospective study the strong prognostic value of late H/M ratio in patients with HF. Blind review and prospective quantitative reanalysis of the late H/M ratio of 290 patients with ischemic and nonischemic HF (NYHA class II–IV, 262 patients with LVEF <50%) with follow-up data for 2 years permitted the identification of potential late H/M ratio threshold values for defining groups with high and very low likelihood of major cardiac events. Mean H/M ratio was significantly different between patients with and without events (1.51 versus 1.97). Based on receiver operating characteristic (ROC) curve analysis, a threshold value for H/M ratio of 1.75 yielded a sensitivity of 84% and specificity of 60% to predict events. Based on this threshold value, the 2-year event-free survival was 62% for late H/M ratio <1.75 versus 95% for late H/M ratio of 1.75. Logistic regression showed late H/M ratio and LVEF as the only significant predictors of major cardiac events. When the late H/M ratios were divided into quartiles, the 2-year event-free survival rates in the lowest (1.45) and highest (2.17) quartiles were 52 and 98%, respectively. Tamaki et al. [21] prospectively compared the predictive value of cardiac [^{123}I]-MIBG imaging for SCD with that of the signal-averaged electrocardiogram (SA-ECG), HRV, and QT dispersion in 106 consecutive outpatients with mild-to-moderate stable HF due to ischemic heart disease in 55 patients and idiopathic DCM in 51 patients. During a follow-up period of 65 $\pm$ 31 months, 18 of 106 patients died suddenly. A multivariate Cox analysis revealed that only WR and LVEF were significantly and independently associated with SCD. Patients with an abnormal WR (>27%) had a significantly higher risk of SCD (adjusted HR: 4.79, 95% CI 1.55–14.76). Even when confined to patients with LVEF >35%, SCD was significantly more frequently observed in patients with than without abnormal WR.

In a systematic review, Verberne et al. [8] assessed existing evidence on the prognostic value of semiquantitative parameters of myocardial [^{123}I]-MIBG uptake in patients with HF. The pooled HR estimates for cardiac death and cardiac events associated with [^{123}I]-MIBG washout were 1.72 (95% CI 1.72–2.52; $p = 0.006$) and 1.08 (95% CI 1.03–1.12; $p < 0.001$), respectively. Pooled HR estimates for cardiac death and cardiac events associated

with early H/M and late H/M ratios showed significant heterogeneity ($I^2 \geq 75\%$). Limiting pooling to the qualitative best three studies rendered I^2 insignificant ($I^2 = 0$) and resulted in a pooled HR of late H/M ratio for cardiac death of 1.82 (95% CI 0.80–4.12; $p = 0.15$) and for cardiac events of 1.98 (95% CI 1.57–2.50; $p < 0.001$). These results indicate that patients with CHF and decreased late H/M ratio or increased myocardial [^{123}I]-MIBG WR have a worse prognosis than those with normal semi-quantitative myocardial [^{123}I]-MIBG parameters. Jacobson et al. [10], in the largest prospective multicenter trial, showed the potential role of cardiac [^{123}I]-MIBG imaging in HF is the AdreView Myocardial Imaging for Risk Evaluation in Heart Failure (ADMIRE-HF) trial in which [^{123}I]-MIBG myocardial imaging was performed in 961 patients with HF (NYHA II/III) and a reduced LVEF (<35%). A predefined late H/M ratio cutoff value of 1.6 was used. During a 2-year follow-up, 25% of patients had a cardiac event (i.e., NYHA functional class progression, potentially life-threatening arrhythmic event, or cardiac death). Cox proportional hazard analysis showed that there was a highly significant relationship between time to HF-related events and the H/M ratio, independent of other commonly measured parameters such as LVEF and brain natriuretic peptide (BNP). In addition, the study showed a clear association between severity of myocardial sympathetic neuronal dysfunction and risk for subsequent cardiac death. Gerson et al. [22] demonstrated the prognostic power of [^{123}I]-MIBG for detecting the clinically relevant end point of HF progression in the subgroup of patients with diabetes in the ADMIRE-HF trial. H/M ratio can complement data derived from LVEF, B-type natriuretic peptide, and diabetes status for predicting HF progression.

The Seattle Heart Failure Model (SHFM) is a multivariate model that predicts survival in patients with HF. Kuramoto et al. [23] showed that cardiac MIBG WR imaging improved the prognostic power of the SHFM in 106 patients with chronic HF (LVEF < 40%) during a mean follow-up of 6.8 ± 3.5 years. In the same field, Ketchum et al. [24] investigated combining [^{123}I]-MIBG cardiac imaging and the SHFM to predict mortality in the ADMIRE-HF EXtension (ADMIRE-HFX) trial. Survival data from the 961 NYHA II–III participants in the original study and additional follow-up on 470 participants was included in that analysis. Mortality predictions from the SHFM, the late H/M ratio, and a combined model were compared. There were 101 deaths during a median follow-up of 2 years. Cox modeling showed improvement in SHFM discriminant ability for all-cause mortality with the addition of H/M ratio ($p < 0.0001$). For a 1-standard deviation (SD) increase in SHFM score, risk increased by 82% ($p < 0.001$), whereas for a 1-SD decrease in H/M ratio, the risk increased 60% ($p < 0.001$). Observed 2-year survival in the highest risk SHFM participants varied from 54% with H/M ratio <1.2 to 100% with H/M ratio ≥1.80. The integrated discrimination improvement was significant ($p < 0.0001$), whereas the area under the receiver-operator characteristic curve (AUC) at 1 year improved from 0.658 for H/M ratio and from 0.692 for SHFM to 0.731 for the combined model ($p = 0.03$). The authors concluded that abnormalities of H/M ratio and SHFM risk scores are associated with increased mortality rates in HF patients. A combined model offers additional prognostic information over either score alone.

Verberne et al. [25] determined the most appropriate prognostic endpoint for use of MIBG imaging based upon aggregate results from multiple studies published in the past decade. Then, published studies from Europe and the United States were identified for which original individual patient data for H/M ratio from late (3–5 h) planar MIBG imaging were available. Data submitted by the participating investigators were pooled, and Cox proportional hazards analyses were performed. Endpoints of all-cause mortality, cardiac mortality, arrhythmic events, and heart transplantation were investigated to determine which one provided the strongest prognostic significance for MIBG imaging data. Data from six studies with a total of 636 HF patients were retrieved. The majority

of patients was male (78%), had a decreased LVEF (31.1 ± 12.5%), and a mean late H/M ratio of 1.67 ± 0.47 (first quintile ≤ 1.32; second to fourth quintile 1.33–1.97, fifth quintile ≥ 1.98). During follow-up (mean 42.1 ± 26.5 months), there were 95 deaths, 79 cardiac deaths, 38 arrhythmic events, and 57 heart transplants. In univariate Cox analyses, late H/M ratio was a significant predictor of all event categories, but the highest Chi squares and lowest HRs were for all-cause ($\chi^2 = 17.68$, HR = 0.37, 95% CI 0.22–0.61) and cardiac ($\chi^2 = 14.57$, HR = 0.37, 95% CI 0.21–0.65) mortality. In multivariate analysis for the composite of any event, H/M ratio was a significant predictor (HR = 0.53, 95% CI 0.36–0.78), with LVEF, gender, and NYHA class also included in the model. In similar analyses for the individual event categories in patients with reduced LVEF (<50%, $n = 580$), H/M ratio was a significant predictor of all-cause (HR = 0.49, 95% CI 0.27–0.89) and cardiac (HR = 0.45, 95% CI 0.23–0.87) mortality, with LVEF, age, and HF etiology also included in the model. The same four variables were significant in models using a dichotomous H/M ratio split at 1.20 (1 SD below the mean), with patients with late H/M ratio <1.2 having the highest mortality (median survival 71 months) and with an H/M HR for cardiac death and all-cause mortality of 0.39 (95% CI 0.22–0.71) and 0.49 (95% CI 0.28–0.86), respectively. Finally, late H/M ratio is strongest as a univariate predictor of all-cause and cardiac mortality in HF patients. In multivariate analyses, MIBG imaging tends to be strongest as a predictor of cardiac death.

4.1.5.5 In Treatment Assessment of HF Patients

Neurohormonal blockers [beta-blockers, angiotensin-converting enzyme inhibitors (ACEIs), angiotensin receptor blockers (ARBs), and aldosterone antagonists) are the main treatments for HF. However, the appropriate time to initiate treatment and the best sequence and combination of medications are uncertain at present. Cardiac [^{123}I]-MIBG imaging can detect drug-induced changes in cardiac adrenergic activity. Gerson et al. [26] studied the effect of chronic carvedilol treatment in patients with HF and cardiac sympathetic nerve dysfunction of varying severity due to idiopathic cardiomyopathy. Most patients showed a favorable response in LV function to the treatment, regardless of the baseline level of cardiac SNS function, as assessed by cardiac [^{123}I]-MIBG imaging. Patients with relatively advanced cardiac sympathetic dysfunction (baseline late H/M ratio <1.40 in [^{123}I]-MIBG studies) were the most likely to show evidence of improved cardiac SNS function in response to carvedilol treatment. Kasama et al. [27], taking into account that [^{123}I]-MIBG imaging improves medical treatment for HF, analyzed the usefulness of serial [^{123}I]-MIBG studies for prognostication in 208 patients with stabilized mild to moderate HF and LVEF <45% of both ischemic and nonischemic origin. The [^{123}I]-MIBG and ECG studies were performed once patients were stabilized and after 6 months of treatment that included ACEIs, ARBs, β-blockers, loop diuretics, and spironolactone. Treatment did not change during the follow-up. Fifty-six patients experienced fatal cardiac events during the study period (13 SCD). Clinical characteristics were similar in both noncardiac and cardiac death groups. With respect to pharmacotherapy in the two groups, only the use of β-blockers in the noncardiac death group was significantly higher than in the cardiac death group. Variation in the WR between the sequential [^{123}I]-MIBG (Δ-WR) was the only independent predictor of cardiac death. The Δ-WR was significantly lower in the noncardiac death group (<−5%) than that in the cardiac death group (≥−5%). Moreover, this parameter was also useful for predicting SCD in patients with HF, indicating that serial [^{123}I]-MIBG imaging is useful for predicting cardiac death and SCD in stabilized patients with HF.

In Caen Hospital, we followed severe heart failure patients under treatment with LVAD(Jarvik 2000 and Heartmate II) (unpublished data). Symptom assessment based on NYHA class, BNP level, peak $V0_2$, and number

of episodes of ventricular arrhythmias recorded by implantable defibrillators were searched for every patient. MIBG scintigraphy , BNP, and peak $V0_2$ were measured during the same week. Five patients had severe HF, were in NYHA stage 4 before implantation of the LVAD, with low ejection fraction (LVEF < 0.3) and high BNP levels (>1,000 pg/mL). Peak VO_2 measured in four patients was <12 mL/kg per min. Symptom assessment, BNP level, and peak VO_2 improved significantly under LVAD support (for all patients: NYHA $= 2$, BNP level < 400 pg/mL, peak $VO_2 > 15$ mL/kg per min). However, H/M ratio remained very low in all patients, suggesting the absence of improvement of sympathetic neuronal function (H/M ratio $= 1.46 \pm 0.2$; range 1.2–1.7; normal range: 2.2 ± 0.3), even after long-term support (up to 68 months). Interestingly, no patient presented symptomatic or asymptomatic ventricular arrhythmias during follow-up. Whereas classical markers of chronic HF severity improved significantly under LVAD and were considered to be of good prognosis, H/M ratio remained very low, suggesting the absence of improvement in sympathetic neuronal integrity under LVAD.

4.1.5.6 In Stress Cardiomyopathy

Takotsubo syndrome is a clinical entity characterized by acute but rapidly reversible LV systolic dysfunction, with midventricular-wall-motion abnormalities, apical akinesia or dyskinesia, and preserved or hyperkinetic contractile function of the basal LV segments in the absence of atherosclerotic coronary artery disease (CAD) triggered by acute emotional or physical stress. Several hypotheses are advocated as possible pathophysiologic mechanisms, including catecholamine-mediated multivessel epicardial spasm, microvascular coronary spasm, and direct catecholamine-mediated myocyte toxicity. However, it remains unclear whether these abnormalities are the primary cause of the disorder or secondary events. As the entity is much more common in postmenopausal women, important influences of sex hormones on the sympathetic neurohormonal axis and on coronary vasoreactivity have been suggested. [^{123}I]-MIBG imaging shows reduced uptake in the akinetic LV apex, with normal or only mildly reduced perfusion within this region [28].

4.2 Cardiac Neurotransmission Imaging Using [^{123}I]-MIBG Scintigraphy in Brain Disease

Application of [^{123}I]-MIBG in neurological diseases has increased due to the increasing number of [^{123}I]-MIBG images in a group of Lewy body diseases (LBD). MIBG study demonstrated its effectiveness in differentiating LBD from other types of neurodegenerative diseases with cognitive impairment. Clinical application of [^{123}I]-MIBG began with the observation of markedly reduced cardiac [^{123}I]-MIBG uptake in patients with neurological diseases presenting orthostatic hypotension and other autonomic failures [29]. Thereafter, decreased cardiac [^{123}I]-MIBG activity in patients with Parkinson's disease and dementia with Lewy bodies has been extensively investigated in comparison with other types of neurological disorders [30]. These disease entities showed a common pathological base of Lewy-body deposition in multiple organs. Subsequently, low [^{123}I]-MIBG uptake has also been reported in patients with pure autonomic failure and rapid-eye-movement sleep-behavior disorder. In the neurological patient groups, reduced [^{123}I]-MIBG activity in the heart has been recognized as a biomarker of LBD.

4.2.1 Pathological Backgrounds

The reason for decreased [^{123}I]-MIBG uptake is supported by pathological investigations. The important issue was why brain disorder decreased [^{123}I]-MIBG uptake in the heart. The decrease in myocardial [^{123}I]-MIBG uptake reflected the fact that abnormality is not only restricted to the brain

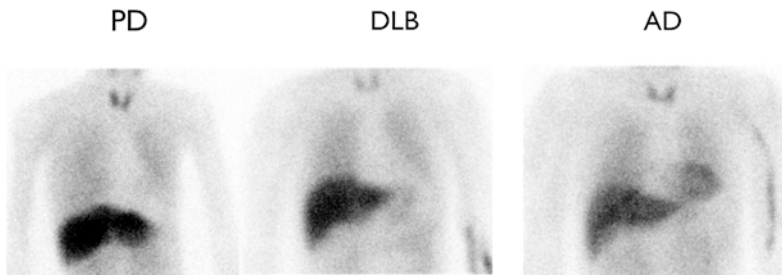

Fig. 4.4 [^{123}I]-MIBG imaging in patients with Parkinson's disease (*PD*, *left*), dementia with Lewy bodies (*DLB*, *middle*), and Alzheimer's disease (*AD*, *right*). Anterior planar images

but involves more extensive derangement of sympathetic neuronal function in multiple organs. A major lesion in Parkinson's disease is neuronal degeneration with an appearance of Lewy bodies, and loss of neurons in the following predilection sites was demonstrated by post-mortem studies [31]. Lewy bodies distributed widely in the hypothalamus and sympathetic and parasympathetic systems were also found in the enteric nervous system of the alimentary tracts, cardiac plexus, pelvic plexus, and adrenal medulla. Lewy bodies and α-synuclein-positive neurites were identified in hearts of patients with Parkinson's disease [32]. In an autopsy-proven patient with Parkinson's disease, cardiac plexus was more heavily involved than were sympathetic ganglia, which could have been direct evidence for explaining low cardiac MIBG uptake. The only neuropathological requirement for diagnosing dementia with Lewy bodies was the presence of Lewy bodies somewhere in the brain of a patient with a clinical history of dementia [33]. Central, core, and suggestive features have been summarized from clinical viewpoints in the consortium on dementia with Lewy bodies. However, diagnosis of LBD seems to be underestimated. Its differential diagnosis from Alzheimer's disease, which is the most common type of dementia, and other pathology of dementia-related diseases is still challenging, even for neurologists. As Parkinson's disease and dementia with Lewy bodies are considered as a generalized neuronal disorder, myocardial [^{123}I]-MIBG defects could be representative of pathological progression of extensive autonomic involvement.

4.2.2 [^{123}I]-MIBG Findings in Parkinson's Disease

Typical [^{123}I]-MIBG images of patients with Parkinson's disease, dementia with Lewy bodies, and Alzheimer's disease are shown in Fig. 4.4. In patients with Parkinson's disease, decrease in cardiac [^{123}I]-MIBG uptake is observed in 80–90%. [^{123}I]-MIBG uptake is globally decreased in both planar imaging and SPECT studies. The decrease is observed even in early-onset stages. However, as some patients show normal myocardial activity in the mild or early stage, normal [^{123}I]-MIBG uptake cannot readily exclude the possibility of Parkinson's disease. Although [^{123}I]-MIBG activity seems to decrease progressively during the clinical course, the temporal change from a normal uptake to the typically decreased [^{123}I]-MIBG uptake was not well demonstrated in the same cohort. In studies with a large number of patients, however, stage progression and H/M ratio showed weak negative correlation. Although WR was also calculated to be higher in patients with Parkinson's disease, it should be carefully interpreted, as initial uptake is low and washout variation becomes large. Those who have orthostatic hypotension tend to show a low [^{123}I]-MIBG uptake. Based on a meta-analysis of studies with a total of 246 cases of Parkinson's disease and 45 of multiple system atrophy, overall sensitivity to positively identify patients with Parkinson's disease was 89.7% and specificity was 94.6%. When H/M ratios were surveyed in the literature, early H/M ratios ranged from 1.3 to 1.7 (median 1.58) and late H/M

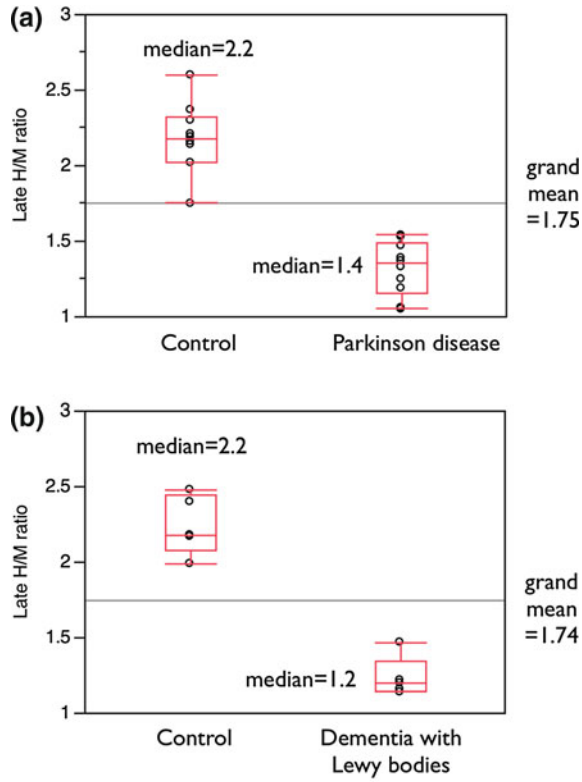

Fig. 4.5 **a** Distribution of average late heart-to-mediastinum (*H/M*) ratios in ten studies of patients with Parkinson's disease and controls [Iwasa et al. (Acta Neurol Scand 1998;97:303), Yoshita et al. (J Neurol Sci 1998;155:60), Orimo et al. (J Neurol Neurosurg Psychiatry 1999;67:189), Braune et al. (Acta Neurol Scand 1998;97:307), Reinhardt et al. (Eur J Nucl Med 2000;27:595), Druschky et al. (J Neurol Sci 2000;175:3), Takatsu et al. (J Nucl Med 2000;41:71), Taki et al. (Eur J Nucl Med 2000;27:566), Hamada et al. (J Neurol Neurosurg Psychiatry 2003;74:423), and Orimo et al. (Intern Med 2003;42:127)]. **b** Distribution of average late H/M ratios in five studies of patients with dementia with Lewy bodies and controls [Watanabe et al. (J Neurol Neurosurg Psychiatry 2001;70:781), Saiki et al. (J Neurol Sci 2004;220:105), Yoshita et al. (Neurology 2006;66:1850), Kashihara et al. (J Nucl Med 2006;47:1099), and Novellino et al. (Neurobiology of Aging 2010;31:1903)]

ratios from 1.1 to 1.6 (median 1.25), showing significantly lower values than in control patients [30]. The distribution of average H/M ratio values in ten studies of both Parkinson disease and control patients is shown in Fig. 4.5a.

4.2.3 [^{123}I]-MIBG Findings in Dementia with Lewy Bodies

A meta-analysis of [^{123}I]-MIBG in dementia with Lewy bodies showed that pooled sensitivity of [^{123}I]-MIBG scintigraphy for differentiating from other dementia was 98% (95% CI 94–100) and specificity was 94% (95% CI 90–97) [34]. A 4-year follow-up of 65 patients showed H/M ratio significantly decreased in patients with dementia with Lewy bodies compared with that of the other neurodegenerative diseases, and the best H/M ratio cutoff point was 1.36, with sensitivity 94% and specificity 96% [35]. Regarding differential diagnosis between dementia with Lewy bodies and Alzheimer's disease, a Japanese study showed that late H/M ratio had sensitivity of 100%, specificity of 100%, and

positive predictive value (PPV) of 100% at a cutoff value of 1.68 [36]. The distribution of average H/M values in five studies in which H/M ratios of both patients with dementia with Lewy bodies and control patients were available, is shown in Fig. 4.5b. In the consortium guidelines, abnormally low [^{123}I]-MIBG uptake in myocardial scintigraphy is suggested as being one of the supportive features. A multicenter study for determining the role of [^{123}I]-MIBG study in patients with dementia with Lewy bodies is under investigation in Japan [37]. Preliminary data indicate that late H/M ratio was 2.55 ± 0.53 for Alzheimer's disease and 1.54 ± 0.60 for dementia with Lewy bodies ($p < 0.0001$) after standardization of the H/M ratio among institutions.

King et al. show in the meta-analysis of [^{123}I]-MIBG cardiac scintigraphy for diagnosing Lewy-body-related disorders that the AUC was 0.987 at the cluster discriminatory late H/M threshold of 1.77. They concluded that [^{123}I]-MIBG scintigraphy can accurately distinguish between two movement disorders (Parkinson's disease and multiple-system atrophy) and between two common causes of dementia (Alzheimer's disease and dementia with Lewy bodies) [38].

Some studies indicated positive differences in perfusion patterns on brain perfusion SPECT and [^{18}F]-fluorodeoxyglucose positron-emission tomography ([^{18}F]FDG-PET). A greater degree of occipital hypoperfusion or hypometabolism was observed in patients with dementia with Lewy bodies in comparison to patients with Alzheimer's disease. However, when the [^{123}I]-MIBG study was compared with brain perfusion SPECT, it seemed to be more accurate as a means of discriminating these two diseases [39].

4.2.4 Other Neurological Diseases

Marked reduction in [^{123}I]-MIBG uptake is observed in Parkinson's disease, dementia with Lewy bodies, and pure autonomic failure, which are recognized as characteristic findings of LBD. Markedly reduced cardiac [^{123}I]-MIBG uptake is also found in idiopathic rapid-eye-movement sleep-behavior disorder. This finding is consistent with the loss of sympathetic terminals and suggests a *form fruste* (i.e., an incomplete form) of LBD. More experience using [^{123}I]-MIBG studies is required for this group of patients. As it is well known that various types of cardiac diseases exhibit low [^{123}I]-MIBG uptake, patients with underlying diseases should be comprehensively assessed.

Table 4.2 Indications for [^{123}I]-MIBG imaging

Pathology	
Cardiac	Neurological
Ischemic injury or denervation	Lewy body diseases
Area at risk in acute coronary syndrome	Parkinson's disease
Denervated but viable myocardium	Dementia with Lewy bodies
Infarction	Pure autonomic failure
Cardiomyopathy	
Heart failure	
Therapeutic effect	
Prognosis	
Arrhythmia	
Life-threatening arrhythmia and cardiac death	

4.3 Conclusions

Evidence provided by [^{123}I]-MIBG scintigraphy implicates the SNS in the development and progression of HF (Table 4.2). Sympathetic myocardial innervation as assessed with [^{123}I]-MIBG has a powerful prognostic value in HF patients. CHF patients with the lowest myocardial [^{123}I]-MIBG uptake tend to have the poorest prognosis. However, additional studies are necessary to determine whether [^{123}I]-MIBG can assist in triaging patients being considered for ICD placement.

In the meantime, in neurology, cardiac presynaptic reuptake and storage of sympathetic neurotransmitters can be measured and analyzed

in vivo using myocardial [^{123}I]-MIBG scintigraphy in patient with parkinsonism. Assessing cardiac neuronal function can be helpful in characterizing Parkinson's disease and multiple system atrophy and between two common causes of dementia: Alzheimer's disease and dementia with Lewy bodies (Table 4.2).

Advances in cardiac neurotransmission SPECT imaging include the development of tracers for adrenergic receptors, which may allow differentiation of structural denervation (loss of nerve terminals) from dysinnervation (down-regulation of the uptake l mechanism). Future challenges include development of tracers for parasympathetic neurotransmission and other receptor systems, as well as targeting second-messenger molecules.

References

1. Carrio I (2001) Cardiac neurotransmission imaging. J Nucl Med 42:1062–1076
2. Zipes DP (1995) Autonomic modulation of cardiac arrhythmias. In: Zipes DP, Jalife J (eds) Cardiac electrophysiology: from cell to bedside, 2nd edn. Saunders Company, Phildelphia, pp 441–442
3. Bristow MR (1984) The adrenergic nervous system in heart failure. N Engl J Med 311:850–851
4. Wieland DM, Wu J, Brown LE, Mangner TJ, Swanson DP, Beierwaltes WH (1980) Radiolabeled adrenergi neuron-blocking agents: adrenomedullary imaging with [^{131}I] iodobenzylguanidine. J Nucl Med 21:349–353
5. Kline RC, Swanson DP, Wieland DM, Thrall JH, Gross MD, Pitt B, Beierwaltes WH (1981) Myocardial imaging in man with I-^{123} meta-iodobenzylguanidine. J Nucl Med 22:129–132
6. Merlet P, Valette H, Dubois-Rande et al (1992) Prognostic value of cardiac metaiodobenzylguanidine imaging in patients with heart failure. J Nucl Med 33:471–477
7. Merlet P, Benvenuti C, Moyse D et al (1999) Prognostic value of MIBG imaging in idiopathic dilated cardiomyopathy. J Nucl Med 40:917–923
8. Verberne HJ, Brewster LM, Somsen GA, van Eck-Smit BLF (2008) Prognostic value of myocardial ^{123}I-metaiodobenzylguanidine (MIBG) parameters in patients with heart failure: a systematic review. Eur Heart J 29:1147–1159
9. Arora R, Ferrick KJ, Nakata T et al (2003) I-^{123} MIBG imaging and heart rate variability analysis to predict the need for an implantable cardioverter defibrillator. J Nucl Cardiol 10:121–131
10. Jacobson AF, Senior R, Cerqueira MD et al (2010) Myocardial iodine-123 meta-iodobenzylguanidine imaging and cardiac events in heart failure results of the prospective ADMIRE-HF (adreview myocardial imaging for risk evaluation in heart failure) study. J Am Coll Cardiol 55:2212–2221
11. Boogers MJ, Borleffs CJ, Henneman MM et al (2010) Cardiac sympathetic denervation assessed with 123-iodine metaiodobenzylguanidine imaging predicts ventricular arrhythmias in implantable cardioverter-defibrillator patients. J Am Coll Cardiol 55:2769–2777
12. Somsen GA, Borm JJ, Dubois EA, Schook MB, van der Wall EE, van Royen EA (1996) Cardiac ^{123}I-MIBG uptake is affected by variable uptake in reference regions: implications for interpretation in clinical studies. Nucl Med Commun 17:872–876
13. Nakajima K (2010) Normal values for nuclear cardiology: Japanese databases for myocardial perfusion, fatty acid and sympathetic imaging and left ventricular function. Ann Nucl Med 24:125–135
14. Flotats A, Carrio I, Agostini D et al (2010) Proposal for standardization of ^{123}I-metaiodobenzylguanidine (MIBG) cardiac sympathetic imaging by the EANM cardiovascular committee and the European council of nuclear cardiology. Eur J Nucl Med Mol Imaging 37:1802–1812
15. Matsunari I, Schricke U, Bengel FM et al (2000) Extent of cardiac sympathetic neuronal damage is determined by the area of ischemia in patients with acute coronary syndrome. Circulation 101:2579–2585
16. Bax JJ, Kraft 0, Buxton AE et al (2008) [^{123}I]-MIBG Scintigraphy to predict inducibility of ventricular arrhythmias on cardiac electrophysiology testing: a prospective multicenter pilot study. Circ Cardiovasc Imaging 1:131–140
17. Akutsu Y, Kaneko K, Kodama Y et al (2011) Iodine-123-mibg imaging for predicting the development of atrial fibrillation. JACC Cardiovasc Imaging 4:78–86
18. Cohen-Solal A, Esanu Y, Logeart D et al (1999) Cardiac metaiodobenzylguanidine uptake in patients with moderate chronic heart failure: relationship with peak oxygen uptake and prognosis. J Am Coll Cardiol 33:759–766
19. Wakabayashi T, Nakata T, Hashimoto A et al (2001) Assessment of underlying etiology and cardiac sympathetic innervation to identify patients at high risk of cardiac death. J Nucl Med 42:1757–1767
20. Agostini D, Verberne HJ, Burchert W et al (2008) I-123- MIBG myocardial imaging for assessment of risk for a major cardiac event in heart failure patients: insights from a retrospective European multicenter study. Eur J Nucl Med Mol Imaging 35:535–546
21. Tamaki S, Yamada T, Okuyama Y et al (2009) Cardiac iodine-123 metaiodobenzylgunidine I-123-MIBG predicts sudden cardiac death independently of left ventricular ejection fraction in patients with

chronic heart failure and left ventricular systolic dysfunction. J Am Coll Cardiol 53:426–435
22. Gerson MC, Caldwell JH, Ananthasubramaniam K et al (2011) Influence of diabetes mellitus on prognostic utility of imaging of myocardial sympathetic innervation in heart failure patients. Circ Cardiovasc Imaging 4:87–93
23. Kuramoto Y, Yamada T, Tamaki S et al (2011) Usefulness of cardiac iodine-123 MIBG imaging to improve prognostic power of seattle heart failure model in patients with chronic heart failure. Am J Cardiol 107:1185–1190
24. Ketchum ES, Jacobson AF, Caldwell JL et al (2012) Selective improvement in seattle heart failure model risk stratification using iodine-123 meta-iodobenzylguanidine imaging. J Nucl Cardiol (in press)
25. Verberne HJ, Verschure DO, Veltman CE et al (2012) For what endpoint does myocardial ^{123}I-MIBG scintigraphy have the greatest prognostic value in patients with heart failure? results of a pooled individual patient data meta-analysis. Eur Heart J (in press)
26. Gerson MC, Craft LL, McGuire N, Suresh DP, Abraham WT, Wagoner LE (2002) Carvedilol improves left ventricular function in heart failure patients with idiopathic dilated cardiomyopathy and a wide range of sympathetic nervous system function as measured by iodine123 metaiodobenzylguanidine. J Nucl Cardiol 19:608–615
27. Kasama S, Toyama T, Sumino H et al (2008) Prognostic value of serial cardiac ^{123}I-MIBG imaging in patients with stabilized chronic heart failure and reduced left ventricular ejection fraction. J Nucl Med 49:907–914
28. Akashi YJ, Nakazawa K, Sakakibara M, Miyake F, Musha H, Sasaka K (2004) ^{123}I-MIBG myocardial scintigraphy in patients with takostubo cardiomyopathy. J Nucl Med 45:1121–1127
29. Hakusui S, Yasuda T, Yanagi T et al (1994) A radiological analysis of heart sympathetic functions with meta-[^{123}I] iodobenzylguanidine in neurological patients with autonomic failure. J Auton Nerv Syst 49:81–84
30. Nakajima K, Yoshita M, Matsuo S, Taki J, Kinuya S (2008) Iodine-123-MIBG sympathetic imaging in Lewy-body diseases and related movement disorders. Q J Nucl Med Mol Imaging 52:378–387
31. Wakabayashi K, Takahashi H (1997) Neuropathology of autonomic nervous system in Parkinson's disease. Eur Neurol 38(Suppl 2):2–7
32. Iwanaga K, Wakabayashi K, Yoshimoto M et al (1999) Lewy body-type degeneration in cardiac plexus in Parkinson's and incidental Lewy body diseases. Neurology 52:1269–1271
33. McKeith IG (2006) Consensus guidelines for the clinical and pathologic diagnosis of dementia with Lewy bodies (DLB): report of the consortium on DLB international workshop. J Alzheimers Dis 9:417–423
34. Treglia G, Cason E, Giordano A (2012) Diagnostic performance of myocardial innervation imaging using MIBG scintigraphy in differential diagnosis between dementia with Lewy bodies and other dementias: a systematic review and a meta-analysis. J Neuroimaging 22:111–117
35. Estorch M, Camacho V, Paredes P et al (2008) Cardiac ^{123}I-metaiodobenzylguanidine imaging allows early identification of dementia with Lewy bodies during life. Eur J Nucl Med Mol Imaging 35:1636–1641
36. Yoshita M, Taki J, Yokoyama K et al (2006) Value of ^{123}I-MIBG radioactivity in the differential diagnosis of DLB from AD. Neurology 66:1850–1854
37. Nakajima K, Okuda K, Matsuo S et al (2012) Standardization of metaiodobenzylguanidine heart to mediastinum ratio using a calibration phantom: effects of correction on normal databases and a multicentre study. Eur J Nucl Med Mol Imaging 39:113–119
38. King AE, Mintz J, Royall DR (2011) Meta-analysis of ^{123}I-MIBG cardiac scintigraphy for the diagnosis of Lewy body-related disorders. Mov Disord 26:1218–1224
39. Hanyu H, Shimizu S, Hirao K et al (2006) Comparative value of brain perfusion SPECT and [^{123}I]MIBG myocardial scintigraphy in distinguishing between dementia with Lewy bodies and Alzheimer's disease. Eur J Nucl Med Mol Imaging 33:248–253

How to Reduce the Radiation Burden in Cardiac CT

5

Gianluca Pontone

5.1 Introduction

In the last 30 years, the introduction of new technologies in cardiology has allowed a noninvasive description of cardiac anatomy, function, perfusion, and metabolism, with several billion tests per year performed worldwide. Therefore, the cost and efficacy balance of each diagnostic test needs to be considered in the diagnostic workup of the patient, and the radiation dose associated with some common imaging tests needs to be taken into account in this "cost" analysis [1]. Great benefit is derived from multidetector computed tomography coronary angiography (MDCT-CA), which was introduced in the late 1990s to evaluate coronary artery anatomy.

Standard MDCT equipment is based on an X-ray source, producing a narrow X-ray beam with different widths depending on the number of slices, coupled with a matrix detector with different numbers of rows. The X-ray source and matrix detector rotate simultaneously around the patient while the table moves (helical scan modality) or remains stationary (axial scan modality). Due to its noninvasive nature, this technique was hailed as a promising alternative to invasive CA being used to rule out coronary artery disease (CAD) in low- to intermediate-risk patients with disagreement between symptoms and functional stress-tests findings, to evaluate coronary and cardiac vein anatomy in patients with dilated cardiomyopathy of unknown etiology, and to evaluate coronary artery bypass graft (CABG) and stent patency [2]. The promising results in terms of feasibility and accuracy in CAD detection meant that MDCT CA volume doubled by the early 2000s and has continued to grow exponentially. This demand for noninvasive coronary artery imaging is responsible for the rapid advances in MDCT imaging technology that now provide higher spatial and temporal resolution.

Many technical factors that now enhance image quality also affect the radiation dose received by the patient. Indeed, detector width and X-ray tube rotation time are the major determinants of spatial and temporal resolution, respectively, and high spatial and temporal resolutions are mandatory for accurate assessment of small anatomical structures characterized by continuous movement, such as coronary arteries. Modern scanners are therefore equipped with an increasing number of thinner slices (up to 350 slices with 0.5-mm slice width) and gantries with often faster rotation time (up to 270 ms) [2]. However, there is a tradeoff between the need for low-noise images and the benefit of using lower doses of radiation. Therefore, to maintain high image quality with reduced slice width and high gantry rotation speed, the number and speed of photons received by the detector array usually need to be increased by

G. Pontone (✉)
Centro Cardiologico Monzino, IRCCS, Milan, Italy
e-mail: gianluca.pontone@ccfm.it

P. Marzullo and G. Mariani (eds.), *From Basic Cardiac Imaging to Image Fusion*,
DOI: 10.1007/978-88-470-2760-2_5,

increasing tube current (up to 650–700 mA) and voltage (up to 120 KVp), resulting in a higher effective radiation dose to the patient. Conversely, with the increased number of simultaneously acquired slices, scanning time is shorter, which results in lower radiation exposure . Despite the balance between these three factors, the preliminary experience with MDCT was associated with an impressive increase in radiation dose [3]. Indeed, it is estimated that the annual per capita radiation dose associated with medical diagnostic tests increased from 0.53 to 3 mSv, which is close to the natural radiation background. Of this 3.0 mSv, approximately half comes from CT scans 0.6 mSv from nuclear stress tests and 0.4 mSv from interventional fluoroscopy procedures performed annually [4].

Two different effects could be expected by this radiation exposure increase: deterministic and stochastic risks. The only deterministic effect described in clinical practice is skin injury, which only occurs above a threshold level of radiation, which is usually higher than levels occurring from a single noninvasive imaging procedure such as MDCT-CA. Most important is the stochastic effect of potential genetic mutation or cancer. More specifically, ionizing radiation is energetic enough to overcome the binding energy of the electrons orbiting atoms and molecules, thus creating ions such as hydroxyl radicals. These radicals interact with nearby DNA to cause strand breaks or base damage. Usually, this damage is rapidly repaired by various cellular systems, but occasional "misrepair" can lead to genetic mutations and cancer.

Moreover, there is no agreement regarding the relationship between radiation dose and the stochastic risk of cancer. Two main theories are usually accepted. The first, known as "linear quadratic hypothesis," suggests that at low radiation dose, the risk of malignancy is low and unquantifiable in humans but that the risk rises exponentially at higher doses (>100 mSv), which are usually far higher than the radiation dose usually used in medical clinical practice. The second theory, known as "linear no-threshold hypothesis," suggests that the relationship between the risk of developing cancer over the long term and genetic damage is assumed as being linear, and therefore, any ionizing radiation dose can result in a reduction of life expectancy [5]. According to the last hypothesis, the relationship between dose and lifetime attributable risk is derived from studies of survivors of the atomic bombs dropped on Japan in 1945 [6] and large-scale study of radiation workers in the nuclear industry [7]. A study of 105,427 atomic bomb survivors exposed at a mean dose of 29 mSv shows an excess of 81 solid cancers over the number expected based on cancer rates in the unexposed cohort, corresponding to an excess relative risk (RR) of 2% [6]. Similar results were observed in the 15-country study of >400,000 radiation workers exposed to a mean dose of 19.4 mSv in whom an excess RR of 2% was also described [7]. According to this approach, the estimated cancer risk in the United States attributable to overall CT radiation has grown from 0.4 to 1.5–2.0% [8].

Regarding to MDCT-CA, the probability of cancer induction ranges between 0.0176% (or 176 of one million patients) to 0.0737% (or 737 of one million patients) based on the MDCT-CA protocol used. Of note, these estimates are not universally accepted for several reasons [9]. First, survivors of the atomic bombs were exposed to a fairly uniform dose of radiation throughout the body, whereas MDCT involves highly nonuniform exposure. Second, radiation-induced malignancies are indistinguishable from malignancies related to other carcinogens or biologic processes. Therefore, the small potential risk of carcinogenesis would be difficult to differentiate from the substantial intrinsic average lifetime risks. Third, the general population is exposed to natural background radiation, to geographically varying degrees, that averages approximately 3.5 mSv per year. It is conceivable that even the low levels of background radiation could contribute to the development of malignancies, which would be difficult to differentiate from the effects of a single exposure to

medical radiation [9]. Fourth, the life-attributable cancer risk reported is a mean value, whereas cancer risk from X-ray exposure is also dependent on specific patient factors, such as gender and age. Finally, the relative rosk for cancer estimated is applied from the Japanese to the US populations, which have differing patterns of cancer in terms of incidence and mortality rates. Thus, in the absence of certainty, the consensus opinions of expert panels suggest adopting a conservative estimation of radiation risks, and therefore, the linear no-threshold hypothesis is usually more accepted. Despite this crucial issue, in a survey of radiologists and emergency-room physicians, ~75% of the entire group significantly underestimated the radiation dose from CT scans, and 53% of radiologists and 91% of emergency-room physicians did not believe that CT scans increase the lifetime risk of cancer [8]. Therefore, controlling overall radiation exposure in cardiac MDCT is mandatory.

There are two ways to reduce this exposure in the population. The first is simply to decrease the number of MDCT-CA studies, replacing them with other options, such as ultrasonography (US) and magnetic resonance imaging (MRI) in which X-ray are not used. This approach is based on the "principle of justification," that states that any decision that affects the existing radiation exposure situation should do more good than the standard of care [1]. This is an issue of concern, as several studies observed 14–22% of cardiac imaging tests, included MDCT-CA, are performed inappropriately [10]. Second, according to the "principle of optimization," as noted by the International Commission on Radiological Protection (ICRP), the number of individuals exposed and the magnitude of doses administered to them should all be kept as low as reasonably achievable (ALARA).

The aim of this chapter is to define overall radiological risk and assess protocol strategy of MDCT-CA in clinical practice to minimize radiation exposure to patients according to the ALARA principle.

5.2 How is Radiation Dose Estimated in MDCT Coronary Angiography?

The common general terminology used in the field of radioprotection is a result of the activity of multiple international organizations. One of these is the ICRP, which was founded in 1928 from the International Society of Radiology. The following terminology used in this chapter is from this organization:

- Computed tomography dose index (CTDI): area under the radiation-dose profile for a single rotation and fixed table position along the axial direction of the scanner divided by the total number of detectors for slice thickness and is expressed in coulomb/kg
- $CTDI_{100}$: integrated radiation dose from acquiring a single scan over a length of 100 mm
- CTDIw: average radiation dose to a cross-section of a patient's body determined with the equation CTDIw = 2/3CTDI100 at periphery + 1/3CTDI100 at center
- CTDIvol: average radiation dose over the volume scanned determined by the equation CTDIvol = CTDIw/pitch, where pitch is defined as table movement expressed in millimeters for each 360° gantry rotation, divided by the product of the number of slices and slice width. It is measured in milligray
- Dose length product (DLP): integrated radiation dose for a complete CT examination measured in milligray × centimeters and calculated by the formula DLP = CTDIvol × length irradiated
- Effective dose (ED): measured as the product between DLP and k, the region-specific conversion factor.

In clinical practice the ED is the most common parameter for estimating radiation exposure associate with a specific diagnostic test and for comparing the different biological effects. However, it is important to note that all reported radiation doses are obtained from numerous assumptions that may result in difference from the true value. In particular, the k factor is

determined from population averages of survivors of atomic bomb explosions, and therefore, ICRP published slightly differing values in different reports, ranging between 0.014 and 0.017 for chest scan. Accordingly, the European Guidelines on Quality Criteria for Computed Tomography [11] suggested a simplified method for estimating ED using a fixed chest k-value of 0.017 mSv/mGy × cm for MDCT-CA as well. However, ED calculated with chest CT conversion factor significantly underestimates the ED delivered during MDCT-CA [12]. The reason is that the scanning field for MDCT-CA is different to that for standard chest CT scan. Indeed, MDCT-CA dose not examine the entire chest but only the lower chest and upper abdomen, irradiating breast tissue for the majority of the volume scan. Based on this evidence, the last ICRP report [13] concluded that a conversion factor of 0.030 is more realistic. Therefore, when applied, ED results in an increase of 60% in comparison with the ED reported in all recent papers, including scientific reports discussed in this chapter.

5.3 A Brief History of MDCT Coronary Angiography

By 1999, performing MDCT electrocardiography (ECG)-triggered examinations of the coronaries became available. With four-detector-row MDCT systems, temporal resolution (~250 ms) allowed for motion-free imaging of the heart only in patients with a very low heart rate (HR). Despite the subsequent introduction of the 16-detector-row MDCT scanners with faster gantry rotation times, which led to improved spatial and temporal resolution, coronary artery motion remained the major reason for segments being nonassessable and was commonly reported to correlate with the patient's HR. In 2004, 64-slice MDCT systems were introduced, providing further increased spatial resolution and using the advanced z-sampling technique, with improved temporal resolution by reducing the gantry rotation time to 0.33 s [3], providing higher image quality but without satisfactory results at higher HR. In the "post-64" era, MDCT technology was taken in various directions to overcome these limitations. The first was dual-source CT (DSCT) to improve temporal resolution [14–16]. The second was the increased number of detector elements and, therefore, volume coverage along the z-axis of the detector block [17, 18]. The third is the use of iterative image reconstruction algorithms [adaptive statistical iterative reconstruction (ASIR)] [19–21]. Next came DSCT scanners with larger number of detectors that use a high-pitch acquisition strategy [22] to capture the entire heart within one heart beat. At the same time, the development of ECG triggering from the retrospective to prospective approach has been applied to all scanner modalities [23–25]. Several of these technical aspects and their relationships with radiation exposure are discussed below.

5.4 Strategies to Minimize Radiation Dose from Cardiac MDCT

Strategies to minimize radiation dose in MDCT are based on a main concept: contrast attenuation and image noise are directly and inversely proportional to the number of photons received by the detector array, respectively. The main variables involved in the ED-sparing protocol, but at the same time being responsible for image quality, are:

- tube current, expressed in milliampere (mA) that influences photon flux
- tube voltage, expressed in peak kilovolt (kVp) that influences photon energy
- exposure time, determined by pitch
- degree of photon attenuation, influenced by the patient's body mass index (BMI)
- two Sources of undesired patient radiation exposure. The first is Z-overbeaming that is defined as the penumbra-to-umbra ratio. It degrades the geometric dose utilization of an MDCT scanner. It is reduced as the z-axis detector coverage increases. The second is

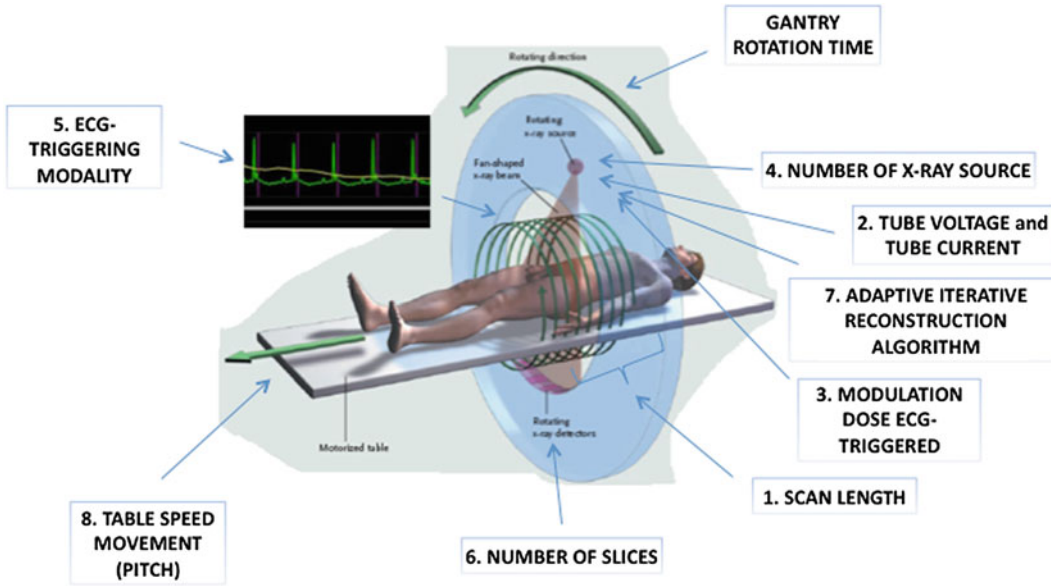

Fig. 5.1 Standard computed tomography equipment. An X-ray source, producing a *narrow*, *fan-shaped beam* with different widths depending on the number of slices, is coupled with a matrix detector with different rows of identical width based on the individual scanner. The X-ray source and matrix detector rotate simultaneously around the patient while the table moves (helical-scan modality) or remains stationary (axial-scan modality). All variables that contribute to image production may be used as dose-saving strategy. Modified from [8]

Z-overscanning that is usually higher in spiral acquisitions in comparison with axial acquisitions. Therefore, all strategies to reduce radiation exposure can be classified into two categories: those that modify X-ray output (such as tube current or tube voltage), and those that reduce the extent or duration of X-ray exposure. These strategies translate to reduction of z-overbeaming and/or z-overscanning. The most important techniques, described in Fig. 5.1, need to take these principles into account.

5.4.1 Scan Length Optimization

The total radiation dose delivered is directly proportional to scan coverage, and therefore, scan coverage optimization is crucial for reducing overall ED. According to this approach, only structures of interest should be included in the scan. For coronary artery imaging, scanning should begin at the trachea bifurcation and finished at the inferior cardiac profile. However, cardiac anatomy differs among individuals, and in thin patient with a vertically oriented heart, the region of interest (ROI) could be extremely different from another patient. In this regard, a topogram performed before the contrast-enhanced scan could minimize scan length and therefore overall ED. However, some patients have difficulty maintaining the same breath-hold between topogram and enhanced scan, and the risk that some segments of the coronary tree may be not included in the scan needs to be taken into account.

5.4.2 Tube Voltage and Tube Current Setup

ED increases linearly with tube current and with the voltage squared [3]. Therefore, these parameters need to be at the lowest level expected to reach good image quality for a specific diagnostic aim. By reducing tube

current and voltage, image noise increases significantly [3]. At the same time, using a low tube voltage, the increased attenuation of photons by iodine that occurs at lower photon energy (phenomenon known as Compton effect) increases the contrast between the coronary artery lumen and the surrounding tissue [3]. Therefore, by reducing tube current and voltage, a tradeoff between higher image noise and lower contrast resolution must be considered. For MDCT-CA, individually weight-adapted protocols have been successfully applied by adjusting tube voltage and current to the patient's BMI. There are obviously considerable differences in chest attenuation between men and women because of the breasts and large differences in fat distribution among individuals. Consequently, the impact of this approach, with its inaccuracies, could be limited. Some authors suggest providing individual scanning parameter protocol according to chest diameter rather than to BMI because chest diameter better predicts the real contrast attenuation in the ROI. Paul et al. [26] proposed a "noise-based" approach to define optimal individual scanning parameters. The principle is to calculate noise on an unenhanced image, thereby predicting sufficient—and necessary—radiation required for imaging the individual. Because there is substantial difference in attenuation between the upper and lower portions of the heart, the authors suggest to use the bottom part of the heart for the precontrol scan to determine the region with maximum attenuation as the reference. They then trace an ROI over the left ventricle on the precontrol scan, and the noise corresponds to the value of the standard deviation (SD) within the ROI. Tube voltage and current are then adapted to the noise measured. This approach requires a further unenhanced scan and thus additive radiation exposure . In clinical practice the most common protocol used consists in a tube voltage of 100 kVp and 120 kVp for patients with BMI < 30 and ≥ 30, respectively. This kind of approach allows the best compromise between image quality and radiation dose regardless the scanner used.

5.4.3 ECG-Triggered Tube-Current Modulation

First-generation MDCT scanners used a continuous helical scan with a low table speed, and the patient's ECG signal was acquired simultaneously with image data, allowing the user to retrospectively reconstruct and visualize the anatomy at multiple physiologic phases of the cardiac cycle. This approach, better known as retrospective ECG-triggering, is usually associated with high radiation exposure because low pitch values are used, resulting in considerable z-over scanning of tissue and because X-rays are delivered during the entire scan. Multiple reconstructions at different points of the cardiac cycle should not be mandatory to reconstruct the images for clinical diagnosis. Because cardiac motion is greatest during systole and least during diastole, the "useful" radiation corresponds to a mid-diastole phase [26], which is only 20% of the overall radiation burden [3]. Therefore, according to this principle, the highest tube current necessary to attain the best image quality is produced only during mid diastole and is reduced by 80% in the remaining cardiac cycle. During the scan, the desired time window is prospectively chosen by the operator but usually ranges between the 40 and 80% range of the cardiac cycle.

Of note, tube current reduction is based on the average of the prior RR intervals. Therefore, in patients with arrhythmias, it could be inappropriately reduced, providing lower tube current during the phase of the cardiac cycle that is desirable as the diagnostic window. New algorithms will be provided by manufacturers to automatically detect premature contraction of the heart and thereby eliminate ECG-dependent dose modulation in a real-time mode during acquisition. Moreover, ECG-controlled tube-current modulation may be limited in patients with high HRs during the scan, because in these patients, the best image quality may be reached in the systolic phase rather than in mid diastole. This limitation can be overcome with some scanners by manually changing the full dose

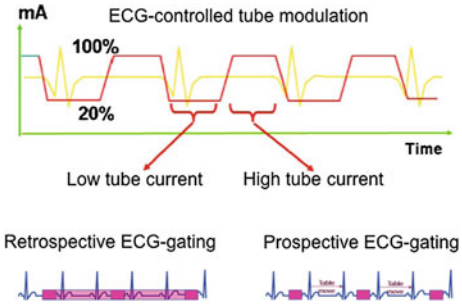

Fig. 5.2 **a** Electrocardiograph (*ECG*)-controlled tube-current modulation. Using this technique, full tube current is applied during diastole, when the heart stands still, and is lowered in systole. **b** Helical retrospective ECG gating. This technique consists of a continuous spiral scanning of the heart with simultaneous ECG recording. **c** Axial prospective ECG gating. With this technique, the table remains stationary while the X-ray tube rotates around the patient and is advanced for the subsequent scan only when data acquisition is completed, thus obtaining a significant reduction of total X-ray exposure time. Modified from [2]

(70–80% of the R–R cycle for low HR and 40–50% of the R–R cycle for higher hear rate). This technique, known as tube-current-modulation ECG-triggered approach, has been determined as the most effective technical tool for radiation-dose reduction in first-generation MDCT-CA using retrospective ECG triggering. Retrospective ECG triggering and tube-current-modulation ECG-triggered approaches are described in Fig. 5.2.

5.4.4 Dual-Source Computed Tomography

Despite the technological advances in the latest generation of 64-slice MDCT systems, the limited temporal resolution (135 ms for scanners with gantry rotation time of 270 ms) is responsible for 12% of nonevaluable scans due to the presence of motion artefacts mainly at higher HRs. Consequently, HRs of <65 bpm are usually suggested in order to achieve good image quality [14]. Higher HRs in clinical practice are common, and therefore, higher temporal resolution can be reached only with a multi segment reconstruction using low pitch and therefore with increased ED, with limited benefits to image quality because data are acquired during consecutive cardiac cycles and averaged to generate each cross-sectional image [14]. Indeed, a systematic approach with beta-blocker medication allows a target HR < 60 bpm in only 55% of patients with suspected CAD [14].

In 2008, DSCT was introduced. This system combines two arrays consisting of one tube and one detector each, arranged within the same gantry at a 90° offset, so that a one-quarter rotation is sufficient to sample X-ray transmission data over 180° of projections. With a gantry rotation time of 330 ms, the system could achieve a temporal resolution of 83 ms, which is significantly higher than single-source MDCT. Achenbach et al. [14] demonstrated that image quality and diagnostic accuracy remain unaffected in DSCT by systematic HR control, with significant improvement in coronary visualization in comparison with 64-slice single-source MDCT. The increased temporal resolution of DSCT can be used to reduce radiation compared with single-source MDCT by using a smaller tube-current modulation pulse and higher pitch [15]. The ED reduction reached by DSCT seems to be more evident at higher HRs, where higher pitch is usually employed. Indeed, McCollough et al. [15] showed that increasing pitch with a DSCT reduced CTDIvol by 25% at a HR of 60 bpm (0.265 pitch), 44% at 78 bpm (0.36 pitch), and 57% at 100 bpm (0.46 pitch) compared with a standard protocol with a single source MDCT with pitch of 0.2. According to these evidences, Ropers et al. [15] have demonstrated that no significant differences were found between patients with low and high HRs in terms of feasibility and accuracy versus invasive CA with a mean effective radiation dose of 15.3 mSv for patients with HR <65 bpm and 15.9 mSv for patients with a HR >65 bpm. Comparison between DSCT and single-source MDCT is shown in Fig. 5.3.

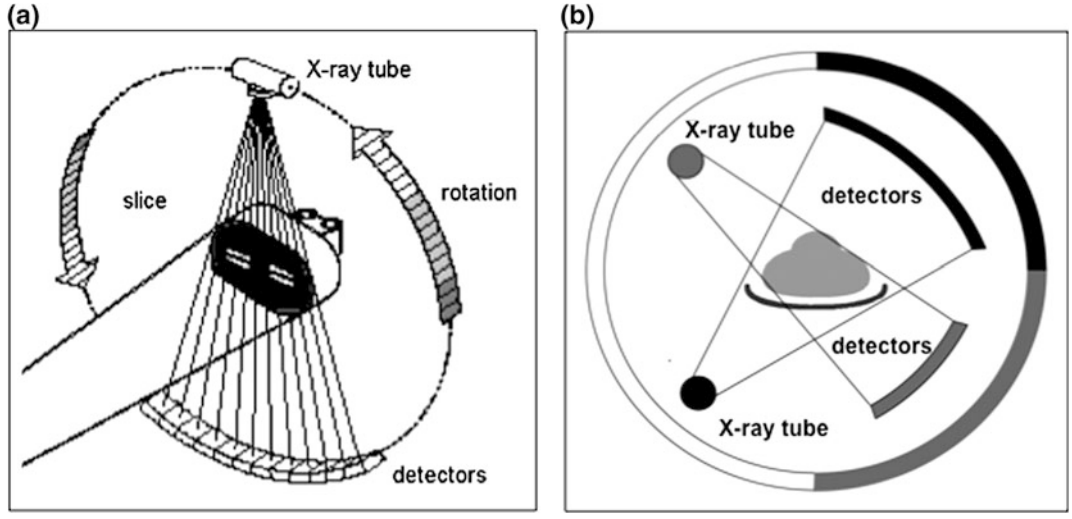

Fig. 5.3 **a** Single-source multidetector computed tomography (*MDCT*) technology. With this technology, a single X-ray tube is coupled with a single matrix of detectors. **b** Dual-source MDCT (DSCT). This scanner is equipped with two sets of X-ray tubes, and the detectors are arranged in a single gantry at 90° offset, operating simultaneously. Modified from [2]

5.4.5 Prospective ECG Triggering

MDCT-CA with standard retrospective ECG triggering uses backward-looking measurement of R-wave timing, spiral scanning during table motion with a very low pitch (~0.22), and a more traditional cone-beam reconstruction. Prospective ECG triggering was introduced in 2008 [23]. This technique uses forward-looking prediction of R-wave timing, step-and-shoot nonspiral acquisition with no table motion during imaging, and unique cone-beam reconstruction. This acquisition relies on the accurate prediction of RR duration based on evaluation of the previous cardiac cycle. Following QRS detection, the delay necessary to trigger at a quiescent phase of the cardiac cycle is calculated. During ECG analysis, the table moves to the next position and waits for the subsequent QRS trigger to initiate the scan, which is performed without table movement. The process is repeated until the entire volume of interest is covered. Therefore, the effective pitch is 1.0 with prospective ECG triggering. The X-ray beam is turned on for only a short portion of the cardiac cycle and is turned off during the rest of the R–R. Therefore, radiation is only administered at one predefined time window of the cardiac cycle, which is defined as "padding" with nonspiral scanning. The main advantage is that the entire exposure time is used for one image, and there is no unnecessary radiation exposure during any other phase of the cardiac cycle. Consequently, in a prospective acquisition, exposure time is optimized and radiation exposure is about four times less than in retrospective acquisition.

The second advantage of prospective ECG-triggering is the better management of extrasystolic beats. Indeed, some scanners can wait at an axial location for premature contractions and proceed to a further scan CT only at the detection of normal QRS complexes. A disadvantage of this feature is that only a short diastolic phase is acquired, and therefore, HR control is mandatory for prospective ECG triggering [23]. Rigorous patient selection is thus recommended, including low HR (usually <65 bpm) and low HR variability. Indeed, the step-and-shoot protocol only permits a half-reconstruction method, and in patients with HR >65 bpm, multi sector reconstruction is recommended instead of half

reconstruction [24]. If high HR is an absolute contraindication for prospective ECG triggering, the limitation of HR variability can be overcome using larger padding to improve interpretability of the images by providing additional cardiac phases. It has been suggested to use padding 0, corresponding to a window of 100-ms scanning time at only one distinct end-diastolic phase (i.e., 75% of R–R cycle) in patients without HR variability; padding 100, which corresponds to a window of 200-ms scanning time at 2 distinct end-diastolic phases (i.e., 70–80% of R–R cycle) in patients with HR variability ≤2 bpm; and padding 200, corresponding to a window of 400-ms scanning time at four distinct phases (i.e., 40–80% of R–R cycle) in patients with HR variability >2 bpm 25. However, it would be expected that greater amounts of padding would increase radiation dose.

The second limitation is that the discrete nature of the prospective ECG-triggering acquisition mode may result in transition artefacts between axial shots, resulting from MDCT contrast transitions and/or minor anatomical shifts attributed to physiological phase. A further limitation is the scan length. Whereas scan range can be defined accurately to a millimeter in conventional helical CT, it must be a multiple of scan coverage less the overlapping zones in sequential scans. Therefore, in some cases, the scan range must be larger in sequential scans than one would have defined it in conventional helical MDCT. Finally, this approach is not useful for function evaluation because no systolic data are available. This, however, is generally assessed primarily with other imaging modalities.

5.4.6 Increase in Number of Slices

Craniocaudal coverage of 64-slice MDCT-CA is typically <40 mm, giving limited coverage width. ECG triggering overcomes this limitation by assuming that heart motion remains mostly periodic [17]. The development of wide-area MDCT detector [18] enabled greater coverage per gantry rotation, and the extension from 64 slices to 256- and 320-detector-row MDCT systems allows whole-heart coverage [18]. The 256-slice MDCT has 912 (transverse) × 256 (craniocaudal) elements, each approximately 0.5 × 0.5 mm at the center of rotation, with craniocaudal coverage of 128 mm per rotation [3]. The 320-MDCT system uses a detector element consisting of 320 × 0.5 mm elements and provides 160 mm of coverage in the z-direction [17]. Both scanners allow comprehensive anatomic imaging of the whole heart and coronary vessel in a single heart beat in cine, non spiral scan mode without ECG gating. The 256- and 320-slice systems have a standard temporal resolution of approximately 135 and 175 ms, respectively. This remains significantly longer than the temporal resolution of invasive CA; therefore, HR control is mandatory to attain excellent image quality. However, in patients with high HR despite β-blocker treatment, multi segment reconstruction can be used. In this approach, a data set for image reconstruction is acquired over two cardiac cycles. Only data from the 90° rotation during each cardiac cycle are used, improving the effective temporal resolution by a factor of 2.

From a theoretical point of view, radiation exposure with the 256- or 350-slice system would be much higher than with conventional MSCT due to the greater beam width of this equipment. However, doses were found to be lower for both scanners in comparison with 64-slice MDCT CA. Three main factors explain this paradox. First, the total acquisition time is approximately 20–30 s for 16-slice MSCT and 8–12 s for 64-slice MSCT, whereas 256- and 350-slice MDCT provide images within the duration of one heartbeat at the most, without ECG gating [17]. Second, helical scans with a low pitch, such as in 64-slice scanners with retrospective ECG triggering, are characterized from regions of overlap, which receive a higher dose. Third, the penumbra, defined as the marginal portions of X-ray beam and that do not contribute to images but only improve radiation dose, decreases as nominal beam width increases [17]. Therefore, the larger beam width of the 256- or 320- slice MDCT provides smaller

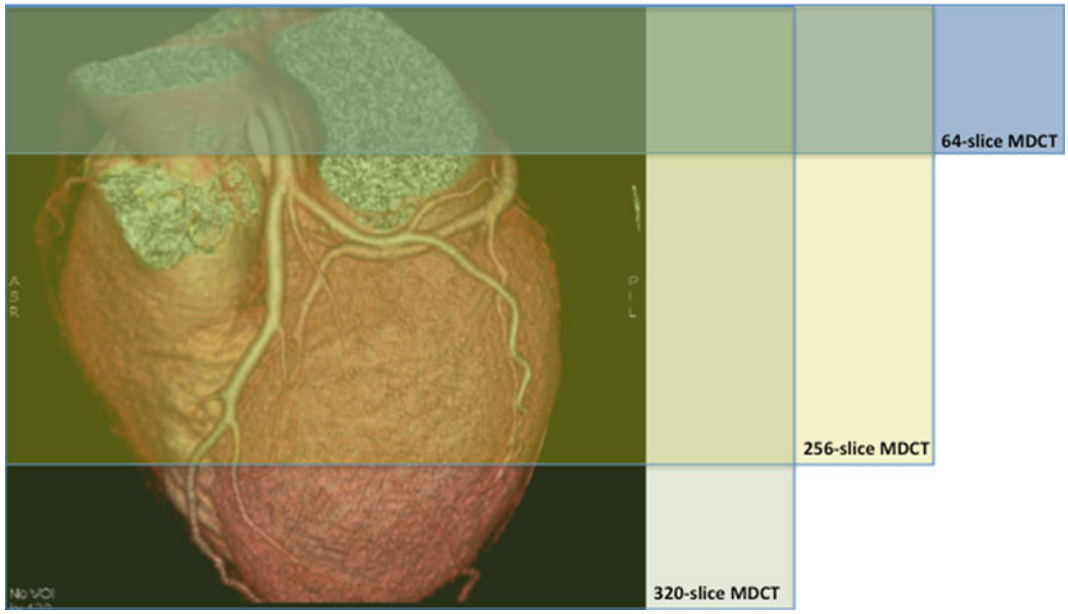

Fig. 5.4 Different coverage of MDCT. The 64-slice MDCT has 64x0.625 mm detectors covering 40 mm in the z-direction (*blue area*). The 256-slice MDCT has 912x256 (cranio-caudal) elements, each approximately 0.5x0.5 mm at the center of rotation with cranio-caudal coverage of 128 mm per rotation (*yellow area*). The 320-slice MDCT system used a detector element consisting of 320x0.5 mm detector and provides 160 mm of coverage in the z-direction (*light blue area*). The first scanner needs multiple heart beats with ECG-gating to image the whole heart. On the contrary, the last two scanners allow a comprehensive anatomic imaging of the whole heart and coronary vessel in a single heart beat in cine non-spiral scan mode without ECG gating

radiation exposure than the 16- and 64-slice scanners [17]. If the HR increases >65 bpm, the scanner automatically changes from single-segment to multisegment reconstruction, imaging the heart in two beats at the expense of higher radiation dose.

Other advantages are expected in terms of image quality. First, these scanners eliminates "stair-step" artefacts shown in 64-slice scanners that image sub volumes of the entire cardiac volume over multiple gantry rotations. Second, the fast acquisition of the entire cardiac volume allows the contrast bolus to be imaged at a single time point [18] so that the contrast volume for MDCT CA can be lowered. Third, these scanners present a significant opportunity for expanding the use of low-dose prospectively gated imaging in patients with concomitant noncoronary indications such as CABG, aortic disease, or triple rule out due to the combination of wide coverage with faster rotation speeds. The 256- and 320-slice MDCT CA scanners are shown in Fig. 5.4.

5.4.7 Adaptive Iterative Reconstruction Algorithm

The use of low tube voltage provides a significant ED reduction. Despite the fact that reduced tube voltage results in increased contrast attenuation due to reduced mean photon energy closer to the k-absorption edge of iodine, with an increase in photoelectric effect and decrease in Compton scattering, a concomitant image noise increase is described. MDCT-CA usually use a class of algorithm called filtered backprojection (FBP) to provide cardiac images. In this algorithm, each projection data is calibrated, filtered, back-projected, and weighted, and when the last projection view is processed, the reconstruction is complete and reconstructed images are

generated. Although FBP algorithms are fast and have served us well over the past 30+ years, they are highly sensitive to noise. This limits dose reduction by reducing tube current and/or voltage. As an alternative to FBP, ASIR was introduced to compensate for the increased image noise produced at low tube current and voltage settings, thus allowing the use of 100 kVp in overweight patients with BMI > 25 as well [19].

The underlying approach of ASIR is that, in a particular view angle, the device first calculates a synthesized projection by performing "forward projection" on images of the estimated object. Basically, this estimate mimics, as much as possible, the process in real CT scanning in which X-ray photons traverse through the object and reach the detector. It mimics the finite (known) focal-spot size by placing the initial location of the X-ray photons over a small area instead of a single point. During the modelling of X-ray photon interaction with the object, the size and shape of the image voxel (not an assumed point) is considered by calculating different path lengths for X-ray photons entering the voxel at slightly different orientations and locations. In a similar fashion, detector shape and size are considered through modeling of the detector response function. Thus, system optics are modeled with an iterative reconstruction and not with FBP. In other words, with ASIR, it is not assumed that noise is evenly distributed across the entire image, but the matrix algebra is used to selectively identify and then subtract noise from the image with a mathematic model. The result is a less noisy image than with FBP techniques [19].

A limitation of iterative reconstruction, however, is the long computing time. Therefore, a modified and computationally faster iterative reconstruction technique—adaptive statistical iterative reconstruction—was developed in which only one corrective model is used to address image noise [19]. Leipsic et al. [20] compared FBP versus the use of 20, 40, 60, 80, and 100% ASIR, resulting in reduced image noise of −7, −17, −26, −35, and −43%, respectively ($p < 0.001$) and increased signal-to-noise ratio (SNR) (mean increase in SNR of 8, 21, 36, 58, and 81%, respectively). On the contrary, in comparison with FBP, both 40 and 60% ASIR were associated with a statistically significant increase in contrast-to-noise ratio (CNR). Therefore, the authors concluded that although the largest reduction in noise was observed with 100% ASIR, reconstruction with 40 and 60% ASIR appeared to provide optimal image quality. Indeed, a fully converged 100% ASIR image tends to have a noise-free appearance with unusually homogeneous attenuation, showing a higher degree of smoothness and resulting in a "plastic" or "artificial" appearance [20]. Similarly, Pontone et al. [21] showed lower noise (−15%), higher SNR (+21%) and CNR (+22%), and better feasibility (97 versus 91%) with 40% ASIR versus FBP.

In conclusion, noise reduction properties of ASIR may permit the use of lower tube setup with stable image noise and quality when compared with FBP. Therefore, although ASIR is not a dose-saving strategy per se, it allows the use of low tube voltage and current in overweight patients also, thus indirectly influencing the overall effective radiation dose. This may represent a valuable method of radiation-dose reduction that would be additive to existing dose-reduction strategies.

5.4.8 High-Pitch Computed Tomography Coronary Angiography

Single-source MDCT-CA, which is based on one X-ray tube and one set of detectors, reconstructs one cross-sectional image with data acquired from projections over a range of 180°. Therefore, one half rotation of the gantry is required to collect this data set. DSCT uses two X-ray tubes and two detectors arranged in a 90° angle; therefore, only one quarter rotation of the system is necessary, which doubles temporal resolution [22]. Application of these principles allowed the introduction of second-generation DSCT at the end of 2008. This scanner has a rotation time of 280 ms, so that the temporal resolution is approximately 75 ms. It uses a

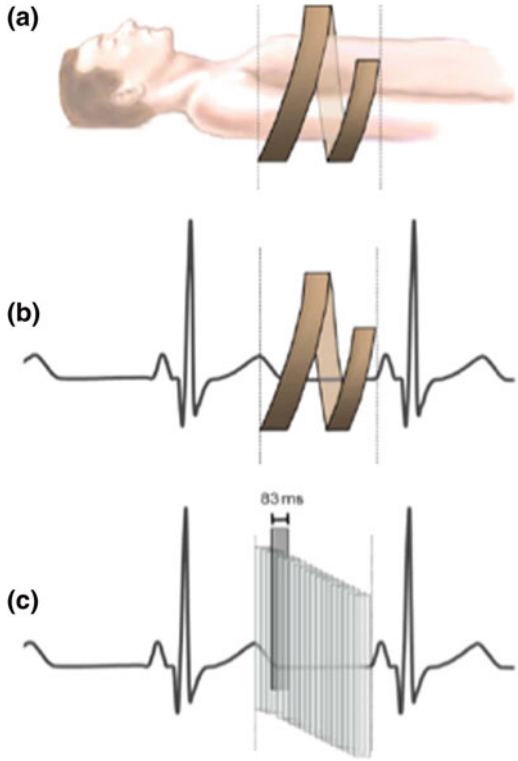

Fig. 5.5 High-pitch dual-source computed tomography coronary angiography. **a** In this scanner, a very high pitch value is used so that the X-ray tube and detector rotate around the patient without overlap. **b** Image acquisition starts in late systole and is completed within one cardiac cycle. **c** Images are reconstructed with a temporal resolution that corresponds to approximately one quarter of the gantry rotation time (here, 83 ms for a gantry rotation time of 330 ms). Modified from [22]

wider detector (2 × 64 detector elements, which allows acquisition of 2 × 128 slices), with a pitch up to 3.2 that allows an overall scan time of about 0.27 s to cover the entire heart. Therefore, an increase in pitch decreases radiation exposure. However, HR must be low and regular to create a long enough diastole to accommodate data acquisition and because the start of image acquisition is triggered by the R wave of the heart beat preceding the scan window [22]. This scan mode, known as Flash CT, enables complete image acquisition within one cardiac cycle so that the X-ray tube and detector rotates around the patient without overlap and with very short exposure time. This technique is associated with a very low radiation dose, especially if combined with a low tube voltage, offering a potential dose reduction of >80% with an ED <1 mSv. The high-pitch scan modality is described in Fig. 5.5.

5.5 Radiation Dose Associated with Different Generations of MDCT

5.5.1 Low Generation Scanner Up to 64-MDCT

Preliminary experience with early-generation scanners (up to 40 slices) reported a mean ED of 8.6 mSv [2]. Hausleiter et al. [3] found an ED of 9 mSv using a 64-MDCT with retrospective ECG triggering and modulation dose approach. They found that despite the increased spatial and temporal resolution of the 64-slice MDCT, ED was approximately 40% higher than with the 16-slice MDCT because the craniocaudal scan region is covered twice, whereas the helical pitch value is almost the same. The same authors published the Prospective Multicenter Study on Radiation Dose Estimates of Cardiac CT Angiography in Daily Practice (Protection I) study in 2009 [27]. In this multicenter study, 1,965 patients undergoing 64-slice MDCT were evaluated in daily practice, with an estimated ED of 12 mSv (range, 8–18 mSv). In the multivariate analysis, a 1 cm decrease in scan length, use of ECG-controlled modulation dose, low tube voltage of 100 kVp, and prospective ECG triggering resulted in a reduction of 5, 25, 46, and 78%, respectively. The diagnostic image quality did not differ between patients studied with versus without ED-saving strategy, except for patients scanned with 100 kV tube voltage in which the percentage of evaluable coronary artery segments was higher in comparison with the 120 kVp tube voltage group (100 versus 96.3%). Of note, ECG-controlled modulation dose was used in 73% of the population, whereas prospective ECG-triggered scanning and low

tube voltage from 120 to 100 kVp were used only in 6 and 5% of overall examinations, respectively. Moreover, 100 kVp tube voltage was used only in normal-weight patients, excluding those with BMI >25 [27].

5.5.2 Low Tube Voltage

Bischoff et al. [28] tested the effect of lowering the tube voltage from 120 to 100 kV in a predefined subgroup analysis of the PROTECTION I study concerning image quality and radiation dose. This resulted in an increased image noise of 26.3% and SNR and CNR increase of 7.9 and 10.8%, respectively. More importantly, qualitative assessment of diagnostic image quality did not differ between patients scanned with 100 and with 120 kV tube voltage and was associated with 53% reduction in radiation dose when compared with the conventional 120 kV scan protocol. However, the authors applied the 100 kV scan protocol in patients with a significantly lower body weight.

Hausleiter et al. [29] in the Protection II study, compared image quality and radiation dose using a 100 kVp tube voltage scan protocol compared with standard 120 kVp for MDCT-CA in over weighted but not obese individuals. They found similar mean image quality scores (3.30 versus 3.28, respectively), similar none-valuable coronary artery segments (15.3 versus 16.2%, respectively), and relative 31% reduction in estimated radiation dose for the 100 kVp scan protocol. On the basis of these preliminary results, the 100 kV scan technique is recommended for slim patients and advocates the introduction of a dedicated reconstruction algorithm that would reduce image noise and consequently improve SNR and CNR.

5.5.3 Prospective ECG-Triggering

The introduction of prospective gating subsequently represented a crucial step in the strategy of dose reduction in MDCT. The first experience regarding the feasibility of prospective ECG triggering in MDCT-CA was published in 2007 by Husmann et al. [23]. In 41 consecutive patients, they found 95% of segments rated as valuable, with 54.6% of coronary segments rated to have excellent image quality. Non-diagnostic image quality was caused by severe coronary motion or stair-step artefacts due to slice misalignment. The most relevant impact of coronary artery image quality was determined by patient HR, resulting in only 1.1% of nondiagnostic coronary segments in patients with HR <63 bpm compared with 14.8% in patients with HR >63 bpm. Overall ED was 2.1 mSv. Similarly Herzog et al. [30] found a feasibility of 96%, and patient-based analysis revealed sensitivity, specificity, positive predictive value (PPV), and negative predictive value (NPV) of 100, 83.3, 90, and 100%, respectively, using prospective ECG triggering, with a mean ED of 2.1 mSv. Both studies used 100 kVp in patients with BMI <25 and the smallest window at only one distinct end-diastolic phase of the RR cycle (usually 75% of cardiac cycle) due to the very low HR at the moment of scan. Notably, mean BMI is usually higher in patients with suspicion of CAD, and a low HR or low HR variability, which are mandatory for the use of prospective ECG triggering with the shortest padding duration, remains a challenge in clinical practice. Maruyama et al. [24] showed similar feasibility, sensitivity, specificity, and accuracy between prospective and retrospective ECG triggering with 64-slice MDCT in a patient-based analysis (86, 100, 92, and 95% versus 85, 96, 94, and 95%, respectively), with a reduction of ED by 79% (4.3 versus 21.1 mSv, respectively). The ED of prospective ECG triggering in their study was higher than that in the previous reports [23, 30]. HR variability of patients in their study was more remarkable than that in the previous reports, and average padding time of 30.4 ms was added according to the grades of HR variability to determine an optimal time period during the diastolic phase in patients with HR variations during which to minimize the stair-step artifacts. This resulted in an increase in dose exposure.

Pontone et al. [25] compared accuracy and ED of prospective versus retrospective ECG triggering in a randomized study. They found a mildly lower feasibility (96 versus 97%, $p < 0.01$) and accuracy in a segment-based analysis (91 versus 94%, $p < 0.01$) and similar accuracy in a patient-based model (98 versus 98%). A 72% reduction (from 20.5 to 5.7 mSv) of ED was observed with prospective ECG triggering. Moreover, when the shortest padding was used, ED was further reduced to an average dose as low as 3.8 mSv. As in the study by Maruyama et al. [24], radiation dose was slightly higher than that reported in published data, likely because individual adaptation of effective tube current and kilovoltage was not used and because only 4% of the population was studied with the shortest padding. LaBounty et al. [31] showed a positive linear relationship between padding duration and radiation exposure (−43% per 100 ms padding decrease) without differences in per-patient or per-artery image interpretability between groups stratified by padding duration. Although theoretically having fewer phases available might have resulted in lower diagnostic interpretability, this is mainly true when padding 200 is used, because 40–80% of cardiac phases are available. Conversely, when padding 100 is used, only two cardiac phases (70 and 80%) are available, with a limited influence on number of artefacts and, therefore, on overall feasibility [21].

The performance of prospective ECG-triggering was tested in a multicenter study design in the Protection III study [32], where 400 patients with low and stable HRs were randomized to either an axial or a helical coronary CTA scan protocol with a primary end-point of non inferior image quality when compared with the axial scan protocol and a second endpoint of lower radiation dose. The mean image quality score was 3.36 in the cohort scanned with prospective ECG-triggered axial acquisition and 3.37 in patients scanned with retrospective ECG-gated helical acquisition. Nondiagnostic coronary CTA studies were observed in 13.0 and 11.5% of axial and helical scans, respectively. Mean ED was significantly lower for the axial (3.5 mSv) than for the helical (11.2 mSv) scan protocol, corresponding to a 69% reduction in estimated ED for the axial scan protocol. In a subgroup analysis of patients scanned with a 100 kVp protocol, ED was reduced by 72% for axial versus helical scanning (2.2 versus 7.9 mSv).

5.5.4 Dual Source Computed Tomography

In the previous section we discussed the role of prospective ECG-triggering in the reduction of ED. Although prospective ECG triggering is a robust tool for reducing radiation exposure, low and stable HRs are mandatory to reach good image quality and therefore diagnostic accuracy. In high-HR settings, DSCT seems to provide better ED reduction. Fang et al. [33] found a similar percentage of evaluable coronary artery segments regardless the HR using a DSCT with retrospective ECG triggering, providing a lower ED at higher HR in comparison with ED of patients with a low HR. Indeed, because pitch increases with HR increase, it decreases scan time and therefore ED. This means that the benefits of DSCT are partially neglected in patients with a low HR but seem impressive at a higher HR.

A second advantage of DSCT is that the combination of these scanners and prospective ECG triggering, due to the higher temporal resolution versus single-source MDCT, seems to better tolerate HR increase and variability despite the use of axial scanning. This is a critical issue because, as previously described, HR >65 bpm precludes implementation of prospective scanning because only a narrow, predefined reconstruction interval is available with this technique. Stolzmann et al. [34] showed no significant difference in the rate of nonassessable coronary segments between DSCT with prospective (1.6%) and retrospective (1.4%) ECG triggering. However, mean effective radiation dose of prospective ECG-gated MDCT was significantly smaller than that of retrospective ECG-gated MDCT (2.2 versus 8.1 mSv). Of

note in almost all studies with DSCT and prospective ECG triggering, the HR identified as exclusion threshold was higher (up to 70–75 bpm) in comparison with previous studies with single-source MDCT and prospective ECG triggering.

5.5.5 256- and 320-MDCT Scanner

The development of wide-area coverage MDCT is an alternative to DSCT to overcome 64-slice single-source scanners. Mori et al. [17] showed effective doses for male and female phantoms were similar, with mean values of 14.1 mSv for the 256-slice MDCT in nonspiral, whole-organ imaging, 22.7 mSv for the 16-slice MDCT, and 27.8 mSv for the 64-slice MDCT, both with retrospective ECG triggering and without a dose-modulation approach. ED with the 256-slice scanner was approximately 38 and 49% less, respectively, than for the 16- and 64-slice scanners.

Rybicki et al. [18] found a lower dose in patients studied with 326-slice and prospective ECG triggering versus 326-slice and retrospective ECG triggering (6.7 versus 12.6 mSv) modalities, with similar imaging quality. As multiple cycles are needed to depict coronary arteries when helical scanning is employed, wide-coverage scanners have advantage in terms of continuity of coronary artery images. The inferior anatomic coverage of 64-slice scanners compared with these systems leads to increases in scan times, contrast-medium dose, and image artefacts in proximal segments of coronary arteries. Covering the entire heart with two to three acquisitions using 256- or 320-slice MDCT, only one or two transition zones between axial acquisition slabs are present compared with the two to four zones using 64-slice MDCT, thus reducing the potential for stair-step artefacts. Therefore, this system potentially enables prospective scanning beyond these thresholds and thus the possibility that more patients could have been included in the prospective group. In patients with a HR >65 bpm, radiation dose was significantly greater with the 320-slice than with the 64-slice scanner (8.7 versus 5.8 mSv). This occurs when HR increases to >65 bpm/min, as the scanner automatically changes from single- to multi segment reconstruction, capturing the heart in two beats and thus doubling the ED [18].

Similarly, Dewey et al. [35] showed in 30 patients studied with 320-slice MDCT-CA sensitivity and specificity of 100 and 94%, respectively, in a patient-based analysis and 89 and 96%, respectively, in a vessel-based analysis. NPV on the per-segment, per-vessel, and per-patient levels were 99, 98, and 100%, respectively. Mean ED was 4 mSv. As in previous reports, radiation exposure reduction was greatest in patients with HRs <65 bpm, whereas ED was significantly higher in those with higher HRs because of the need to acquiring data over multiple cardiac cycles to increase temporal resolution.

5.5.6 Adaptive Statistical Iterative Reconstruction Algorithm (ASIR)

Until 2008, regardless of the scanner used, application of low tube voltage and current in a large population remained a challenge. Since the introduction of adaptive or—more recently—hybrid iterative reconstruction algorithms, more patients could have been included in low tube current and voltage studies, in comparison with only 4% of patients studied with 100 kVp in the Protection I study [27]. The Estimated Radiation Dose Reduction using Adaptive Statistical Iterative Reconstruction in Coronary CT Angiography (ERASIR) study [20] shows that examinations performed using ASIR had lower median tube parameter settings than those obtained using FBP (2.3 versus 4.1 mSv), with a 44% reduction in median radiation dose without differences between FBP and ASIR for interpretability per coronary artery (98.5 versus 99.3%) or per patient (96.1 versus 97.1%). One further advantage of low tube voltage is the possibility of reducing the total amount of contrast agent due to the increased contrast attenuation associated with low tube voltage. Of note,

very low tube voltage may increase blooming artefacts from coronary calcifications and metallic stents. Therefore, further studies are needed to evaluate the effect of these algorithms on calcifications and coronary stents.

5.5.7 Meta-Analysis

Several meta-analyses have been published regarding the balance between ED reduction and accuracy. Pontone et al. [2] show that overall accuracy was 95% and mean ED was 10.4 mSv. The old-generation scanners showed the lowest feasibility compared with more recent technology. Similarly, 64-slice scanners with prospective ECG triggering showed a lower feasibility versus DSCT with retrospective ECG triggering and 320-slice scanners. The 4- and 40-slice scanners showed the worst diagnostic accuracy versus all other technologies, whereas 64-slice scanners with prospective ECG triggering showed lower diagnostic accuracy than DSCT, regardless of the ECG gating protocol used. However, no difference was found in terms of diagnostic performance between 64-slice MDCT with prospective ECG triggering versus DSCT or 320-slice scanners when a low HR was reached. ED below the safety threshold of 10 mSv, as recommended by the American Heart Association, was achieved by old-generation scanners including 4- and 40-slice scanners (8.6 mSv), 64-slice scanners with prospective ECG gating (4.6 mSv), DSCT with retrospective (10 mSv) and prospective (2.5 mSv) ECG gating, and 320-slice scanners (4.2 mSv). In the multivariate analysis, DSCT, low tube voltage, and prospective ECG triggering provided a reduction of 35, 43, and 84% in ED, respectively. In their meta-analysis, according to predetermined selection criteria, no studies using 64-slice MDCT without modulation dose were available, and therefore, no inference concerning ED reduction of this system could be drawn. Moreover, at the time of the meta-analysis, no study using ASIR or Flash Spiral imaging meeting the predetermined inclusion criteria was available. Another, more recent, meta-analysis [36] showed that tube modulation, low tube voltage, and prospective ECG triggering are the most robust techniques to attain ED reduction, producing an ED decrease by 20 and 50% depending on HR, 33–48% and 66–73%, respectively.

Finally, in view of the multiplicity of available techniques, the experience of radiologist and/or cardiologist seems to play a crucial role. Raff et al. [37] tested the effect of a collaborative ED reduction educational program in clinical practice. In a total of 4,863 consecutive patients undergoing MDCT, they compared overall ED and image quality of coronary arteries between the control and follow-up periods after focusing on minimizing scan range, reducing HR using beta-blockade, ECG-gated tube-current modulation dose, and reduced tube voltage. The estimated mean ED was reduced by 53.3%, from 21 to 10 mSv, without significant changes in image quality. Of note, the greatest reduction in dose occurred at low-volume sites (<30 MDCT-CA performed each month). Similarly Labounty et al. [38] evaluated 80 consecutive patients from three sites. All sites initially used nonstandardized protocols; two sites then initiated a standardized protocol, and one site continued its nonstandardized protocol as a time-overlapping control. There were no statistically significant differences between protocols in sensitivity, specificity, or accuracy on a per-patient, per-artery, or per-segment level with ED reduced by 65% (from 5.7 to 2.0 mSv), thus reassuring practicing physicians that radiation-dose decrease by a standardized protocol permits retention of high diagnostic accuracy for MDCT.

5.6 Patient Preparation and Contrast Agent Protocol

Despite this point is beyond the aim of this chapter, a brief summary regarding patient preparation and scan protocol is mandatory. Because of the limited temporal resolution of MDCT, low heart rates are desirable to avoid motion artifacts. Indeed, even though heart rate lowering depends on the temporal resolution of

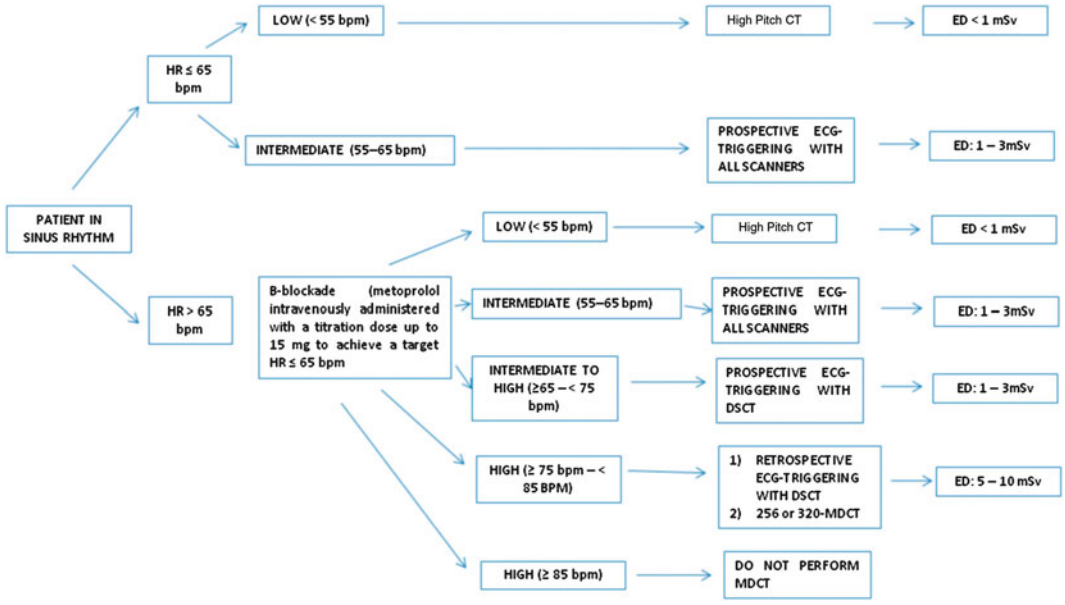

Fig. 5.6 Work-up decision making for the choice of protocol and scanner most appropriate to obtain the best compromise between accuracy and diagnostic radiation exposure. The effective doses reported are estimated considering the use of 100 kVp tube voltage in patients with BMI < 30 and 120 kVp tube voltage in patients with BMI ≥ 30. *ED* effective radiation dose, *HR* heart rate

the scanner used, a target HR<65 bpm is always desirable. This aim is achieved through oral administration of b-blockade 60-90 minutes before the scan or intravenous administration, immediately before the scan or both. Besides, as the use of nitroglycerin has been shown to improve image quality, the administration of sublingual nitrates immediately before the scan to achieve maximum coronary vasodilatation is usually suggested.

Concerning the contrast agent injection protocol, two different approaches are possible: a) bolus tracking protocol in which the patient received a high-concentration volume (ranging between 60-90 mL) of low-osmolar and non-ionic contrast medium at a high rate infusion (5-6 mL/sec), followed by saline solution. In this protocol the scan begins when a pre-defined contrast attenuation threshold in a region of interest (generally left atrium or ascending aorta) is reached; b) test bolus protocol in which a low amount of contrast agent is injected followed by saline solution to calculate the time to peak in the region of interest. Even though the bolus tracking is faster and more reliable, the "test bolus" allows a more precise scan delay.

Figure 5.6 shows a practical work-up to choose the best protocol and scanner based on the patient's characteristics, according to the ALARA principle. The first mandatory condition is that the patient is in sinus rhythm. The second step is to evaluate the HR of the patients. If there is no contraindication, we suggest to treat all patients with HR ≥ 65 bpm and without contraindications to B-bockades using with metoprolol intravenously administered, with a titration dose up to 15 mg to achieve a target HR ≤ 65 bpm. After 5 minutes a new HR evaluation is performed choosing the scanner and the type of ECG-triggering as shown in Figure 5.6. The effective doses reported in the figure are estimated considering the use of 100 kVp tube voltage in patients with BMI < 30 and 120 kVp tube voltage in patients with BMI ≥ 30.

5.7 Conclusions

Diagnostic value of MDCT-CA in CAD has improved significantly with technological developments in MDCT techniques, leading to increased application of MDCT in cardiac imaging. Because radiation exposure with cardiac MDCT is high, it is essential to use radiation-dose-reduction strategies whenever possible. With the latest MDCT scanners achieving high diagnostic accuracy, radiation-dose reduction has become a major concern to clinicians and manufacturers. Furthermore, awareness among clinicians to reduce radiation doses because of the risks associated with radiation has increased.

To this end, careful selection of scanning protocols is needed to keep radiation exposure as low as reasonably achievable while producing high-quality images. Thus, MDCT-CA should be performed using new dose-saving scanning techniques, such as ECG-controlled dose modulation, BMI-adapted scanning protocols, prospective ECG gating, ASIR, and fast scanners such as dual-source MDCT, 320-slice scanners or Flash Spiral MDCT. Of note, use of these techniques is possible without impairing imaging feasibility and diagnostic accuracy. Future research should focus on newer patient- and technology-based methods to achieve the maximal radiation-dose reduction while maintaining diagnostic image quality.

References

1. Picano E (2005) Economic and biological costs of cardiac imaging. Cardiovasc Ultrasound 25:3–13
2. Pontone G, Andreini D, Bartorelli AL, et al (2012) Radiation dose and diagnostic accuracy of multidetector computed tomography for the detection of significant coronary artery stenoses a meta-analysis. Int J Cardiol 160:155–164
3. Hausleiter J, Meyer T, Hadamitzky M, et al (2006) Radiation dose estimates from cardiac multi slice computed tomography in daily practice: impact of different scanning protocols on effective dose estimates. Circulation 113:1305–1310
4. Mettler FA Jr, Thomadsen BR, Bhargavan M, et al (2008) Medical radiation exposure in the, U. S. in 2006: preliminary results. Health Phys 95:502–507
5. International commission on radiological protection (1991) Radiological protection in biomedical research. Pergamon Press, UK
6. Preston DL, Ron E, Tokuoka S, et al (2007) Solid cancer incidence in atomic bomb survivors: 1958–1998. Radiat Res 168:1–64
7. Cardis E, Vrijheid M, Blettner M et al (2007) The 15-country collaborative study of cancer risk among radiation workers in the nuclear industry: estimates of radiation related cancer risks. Radiat Res 167:396–416
8. Brenner DJ, Hall EJ (2007) Computed tomography–an increasing source of radiation exposure. N Engl J Med 357:2277–2284
9. Gerber TC, Kantor B, McCollough CH (2009) Radiation dose and safety in cardiac computed tomography. Cardiol Clin 27:665–677
10. Gibbons RJ, Miller TD, Hodge D, Urban L, Araoz PA, Pellikka P, McCully RB (2008) Application of appropriateness criteria to stress single-photon emission computed tomography sestamibi studies and stress echocardiograms in an academic medical center. J Am Coll Cardiol 51:1283–1289
11. European Commission (2000) European guidelines on quality criteria for computed tomography, EUR 16262EN. Office for Official Publications of the European Communities, Luxembourg
12. Geleijns J, Joemai RM, Dewey M, de Roos A, Zankl M, Cantera AC, Artells MS (2011) Radiation exposure to patients in a multicenter coronary angiography trial (CORE 64). AJR Am J Roentgenol 196:1126–1132
13. International Commission on Radiological Protection (2007) Recommendations of the international commission on radiological protection (ICRP Publication 103). Ann ICRP 37:1–332
14. Achenbach S, Ropers U, Kuettner A, et al (2008) Randomized comparison of 64-slice single- and dual-source computed tomography coronary angiography for the detection of coronary artery disease. JACC Cardiovasc Imaging 1:177–186
15. McCollough CH, Primak AN, Saba O, et al (2007) Dose performance of a 64-channel dual-source CT scanner. Radiol 243:775–784
16. Ropers U, Ropers D, Pflederer T, et al (2007) Influence of heart rate on the diagnostic accuracy of dual-source computed tomography coronary angiography. J Am Coll Cardiol 50:2393–2398
17. Mori S, Nishizawa K, Kondo C, Ohno M, Akahane K, Endo M (2008) Effective doses in subjects undergoing computed tomography cardiac imaging with the 256-multi slice CT scanner. Eur J Radiol 65:442–448
18. Rybicki FJ, Otero HJ, Steigner ML, et al (2008) Initial evaluation of coronary images from 320-detector row computed tomography. Int J Cardiovasc Imaging 24:535–546
19. Hara AK, Paden RG, Silva AC, Kujak JL, Lawder HJ, Pavlicek W (2009) Iterative reconstruction

technique for reducing body radiation dose at CT: feasibility study. AJR Am J Roentgenol 193:764–771
20. Leipsic J, Nguyen G, Brown J, Sin D, Mayo JR (2010) A prospective evaluation of dose reduction and image quality in chest CT using adaptive statistical iterative reconstruction. AJR Am J Roentgenol 195:1095–1099
21. Pontone G, Andreini D, Bartorelli AL, et al (2012) Feasibility and diagnostic accuracy of a low radiation exposure protocol for prospective ECG-triggering coronary MDCT angiography. Clin Radiol 67:207–215
22. Achenbach S, Marwan M, Schepis T, et al (2009) High-pitch spiral acquisition: a new scan mode for coronary CT angiography. J Cardiovasc Comput Tomogr 3:117–121
23. Husmann L, Valenta I, Gaemperli O, et al (2007) Feasibility of low-dose coronary CT angiography: first experience with prospective ECG-gating. Eur Heart J 29:191–197
24. Maruyama T, Takada M, Hasuike T, Yoshikawa A, Namimatsu E, Yoshizumi T (2008) Radiation dose reduction and coronary accessability of prospective electrocardiogram-gated computed tomography coronary angiography: comparison with retrospective electrocardiogram-gated helical scan. J Am Coll Cardiol 52:1450–1455
25. Pontone G, Andreini D, Bartorelli AL, et al (2009) Diagnostic accuracy of coronary computed tomography angiography: a comparison between prospective and retrospective electrocardiogram triggering. J Am Coll Cardiol 54:346–355
26. Paul JF, Abada HT (2007) Strategies for reduction of radiation dose in cardiac multi slice CT. Eur Radiol 17:2028–2037
27. Hausleiter J, Meyer T, Hermann F, et al (2009) Estimated radiation dose associated with cardiac CT angiography. JAMA 301:500–507
28. Bischoff B, Hein F, Meyer T, Hadamitzky M, Martinoff S, Schömig A, Hausleiter J (2009) Impact of a reduced tube voltage on CT angiography and radiation dose: results of the Protection I study. JACC Cardiovasc Imaging 2:940–946
29. Hausleiter J, Martinoff S, Hadamitzky M, et al (2010) Image quality and radiation exposure with a low tube voltage protocol for coronary CT angiography results of the Protection II Trial. JACC Cardiovasc Imaging 3:1113–1123
30. Herzog BA, Husmann L, Burkhard N, et al (2008) Accuracy of low-dose computed tomography coronary angiography using prospective electrocardiogram-triggering: first clinical experience. Eur Heart J 29:3037–3042
31. Labounty TM, Leipsic J, Min JK, Heilbron B,Mancini GB, Lin FY, Earls JP (2010) Effect of padding duration on radiation dose and image interpretation in prospectively ECG-triggered coronary CT angiography. AJR Am J Roentgenol 194:933–937
32. Hausleiter J, Meyer TS, Martuscelli E, et al (2012) Image quality and radiation exposure with prospectively ECG-triggered axial scanning for coronary CT angiography: the multicenter, multivendor, randomized Protection-III study. JACC Cardiovasc Imaging 5:484–493
33. Fang XM, Chen HW, Hu XY, et al (2010) Dual-source CT coronary angiography without heart rate or rhythm control in comparison with conventional coronary angiography. Int J Cardiovasc Imaging 26:323–331
34. Stolzmann P, Goetti R, Baumueller S, et al (2011) Prospective and retrospective ECG-gating for CT coronary angiography perform similarly accurate at low heart rates. Eur J Radiol 79:85–91
35. Dewey M, Zimmermann E, Deissenrieder F, et al (2009) Non invasive coronary angiography by 320-row computed tomography with lower radiation exposure and maintained diagnostic accuracy: comparison of results with cardiac catheterization in a head-to-head pilot investigation. Circulation 120:867–875
36. Sabarudin AJ (2012) A systematic review of radiation dose associated with different generations of multidetector CT coronary angiography. J Med Imaging Radiat Oncol 56:5–17
37. Raff GL, Chinnaiyan KM, Share DA, et al (2009) Advanced cardiovascular imaging consortium co-investigators. Radiation dose from cardiac computed tomography before and after implementation of radiation dose-reduction techniques. JAMA 301:2340–2348
38. LaBounty TM, Earls JP, Leipsic J, et al (2010) Effect of a standardized quality-improvement protocol on radiation dose in coronary computed tomographic angiography. Am J Cardiol 106: 1663–1667

How to Reduce the Radiation Burden in Cardiac SPECT

6

Assuero Giorgetti and Dario Genovesi

6.1 Introduction: Living at the Time of "The Radiation Issue"

Cardiac imaging techniques incorporating ionizing radiation have improved the ability of cardiologists to assess and treat cardiovascular diseases. As a consequence, the number of radiological and nuclear medicine exams continues to grow. In the United States, the number of myocardial perfusion imaging studies has grown from <3 to 10 million exams per year over a 12-year period (from 1990 to 2002) [1]. Similarly, cardiac catheterization procedures showed a 9% increase from 2002 to 2006 [2], and cardio-computed tomography (cardio-CT) and the use of hybrid imaging is expected to rise dramatically in the next decades [3]. Despite the paucity of available data, it is likely that the US trend reflects a wider one that concerns all industrialized countries in the Western world. This growth in medical "ionizing" imaging has raised the issue of whether the increase in radiation exposure, even at the low levels used, is associated with an augmented risk of cancer. From a single diagnostic procedure, such risk is certainly low, but on a population basis, cancers become more likely as the number of performed procedures increases. Approximately 10 years ago, the "linear-no threshold" model was brought to the attention of the cardiological community. This model in radioprotection assumes that no safe dose exists; the risk increases linearly with increasing radiation dose; all doses add up in determining cancer risk. Although there are no data showing that ionizing medical studies have actually increased the incidence of cancer, the radiation issue induced the American College of Cardiology Foundation to emphasize that "the responsibility of all physicians is to minimize the radiation injury hazard to their patients, to their professional staff and to themselves" [4]. Moreover, as suggested by the US Food and Drug Administration (FDA) in 2010, all physicians should make every effort to see that "each patient should get the right imaging exam, at the right time, with the right radiation dose" [5]. Undoubtedly, adhering to indications for exams may be one possible solution for reducing radiation burden to the patient. Another possible strategy is to perform, whenever possible, stress-only clinical protocols, thus avoiding radiotracer administration at rest. Nevertheless, it appears clear that the technology used until today is often inadequate to satisfy the ethical and socioeconomic aspects of modern medicine.

In light of this, and in trying to overcome the well-known limitations of conventional nuclear imaging, important innovations in hardware and

A. Giorgetti (✉) · D. Genovesi
Department of Nuclear Medicine, Fondazione Toscana Gabriele Monasterio, Pisa, Italy
e-mail: asso@ftgm.it

D. Genovesi (✉)
e-mail: dgenovesi@ftgm.it

P. Marzullo and G. Mariani (eds.), *From Basic Cardiac Imaging to Image Fusion*,
DOI: 10.1007/978-88-470-2760-2_6, © Springer-Verlag Italia 2013

software have emerged. This evolution in technology may revolutionize the practice of nuclear cardiology and substantially reduce the importance of these drawbacks. In fact, these improvements in imaging camera engineering, image acquisition protocols, and image post-processing analysis promise to substantially reduce patient radiation exposure while ameliorating imaging quality and diagnostic accuracy.

6.2 Advances in Single-Photon-Emission Computed Tomography Cameras

Conventional gamma cameras with parallel-hole collimators, coupled with filtered backprojection reconstruction algorithms, have been used for >30 years and, since the mid-1970s, stress myocardial perfusion imaging (MPI) has become the most frequently used test to noninvasively image the heart. Despite its clinical success, conventional single-photon-emission computed tomography (SPECT) (C-SPECT) cameras have suffered of important technical limitations, such as suboptimal system sensitivity and low spatial and energy resolutions. Strategies to partially overcome these limitations have been the use of radiotracers with better energy spectrum [such as technetium-99 m (^{99}Tc)-labelled radiotracers versus thallium-201], longer acquisition times, and greater dose injection. Despite the increase in count statistics and image quality, these strategies, especially the last two, pay a price in terms of augmented discomfort (often generating technical artifacts) and radiation burden to the patient. Software improvements in iterative reconstruction algorithms have been implemented permitting consideration of the loss of resolution with distance inherent in parallel-hole collimators and development of mathematic correction of resolution degradation (resolution recovery) [6–8]. Furthermore, to definitely eliminate the limitations linked to the physics of standard SPECT, manufacturers began creating innovative dedicated cardiac cameras in which detectors are arranged to imaging almost exclusively the cardiac field.

6.2.1 Cadmium-Zinc-Telluride Technology

Electromagnetic radiation, such as gamma rays, can interact with a solid-state detector via four mechanisms: elastic scattering, photoelectric absorption, Compton scattering, and pair production. Photoelectric absorption is the ideal process for detector operation. In this process, all the energy of an incident photon is absorbed by one of the orbital electrons of atoms in the detector material. This photoelectron will lose kinetic energy while interacting with the semiconductor, creating many electron–hole pairs. Detecting these charges as a current pulse via an external circuit allows the creation of a histogram of pulse heights—the pulse-height spectrum—the peak due to this interaction being called the photopeak. The output signal is ~50 times greater than the signal amplified in the C-SPECT system by photomultipliers. Specific collimation allows correction for variability in the depth gamma-ray interaction with the solid detector. Thus, the count statistics and energy resolution of the system are dramatically improved. On the other hand, the intrinsic spatial resolution of the cadmium-zinc-telluride (CZT) technology is determined by the combination of pixel size and system geometry. CZT pixels are physically 2.46 × 2.46 mm in size and have negligible crosstalk due to direct conversion to an electrical charge. Each CZT pixel is an independent detector provided with its own electronic processing unit using miniaturized attached electronics. Therefore, the system is capable of linear detection response even at very high count rates, with high spatial resolution. As collimated detectors are usually arranged to simultaneously explore the entire cardiac field of view, and data are acquired in list mode, imaging is a true 3D positron emission tomography (PET)-like modality.

The first camera built with solid-state detectors was D-SPECT by Spectrum Dynamics [9] and uses an array of nine crystals arranged in a curved configuration to conform to the left side of the patient's chest. The detectors are collimated with square, parallel-hole, tungsten

collimators shorter and with larger holes than those used in standard cameras, resulting in an acceptance solid angle approximately eight times greater, with a substantial increase in count sensitivity. Each collimated detector column rotates and translates independently, allowing the object of interest to be viewed from hundreds of different angles. The patient is positioned on a dentist-like chair, and images are acquired in a reclining position. Images are then reconstructed using an iterative algorithm that compensates for the loss of spatial resolution that results from using large-hole collimators. This is achieved by mathematical modeling of the acquisition and collimator geometry.

The second innovative CZT-based camera, developed by GE Healthcare (Discovery NM530c), exploits the Alcyone Technology that comprises an array of 19 pinhole collimators, each with four solid-state CZT pixilated detectors [10]. Nine of the 19 detectors are oriented perpendicular to the chest's long axis and five are angulated above and five below the axis. The views are simultaneously acquired in list mode and in true 3D acquisition geometry, with an important increase in system sensitivity, and permitting both dynamic studies and reduction of possible motion artifacts. In the hybrid system (Discovery NM570c), a volumetric CT permits attenuation correction algorithms with a further increase in regional count statistics. The patient is positioned on the Alcyone camera bed, and images can be acquired in the supine or prone position and then reconstructed using a modified iterative algorithm that combines accurate modeling of the camera's geometric and physical characteristics with optimized statistical techniques. In comparison with C-SPECT, Alcyone Technology shows better system sensitivity (up to ten times greater, Fig. 6.1), energy resolution (5.7 versus 9.4%), and spatial resolution (5 versus 11 mm).

6.2.2 Other SPECT Cameras

Conventional SPECT devices can be improved to the multipinhole SPECT approach. Eagle Heart Imaging (Westminster, CO, USA) has integrated multipinhole methodology with the Emory Reconstruction Toolbox (Syntermed, Atlanta, GA, USA) to provide a commercial multipinhole upgrade product called MP-SPECTTM for existing dual-head SPECT gamma cameras, permitting an up to fivefold increase in counts statistic with spatial resolution comparable with that of a C-SPECT [11].

Another camera completely new in design (CardiArc, Canton, MI, USA) [12] exploits thallium-activated sodium iodide [NaI(Tl)] crystals, although this system was originally designed to use arrays of CZT crystals as detectors. However, due to high costs and potential long-term stability issues with CZT, the detector material was changed to enable commercial production. The system uses three side-by-side curved detectors with 60 photomultiplier tubes arranged in three rows to cover 180°. Horizontal collimation is obtained by means of a curved lead sheet with six vertical slots (aperture arc), with a movement synchronized electronically with the six areas of crystals that are imaging the photons passing through the slots. Vertical collimation is achieved using stationary lead vanes, which are placed vertically between aperture arc and crystal. Data are collected in 1 mm-thick slices using the six vertical apertures to collimate photons so that they are detected continuously across the detector surface, with no overlap of data from different apertures. During acquisition, the aperture arc rotates to acquire data from multiple projections, providing 1,280 angular samples in 0.14° increments over 180°, which is a factor of 21 greater than a conventional camera angular sampling (typically 3°). All detector pixels are active simultaneously, and photons are detected from multiple angles, which provide high-efficiency imaging. Movement of the aperture arc is synchronized electronically with the areas of NaI(Tl) crystals, which are imaging the photons passing through the individual slots. There is no visible movement of the acquisition system, and the patient is imaged in upright position with arms over the detector. These imaging systems can acquire a SPECT study in 2–8 min, with increased count sensitivity and image quality.

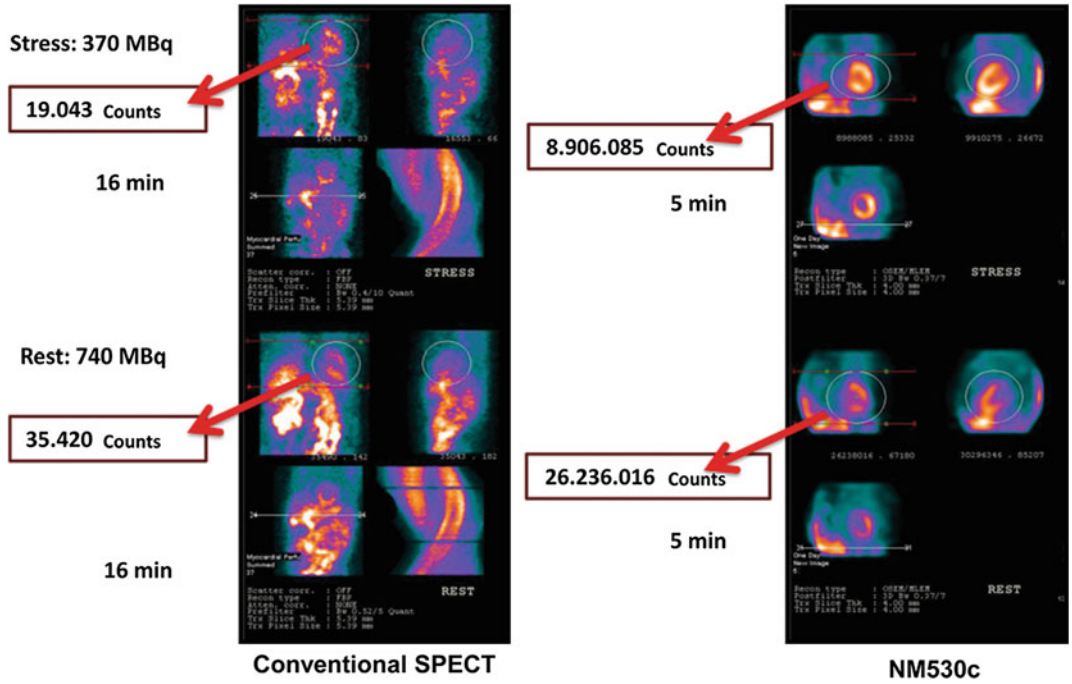

Fig. 6.1 Raw data obtained using a conventional single-photon-emission computed tomography (SPECT) camera (*left*) and a cadmium-zinc-telluride (CZT) device (*right*) and standard doses of technetium-99m (^{99m}Tc)-tetrofosmin. The emerging technology (CZT device) has dramatically increased sensitivity and myocardial count statistics while significantly reducing imaging time

Other cameras have been implemented that modify electronics, system geometry, or collimation of rotating SPECT devices. Cardio 3 XPO, developed by Digital, uses pixilated, thallium-activated cesium iodine [CsI(Tl)] and photodiodes to configure detector heads that are more compact than those of conventional cameras. Each detector head is 21.2 × 15.8 cm and contains an array of 768 6.1 × 6.1 × 6 mm thick CsI(Tl) crystals coupled to individual silicon photodiodes. Digital Anger electronics are used to create planar projection images for reconstruction [13]. In the three-detector system, detector heads are positioned at 67.5° between heads. The patient is positioned on a chair with arms placed on an arm rest above the detectors, and camera heads can be moved closer to or farther away from the patient. Acquisition is obtained by rotating the patient chair by 67.5°, producing a total acquisition arc of 202.5°. With this system, the manufacturer reports a reconstructed spatial resolution of 8.95 mm and a sensitivity of 234 cpm/μCi using the system's cardiac collimator and a 3D version of the ordered subsets expectation maximization (OSEM) approach for reconstruction. Typical acquisition times are 7.5 min, with up to 38% more count sensitivity than with conventional dual-head systems and with comparable image quality.

Finally, increased system sensitivity and spatial resolution have been obtained by Siemens with IQ•SPECT, which consists of three components: an astigmatic collimator, an optimized organ acquisition, and iterative reconstruction. Two collimators are mounted on camera heads separated by 90° and rotate around the patient to obtain a 180° reconstruction arc. The astigmatic collimation is an evolution of the previously developed cardiofocal concept [14], with the fields of view of these collimators most convergent at their center and relaxed toward the edge. The astigmatic collimation magnifies the heart while increasing the number of detected

events. It is combined with an iterative reconstruction algorithm based on Flash3D [15], which takes into account the altered geometry. IQ•SPECT reconstruction also includes distant dependent isotropic (3D) resolution recovery, CT-based attenuation correction, and energy-window-based scatter correction. Image acquisition time can be as short as 4 min.

6.3 Advances in Reconstruction Software

In C-SPECT, patient data is acquired in a series of 2D images, or projections, and are backprojected in the reconstruction process into a virtual 3D space, yielding an image or a series of images very similar to the real 3D distribution of the radioisotope within the body. Filtered backprojection is, however, affected by various artifacts caused by variations in attenuation, scatter, resolution, and count density. To bypass these limitations, new proprietary algorithms based on maximum likelihood expectation maximization (MLEM) [16] and accelerated method of OSEM [17] have been introduced. Moreover, scatter and attenuation compensation and resolution recovery techniques can be incorporated within iterative reconstruction to correct for losses in spatial resolution due to image blurring by the collimator.

One such new software is Philips Astonish (San Jose, CA, USA), which is based on the OSEM reconstruction method, with noise reduction during the iterative process, and corrections for photon scatter, photon attenuation, and variations in spatial resolution. The result is an improved image contrast, a more accurate representation of myocardial counts that are at different depths inside the patient, and a better spatial resolution. This technique has been used to shorten image acquisition time, resulting in ultrafast imaging when a stress-only attenuation-corrected protocol is performed [18].

Evolution for Cardiac is an innovative SPECT reconstruction package for both gated and nongated ^{99m}Tc-based myocardial perfusion imaging (GE Healthcare, Waukesha, WI, USA), which is a modification of the OSEM algorithm that includes modeling of the collimator and detector response function (CDR) and incorporates resolution recovery [19–21]. Furthermore, the iterative reconstruction algorithm incorporates noise suppression, which is required because resolution recovery amplifies noise, causing artifact hot spots in the final image. The software permits significantly reduced acquisition time while maintaining image quality.

Siemens implemented a new software (Flash3D) incorporating OSEM reconstruction with 3D resolution recovery, 3D CDR, and attenuation and scatter compensation [22]. In healthy patients, Flash3D demonstrates the possibility of reduced acquisition time up to 50%, with no change in normal perfusion distribution [23]. The software, developed for use on Siemens e.cam gamma cameras with new e.soft processing workstations, increases spatial resolution; reduces image noise, distortions, and artifacts; and improves contrast and lesion detection.

UltraSpect, Inc. (Haifa, Israel) developed a standalone workstation (Xpress.cardiac), which utilizes the patented wide-beam reconstruction (WBR) algorithm and employs an iterative image reconstruction process that enables simultaneous resolution and contrast recovery coupled with noise suppression based on an accurate physical modeling of photon emission and detection. The model compensates for the collimator's "beam-spread function" effect and automatically adjusts for the distance from the patient. This system is available as an additional workstation and can reconstruct data from most existing gamma cameras with standard collimators and can be used to either dramatically shorten acquisition time or significantly improve image quality for the same acquisition parameters [24, 25].

6.4 One Face of the Coin: Reducing Imaging Time and Saving Money

Long acquisition time has always been a problem in nuclear medicine, resulting in discomfort for the patient and, often, degraded image quality due

to movement artifacts. In this regard, the concept of fast imaging is relatively recent in nuclear cardiology. Optimized clinical protocols, such as ^{99m}Tc-labelled radiotracers early imaging, or dual isotopes [26, 27], which save time, increase laboratory efficiency, and allow more patients to be studied per day per camera, are highly cost-effective. Moreover, they maintain the advantage of having two sets of images for differentiation of ischemia (reversible abnormality) from scar (irreversible abnormality), for increasing confidence in recognition of artifacts, for assessing nonperfusion variables such as transient left ventricular dilation, and more precise assessment of left ventricular function (both at rest and poststress, with the possibility of identifying myocardial stunning). Alternatively, and with the same goal of saving time and money, the stress-only paradigm has been proposed [28]. This practical approach requires review of stress images as soon as they are completed; if they are unequivocally normal, the rest of the study may be omitted, thus reducing time, costs, and radiation burden to the patient. Obviously, good-quality images and an experienced reader are necessary for this protocol.

Advances in technology applied to nuclear cardiology have opened new and interesting horizons. Although there are differences in hardware and software, all new algorithms have in common a dramatic increase in count statistics and spatial and energy resolution and have been utilized clinically to reduce overall duration of myocardial scintigraphy.

Studies of emerging technology have been validated by comparison with studies performed with the same injected activity during the same patient visit on a conventional dual-head SPECT camera (Table 6.1) [29–37]. Herzog et al. [29] attempted to establish the most optimal imaging time for the CZT multipinhole Discovery NM 530 c detectors in a single-day protocol and found that scans as short as 2 min poststress and 3 min at rest provide images equivalent to 15 min acquisitions with the standard camera using an average total activity of 1,240 MBq ^{99m}Tc-labelled radiotracer. Similarly, high correlations with conventional SPECT were found using standard activities and shorter acquisition times by the Emory University group [30]. In a study from our institute [31], early (acquisition start within 15 min from ^{99m}Tc-tetrofosmin standard activities stress/rest 1 day protocol) and fast (5 min poststress and 4 min at rest scans) imaging using Alcyone Technology was compared with longer C-SPECT acquisition time, and demonstrated a more accurate evaluation of both extent and severity of myocardial ischemia in patients with coronary artery disease (CAD).

The D-SPECT camera was compared with a C-SPECT device; shorter imaging time (4 min stress/2 min rest) and higher image quality was reported with D-SPECT [32]. In another study, a novel stress thallium-201 (^{201}Tl)/rest ^{99m}Tc protocol was compared with a standard ^{99m}Tc/^{99m}Tc protocol on the same fast camera [33]. The authors concluded that the ^{201}Tl/^{99m}Tc protocol offers similar image quality and dosimetry (11.9 versus 11.2 mSv) but also provides a total stress/rest imaging time <20 min. In another large study of D-SPECT, Sharir et al. [34] used fully automated quantitative software with normal limits for their data analysis, demonstrating a high correlation in terms of the extent of perfusion defects with C-SPECT at the same injected activities while significantly reducing imaging time (4 min stress/2 min rest).

In a large, multicenter trial using the nSPEED resolution recovery software and the Cardius 3 system, Maddahi et al. [35] showed that 5 min rest/4 min stress acquisitions yielded perfusion and functional results diagnostically equivalent to full-time acquisition and 2D OSEM iterative reconstruction.

Performing a fast imaging with a conventional camera system (GE, Ventri), using an optimized WBR reconstruction with image resolution recovery and novel approach to noise control, DePuey et al. [36] reported equivalent perfusion defect extent with similar image quality at rest and superior at stress. WBR imaging was four times shorter than the full-time standard OSEM reconstruction.

Table 6.1 Relationship between injected activity, acquisition time, and radiation exposure in published papers

Study	Camera	Radiotracer	Total injected activity (MBq)	Acquisition time (min) stress/rest	Average exposure (mSv)
Herzog [29]	GE NM530c	^{99m}Tc-tetrofosmin	1,254	3/2	9
Esteves [30]	GE NM530c	^{99m}Tc-tetrofosmin	1,480–2,220	4/2	10.7–16
Gimelli [31]	GE NM530c	^{99m}Tc-tetrofosmin	1,110	5/4	7.8
Sharir [32]	D-SPECT	^{99m}Tc-sestamibi	1,443	4/2	11.4
Bermann[33]	D-SPECT	^{201}Tl/^{99m}Tc	92.5/370	6/4	11.9
Sharir [34]	D-SPECT	^{99m}Tc-tetro/mibi	1,480	4/2	10.7
Maddahi [35]	Cardius3/nSpeed	^{99m}Tc-sestamibi	999–1,480	5/4	8.1–12
DePuey [36]	Ultra-SPECT	^{99m}Tc-sestamibi	1,517	4/4.5	12
Corbett [37]	IQ-SPECT	–	–	4/4	–

SPECT single-photon-emission computed tomography

A single-center clinical trial concluded that 4 min attenuation-corrected myocardial perfusion scans with IQ•SPECT provided images of comparable quality and normalcy with 15 min-acquisition standard attenuation-corrected C-SPECT/CT [37].

All these investigations demonstrate that the emerging technology makes it possible to reduce acquisition time for a myocardial perfusion scan from half the conventional time to a minimum 2 min acquisition. This "fast and furious" nuclear cardiology imaging is now a reality that improves patient compliance, increases nuclear laboratory efficiency, and reduces costs.

6.5 The Other Face of the Coin: Reducing Administered Activity and Radiation Burden to the Patient

The key point in determining image quality in nuclear cardiology is the appropriate count statistic into the myocardium for a specific activity of injected radiotracer. From a physics perspective, reducing time or radiotracer administered activity is exactly equivalent. As previously reported, new cameras and software allow a dramatic increase in system sensitivity and detected counts that are in the order of five to eight fold greater. Thus, the administered activity can theoretically be reduced by the same amount with standard imaging times. However, the translation of this assumption into actual practice is not easy, because other factors can determine image degradation (such as movement artifacts for longer acquisition time). Also, prospective assessment of the lowest achievable imaging dose is limited by the need to be conservative to avoid scans that are inadequate for clinical interpretation. The new technology permits list mode acquisition, making it possible to simulate retrospectively a scan with an arbitrary activity from the original full-dose acquisition data. Herzog et al. [29], using retrospective list mode reconstruction, showed that 2 min acquisition time is the lowest limit for preserving image quality using the GE Healthcare ultra-fast cardiac (UFC) scanner; therefore, we could suggest a dose reduction to half the standard dose (Fig. 6.2).

Duval and coworkers [38] studied 131 patients with a BMI <35 kg/m^2 using CZT Alcyone Technology and ^{99m}Tc-sestamibi (5 mCi rest and 15 mCi stress doses). Rest images were processed at 5 and 8 min and stress images at 3 and 5 min acquisition times, and no significant difference in image quality and mean summed scores was found between shorter and longer acquisition times. When compared with a conventional SPECT camera in 27 patients, total rest and stress perfusion deficits and calculated left ventricular ejection fraction (LVEF) results were similar. The effective dose (ED) was

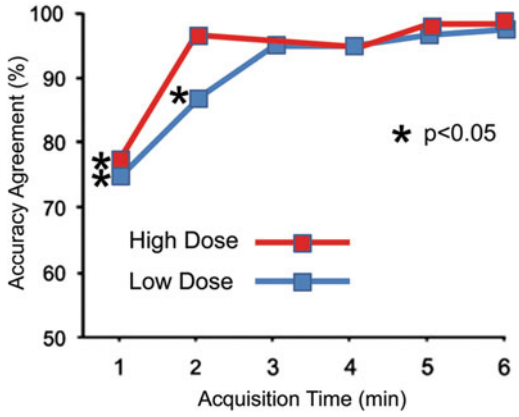

Fig. 6.2 Diagnostic accuracy agreement between a standard camera and a cadmium-zinc-telluride (CZT) device using high (*red squares*) and low (*blue square*) activities of radiotracers. Diagnostic accuracy of CZT increases after scan intervals are prolonged to 3 min for low doses and 2 min for high doses. These results also suggest the possibility of reducing the high activity by one-third and the lower activity by one half if standard acquisition times are maintained (redrawn from [29])

5.8 mSv for this protocol, which is 49.2% less than with conventional ^{99m}Tc studies and 75.7% less than with conventional ^{201}Tl/^{99m}Tc dual isotope studies. Similarly, in a study from our institute [39], we investigated 137 consecutive patients with known or suspected CAD using single-day low-dose stress–rest myocardial UF SPECT perfusion imaging, with invasive coronary angiography as the gold standard. Patients underwent the first scan with a 7 min acquisition time 10 min after the end of the stress protocol (activity range 185–222 MBq of ^{99m}Tc-tetrofosmin). The rest scan (activity range 370–444 MBq of ^{99m}Tc-tetrofosmin) was acquired with a 6 min acquisition time. Overall, the area under the receiver operating characteristic (ROC) curve for the summed stress score values was 0.904, and for each vascular territory was 0.982 for the left anterior descending artery, 0.931 for the left circumflex artery, and 0.889 for the right coronary artery. An example of a patient studied in our institute is shown in Fig. 6.3.

These studies demonstrate the feasibility of a clinical protocol with both reduced acquisition time and radiotracer activity while maintaining a high overall diagnostic performance. In another study, patient dose was reduced to 4.3 mSv for stress/rest protocols using a background activity subtraction algorithm [40]. Comparison between standard- and low-dose background subtracted protocols demonstrated a clinical agreement of 98%, confirming the possibility of significantly reducing radiation exposure while maintaining the diagnostic power of myocardial scintigraphy.

As mentioned, radiation burden to the patient can be reduced by avoiding, when possible, rest imaging, as in the stress-only protocol. If appropriateness criteria for myocardial perfusion imaging are accurately complied with, a reduction of >50% of normal stress studies can theoretically be expected. It is conceivable that the ameliorated imaging characteristics of the emerging scanners can be utilized to obtain high-quality poststress images, possibly reducing the need for rest scans. In a recent study [41], the diagnostic accuracy of a high-speed camera with an automated quantification of total perfusion defect was tested versus invasive coronary angiography. The authors observed that with the combined upright–supine approach, sensitivity for detecting significant CAD was 94% and specificity was 86%. For individual coronary territories, they found a sensitivity and specificity of 70 and 97%, respectively. Results were comparable with those found using the rest/stress ^{99m}Tc-sestamibi or stress ^{201}Tl/rest ^{99m}Tc-sestamibi protocols. Although limited in the sample of patients studied, that paper summarizes the potentiality of emerging technology permitting a very-low-dose (<2.5 mSv), ultrafast (4 min upright acquisition +4 min supine scan) myocardial perfusion scintigraphy. In this respect, a recent investigation [42] studied prospectively 100 patients referred for diagnostic stress imaging. The authors used a CZT camera and a very-low-activity stress sestamibi (1.75 MBq/kg), followed by rest imaging only in the case of equivocal poststress results. Image quality was suitable for clinical interpretation in all exams, and the mean ED at stress was 0.79 mSv for men and 1.02 mSv for women. When rest imaging was performed, the additional mean ED was 3.02 mSv for men and

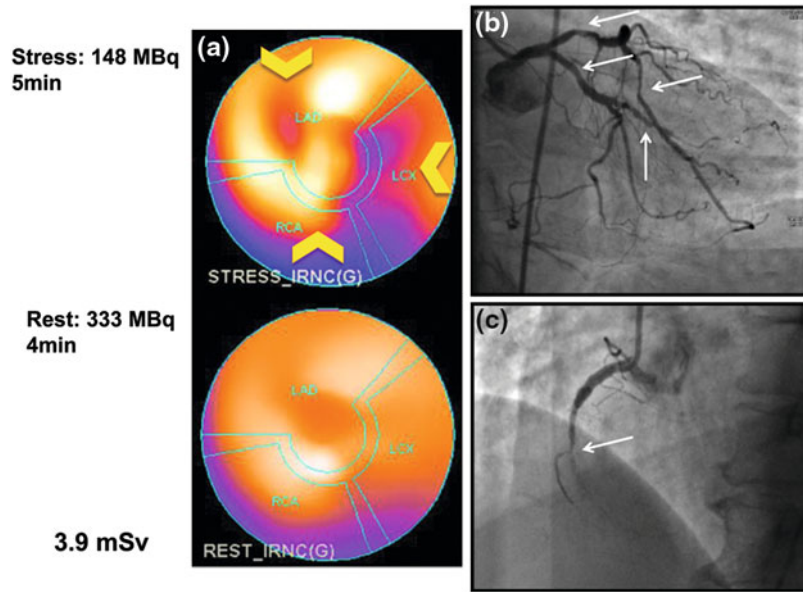

Fig. 6.3 Scintigraphic bull's eye views (**a**) obtained in a 65 year-old patient with typical angina and multivessel coronary artery disease (**b**, **c**). Using a low-activity protocol and reduced scan times, myocardial perfusion images show multiple perfusion defects (*yellow arrows*), in agreement with the coronary anatomy. Patient radiation exposure was <4 mSv

3.89 mSv for women. Therefore, use of CZT technology determined a low radiation burden to the patient, with many cases below 1 mSv.

Thanks to these findings, nuclear cardiology remains an attractive modality for incorporation into multimodality or hybrid imaging systems. Cardiac hybrid imaging allows the combination of morphological information from CT coronary angiography and functional information from myocardial perfusion imaging in the evaluation of CAD. In this respect, ED constitutes an important limitation because of the summation of two sources of risk. Herzog and coworkers [43], in a case report in which hybrid imaging (fused low-activity SPECT low-dose CT angiography), solved the clinical question with an ED for hybrid imaging <3 mSv. Furthermore, they described a novel dose-saving, fast-track hybrid algorithm [44]. The clinical protocol included CT coronary angiography first, followed by a stress-only low-dose myocardial scintigraphy (using Evolution for cardiac software) if a coronary stenosis (≥50% diameter narrowing) or equivocal findings were observed. Only abnormal stress MPI scans were followed by rest perfusion scintigraphy. The mean ED was significantly lower for the individualized (4.8 ± 3.4 mSv) versus the comprehensive (8.1 ± 1.5 mSv) method, resulting in a significant total population radiation dose reduction. These studies, summarized in Table 6.2, and expression of the technological evolution in cardiovascular imaging, need to be validated in larger patient populations, but they indicate the possibility of nuclear cardiology playing a leading role in assessing patients with coronary artery disease in the near future.

6.6 Conclusion: Nuclear Cardiology at the Time of the "Ulysses Syndrome"

Some cardiologists have raised the issue that marketing messages, high patient demand, and defensive medicine lead to the vicious circle of the so-called Ulysses syndrome [45]. Mr. Ulysses, a middle-aged, "worried-well", asymptomatic individual with an A-type coronary personality, a heavy opium smoker, and leading a stressful life, is advised to have a cardiological checkup after 10 years of being at war. After a long journey across imaging laboratories, he has many cardiological exams, with a cumulative radiation dose cost of >100 times a simple exercise-ECG test and a cumulative radiation

Table 6.2 Evidence for reduced radiotracer dose and patient radiation exposure using new camera and software technology

Study	Camera	Radiotracer	Total injected dose (MBq)	Average radioexposure (mSv)
Duvall [38]	GE NM530c	^{99m}Tc-sestamibi	740	5.8
Gimelli [39]	GE NM530c	^{99m}Tc-tetrofosmin	666	5.10 men; 6.12 women
Nkoulou [40]	GE DNM/CT 570c	^{99m}Tc-tetrofosmin	950	4.3
Nakazato [41]	D-SPECT	^{99m}Tc-sestamibi Supine/upright	296–370	2.4
Songy [42]	GE NM530c	^{99m}Tc-tetrofosmin Stress only	1.75/kg	0.79 men; 1.02 women
		Stress/rest		3.02 men; 3.89 women
Herzog [43]	GE NM530c	Low-activity CTA Stress-only ^{99m}Tc	173	2.62
Pazhenkottil [44]	Evolution for Cardiac	Low-activity CTA Stress only ^{99m}Tc	150–200	4.08 ± 3.4

SPECT single-photon-emission computed tomography, ^{99m}*Tc*, technetium-99m

dose of >4,000 chest X-rays, creating a cancer risk of 1 in 100. Mr. Ulysses is tired of useless examinations, exorbitant costs, and unacceptable risks.

Indeed, it is impossible not to agree with Mr. Ulysses. However, one could argue that the issue is not intrinsic to the technology but the way the technology is used. In this regard, this exaggerated metaphor, which is also reductive of modern evidence-based medicine, has the advantage of focusing the cardiologist's attention on the appropriateness of indications in cardiac imaging. Undoubtedly, because any exams—even nonionizing exams—have risks, appropriateness criteria must always guide medical intervention, taking into account risks versus benefits. In the case of nuclear cardiology, there is an additional risk to be considered—the radiation burden to the patient—and every effort should be made to minimize this risk. Advances in hardware and software provide a significant reduction in the ED to the patient, allowing nuclear cardiology to remain appealing to the cardiological community. It is conceivable that in the near future aggressive clinical dose reduction algorithms will be customized to patient age, as radiation risk models assume that risk is inversely proportional to patient age. In this respect, stress-only acquisitions, dynamic imaging, and hybrid multimodality protocols are being explored to further reduce radioactive dose and at the same time improve diagnostic information.

References

1. IMV (2003) Nuclear medicine census market summary report. Des Plaines, IL: IMV Medical Information Division
2. IMV (2006) Cardiac catheterization lab census market summary report. Des Plaines, IL: IMV Medical Information Division
3. IMV (2008) present practices and future directions in cardiac imaging, The Cardiologist's perspective 2008–2011. Des Plaines, IL: IMV Medical Information Division
4. Hirshfeld JW Jr, Balter S, Brinker JA et al (2005) ACCF/AHA/HRS/SCAI clinical competence

statement on physician knowledge to optimize patient safety and image quality in fluoroscopically guided invasive cardiovascular procedures: a report of the American college of cardiology foundation/American heart association/American college of physicians task force on clinical competence and training. Circulation 111:511–532
5. Food and drug administration white paper: initiative to reduce unnecessary radiation exposure from medical imaging. Initiative to reduce unnecessary radiation exposure. http://www.fda.gov/RadiationEmittingProducts/RadiationSafety/RadiationDoseReduction/ucm199994.htm
6. Borges-Neto S, Pagnanelli RA, Shaw LK et al (2007) Clinical results of a novel wide beam reconstruction method for shortening scan time of Tc-99m cardiac SPECT perfusion studies. J Nucl Cardiol 14:555–565
7. Venero CV, Heller GV, Bateman TM et al (2009) A multicenter evaluation of a new bpost-processing method with depth-dependent collimator resolution applied to full and half-time acquisitions with and without AC. J Nucl Cardiol 16:714–725
8. DePuey EG, Gadraju R, Clark J et al (2008) Ordered subset expectation maximization and wide beam reconstruction "half-time" gated myocardial perfusion SPECT functional imaging: a comparison to "fulltime" filtered backprojection. J Nucl Cardiol 15:547–563
9. Gambhir SS, Berman DS, Ziffer J et al (2009) A novel high-sensitivity rapid-acquisition single-photon cardiac imaging camera. J Nucl Med 50:635–643
10. Bocher M, Blevis IM, Tsukerman L et al (2010) A fast cardiac gamma camera with dynamic SPECT capabilities: design, system validation and future potential. Eur J Nucl Med Mol Imaging 37:1887–1902
11. Funk T, Kirch DL, Koss JE et al (2006) A novel approach to multipinhole SPECT for myocardial perfusion imaging. J Nucl Med 47:595–602
12. Patton JA, Slomka PJ, Germano G et al (2007) Recent technologic advances in nuclear cardiology. J Nucl Cardiol 14:501–513
13. Slomka PJ, Patton JA, Berman DS et al (2009) Advances in technical aspects of myocardial perfusion SPECT imaging. J Nucl Cardiol 16:255–276
14. Hawman PC, Haines EJ (1994) The cardiofocal collimator: a variable focus collimator for cardiac SPECT. Phys Med Biol 39:439–450
15. Romer W, Reichel N, Vija HA et al (2006) Isotropic reconstruction of SPECT data using OSEM3D: correlation with CT. Acta Radiol 13:496–502
16. Lange K, Carson R (1984) EM reconstruction algorithms for emission and transmission tomography. J Comput Assist Tomogr 8:306–316
17. Hudson HM, Larkin RS (1994) Accelerated image reconstruction using ordered subsets of projection data. IEEE Trans Med Imaging 13:601–609
18. Bateman TM, Heller GV, McGhie AI et al (2009) Multicenter investigation comparing a highly efficient half-time stress-only attenuation correction approach against standard rest-stress Tc-99m SPECT imaging. J Nucl Cardiol 16:726–735
19. Tsui BMW, Hu HB, Gilland DR et al (1988) Implementation of simultaneous attenuation and detector response correction in SPECT. IEEE Trans Nucl Sci 35:778–783
20. Tsui BMW, Gullberg GT (1990) The geometric transfer-function for cone and fan beam collimators. Phys Med Biol 35:81–93
21. Tsui BMW, Frey EC, Zhao X et al (1994) The importance and implementation of accurate 3D compensation methods for quantitative SPECT. Phys Med Biol 39:509–530
22. Vija AH, Zeintl J, Chapman JT et al (2006) Development of rapid SPECT acquisition protocol for myocardial perfusion imaging. IEEE Nucl Sci Symp Conf Rec 3:1811–1816
23. Ficaro EP, Kritzman JN, Corbett JR (2008) Effect of reconstruction parameters and acquisition times on myocardial perfusion distribution in normals. J Nucl Cardiol 15:S20–S20
24. Borges-Neto S, Pagnanelli RA, Shaw LK et al (2007) Clinical results of a novel wide beam reconstruction method for shortening scan time of Tc-99m cardiac SPECT perfusion studies. J Nucl Cardiol 14:555–565
25. Marcassa C, Campini R, Zoccarato O et al (2011) Wide beam reconstruction for half-dose or half-time cardiac gated SPECT acquisitions: optimization of resources and reduction in radiation exposure. Eur J Nucl Med Mol Imaging 38:499–508
26. Giorgetti A, Rossi M, Stanislao M et al (2007) Feasibility and diagnostic accuracy of a gated SPECT early-imaging protocol: a multicenter study of the myoview imaging optimization group. J Nucl Med 48:1670–1675
27. Berman DS, Kiat H, Friedman JD et al (1993) Separate acquisition rest thallium-201/stress technetium-99m sestamibi dual-isotope myocardial perfusion single-photon emission computed tomography: a clinical validation study. J Am Coll Cardiol 22:1455–1464
28. Iskandrian AE (2010) Stress-only myocardial perfusion imaging. A new paradigm. J Am Coll Cardiol 55:231–233
29. Herzog BA, Buechel RR, Katz R et al (2010) Nuclear myocardial perfusion imaging with a cadmium-zinc-telluride detector technique: optimized protocol for scan time reduction. J Nucl Med 51:46–51
30. Esteves FP, Raggi P, Folks RD et al (2009) Novel solid-state-detector dedicated cardiac camera for fast myocardial perfusion imaging: multicenter comparison with standard dual detector cameras. J Nucl Cardiol 16:927–934
31. Gimelli A, Bottai M, Giorgetti A et al (2011) Comparison between ultrafast and standard single-photon emission CT in patients with coronary artery

disease: a pilot study. Circ Cardiovasc Imaging 4:51–58
32. Sharir T, Ben-Haim S, Merzon K et al (2008) High-speed myocardial perfusion imaging: initial clinical comparison with conventional dual detector anger camera imaging. JACC Cardiovasc Imaging 1:156–163
33. Berman DS, Kang X, Tamarappoo B et al (2009) Stress thallium-201/rest technetium-99m sequential dual isotope high-speed myocardial perfusion imaging. JACC Cardiovasc Imaging 2:273–282
34. Sharir T, Slomka P, Hayes S et al (2010) Multicenter trial of high-speed vs. conventional SPECT imaging: quantitative results of myocardial perfusion and left ventricular function. J Am Coll Cardiol 55:1965–1974
35. Maddahi J, Mendez R, Mahmarian J et al (2009) Prospective multi-center evaluation of rapid gated SPECT myocardial perfusion upright imaging. J Nuc l Cardiol 16:351–357
36. DePuey EG, Bommireddipalli S, Clark J et al (2009) Wide beam reconstruction "quarter-time" gated myocardial perfusion SPECT functional imaging: a comparison to "full-time" ordered subset expectation maximum. J Nucl Cardiol 16:736–752
37. Corbett J, Meden J, Ficaro E (2010) Clinical validation of attenuation corrected cardiac imaging with IQ-SPECT SPECT/CT (abstract). J Nucl Med 51(suppl 2):360P
38. Duvall WL, Croft LB, Ginsberg ES et al (2011) Reduced isotope dose and imaging time with a high-efficiency CZT SPECT camera. J Nucl Cardiol 18:847–857
39. Gimelli A, Bottai M, Genovesi D et al (2012) High diagnostic accuracy of low-dose gated-SPECT with solid-state ultrafast detectors: preliminary clinical results. Eur J Nucl Med Mol Imaging 39:83–90
40. Nkoulou R, Pazhenkottil AP, Kuest SM et al (2011) Semiconductor detectors allow low-dose–low-dose 1-day SPECT myocardial perfusion imaging. J Nucl Med 52:1204–1209
41. Nakazato R, Tamarappoo BK, Kang X et al (2010) Quantitative upright supine high-speed SPECT myocardial perfusion imaging for detection of coronary artery disease: correlation with invasive coronary angiography. J Nucl Med 51:1724–1731
42. Songy B, Mirensky O, Lussato D et al (2012) Very low dose myocardial perfusion imaging with 1 mSv using cadmium-zinc-telluride (CZT) camera and Tc99 m-Sestamibi. Arch Cardiovasc Dis Suppl 4:1–29
43. Herzog BA, Husmann L, Landmesser U et al (2009) Low-dose computed tomography coronary angiography and myocardial perfusion imaging: cardiac hybrid imaging below 3 mSv. Eur Heart J 30:644
44. Pazhenkottil AP, Herzog BA, Husmann L et al (2010) Non-invasive assessment of coronary artery disease with CT coronary angiography and SPECT: a novel dose-saving fast-track algorithm. Eur J Nucl Med Mol Imaging 37:522–527
45. Picano E (2009) The risks of inappropriateness in cardiac imaging. Int J Environ Res Public Health 6:1649–1664

Will 3D Imaging of the Heart Replace Pathology?

7

Alessia Gimelli and Elena Filidei

7.1 Introduction

Radiographic, ultrasound (US), nuclear (NR), and magnetic resonance (MR) methods have become mandatory in the management of coronary artery disease (CAD). Noninvasive coronary imaging is a validated aid in establishing new prevention and treatment strategies in a wide range of clinical scenarios, ranging from early subclinical diagnosis of atherosclerosis in asymptomatic individuals to evaluation and monitoring of coronary stenoses in symptomatic patients with recent onset of symptoms or with known CAD. Imaging is widely used for decision making in CAD, not only for detecting ischemia but also for evaluating left ventricular (LV) systolic and diastolic function and for selecting medical, device, and revascularization therapy. Large numbers of patients require imaging to guide clinical decision making regarding treatment. The sources of this information need to be expeditious, inexpensive, and preferably objective and quantitative. To this aim, a number of new technologies will enhance the future accuracy and reliability of the required measures.

A. Gimelli (✉) · E. Filidei
Fondazione Toscana Gabriele Monasterio,
Pisa, Italy
e-mail: gimelli@ftgm.it

E. Filidei
e-mail: gimelli@ftgm.it

7.1.1 Limitations of 2D Imaging

Two-dimensional imaging approaches require expert acquisition and observers, and have limited reliability in obtaining appropriate cut planes in sequential studies. 2D echocardiography is particularly affected by this problem due to the limited imaging windows, which does not always permit imaging on correct axes. To optimize structure resolution, images are often obtained off axis. Portrayal of a 3D object in two dimensions has adverse consequences with regard to LV measurement reproducibility. The increasing sophistication of medical treatments, e.g., for LV dysfunction, has created the need for accurate and reproducible measurements of chamber dimensions. In particular, variations of imaging planes may pose problems for long-term follow-up of LV volume, mass, and ejection fraction (EF), and the evolution of these measurements may have important treatment implications.

7.1.2 Possibilities Using 3D Imaging

Due to limitations of 2D imaging, 3D imaging, made possible 3D echocardiography (3DE), cardiac magnetic resonance (CMR), single-photon-emission computed tomography (SPECT), and cardiac CT, is likely to become increasingly important in providing accurate measurement of LV size and function.

Establishing 3D imaging as the standard imaging approach of the future will require further evolution in image acquisition,

P. Marzullo and G. Mariani (eds.), *From Basic Cardiac Imaging to Image Fusion*,
DOI: 10.1007/978-88-470-2760-2_7, © Springer-Verlag Italia 2013

processing, and display. Although CMR images offer a clear distinction between blood and myocardium, this process may be difficult with 3DE. Nonetheless, in 60–70% of patients with adequate images, a number of trials, including a recent multicenter study, have confirmed the accuracy of 3DE relative to CMR. When image quality poses a problem for echocardiography, echocardiographic contrast agents improve endocardial detection. The accuracy of 2D echocardiography is increased with contrast [1, 2], and it appears likely that 3DE with contrast (perhaps using a highly stable microbubble) will be the optimal approach. A secondary goal of the move to 3D imaging will be to provide rapid acquisition of 3D data sets, even obtained remotely, with most of the processing being performed offline.

The possibility to use several new technological tools should be carefully evaluated by cardiologists. As a matter of fact, imaging can help in clinical decision making only if a robust pathophysiologic background supports every choice. To this aim, three different integration levels between clinical questions and imaging measurements should be identified in order to clarify the real impact of 3D-imaging in the evaluation of pathology.

7.2 Anatomical Measurements

7.2.1 Left Ventricular Morphology

LV morphology, including mass and shape, is an important component of the imaging evaluation of the heart, especially when dealing with hypertension, hypertrophic cardiomyopathy, and heart failure (HR). Mass is most accurately measured by CMR [3] and 3DE [4], which should supersede M-mode echocardiography. Technical advances also mean that mass can now be measured using SPECT [5].

The LV shape is a marker of the severity of heart failure and predicts outcome. This is most simply measured as the sphericity index (ratio of the maximum long- and short-axis dimensions), although this may be limited by regional problems and a more global measurement may be more useful [6]. Imaging using 3DE, CMR, and SPECT have been used in planning LV reconstruction [7, 8], and measuring curvature with more sophisticated measurement techniques may become important. Current techniques assume wall stress is uniform for the entire LV, and it is hoped that 3D methods will become available for measuring curvature to enable regional assessment of wall stress.

7.2.2 Right Ventricular Function

Right ventricular (RV) function is an important correlate of survival for patients with HF. The nongeometric nature of the RV makes the size and function of this chamber difficult to characterize by conventional methods. Nongeometric techniques, such as tissue Doppler, are the simplest approach [9]. CMR avoids dependence of standard echocardiography on standard imaging windows, as RV evaluation with this technique has been shown to correlate with outcomes [10]. Methods that allow the chamber to be portrayed in 3D (3DE, CMR) may circumvent the lack of a geometric shape, and such methods appear likely to be the future techniques of choice (Fig. 7.1). Radionuclide techniques (e.g., first-pass radionuclide angiography for quantifying RV systolic function) were developed nearly 40 years ago. Advances in SPECT, positron-emission tomography (PET), and hybrid SPECT/CT and PET/CT systems have greatly improved image quality and contrast resolution of radionuclide imaging of the heart, allowing for co-registered physiologic and anatomic information of the RV in three dimensions. These improvements provide new opportunities for assessing RV myocardial perfusion, function, and anatomy in the same setting. In the future, such imaging approaches may provide assistance with proactive disease management, including early diagnosis of impending RV dysfunction in high-risk patients and for guiding decisions to initiate and/or modify treatment [11].

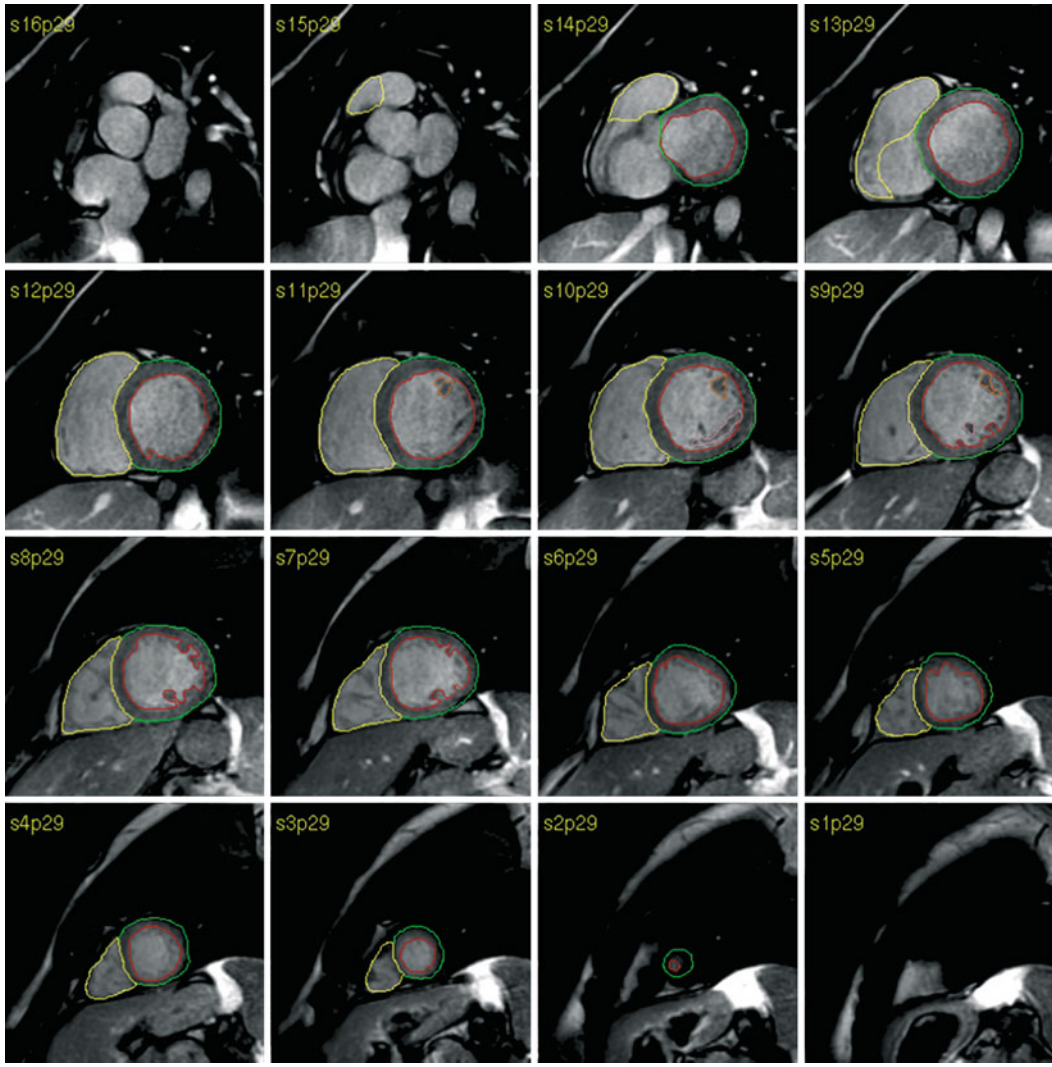

Fig. 7.1 Cardiac magnetic resonance (*CMR*). Right ventricular function evaluation (*yellow line*). Right ventricular ejection fraction: 67%, right end diastolic volume: 178 mL, right end systolic volume: 58 mL, stroke volume: 120 mL, right cardiac output: 7.5 l/min

7.2.3 Myocardial Performance

The EF is load dependent and insensitive to subtle disturbances of myocardial performance. Radial thickening can be measured by techniques with good spatial and contrast resolution, such as CMR; however, because of the fibrous architecture of the heart and the preferential involvement of different components (e.g., endocardium) in some disease conditions, reduction in thickening may be nonuniform. Techniques that examine deformation in multiple axes (especially the long axis) might be expected to be more sensitive than simply determining wall thickening. Tagged CMR or echocardiography may be used to measure motion as velocity (which may be influenced by translation and tethering and is therefore not site specific), strain (an index of deformation), or strain rate. Tissue-Doppler-based measurements derive strain rate from color Doppler velocity, with high temporal resolution but potential

limitations caused by signal noise. Two-dimensional strain (2DS) is based on speckle tracking at rates of 40–80 frames per second. The optimal technique varies according to circumstances: high frame rates (e.g., tissue-velocity imaging) are more important for measuring timing (e.g., postsystolic thickening) and strain rate, as well as at high heart rates. Lower frame rates (e.g., 2DS, MR tagging) may be better at rest, and in remodeled hearts in which wall and imaging axis orientation may be altered along the length of the wall.

7.3 Functional Evaluation

The notion that the prognostic impact of functional risk assessment is superior to angiography is not novel [12]. In patients with defined CAD, exercise variables primarily relating to functional state are known to provide incremental prognostic information over coronary anatomy [13]. The treadmill score also adds independent prognostic information to that provided by clinical data, coronary arteriography, and LVEF [14]. The predictive power of clinical data is also strengthened by adding the results of dobutamine echocardiography [15]; however, the power of the model was increased to a minor degree by the addition of coronary anatomy data. In a group of patients who underwent stress echocardiography with either dipyridamole or dobutamine and who also underwent coronary angiography within a year without an intervening procedure, coronary angiography parameters did not add significant predictive power to the model compared with stress echocardiographic variables [16]. As to nuclear cardiology, the superiority of myocardial perfusion imaging over coronary angiography in risk stratification of patients with ischemic heart disease is also well known. As a matter of fact, all evidence definitively emphasizes the superiority of functional risk stratification over an approach based solely on angiographic coronary anatomy [17, 18].

These observations can be partly explained by the limitations of coronary angiography. First, coronary angiography has a limited sensitivity when compared with necropsy studies [19] and to intravascular US investigations [20]. Furthermore, the identification of significant lesions may be hampered by coronary remodeling and by the extraluminal location of some plaques [21]. Finally, coronary angiography does not allow the exploration of coronary microcirculation, increasingly recognized as an independent determinant of impaired blood flow, disease progression, and adverse prognosis [22]. Functional evaluation of myocardial perfusion should be performed by nuclear cardiology. The clinical use of radiopharmaceuticals in evaluating patients with ischemic heart disease is largely based on noninvasive methodology suitable for visualizing myocardial perfusion. Although contrast echocardiography and MRI were proposed recently for the same purpose, at present, most noninvasive tests for assessing myocardial perfusion reside in nuclear cardiology. Myocardial perfusion can be imaged, and reduced

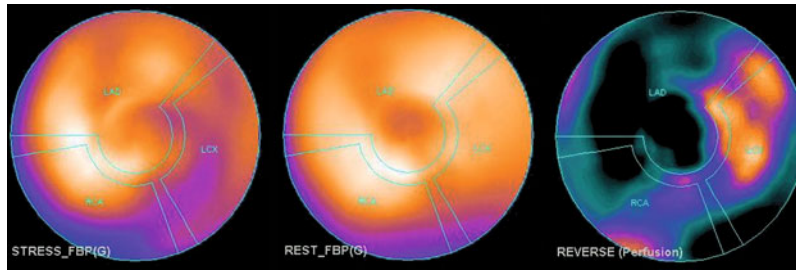

Fig. 7.2 SPECT perfusion images show a reduction in coronary flow reserve in the vascular territory of the right and circumflex coronary

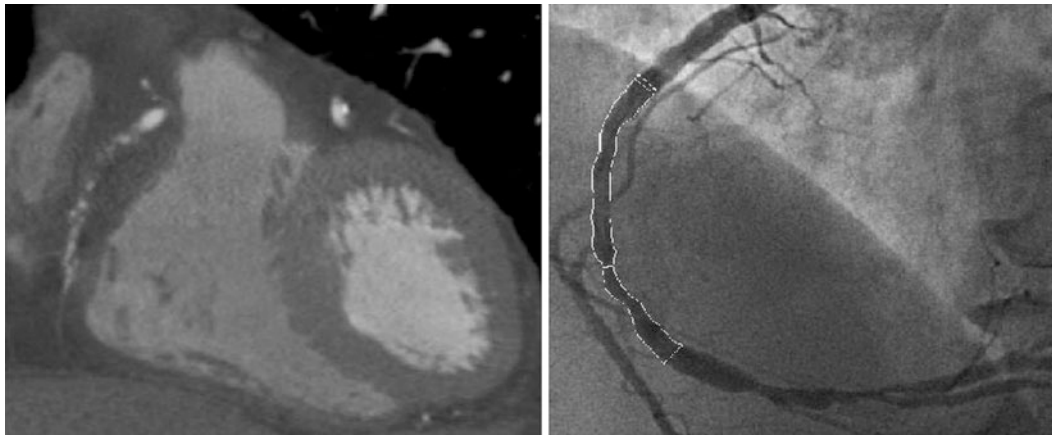

Fig. 7.3 CT angiography (*left image*) and coronary angiography (*right image*) images show stenosis of the middle third of the right coronary

perfusion can be detected as a relative uptake defect compared with the better perfused myocardium. As "significant" coronary stenosis regionally impairs flow reserve, myocardial perfusion imaging has become a common tool for CAD diagnosis and coronary angiography the gold standard for defining its sensitivity and specificity.

The main strength of radionuclide cardiac imaging in patients with CAD is to provide pathophysiological and clinical information related to major objectives of assessment, which include myocardial perfusion, viability, and relationship with LV function. For these assumptions, such data offer additional value over anatomic information provided by other imaging techniques for patient management and outcome.

7.3.1 Functional Risk Assessment Versus Noninvasive Coronary Angiography

The prognostic value of coronary artery calcium (CAC) score has been consistently demonstrated in large series of patients [23–25]. Evidence also suggests that the use of CAC is independently predictive of outcome over and above traditional cardiac risk factors. As to functional risk assessment, CAC scores are predictive of a higher likelihood of ischemia on PET myocardial perfusion imaging [26]. More importantly, patients with and without ischemia on PET perfusion imaging exhibit a stepwise increase in risk of cardiac events with an increase in calcium score. These findings suggest that imaging approaches that combine quantitative information on the anatomic burden of ischemic heart disease with its physiological consequences offer improved risk stratification over the conventional approaches that use myocardial perfusion alone. However, an independent and incremental prognostic value of CAC over clinical, electrocardiographic, laboratory, echocardiographic, and angiographic parameters has not been demonstrated as yet.

A similar consideration applies to CT of coronary arteries. Although the presence of obstructive coronary lesions at 64-slice CT angiography was a predictor of an adverse outcome (death, nonfatal myocardial infarction, unstable angina, coronary revascularization) compared with patients with normal coronary arteries [27], an independent and incremental prognostic value of CT angiography over clinical, electrocardiographic, echocardiographic, and scintigraphic variables has not been demonstrated. Until now, two studies have been designed to test the impact of a combined anatomic and functional noninvasive imaging for detecting and characterizing ischemic heart

disease: the Evaluation of Integrated Cardiac Imaging (EVINCI) study in Europe, and the Study of Myocardial Perfusion and Coronary Anatomy Imaging Roles in Coronary Artery Disease (SPARC) trial in the United States (Figs. 7.2 and 7.3). While we are waiting for the results of these two trials, patient outcomes in stable ischemic heart disease should be estimated using the evidences so far collected.

7.4 Myocardial Fibrosis: 3D Evaluation of Interstitium

Imaging already plays a central role in the distinction of systolic and diastolic HF. Myocytes, which account for only one-third of myocardial cells [28], and collagen compartments both participate in the process of ischemic cardiomyopathy [29] and very likely other cardiomyopathies. In the future, myocardial characterization could play a role in HF diagnosis and perhaps guide therapy.

As a matter of fact, changes in the interstitium relate mainly to fibrosis. There is a major increment of interstitial and perivascular fibrous tissue in pathological hypertrophy. Fibrosis may be either reparative (a regional process that reflects healing and/or replacement by scar) or reactive (a diffuse process). In addition to an increment of the amount of this tissue, its nature is also abnormal, as demonstrated by an increase in type 1 collagen. The consequences of this fibrosis include abnormal coronary flow reserve, probably related to perivascular fibrosis, as well as HF and arrhythmias. Myocardial fibrosis is believed to play a significant role in the abnormal diastolic function occurring in hypertension, diabetes, and the elderly and will likely become a specific target for medical therapy.

7.4.1 Cardiac Magnetic Resonance Methods

Recent technological advances in CMR imaging provide images with high spatial and temporal resolution and excellent myocardial tissue characterization. As a matter of fact, after myocardial infarction, gadolinium late-enhancement MRI images identify regional fibrosis [24] and infarct size and predict functional recovery. The detection of localized fibrosis is ideal for recognition by gadolinium enhancement based on the relative comparison between the region and a normal reference segment. Moreover, cardiac MRI is a valuable imaging technique for detecting and assessing morphology and functional characteristics of non-ischemic cardiomyopathy as well (Fig. 7.4). Black-blood fast spin-echo MRI allows morphologic assessment of the heart with high spatial resolution, whereas T2-weighted MRI can depict acute myocardial edema [27]. Finally, contrast-enhanced images can depict and help quantify myocardial edema, infiltration, and fibrosis.

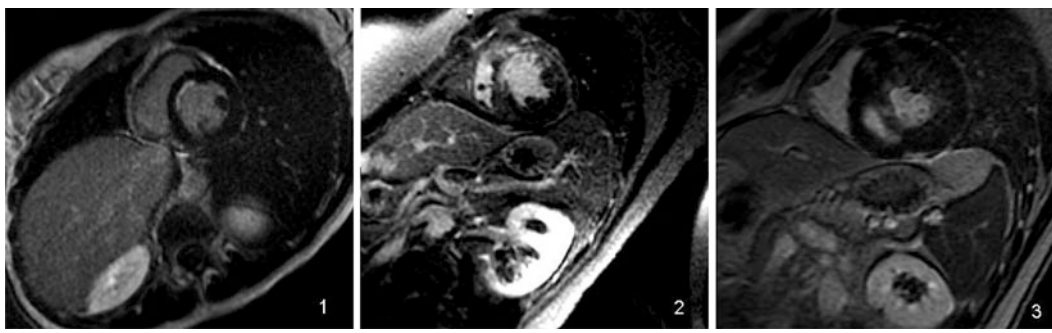

Fig. 7.4 Gadolinium late-enhancement magnetic resonance (*MR*) images. **1** Ischemic transmural fibrosis **2** ischemic subendocardial fibrosis **3** myocardial fibrosis in hypertrophic cardiomyopathy

7.4.2 Nuclear Cardiology Techniques

Scintigraphic methods have limited potential for characterizing myocardial fibrosis. The perfusable tissue index can be obtained with $H_2{}^{15}O$ and $C^{15}O$ PET imaging, which allows measurement of perfusable tissue fraction. The perfusable tissue index is reduced in patients with dilated cardiomyopathy [30]. In addition to the cost and limited availability of PET, these techniques are technically challenging and are unlikely to be adopted for routine clinical use.

New dedicated, ultrafast, solid-state cardiac cameras, introducing a new design of both photon acquisition systems and reconstruction algorithms, have recently been developed [31, 32]. This new technology uses pinhole collimation design and multiple cadmium-zinc-telluride (CZT) crystal arrays. Compared with the standard SPECT camera, this new type of collimation provides a 3- to 5-fold increase in photon sensitivity, thereby reducing imaging times significantly while achieving a 1.7- to 2.5-fold increase in spatial resolution, thus enabling high-quality scans with a significant reduction in imaging time and dose [33]. Recent studies have demonstrated that the new system shows excellent agreement with regard to uptake and clinical findings [31–33]. Moreover, the increased photon sensitivity and spatial resolution should in principle improve the performance of ultrafast SPECT in detecting perfusion abnormalities and myocardial fibrosis.

7.4.3 Contractile Reserve

In preclinical disease, systolic dysfunction is more likely to become apparent under stress than at rest. The 3D delineation of functional data may make CMR and 3DE the optimal tests for quantifying contractile reserve. Evaluating regional function at rest and during stress can be used to identify ischemic and non-ischemic cardiomyopathy. In overt HF, for example, contractile reserve, measured invasively (e.g., dP/dt) or noninvasively (e.g., EF or cardiac output response) is related to outcome [34]. Contractile reserve also mirrors sympathetic dysfunction [35], which makes this an inexpensive surrogate for tests of sympathetic status. In the future, this information may be used in tailoring HF therapy to the status of individual patients.

7.4.4 Cardiac Innervation

Cardiac sympathetic activity can be assessed by iodine-123 metaiodobenzylguanidine ($[^{123}I]$-MIBG) scintigraphy. In patients with HF, sympathetic cardiac activity abnormalities have been observed that result in reduced $[^{123}I]$-MIBG uptake [36]. Abnormal $[^{123}I]$-MIBG uptake predicts cardiac death, arrhythmias, and all-cause mortality in HF patients, with a prognostic power incremental to that of conventional risk markers, and may identify patients at low risk of arrhythmias despite current guideline indications for implantable cardioverter defibrillator (ICD) or patients at high risk for arrhythmias not fulfilling ICD indications (Fig. 7.5). Assessing cardiac sympathetic activity by $[^{123}I]$-MIBG imaging is useful for depicting the occurrence of increased sympathetic hyperactivity in HF and for following its deleterious effects on disease progression. For clinical applications, $[^{123}I]$-MIBG imaging identifies, as well as conventional functional and biochemical parameters, patients at low or high risk of cardiac events and is able to track innervation changes induced by therapies. However, lack of prospective outcome data remains a limitation for routine clinical use, and this should foster future prospective clinical studies aimed at assessing whether $[^{123}I]$-MIBG imaging will ultimately have an impact on HF management in clinical practice.

The positron tracers $[^{11}C]$hydroxyephedrine and $[^{11}C]$epinephrine permit quantification of the density of sympathetic nerve terminals [37, 38]. Myocardial uptake of $[^{11}C]$hydroxyephedrine correlates with norepinephrine tissue concentration and noradrenaline transporter (NAT) density. Postsynaptic receptor density can be assessed with $[^{11}C]$CGP-12177. The use of radiopharmaceuticals in imaging various aspects

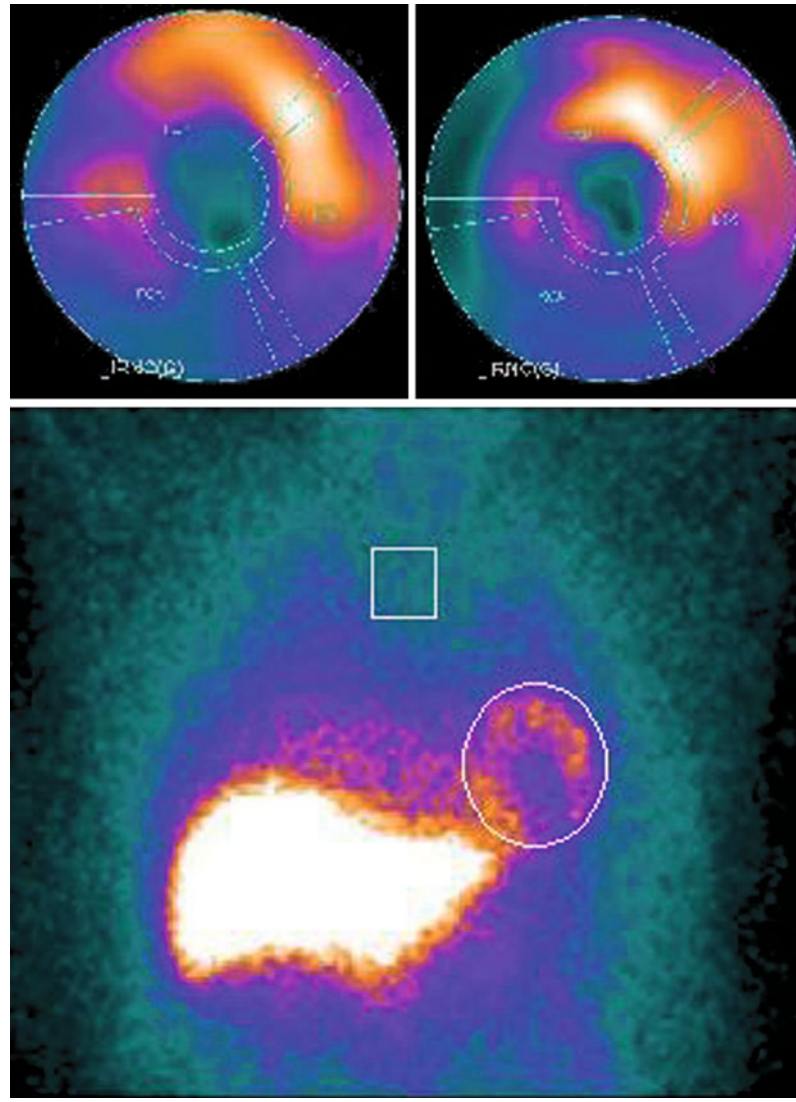

Fig. 7.5 Innervation–perfusion imaging at rest obtained, respectively, with [^{123}I]-MIBG and ^{99m}Tc-Tetrofosmin. Tomographic early acquisitions show a denervation pattern (*top left*) wider than areas with reduced viability in perfusion imaging (*top right*), especially in the left anterior descending coronary artery territory. Heart to mediastinum analysis (H/M ratio) on planar innervation images (*bottom*) show normal values (>1.6)

of neuronal function (transmitter uptake, release, metabolism, and storage) may permit guidance of pharmacological interventions and their effects on cardiac autonomic innervation.

7.5 Myocardial Perfusion Imaging and Revascularization

No differences in composite of death, acute myocardial infarction, and stroke were found between patients with stable ischemic heart disease, objective evidence of ischemia, and significant coronary stenoses randomized to optimal medical therapy with or without percutaneous coronary intervention in the Clinical Outcomes Utilizing Revascularization and Aggressive Drug Evaluation (COURAGE) trial [39]. The relationship between the extent of myocardial ischemia at gated SPECT and coronary revascularization has been explored in a subset of patients enrolled in a nuclear sub-study of the COURAGE trial [40]. In these patients, the addition of percutaneous coronary intervention to optimal medical therapy resulted in more

effective reduction of ischemia than optimal medical therapy alone. This greater reduction in ischemic burden was associated with improvements in angina class and less reliance on nitrate therapy for symptom relief. Moreover, patients with moderate to severe ischemia randomized to percutaneous coronary intervention plus optimal medical therapy more commonly experienced a significant reduction in ischemia at follow-up compared with those receiving optimal medical therapy (78 versus 52%). Thus, the results of the nuclear sub-study suggest that gated SPECT could be used to identify patients who may benefit more from coronary revascularization.

7.6 Proper Diagnostic Workup

In patients with stable ischemic heart disease, myocardial perfusion imaging may be sometimes regarded as an unnecessary or even redundant investigation. As shown previously, functional imaging adds prognostic information that is greater than that provided by coronary angiography. This observation suggests that indications for myocardial perfusion imaging in risk stratification of patients with known or suspected ischemic heart disease should be broadened. In clinical practice, a functional risk assessment may conflict with a health-care delivery policy oriented toward cost saving and direct reperfusion. In this respect, a survey of the European Society of Cardiology shows that noninvasive functional tests are underutilized, with wide variability between different countries [41], so that several patients without significant ischemic heart disease directly undergo invasive coronary angiography. On the other hand, coronary lesions detected by coronary angiography are often revascularized, even without evidence that either myocardial blood supply or mechanical function is altered [42]. This "anatomically oriented" invasive approach may negatively affect patient management, with consequent suboptimal medical treatment, inappropriate revascularizations, additional risks, and increased health-care costs.

7.7 Conclusions

Advancement of cardiac imaging techniques has provided an increasing range of information that can now be obtained without affecting the image process. Successful application of these techniques will be determined not only by methodological progress but also by the integration of this information into clinical care. Moreover, clinical validation in prospective trials that adhere to evidence-based medicine criteria, as well as rational cost-efficient use of imaging technologies, needs to be done.

For this reason, the use of 3D imaging should be used for integrating results obtained by the single imaging modality to address specific questions such as etiology, severity, reversibility of LV function, and prognosis.

References

1. Thomson HL, Basmadjian AJ, Rainbird AJ et al (2001) Contrast echocardiography improves the accuracy and reproducibility of left ventricular remodeling measurements: a prospective, randomly assigned, blinded study. J Am Coll Cardiol 38:867–875
2. Hoffmann R, von Bardeleben S, Kasprzak JD et al (2006) Analysis of regional left ventricular function by cineventriculography, cardiac magnetic resonance imaging, and unenhanced and contrast-enhanced echocardiography: a multicenter comparison of methods. J Am Coll Cardiol 47:121–127
3. Grothues F, Smith GC, Moon JC, Bellenger NG, Collins P, Klein HU, Pennell DJ (2002) Comparison of interstudy reproducibility of cardiovascular magnetic resonance with two-dimensional echocardiography in normal subjects and in patients with heart failure or left ventricular hypertrophy. Am J Cardiol 90:29–34
4. Jenkins C, Bricknell K, Hanekom L, Marwick TH (2004) Reproducibility and accuracy of echocardiographic measurements of left ventricular parameters using real-time three-dimensional echocardiography. J Am Coll Cardiol 44:878–886
5. Mochizuki T, Murase K, Tanaka H, Kondoh T, Hamamoto K, Tauxe WN (1997) Assessment of left ventricular volume using ECG gated SPECT with technetium-99 m. MIBI and technetium-99 m-tetrofosmine. J Nucl Med 38:53–57
6. Mannaerts HF, van der Heide JA, Kamp O, Stoel MG, Twisk J, Visser CA (2004) Early identification of left ventricular remodelling after myocardial

infarction, assessed by transthoracic 3D echocardiography. Eur Heart J 25:680–687
7. Schenk S, McCarthy PM, Starling RC et al (2004) Neurohormonal response to left ventricular reconstruction surgery in ischemic cardiomyopathy. J Thorac Cardiovasc Surg 128:38–43
8. Dor V (2004) Surgical remodeling of left ventricle. Surg Clin North Am 84:27–43
9. Meluzin J, Spinarova L, Hude P, Krejci J, Kincl V, Panovsky R, Dusek L (2005) Prognostic importance of various echocardiographic right ventricular functional parameters in patients with symptomatic heart failure. J Am Soc Echocardiogr 18:435–444
10. Larose E, Ganz P, Reynolds HG et al (2007) Right ventricular dysfunction assessed by cardiovascular magnetic resonance imaging predicts poor prognosis late after myocardial infarction. J Am Coll Cardiol 49:855–862
11. Ramani GV, Gurm G, Dilsizian V, Park MH (2010) Non invasive assessment of right ventricular function: will there be resurgence in radionuclide imaging techniques? Curr Cardiol Rep 12:162–169
12. Gimelli A, Rossi G, Landi P et al (2009) Stress/rest myocardial perfusion abnormalities by gated spect: still the best predictor of cardiac events in stable ischemic heart disease. J Nucl Med 50:546–553
13. Weiner DA, Ryan TJ, McCabe CH et al (1984) Prognostic importance of a clinical profile and exercise test in medically treated patients with coronary artery disease. J Am Coll Cardiol 3:772–779
14. Mark DB, Hlatky MA, Harrell FE Jr, Lee KL, Califf RM, Pryor DB (1987) Exercise treadmill score for predicting prognosis in coronary artery disease. Ann Intern Med 106:793–800
15. Marwick TH, Case C, Sawada S et al (2001) Prediction of mortality using dobutamine echocardiography. J Am Coll Cardiol 37:754–760
16. Sicari R, Pasanisi E, Venneri L, Landi P, Cortigiani C, Picano E, On behalf of the Echo Persantine International Cooperative (EPIC) and Echo Dobutamine International Cooperative (EDIC) Study Groups (2003) Stress echo results predict mortality: a large-scale multicenter prospective international study. J Am Coll Cardiol 41:589–595
17. Pollock SG, Abbott RD, Boucher CA, Beller GA, Kaul S (1992) Independent and incremental prognostic value of tests performed in hierarchical order to evaluate patients with suspected coronary artery disease: validation of models based on these tests. Circulation 85:237–247
18. Iskandrian AS, Chae SC, Heo J, Stanberry CD, Wasserleben V, Cave V (1993) Independent and incremental prognostic value of exercise single-photon emission computed tomographic (SPECT) thallium imaging in coronary artery disease. J Am Coll Cardiol 22:665–670
19. Michalodimitrakis M, Mavroforou A, Giannoukas AD (2005) Lessons learnt from the autopsies of 445 cases of sudden cardiac death in adults. Coron Artery Dis 16:385–389
20. Nissen SE (2003) Pathobiology, not angiography, should guide management in acute coronary syndrome/non-ST-segment elevation myocardial infarction: the non-interventionist's perspective. J Am Coll Cardiol 41:103S–112S
21. Sipahi I, Tuzcu EM, Schoenhagen P et al (2006) Paradoxical increase in lumen size during progression of coronary atherosclerosis: observations from the REVERSAL trial. Atherosclerosis 189:229–235
22. Neglia D, Michelassi C, Trivieri MG et al (2002) Prognostic role of myocardial blood flow impairment in idiopathic left ventricular dysfunction. Circulation 105:186–193
23. Budoff MJ, Shaw LJ, Liu ST et al (2007) Long-term prognosis associated with coronary calcification: observations from a registry of 25,253 patients. J Am Coll Cardiol 49:1860–1870
24. Taylor AJ, Bindeman J, Feuerstein I, Cao F, Brazaitis M, O' Malley PG (2005) Coronary calcium independently predicts incident premature coronary heart disease over measured cardiovascular risk factors: mean three-year outcomes in the prospective army coronary calcium (PACC) project. J Am Coll Cardiol 46:807–814
25. Greenland P, LaBree L, Azen SP, Doherty TM, Detrano RC (2004) Coronary artery calcium score combined with Framingham score for risk prediction in asymptomatic individuals. JAMA 291:210–215
26. Schenker MP, Dorbala S, Hong CT et al (2008) Interrelation of coronary calification, myocardial ischemia and outcomes in patients with intermediate likelihood of coronary artery disease: a combined positron emission tomography/computed tomography study. Circulation 117:1693–1700
27. Gaemperli O, Valenta I, Schepis T et al (2008) Coronary 64-slice CT angiography predicts outcome in patients with known or suspected coronary artery disease. Eur Radiol 18:1162–1173
28. Weber KT (2000) Targeting pathological remodeling: concepts of cardio protection and reparation. Circulation 102:1342–1345
29. Beltrami CA, Finato N, Rocco M et al (1994) Structural basis of end-stage failure in ischemic cardiomyopathy in humans. Circulation 89:151–163
30. Knaapen P, Boellaard R, Gotte MJ et al (2004) Perfusable tissue index as a potential marker of fibrosis in patients with idiopathic dilated cardiomyopathy. J Nucl Med 45:1299–1304
31. Esteves FP, Raggi P, Folks RD et al (2009) Novel solid-state-detector dedicated cardiac camera for fast myocardial perfusion imaging: multicenter comparison with standard dual detector cameras. J Nucl Cardiol 16:927–934
32. Buechel RR, Herzog BA, Husmann L et al (2010) Ultrafast nuclear myocardial perfusion imaging on a new gamma camera with semiconductor detector

technique: first clinical validation. Eur J Nucl Med Mol Imaging 37:773–777
33. Gimelli A, Bottai M, Genovesi D, Giorgetti A, Di Martino F, Marzullo P (2012) High diagnostic accuracy of low-dose gated SPECT with solid-state ultrafast detectors: preliminary clinical results. Eur J Nucl Med Mol Imaging 39:83–90
34. Naqvi TZ, Goel RK, Forrester JS, Siegel RJ (1999) Myocardial contractile reserve on dobutamine echocardiography predicts late spontaneous improvement in cardiac function in patients with recent onset idiopathic dilated cardiomyopathy. J Am Coll Cardiol 34:1537–1544
35. Ohshima S, Isobe S, Izawa H et al (2005) Cardiac sympathetic dysfunction correlates with abnormal myocardial contractile reserve in dilated cardiomyopathy patients. J Am Coll Cardiol 46:2061–2067
36. Bristow MR (1984) The autonomic nervous system in heart failure. N Engl J Med 311:850–851
37. Schwaiger M, Kalff V, Rosenspire K et al (1990) Noninvasive evaluation of sympathetic nervous system in human heart by positron emission tomography. Circulation 82:457–464
38. Caldwell JH, Link JM, Levy WC, Poole JE, Stratton JR (2008) Evidence for pre to postsynaptic mismatch of the cardiac sympathetic nervous system in ischemic congestive heart failure. J Nucl Med 49:234–241
39. Boden WE, O'Rourke RA, Teo KK et al (2007) Optimal medical therapy with or without PCI for stable coronary disease. N Engl J Med 356:1503–1516
40. Shaw LJ, Barman DS, Maron DJ et al (2008) optimal medical therapy with or without percutaneous coronary intervention to reduce ischemic burden results from the clinical outcomes utilizing revascularization and aggressive drug evaluation (COURAGE) trial nuclear substudy. Circulation 117:1283–1291
41. Breeman A, Hordijk-Trion M, Lenzen M et al (2006) Euro heart survey on coronary revascularization. Treatment decisions in stable coronary artery disease: insights from the euro heart survey on coronary revascularization. J Thorac Cardiovasc Surg 132:1001–1009
42. Daly CA, Clemens F, Sendon JL et al (2005) Euro heart survey investigators. The clinical characteristics and investigations planned in patients with stable angina presenting to cardiologists in Europe: from the euro heart survey of stable angina. Eur Heart J 26:996–1010

Image Fusion and Coregistration: State of the (He)art

8

Stephan G. Nekolla, Christoph Rischpler and Martina Marinelli

8.1 Introduction

Almost ten years ago, we wrote a book chapter on hybrid cardiac positron emission tomography–magnetic resonance imaging (PET/MRI) at the invitation of one of the editors of this book [1]. Now, this chapter offers a welcome opportunity to perform a follow-up and "reality check" in light of technological evolution since the writing of that initial chapter. The past decade saw a tremendous increase in systems capable of hybrid imaging, namely PET/CT systems and, to a lesser extent, single-photon-emission computed tomography—CT (SPECT/CT). Although primarily designed and optimized for oncology imaging, those devices—if equipped with a CT component capable of rapid, electrocardiograph (ECG)-gated imaging and between 64 and 128 CT slices—are well suited for applications in cardiac imaging. The combination of functional and morphological imaging provides valuable information, which is discussed in this book as well as in a series of reviews on this topic [2–4]. However, the cost efficiency of integrated over sequential imaging is not yet defined. Furthermore, we see the advent of hybrid PET/MRI systems with either near-simultaneous or a fully integrated design [5, 6]. Both PET/CT and PET/MRI systems provide much more data with higher spatial resolution than conventional nuclear cardiology depicted in the past. In the monomodal world, over a time period of almost two decades, a variety of software packages emerged to facilitate quantitative analysis of perfusion defect size and extent as well as functional, global parameters such as left-ventricular (LV) ejection fraction and volumes [7–9]. In addition, various regional contraction parameters can be assessed utilizing count increase or definition of endo- and epicardial borders. In contrast to these vast possibilities, the tools for multimodal and multiparameter cardiac imaging are still relatively sparse. Thus, this paper describes strategies and capabilities of modalities currently available, attempts to shed light on the reason why this is still a niche market, and once again describes a personal view on potential solutions, as 3D visualization is only the very last step in a rather complex workflow.

8.2 Regulatory Issues and Software Development

Software development in the "good old days"—especially in the academic arena—was driven first by the demand of local users and

S. G. Nekolla (✉) · C. Rischpler
Nuklearmedizinische Klinik, Technische Universität München, Munich, Germany
e-mail: stephan.nekolla@tum.de

C. Rischpler
e-mail: c.rischpler@tum.de

M. Marinelli
Institute of Clinical Physiology, CNR, Pisa, Italy
e-mail: martina.marinelli@ifc.cnr.it

P. Marzullo and G. Mariani (eds.), *From Basic Cardiac Imaging to Image Fusion*,
DOI: 10.1007/978-88-470-2760-2_8,

subsequently by a wider audience. By investigating the documents of the US Federal Drug Administration (FDA), one of the most important regulatory bodies, one can trace back the heritage of the conventional analysis tools in nuclear cardiology of almost three decades. Over the same time interval, the extent of the necessary documents required to define a project, implement it, and track changes increased by orders of magnitude. This development was paralleled with the trend to globalization: the human resources needed for definition, development, and "life-cycle management" can be distributed all over the globe (not always making communication easier). However—and not really unexpectedly—all this ever-increasing complexity did not necessarily result in a huge increase in functionality. Furthermore—and this is especially true for hybrid imaging where radiologist's competence in several fields is required—the degree to which the actual customers are involved in the definition and testing phases seems to be declining as well. This leads to the suboptimal situation that the customer cannot exert influence on the development of analytic tools and is confronted in a phase during which his or her feedback is superfluous. Due to the complex processes described above, integration of ideas from the field will take quite some time, which potentially hampers successful implementation of novel imaging schemes in a competitive environment. The described scenario does not only affect tools for hybrid cardiac imaging but for imaging software in general. Consequently, because today most multimodal imaging applications in nuclear medicine focus on oncology, one must acknowledge the fact that available resources for software development in the area of hybrid cardiac imaging are constrained.

8.3 Combining Functional and Morphology Data: Individualized Analysis

The general relevance of combining functional and morphological data was discussed earlier. From a technical perspective, in particular, the use of CT angiography (CTA) information could facilitate patient-specific identification of segments of the heart supplied by the coronaries. Mostly, the American Heart Association (AHA) standard scheme is used [10], although this will work only in a certain subset of patients due to the biological variability of the vessel tree and the existence of collateral vessels [11]. However, the standard layout for the myocardial supply territories is used in all analysis packages and potentially limits the accuracy of PET and SPECT when strictly interpreted by interventional cardiologists. Javadi et al. [12] showed that the use of CTA clearly improves vessel identification, which would offer a benefit for therapeutical interventions. However, no viable and routine-capable solution seems to be available.

8.4 Necessary Prerequisite: Coregistration

As mentioned above, data sets to be fused are, in most circumstances, not in the same spatial coordinate system with the necessary precision of a few millimeters: for instance, due to sequential acquisition, patient motion, or simply a different state of respiration or contraction. Due to different spatial resolutions and the complexity of differences, no final solution to this issue is known, although substantial progress was made in the last decade [13–15]. To optimize and automate this process as far as possible, it is quite obvious that a basic requirement for more widespread clinical use, such as aligning two or more 3D objects that are not necessarily shifted but also rotated due different respiratory states, is not only cumbersome but also introduces some interobserver variability.

Although out of the scope of this chapter, it is imperative to keep in mind that both alignment between rest and stress studies, as well as correct alignment between nuclear emission data and CT (for attenuation correction), is of utmost importance. Should this alignment fail either for static or for dynamic studies, all downstream data might be corrupted [16, 17].

8.5 Tools for Hybrid Cardiac Imaging

This chapter does not go into details on the ongoing research in advanced visualization but focuses primarily on the nuclear imaging community and the respective vendors. The reason for this is simple: the very sophisticated approaches from the computer sciences community do arrive very slowly in this area—not the least due to regulatory issues and complex marketing considerations, as outlined above. Thus, we provide a summary of tools that are actually available for use. Regardless, we are very well aware that compared with 3D visualization used in cardiac CTA, the degree to which hybrid imaging tools are used today is still limited, as the number of centers with the required imaging hardware and software is rather small. In addition, 3D viewing of CTA data is a common way to communicate results in a comprehensible manner to patients. In other words, such 3D visualization is understood not least as a marketing tool. This favorable situation is driven by the monomodal nature of CT, the excellent contrast, the large number of systems, high clinical throughput, and significant pressure from the clinical user on the vendor to provide fast, reliable, and highly automated tools. Based on this, it is not surprising that established CTA analysis and visualization tools are used technically as a platform for integrating nuclear imaging data. Basically, two strategies exist that—and this is important to note—do not require data from hybrid systems but will work with data from separate systems [18]. It is relevant to realize—as mentioned above—that even with integrated systems, a spatial coregistration between the two morphologic images and functional data is necessary, as CT and MRI are typically acquired in breathhold and for high-resolution data (such as angiography and late contrast media enhancement triggered to the diastole), whereas nuclear imaging techniques (due to the different signal-to-noise situation) are measured over many heart and respiratory cycles, resulting in a potentially significant spatial offset.

8.5.1 Extensions to CTA Visualization Tools

The first approach, extensions to CTA visualization tools, utilizes the standard approach in CTA visualization; namely, a combination of surface- and volume-rendering techniques, which displays the LV endocardium and the coronaries after isolation of the heart. This makes use of the fact that the signal intensity of contrast media as well as coronary calcifications is clearly greater than unenhanced myocardium, and thus, relatively simple thresholding algorithms can be applied, which are subsequently used for automatic identification of coronaries and large vessels, depending on signal quality. Visualization is simplified by this active identification of coronary vessels but also indicates an inherent limitation of the hybrid 3D display: only vessels successfully identified by means of automated algorithms and optional manual interaction can be used. Finer details visible in the original CTA data might be lost in this process.

In order to combine this display with PET or SPECT information, the endocardial surface of the LV is color coded with the normalized SPECT or PET values [18, 19]. This elegant approach allows not only fusion with normalized tracer uptake, but it is also feasible to use with quantitative values such as myocardial blood flow using PET tracers such as [^{15}O]-water [20]. In such a case, parametric image data is generated with suitable software packages and again projected onto the endocardial surface [4]. Generation of parametric images can either be performed with pixel-wise modeling approaches within the dynamic data or using polar-map techniques, in which tissue and blood activity curves are generated from small clusters of voxels. For example, using [^{13}N]-ammonia,

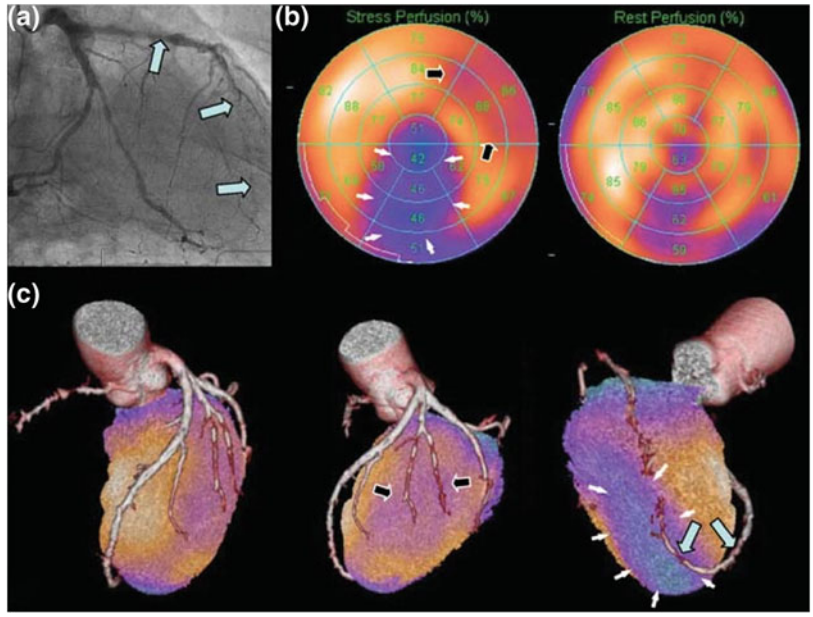

Fig. 8.1 Projection of absolute myocardial blood flow derived from dynamic [^{13}N]-ammonia positron emission tomography (PET) imaging onto the endocardial surface of a computed tomography angiography (CTA) study. For this purpose, regional tissue and blood curves are generated in the form of a polar map. This data is subsequently converted into a parametric (or "virtual") image [22].

myocardial blood flow can be generated using compartment modeling, including spillover, partial volume, and motion correction [21]. This approach basically leads to only a few hundred flow values in the form of a polar map instead of a parametric image, but this can be converted into a "virtual image" that, again, is projected into the CTA (Fig. 8.1) [22]. This projection approach has the tremendous advantage that basically any volume data set can be superimposed with a rendering of the coronary tree, thus allowing advanced clinical users to feed their image or even quantitative data into readily available software.

The other available strategy, instead of using volume rendering and color coding, is to display a 3D polar map within the graphic scene showing the coronary tree [15]. For this purpose, an interface between software generating the 3D rendering and the program extracting the tracer uptake needs to be defined. In this particular case, a data-exchange definition using Extensible Markup Language (XML) allows the transfer of the 3D coordinates and uptake or quantitative values into the main visualization program (Fig. 8.2).

8.5.2 Integration of the Coronary Tree into Tools for Nuclear Cardiology

The second option, of merging CTA and nuclear images, reverses the exchange order as described above. In this option, the main visualization environments are extended tools for analyzing nuclear images, and the image of the coronary tree is exported from the specialized CTA software. One of the first implementations of this option came from the late Faber [23], who extracted the coronary tree image from biplane angiography studies [24]. This approach was later extended to CTA data, with a particular focus on automated alignment between the two modalities [14, 25] (Fig. 8.3). Nakazato and colleagues provided a similar approach [15]. In

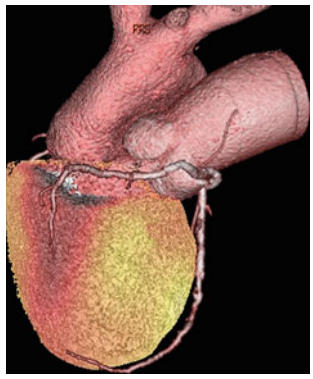

Fig. 8.2 Alternative to rendering and color coding of the endocardial surface is the definition of an exchange format between software generating 3D polar maps from cardiac positron emission tomography (PET) or single-photon-emission computed tomography (SPECT) data and the tool responsible for coronary extraction. In this example, viability analysis was performed in the nuclear analysis environment, and viability scores in the 3D polar map are shown with the coronary tree [22]. This analysis has been developed within the research activities of the Evaluation of Integrated Cardiac Imaging (EVINCI) study funded from the European Community's Seventh Framework Programme (FP7/2007–2013) under grant agreement no. 222915

this contribution, the issue of automated alignment was addressed, but "motion-frozen" nuclear perfusion data was also utilized in which all data over the cardiac cycle was projected into a diastolic contraction state, which further improved the quality of alignment, as the motion states between CTA and nuclear imaging were now more consistent.

8.6 Going Beyond Perfusion SPECT/PET/CTA

The applications discussed so far focus on the fused display of a CTA with either a single nuclear scan using relative or absolute values or with the combined results of a rest and a stress scan, resulting in a segmented polar map pointing to scar or ischemic regions (Fig. 8.4). However, even more information could be extracted from hybrid scans.

Especially in the area of molecular imaging, which is characterized by very focal uptake patterns, coregistration and fusion is not trivial, and those techniques are in general—and, unfortunately—not widely employed [26, 27]. In this modality, anatomical reference images are of high value, but inconsistencies of even a few millimeters might project focal [^{18}F]FDG uptake not into a coronary vessel but into the lung. For this group of applications, conventional fusion display is the primary choice, although imaging tools supporting more than two data sets (e.g., flow, inflammation, and anatomical reference) are rare.

In an animal model, Lautamaki combined the assessment of flow ([^{13}N]-ammonia) and metabolism ([^{18}F]FDG) with a CTA in order to identify the coronary tree and a "late enhancement" CT for high-resolution scar imaging [28]. Such "biomorphological insights into the interrelation between tissue damage, inflammation,

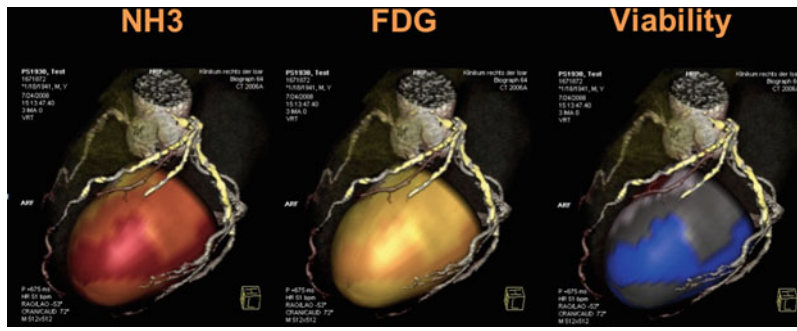

Fig. 8.3 The other exchange path is the extraction of the coronary tree in the specialized computed tomography angiography (CTA) analysis tool and its export into the environment of the nuclear analysis tools. As demonstrated in this example, the 3D polar map is drawn into the scene showing the primary vessels, together with a comprehensive display of all other nuclear images and a monomodal rendering of the CTA. Reprinted from Fig. 8.3, [25], with permission

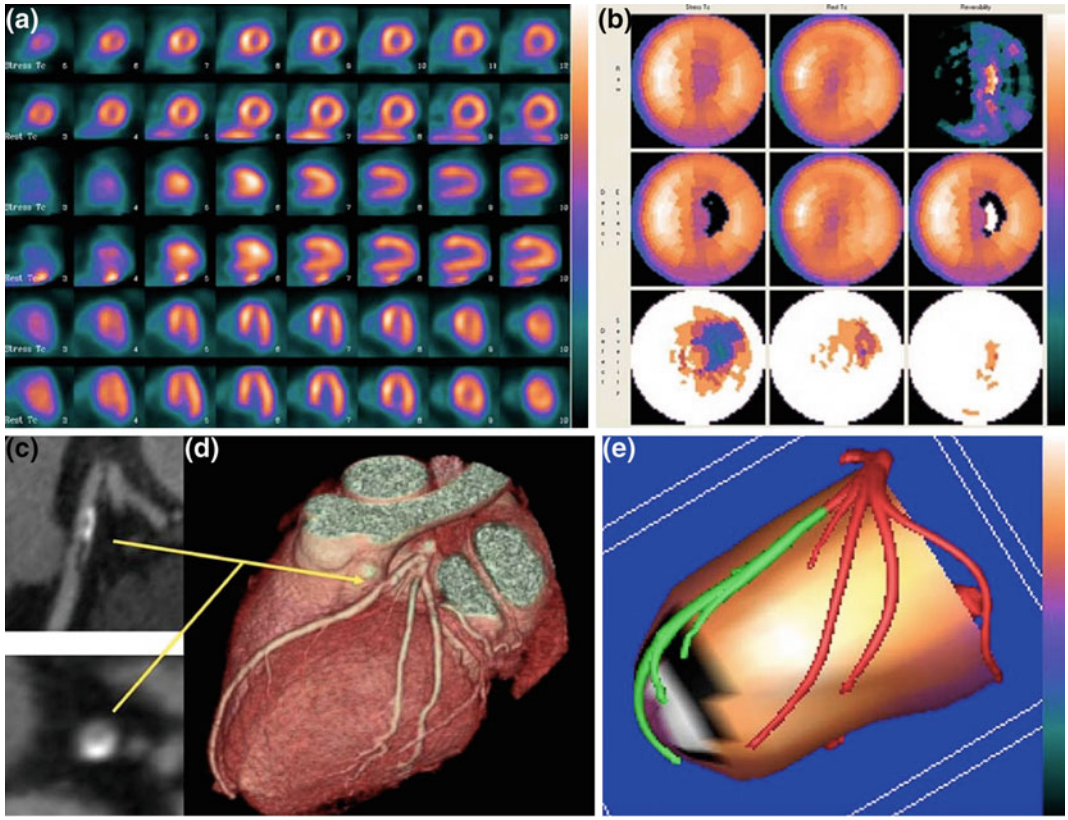

Fig. 8.4 Display of conventional rest and stress polar maps of a myocardial single-photon-emission computed tomography (SPECT) study combined with the color-coded projection of stress tracer uptake on the thresholded endocardial surface. Reprinted from Fig. 8.5, [3], with permission

and microvascular obstruction early after myocardial infarction" could be of high value in a clinical setting. However, how such a huge amount of data could be visualized in an effective manner is not yet clear. Another experimental study from this group integrated PET imaging with invasive electroanatomic mapping [29]. In addition to the highly relevant biological question, it again points to a solution as to how to integrate all this information. The tool, which displays the electroanatomical map, provides an interface with which to read surface models of polar maps. Thus, the advanced user could integrate his or her data into such a system.

The integration of PET/MRI and SPECT/MRI data has been used primarily for validation studies [21, 30, 31] or case reports [32]. The truly synergistic use of sequential examinations was a rather rare application mostly due to logistic constraints. Recent years brought several designs for PET/MRI onto the market and, although targeting the oncologic field, cardiac applications could be promising. However, the fact that cardiac MRI is typically not a volume-oriented but, rather, a slice-oriented approach, makes this extremely demanding. Current techniques allow fusion of the first two imaging series only, thus, how up to 20 different series—e.g., PET (flow, metabolism), MRI (wall motion in short-axis, two-, and four-chamber views; late gadolinium enhancement in short-axis, two-, and four-chamber views; T1 maps pre- and post contrast; T2-weighted images, etc.—can be displayed and viewed in an efficient manner is still open to question, especially when keeping in mind that most MRI data are acquired in

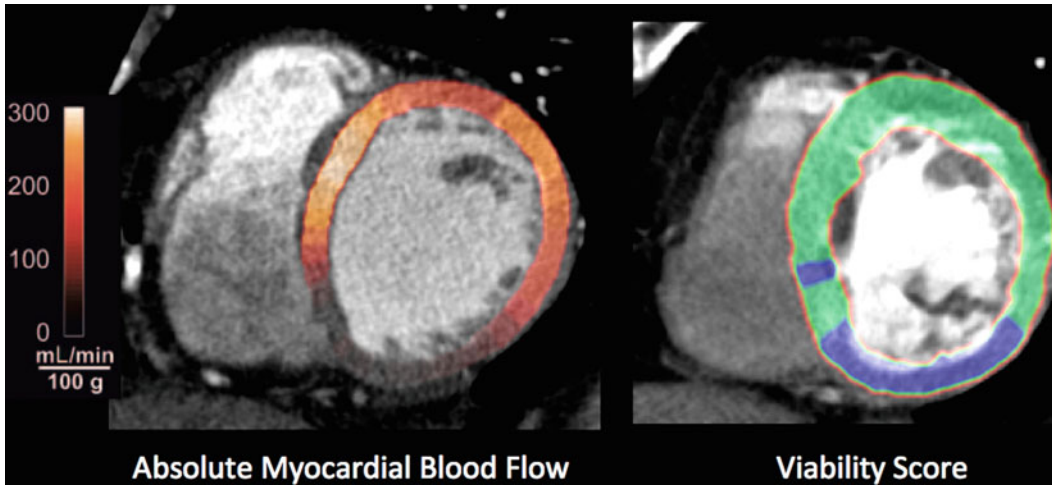

Fig. 8.5 Although 3D visualizations are visually pleasing and highly suitable for communicating results, the clinical reality will be reading the images. For this task, given the increasing amounts of data, new approaches are needed. This example shows projection of functional data, such as absolute myocardial blood flow or viability scores, onto the myocardial segment within a high-resolution, reference image. Such a technique would leave information in the coronaries unchanged, for example, and not obscured by the relatively blurry positron emission tomography (PET) data

breathhold, which is highly dependent on patient collaboration and is hardly reproducible. Basically, a large number of registration matrices will be required to bring all data into the same reference system, and no system supporting this requirement is yet available.

8.7 What is Missing?

As mentioned, several commercial tools offer interfaces for connecting modalities, especially for SPECT/CT and PET/CT. These interfaces are different for every vendor and might not be readily available. However, the fact that they exist already represents huge progress in the last decade. However, multimodal 3D visualization approaches shown above will clearly help increase acceptance of multimodal imaging through visually pleasing images. As a matter of fact, however, the majority of clinical users will employ a rather conventional display program capable of merging just two data sets, which is in many cases is absolutely sufficient. As soon as more than two sets of images need to be combined, the handling gets complicated, and most users will revert to mental data integration.

To the best of our knowledge, no real solution to this situation is yet available. One possibility was brought forward by our group a few years ago (Fig. 8.5) [2]. Basically, we suggested the use of a high-resolution imaging technique such as CTA to define LV endo- and epicardial contours within images (not the 3D display) and then color code this with functional information (absolute blood flow or processed information, such as viability score based on flow and metabolism data). Such an approach would offer the advantage that very fine structures, such as small vessels, are still visible in the original data—something that easily gets lost when using conventional image fusion techniques. In particular, new devices such as hybrid PET/MRI could benefit from this concept.

Although still in its infancy, cardiac PET/MRI already generates such a massive amount of data that the time necessary for image reconstruction and reading far exceeds the time of the actual imaging process. A hybrid image viewing technique integrating several forms of information (e.g., motion + metabolism; flow + late enhancement), as suggested above, would at least reduce the review process to a reasonable amount of time.

8.8 Conclusions

What is the result of the aforementioned reality check? Within the last decade, the integration of CTA data with nuclear data reached a certain level of convenience with available and user-friendly tools that—ten years ago—could hardly be imagined. Thus, it is fair to assume that a similar development can be expected for new trends in hybrid imaging, provided that vendors continue to apply relatively open interfaces to their existing tools. However, visualization is the final element in an increasingly complex multi-modal workflow. Consequentially, especially for hybrid cardiac PET images, huge efforts are needed to provide an efficient workflow for all elements, including generation of quantitative data, data transfers, efficient 2D image reading, and, finally 3D rendering.

References

1. Nekolla SG, Ibrahim T, Balbach T, Klein C, Bengel FM, Schwaiger M (2001) Coregistration and fusion of cardiac magnetic resonance and positron emission tomography studies. In: Marzullo P (ed) Understanding cardiac imaging techniques. IOS Press, Amsterdam
2. Schwaiger M, Ziegler S, Nekolla SG (2005) PET/CT: challenge for nuclear cardiology. J Nucl Med 46:1664–1678
3. Gaemperli O, Bengel FM, Kaufmann PA (2011) Cardiac hybrid imaging. Eur Heart J Res Support, Non-U S Gov't, Rev 32:2100–2108
4. Saraste A, Knuuti J (2012) Cardiac PET, CT, and MR: what are the advantages of hybrid imaging? Curr Cardiol Rep 14:24–31
5. Zaidi H, Ojha N, Morich M et al (2011) Design and performance evaluation of a whole-body ingenuity TF PET-MRI system. Phys Med biol 56:3091–3106
6. Delso G, Furst S, Jakoby B et al (2011) Performance measurements of the Siemens mMR integrated whole-body PET/MR scanner. J Nucl Med 52:1914–1922
7. Germano G, Kavanagh PB, Slomka PJ, Van Kriekinge SD, Pollard G, Berman DS (2007) Quantitation in gated perfusion SPECT imaging: the Cedars-Sinai approach. J Nucl Cardiol 14:433–454
8. Garcia EV, Faber TL, Cooke CD, Folks RD, Chen J, Santana C (2007) The increasing role of quantification in clinical nuclear cardiology: the Emory approach. J Nucl Cardiol: Official Publ Am Soc Nucl Cardiol 14:420–432
9. Ficaro EP, Lee BC, Kritzman JN, Corbett JR (2007) Corridor4DM: the Michigan method for quantitative nuclear cardiology. J Nucl Cardiol 14:455–465
10. Cerqueira MD, Weissman NJ, Dilsizian V et al (2002) Standardized myocardial segmentation and nomenclature for tomographic imaging of the heart: a statement for healthcare professionals from the Cardiac Imaging Committee of the Council on Clinical Cardiology of the American Heart Association Circulation. Consens Dev Conf Rev 105:539–542
11. Koszegi Z, Maes A, Piessens J, Van de Werf F, Mortelmans L (1998) Segmental comparison between coronary angiography and positron emission tomography reveals low predictive value of epicardial flow for viability. Eur Heart J 19:959–967
12. Javadi MS, Lautamaki R, Merrill J, Voicu C, Epley W, McBride G, Bengel FM (2010) Definition of vascular territories on myocardial perfusion images by integration with true coronary anatomy: a hybrid PET/CT analysis. J Nucl Med 51:198–203
13. Slomka PJ, Baum RP (2009) Multimodality image registration with software: state-of-the-art. Eur J Nucl Med Mol Imaging 36(Suppl 1):S44–55
14. Faber TL, Santana CA, Piccinelli M, Nye JA, Votaw JR, Garcia EV, Haber E (2010) Automatic alignment of myocardial perfusion images with contrast cardiac tomography. IEEE nuclear science symposium conference record. Nucl Sci Symp 2010:2996–2997
15. Nakazato R, Dey D, Alexanderson E et al (2012) Automatic alignment of myocardial perfusion PET and 64-slice coronary CT angiography on hybrid PET/CT. J Nucl Cardiol 19:482–491
16. Martinez-Moller A, Souvatzoglou M, Navab N, Schwaiger M, Nekolla SG (2007) Artifacts from misaligned CT in cardiac perfusion PET/CT studies: frequency, effects, and potential solutions. J Nucl Med 48:188–193
17. Nye JA, Faber TL (2011) Current state of hybrid imaging: attenuation correction and fusion. J Nucl Cardiol: Official Publ Am Soc Nucl Cardiol 18:729–740
18. Gaemperli O, Schepis T, Valenta I et al (2007) Cardiac image fusion from stand-alone SPECT and CT: clinical experience. J Nucl Med 48:696–703
19. Gaemperli O, Schepis T, Kalff V et al (2007) Validation of a new cardiac image fusion software for three-dimensional integration of myocardial perfusion SPECT and stand-alone 64-slice CT angiography. Eur J Nucl Med Mol Imaging 34:1097–1106
20. Kajander S, Joutsiniemi E, Saraste M et al (2010) Cardiac positron emission tomography/computed tomography imaging accurately detects anatomically and functionally significant coronary artery disease. Circulation 122:603–613

21. Ibrahim T, Nekolla SG, Schreiber K et al (2002) Assessment of coronary flow reserve: comparison between contrast-enhanced magnetic resonance imaging and positron emission tomography. J Am Coll Cardiol 39:864–870
22. Marinelli M, Positano V, Nekolla SG et al (2012) Hybrid image visualization tool for 3D integration of CT coronary anatomy and quantitative myocardial perfusion PET. International Journal of Computer Assisted Radiology and Surgery. doi: 10.1007/s11548-012-0777-3
23. Garcia EV (2012) A memorial tribute to Tracy L. Faber, PhD. J Nucl Cardiol 19:395–396
24. Faber TL, Santana CA, Garcia EV et al (2004) Three-dimensional fusion of coronary arteries with myocardial perfusion distributions: clinical validation. J Nucl Med 45:745–753
25. Santana CA, Garcia EV, Faber TL et al (2009) Diagnostic performance of fusion of myocardial perfusion imaging (MPI) and computed tomography coronary angiography. J Nucl Cardiol 16:201–211
26. Makowski MR, Ebersberger U, Nekolla S, Schwaiger M (2008) In vivo molecular imaging of angiogenesis, targeting alphavbeta3 integrin expression, in a patient after acute myocardial infarction. Eur Heart J: Case Rep 29:2201
27. Cheng VY, Slomka PJ, Le Meunier L, Tamarappoo BK, Nakazato R, Dey D, Berman DS (2012) Coronary arterial ^{18}F-FDG uptake by fusion of PET and coronary CT angiography at sites of percutaneous stenting for acute myocardial infarction and stable coronary artery disease. J Nucl Med: Official publ Soc Nucl Med 53:575–583
28. Lautamaki R, Schuleri KH, Sasano T et al (2009) Integration of infarct size, tissue perfusion, and metabolism by hybrid cardiac positron emission tomography/computed tomography: evaluation in a porcine model of myocardial infarction. Circ Cardiovasc Imaging 2:299–305
29. Sasano T, Abraham MR, Chang KC et al (2008) Abnormal sympathetic innervation of viable myocardium and the substrate of ventricular tachycardia after myocardial infarction. J Am Coll Cardiol 51:2266–2275
30. Klein C, Nekolla SG, Bengel FM et al (2002) Assessment of myocardial viability with contrast-enhanced magnetic resonance imaging: comparison with positron emission tomography. Circulation 105:162–167
31. Ibrahim T, Hackl T, Nekolla SG, Breuer M, Feldmair M, Schomig A, Schwaiger M (2010) Acute myocardial infarction: serial cardiac MR imaging shows a decrease in delayed enhancement of the myocardium during the 1st week after reperfusion. Radiology 254:88–97
32. Manka R, Kuhn FP, Kuest SM, Gaemperli O, Kozerke S, Kaufmann PA (2011) Hybrid cardiac magnetic resonance/computed tomographic imaging: first fusion of three-dimensional magnetic resonance perfusion and low-dose coronary computed tomographic angiography. Eur Heart J 32:2625

Diagnostic Algorithms in Patients with Suspected Coronary Artery Disease: Guidelines and Evidence-Based Behaviors

9

Stefania Paolillo and Pasquale Perrone Filardi

9.1 Introduction

Cardiovascular (CV) diseases represent the leading cause of morbidity and mortality worldwide despite the introduction of new and sophisticated diagnostic techniques and the progression of therapeutic approaches that have substantially reduced CV mortality and morbidity rates. In particular, coronary artery disease (CAD) is the main manifestation of cardiac disorders and is characterized by several clinical presentations from a common pathophysiological origin. Thus, a correct diagnostic strategy is needed in patients with suspected CAD in order to choose the best therapeutic approach and avoid potentially fatal consequences.

9.2 Epidemiology and Clinical Presentation of Coronary Artery Disease

As observed by Murray et al. in the Global Burden of Disease Study [1], in 2020, ischemic heart disease would be the first of the ten leading causes of disability, with increased rates not only in industrialized countries, as previously reported, but also in developing countries. Atherosclerotic abnormalities of coronary arteries may long be asymptomatic and then suddenly manifest as acute coronary syndromes (ACS) or typical or atypical ischemic symptoms that generally herald an acute event. In the clinical history of CAD, in fact, a chronic stable phase and an acute unstable stage may be identified. A slow chronic inflammatory process characterizes the chronic phase of atherosclerotic plaque development, which is in part genetically determined but largely modified in duration and severity by the presence of CV risk factors. Conversely, the unstable phase of the disease may appear as a dramatic event pathophysiologically characterized by coronary atherosclerotic plaque rupture or erosion or, alternatively, by endoluminal thrombosis, with sudden and critical reduction in blood flow that clinically appear as ACS. Thus, the manifestations of CAD include stable and unstable angina pectoris, myocardial infarction with or without ST-segment elevation, silent ischemia up to heart failure, and sudden cardiac death.

9.2.1 Stable Angina

Stable angina is a clinical condition characterized by the occurrence of chest, arm, shoulder, back, or jaw pain classically stimulated by emotional stress or physical activity, which gradually disappears with rest or nitroglycerin

S. Paolillo · P. Perrone Filardi (✉)
Department of Internal Medicine, Cardiovascular and Immunological Disorders, Federico II University of Naples, Naples, Italy
e-mail: fpperron@unina.it

S. Paolillo
e-mail: paolilloste@gmail.com

P. Marzullo and G. Mariani (eds.), *From Basic Cardiac Imaging to Image Fusion*,
DOI: 10.1007/978-88-470-2760-2_9,

consumption [2]. The prevalence of angina pectoris varies with age, increasing from 0.1–1% in women between 45 and 54 years to 10–15% in women of 55–74 years; and from 2–5% in men aged 45–54 to 10–20% in 55–74 year-old men [2]. The etiology of stable angina lies in atherosclerotic coronary stenosis, and prognosis is determined by baseline clinical condition, presence of CV risk factors, anatomical characteristics, and clinical history.

9.2.2 Unstable Angina and Non-ST-Elevated Myocardial Infarction

These conditions represent two different manifestations of ACS without persistent ST-segment elevation [non-ST-elevated ACS (NSTE-ACS)]. Several clinical manifestations may characterize such conditions, including resting, prolonged angina pain, new-onset angina, instability of chronic stable angina, and post-myocardial infarction angina [3]. The assessment of cardiac troponins distinguishes between Non-ST-Elevated Myocardial Infarction (NSTEMI) and unstable angina. These clinical conditions are pathophysiologically characterized by acute coronary thrombosis due to atherosclerotic plaque rupture or erosion and present an incidence of about 3 per 1.000 individuals, an in-hospital mortality rate of 3–5%, and a 6 month mortality rate of about 13% [4, 5].

9.2.3 ST-Elevated Myocardial Infarction

Conversely, ST-Elevated Myocardial Infarction (STEMI) is an acute event characterized by the presence of ischemic symptoms accompanied by persistent ST-segment elevation on electrocardiogram (ECG). The pathogenesis of STEMI is represented by a total coronary occlusion due to atherosclerotic plaque disruption, with consequent formation of an occluding thrombus [6]. Patients affected by STEMI have a hospital mortality rate of ~7%, higher than those of NSTEMI patients; however, it seems that the 6 months mortality is ~12%, which is very similar between the two clinical conditions [4, 5].

9.2.4 Heart Failure and Sudden Cardiac Death

Clinical presentation of CAD with the occurrence of heart failure and sudden cardiac death is a more rare occurrence; however, great attention should be directed to asymptomatic or silent ischemia because of the evidence that ST-segment depression during ambulatory ECG monitoring occurs more often than symptomatic ST-segment depression in patients with CAD [7].

9.3 Diagnosis of Coronary Artery Disease

The occurrence of typical ischemic symptoms, such as angina pectoris, or of its ischemic equivalents should drive the physician to suspect CAD. This suspicious should be reinforced in the presence of CV risk factors, such as arterial hypertension, dyslipidemia, diabetes mellitus, familiar history of CV disease, smoking, and, moreover, by a clinical history of previous CV events or of coronary revascularization procedures. In case of suspected CAD, application of noninvasive diagnostic tests is the first step by which to confirm or exclude diagnosis. Currently, several noninvasive diagnostic techniques are available, and correct knowledge of their applicability and appropriateness is essential to avoid misdiagnoses.

9.3.1 Assessment of Pretest Probability

The diagnostic management of patients with suspected CAD starts from assessment of the absolute risk of each patient to develop coronary heart disease. Moreover, after this first evaluation, the estimation of pretest probability may be a useful tool to better interpret diagnostic test results and correctly proceed through the

diagnostic algorithm. Absolute risk is defined as the probability of developing CAD, including myocardial infarction or coronary death, over a given time period. Generally, CAD risk refers to 10 year risk for any hard cardiac event. The definition of CAD risk starts from a baseline evaluation of CV risk factors. As reported by the Assessment of Cardiovascular Risk by Use of Multiple-Risk-Factor Assessment Equations of the American College of Cardiology/American Heart Association (ACC/AHA) [8], the major and independent risk factors for CAD are cigarette smoking, high blood pressure, diabetes mellitus, elevated serum total cholesterol and low-density lipoprotein cholesterol, low serum high-density lipoprotein cholesterol and advanced age. Several studies, including the Framingham Heart Study [9], assessed the relationship between these risk factors and CAD risk, showing that those considered as the major risk factors are additive in predictive power. Therefore, patient's total risk can be estimated by a summing of the risk of each of the major risk factors. The same authors also reported that there are two other types of conditions that may confer an increased risk of CAD, classified as conditional and predisposing risk factors. Conditional risk factors are elevated serum triglycerides, small LDL particles, elevated serum homocysteine, elevated serum lipoprotein(a), prothrombotic factors, and inflammatory markers (e.g., C-reactive protein). These factors are associated with increased risk for CAD, although their independent contributions to coronary lesion development have not been well documented. The predisposing factors, which worsen the independent risk factors, include abdominal obesity, physical inactivity, family history of premature CAD, ethnic characteristics, and psychosocial factors. On the basis of different algorithms and recommendations, it is so possible to define a low risk of CAD that represents a 10 year absolute risk <10%; a moderate risk for individuals with a 10 year absolute risk between 10 and 20%; and a high risk defined as the presence of diabetes mellitus in a patient >40 years of age, peripheral arterial disease or other coronary risk equivalents, or a 10 year absolute coronary heart disease risk >20%. Once the absolute CAD risk has been assessed and the presence of typical ischemic symptoms has been confirmed, the pretest probability should be evaluated. Such probability is generally classified as "very low pretest probability" when the pretest probability of CAD is <5%, "low pretest probability" if <10%, "intermediate pretest probability" between 10 and 90%, and "high pretest probability" if the pretest probability of CAD is >90%. Thus, when evaluating a patient with suspected ischemic symptoms, characteristics of symptoms (whether chest pain is substernal, if symptoms are precipitated by exertion, and if there is prompt relief within 10 min with rest or nitroglycerin) should be preliminarily defined. On the basis of these evaluations, symptoms can be divided into typical (or classical) angina when all features are present, atypical angina if any two features are present, and nonanginal chest pain if one or no features are present. Pretest probability can be estimated based on age, gender, and characteristics of chest pain. Several algorithms are available to estimate such probability. Generally, the following scheme can be utilized:

- Low probability (<10%)
  - Asymptomatic men and women of all ages
  - Women <50 years with atypical chest pain
- Intermediate probability (10–90%)
  - Men of all ages with atypical angina
  - Women ≥50 years with atypical angina
  - Women 30–50 years with typical angina
- High probability
  - Men ≥40 years with typical angina
  - Women ≥50 years with typical angina

In recent years, the major international societies of cardiology have developed guidelines and established appropriateness criteria and dedicated algorithms for the use of noninvasive imaging techniques, as described below.

9.3.1.1 Exercise Testing

Exercise testing represents the most used and readily available noninvasive test for the diagnosis of CAD. In recent years, the ACC/AHA

proposed an integration of the old guidelines regarding exercise testing in clinical practice [10]. In particular, a class I indication was determined for performing the test as an initial evaluation in patients with suspected or known CAD, which also included patients with complete right bundle-branch block and those with an ST depression at resting ECG <1 mm. As previously reported [11], little evidence is available for evaluating CAD using exercise testing in patients presenting with complete left bundle-branch block or any interventricular conduction defect with a QRS duration >120 ms, pre-excitation syndromes, electronically paced ventricular rhythm, and presence of ≥1 mm ST depression at resting ECG. In these patients, imaging diagnostic tests are preferred. Stress ECG is also suggested in patients with suspected or known CAD, previously evaluated, presenting with significant changes in clinical status. The last report of the US societies also proposed applying exercise testing in patients with low risk, unstable angina 8–12 h after presentation if they have been free of active ischemic or heart failure symptoms (class Il level of evidence, B) and in intermediate-risk patients with unstable angina 2–3 days after presentation, even if free of ischemic or heart failure symptoms (class I, level of evidence, B). Moreover, an indication in class IIa with a level of evidence B is posed for intermediate-risk patients with unstable angina who have normal values of cardiac markers at the initial evaluation, a repeated ECG without significant changes, and normal cardiac markers 6–12 h after symptom onset and without evidence of ischemia during observation. Patients with severe comorbidity likely to limit life expectancy and/or already candidates for revascularization, and high risk patients with unstable angina—such as those presenting prolonged chest pain at rest, hypotension, rhythm disorders, elevated cardiac markers, and so forth—must not be evaluated with exercise testing because, apart from possibly not being useful, the procedure may be harmful in some cases. Exercise testing is also not recommended in routine screening of asymptomatic men or women, whereas it may be a useful tool for evaluating asymptomatic patients with diabetes mellitus who plan to start strong physical activity, as in evaluating patients with multiple risk factors as a guide to risk-reduction management [10].

In 2005, a working group from the American College of Cardiology Foundation proposed a technical method for evaluating appropriateness of cardiac imaging [12]. In particular, the authors suggested the definition of "appropriate" for any test from which the expected information, combined with clinical findings, exceeds the expected negative consequences by a sufficiently wide margin. In the proposed technical panel, three grades were used to score specific indications: a score between 7 and 9 considers the test appropriate for specific indications (test is generally acceptable and is a reasonable approach); a score between 4 and 6 evaluates the procedure as uncertain for the indication (test may be generally acceptable and may be a reasonable approach for the indication); a score between 1 and 3 refers to inappropriate test for that indication (test is not generally acceptable and is not a reasonable approach). Such scores are used in recently published recommendations of different CV imaging techniques, as subsequently reported.

9.3.2 Cardiac Radionuclide Imaging

Nuclear imaging represents a highly valuable tool for evaluating patients with suspected CAD. Correct knowledge of appropriateness criteria of cardiac radionuclide imaging is required because inappropriate use of cardiac nuclear tests may be potentially harmful and may generate unjustified costs to the healthcare system. Appropriate procedures, on the other hand, should likely improve patients' clinical outcomes. In 2009, the American College of Cardiology Foundation Appropriate Use Criteria Task Force [13] reported a revision of previously published single-photon-emission computed tomography (SPECT) myocardial perfusion imaging appropriateness criteria to evaluate changes in test use on the basis of new clinical data. In particular, in

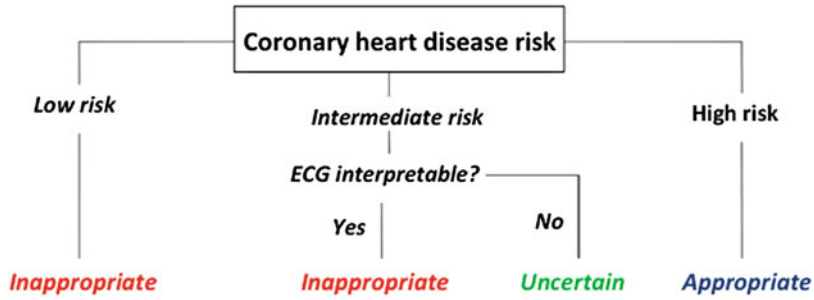

Fig. 9.1 Use of cardiac radionuclide imaging in asymptomatic patients. Modified from [14]

developing these criteria, a technical panel was instituted to establish whether the use of the test for each indication is considered appropriate, uncertain, or inappropriate. Regarding the definition of "appropriate test", the authors refer to negative consequences as procedural risks of radiation or contrast exposure as well as risks related to procedural choice, possibly leading to delay (false negatives) or inappropriate (false positives) diagnosis. On this basis, starting from the group of asymptomatic patients, cardiac radionuclide imaging is considered appropriate in individuals at high risk for coronary heart disease according to Adult Treatment Panel III (ATP III) criteria [14]; uncertain in patients at intermediate-risk for coronary events with uninterpretable ECG; and inappropriate in low risk individuals and intermediate-risk patients with interpretable coronary events on ECG (Fig. 9.1). The definition "uninterpretable ECG" refers to ECGs with resting ST-segment depression, complete left bundle-branch block, pre-excitation, or paced rhythm. Figure 9.2 shows the algorithm proposed for patients presenting with symptoms suggestive of CAD. In such patients, and in case of chronic symptoms, cardiac nuclear tests are reported as appropriate if a high pretest probability is present. The appropriateness is also reported for patients at intermediate risk. In particular, if an intermediate pretest probability is present with an interpretable ECG and the possibility of performing an exercise test, a score of 7 is reported. In the same class of risk, an uninterpretable ECG or a patient unable to exercise increases the score to 9. Conversely, nuclear tests are inappropriate in patients with chronic symptoms, low pretest probability, interpretable ECG, and capability to perform an exercise test. If acute symptoms are present and suspicion of ACS is definite, myocardial nuclear tests are considered inappropriate; if the occurrence of ACS is considered possible, nuclear imaging is appropriate and may help in diagnostic management and adequate treatment selection.

9.3.3 Stress Echocardiography

Douglas et al. [15] proposed appropriateness criteria for stress echocardiography using as technical scores the same panel previously reported for cardiac imaging [12]. The preferred mode of stress testing is exercise for patients able to perform it. Conversely, for patients unable to exercise, dobutamine should be preferred for echocardiographic stress testing. In asymptomatic patients, there are no indications to perform stress echocardiography in individuals at low risk of CAD [8, 9] or in patients with moderate risk and interpretable ECG; echocardiographic stress testing is considered appropriate in asymptomatic patients at high risk for CAD. In patients with chronic chest pain, stress echocardiography is considered inappropriate in case of low CAD pretest probability, interpretable ECG, and ability to perform exercise; in all other cases, stress echocardiography is recommended for evaluating chest pain syndrome or angina equivalent. In individuals with acute chest pain, echocardiographic stress testing is not indicated and should be avoided in the presence of high CAD pretest probability and ST elevation on ECG. It can be performed,

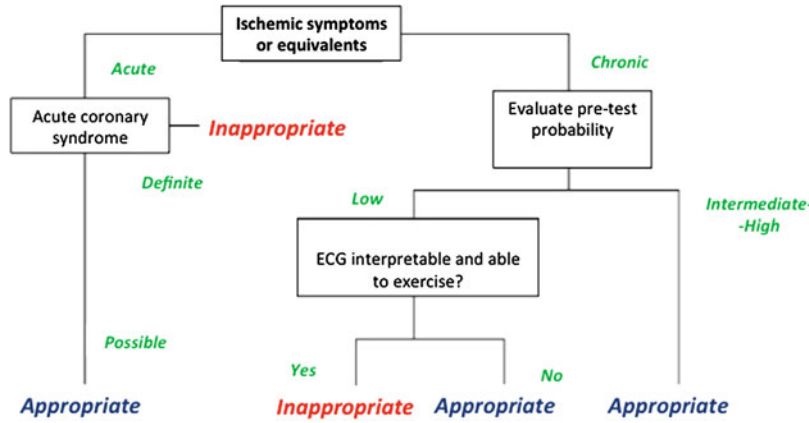

Fig. 9.2 Use of cardiac radionuclide imaging in patients with ischemic symptoms or ischemic equivalents. Modified from [14]

however, in intermediate pretest probability patients with no dynamic ST changes and with negative serial cardiac enzymes.

9.3.4 Cardiac Computed Tomography and Cardiac Magnetic Resonance Imaging

Cardiac computed tomography to study coronary arteries, cardiac structure and morphology, and calcium scoring and cardiac magnetic resonance imaging (MRI) to assess myocardial structure, function, and viability, have been introduced for noninvasive evaluation of coronary heart disease [16]. These tests are still relatively expensive, especially for technical equipment, so that their application should be adequately assessed and weighed. Cardiac computed coronary angiography (CTCA) is currently inappropriate for asymptomatic patients at low or moderate CAD risk (Framingham risk criteria), whereas its indication remains uncertain in asymptomatic individuals at high CAD risk. In symptomatic patients, CTCA should be considered in case of intermediate CAD pretest probability and uninterpretable ECG or patients unable to exercise; similarly the technique is a useful tool in patients with suspected coronary artery abnormalities. When acute symptoms are present, the only appropriate indication is in intermediate-risk patients with no ECG changes and serial-negative cardiac enzymes. In all other cases of acute chest pain, the technique is considered uncertain or inappropriate, especially if ST-segment elevation or positive cardiac markers are present.

Cardiac MRI is limited in the context of suspected CAD. On the contrary, its routine use is largely validated for assessing ventricular and valvular function, evaluating intra- and extracardiac structures, and assessing myocardial viability and scar through the use late gadolinium enhancement in patients with heart failure. Use of MRI-CA may be considered to rule out coronary abnormalities, whereas the application of vasodilator perfusion or dobutamine stress tests may be useful in intermediate-risk patients with uninterpretable ECG or who are unable to exercise to obtain functional assessment of stenosis of borderline hemodynamic significance.

9.4 Diagnostic Strategies in Asymptomatic Patients

Asymptomatic patients with CV risk factors and suspected myocardial ischemia on ambulatory ECG evaluation should be investigated for risk stratification and to assess obstructive CAD [17, 18]. Exercise ECG without an imaging modality represents the first-line diagnostic strategy, even in the presence of Wolff–Parkinson–White syndrome or ST depression at resting ECG. Exercise ECG exhibits a validated prognostic

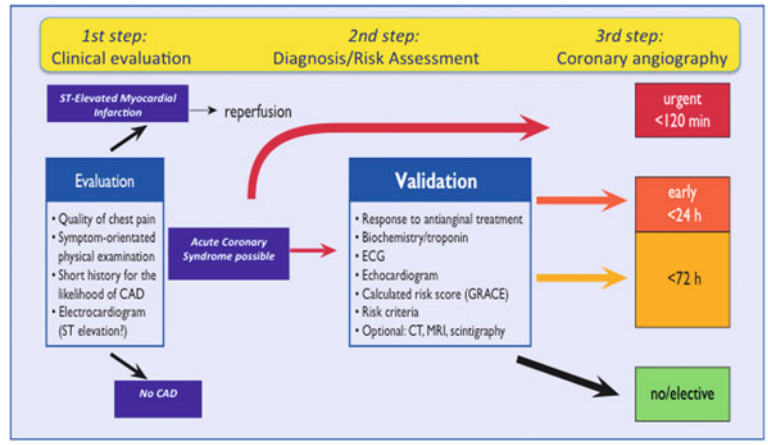

Fig. 9.3 Diagnostic algorithm in patients with suspected acute coronary syndrome. Modified from [3]

importance and is largely available in several diagnostic settings, such as hospitals and outpatient clinics. ECG exercise test prognostic significance improves if the cardiologist not only focuses attention on ischemic changes but also on patient's functional reserve and other performance measures. In addition, the Duke Treadmill score is useful to classify CAD risk; however, with that score, ~50% of patients are classified as at intermediate-risk. Exercise perfusion imaging or exercise echocardiography exhibit greater sensitivity for CAD diagnosis and may be useful in such cases. If small perfusion defects are identified, patients can be classified as low risk and followed up with medical therapy. Conversely, if large perfusion defects are detected, CA represents the next diagnostic step. However, in asymptomatic patients unable to exercise, adenosine or dipyridamole myocardial perfusion imaging or dobutamine echocardiography should be used.

In conclusion, exercise myocardial perfusion imaging or exercise echocardiography after exercise ECG testing must be considered in asymptomatic patients with an intermediate or high risk Duke treadmill score, whereas adenosine or dipyridamole myocardial perfusion imaging or dobutamine echocardiography after exercise ECG testing may be useful for additional, noninvasive assessment in asymptomatic patients with an inadequate exercise ECG. Following noninvasive evaluation, CA should be performed in patients with high risk, extensive (>10% of LV) ischemia on noninvasive testing (class IIa, level of evidence, C) and in patients with inadequate prognostic information after noninvasive testing (class IIb, level of evidence, C).

9.5 Diagnostic Strategies in Patients with Suspected ACS

Diagnostic management of patients with a clinical suspicion of ACS begins with distinguishing between coronary syndromes with or without persistent ST-segment elevation in order to choose as soon as possible the best therapeutic strategy [3, 19] (Fig. 9.3). Clinical evaluation is of crucial importance, as it allows assessment of the characteristics of chest pain, collection of a brief clinical history to assess the likelihood of CAD, and performance of a symptom-oriented physical examination. ECG then confirms or rules out the diagnosis of STEMI and the need to proceed with a reperfusion strategy if such condition occurs. Alternatively, if the diagnosis of ACS without persistent ST-segment elevation is suspected, biomarkers (troponins) further allow differentiating between NSTEMI and unstable angina. Imaging modalities are used to determine or rule out differential diagnoses. When ACS diagnosis is considered possible, several patient characteristics, clinical presentation, and response to therapy may guide the therapeutic approach. In particular, the Global

Registry of Acute Coronary Events (GRACE) risk score [20], together with an echocardiographic evaluation, a serial ECG, biomarker assessment, and response to antianginal treatments helps predict short- and midterm prognosis of ACS and to assess the need for early CA.

9.6 Conclusions

Several diagnostic techniques are available for CAD diagnosis, in both asymptomatic and symptomatic patients. However, each physician should adequately consider patients' characteristics, local availability of noninvasive diagnostic techniques, and the relative risk–benefit ratio.

Regarding emergency department and chronic clinical care, some authors compared noninvasive strategies in terms of costs-effectiveness [21]. In patients with chest pain and low risk of CAD, a diagnostic strategy with coronary CT and myocardial SPECT for indeterminate results seems to be less costly and more effective in a patient group at low risk of CAD, with a prevalence of 2–30%. Diagnostic algorithms in which coronary CT was used were likely to be more convenient in terms of healthcare costs compared with exercise ECG, echocardiography, and SPECT. In addition, further confirmation of intermediate/indeterminate scans with myocardial SPECT is cost saving and results in quality-adjusted life-year gains due to reduced hospitalization of patients who initially returned false-positive coronary CT tests. However, it should be considered that this technique is not readily available or feasible in some emergency departments, particularly in small local hospitals, and greater attention should thus be focused on more simple diagnostic approaches.

Available guidelines and appropriateness criteria usually do not consider problems of healthcare costs, feasibility, and real effectiveness in established subgroups of patients. Ferket et al. [22] performed an interesting analysis of the available guidelines in the English language on imaging in asymptomatic CAD in order to critically evaluate the suggested approaches. They found 14 documents and two independent reviewers and used the Appraisal of Guidelines for Research and Evaluation (AGREE) instrument to evaluate them. The authors found conflicting recommendations, and AGREE scores varied across guidelines from 21 to 93%. In addition, of the 14 analyzed documents, only two guidelines considered cost-effectiveness. This example elucidates how guidelines are not always applicable and how a "correct" approach does not truly exist because of different clinical settings and numerous disease manifestations. More research, including randomized controlled trials, evaluating the impact of diagnostic algorithms on clinical outcomes and costs is needed to improve clinical management of chronic and acute CAD in each different working background and circumstances.

References

1. Murray CJ, Lopez AD (1997) Alternative projections of mortality and disability by cause 1990–2020: Global Burden of Disease Study. Lancet 349:1498–504
2. Fox K, Garcia MA, Ardissino D et al, Task Force on the Management of stable Angina Pectoris of the European Society of Cardiology; ESC Committee for Practice Guidelines (CPG) (2006) Guidelines on the management of stable angina pectoris: executive summary: the task force on the management of stable Angina Pectoris of the European Society of Cardiology. Eur Heart J 27:1341–1381
3. Hamm CW, Bassand JP, Agewall S et al (2011) ESC Guidelines for the management of acute coronary syndromes in patients presenting without persistent ST-segment elevation: the task force for the management of acute coronary syndromes (ACS) in patients presenting without persistent ST-segment elevation of the European Society of Cardiology (ESC). Eur Heart J 32:2999–3054
4. Yeh RW, Sidney S, Chandra M, Sorel M, Selby JV, Go AS (2020) Population trends in the incidence and outcomes of acute myocardial infarction. N Engl J Med 362:2155–65
5. Fox KA, Eagle KA, Gore JM, Steg PG, Anderson FA; GRACE and GRACE2 Investigators (2010) The global registry of acute coronary events, 1999–2009–GRACE. Heart 96:1095–101
6. Van de Werf F, Bax J, Betriu A et al, ESC Committee for Practice Guidelines (CPG) (2008) Management of acute myocardial infarction in patients presenting with persistent ST-segment

elevation: the task force on the management of ST-Segment Elevation Acute Myocardial Infarction of the European Society of Cardiology. Eur Heart J 29:2909–2945
7. Conti CR, Bavry AA, Petersen JW (2012) Silent ischemia: clinical relevance. J Am Coll Cardiol 59:435–441
8. Grundy SM, Pasternak R, Greenland P, Smith S Jr, Fuster V (1999) AHA/ACC Scientific statement: assessment of cardiovascular risk by use of multiple-risk-factor assessment equations: a statement for healthcare professionals from the American Heart Association and the American College of Cardiology. J Am Coll Cardiol 34:1348–1359
9. Wilson PW, D'Agostino RB, Levy D, Belanger AM, Silbershatz H, Kannel WB (1998) Prediction of coronary heart disease using risk factor categories. Circulation 97:1837–1847
10. Gibbons RJ, Balady GJ, Bricker JT et al, American college of cardiology/American heart association task force on practice guidelines Committee to update the 1997 exercise testing guidelines (2002). ACC/AHA 2002 guideline update for exercise testing: summary article. A report of the American College of Cardiology/American Heart Association task force on practice guidelines (committee to update the 1997 exercise testing guidelines). J Am Coll Cardiol 40:1531–1540
11. Gibbons RJ, Balady GJ, Beasley JW et al (1997) ACC/AHA guidelines for exercise testing. a report of the American College of Cardiology/American Heart Association task force on practice guidelines (committee on exercise testing). J Am Coll Cardiol 30:260–311
12. Patel MR, Spertus JA, Brindis RG, Hendel RC, Douglas PS, Peterson ED, Wolk MJ, Allen JM, Raskin IE (2005) American college of cardiology foundation ACCF proposed method for evaluating the appropriateness of cardiovascular imaging. J Am Coll Cardiol 46:1606–1613
13. Hendel RC, Berman DS, Di Carli MF, Heidenreich PA, Henkin RE, Pellikka PA, Pohost GM, Williams KA, American College of Cardiology Foundation Appropriate Use Criteria Task Force, American Society of Nuclear Cardiology, American College of Radiology, American Heart Association, American Society of Echocardiology, Society of Cardiovascular Computed Tomography, Society for Cardiovascular Magnetic Resonance, Society of Nuclear Medicine (2009) ACCF/ASNC/ACR/AHA/ASE/SCCT/SCMR/SNM 2009 Appropriate use criteria for cardiac radionuclide imaging: a report of the American College of Cardiology Foundation appropriate use criteria task force, the American Society of Nuclear Cardiology, the American College of Radiology, the American Heart Association, the American Society of Echocardiography, the Society of Cardiovascular Computed Tomography, the Society for Cardiovascular Magnetic Resonance, and the Society of Nuclear Medicine. J Am Coll Cardiol 53:2201–2229
14. National Institutes of Health: National Heart, Lung, and Blood Institute. Third Report of the National Cholesterol Education Program (NCEP) Expert Panel on Detection, Evaluation, and Treatment of High Blood Cholesterol in Adults (Adult Treatment Panel III). NIH Publication No. 02-5215
15. Douglas PS, Khandheria B, Stainback RF et al, American College of Cardiology Foundation, American Society of Echocardiography, American College of Emergency Physicians, American Heart Association, American Society of Nuclear Cardiology, Society for Cardiovascular Angiography and Interventions, Society of Cardiovascular Computed Tomography, Society for Cardiovascular Magnetic Resonance (2008) ACCF/ASE/ACEP/AHA/ASNC/SCAI/SCCT/SCMR 2008 appropriateness criteria for stress echocardiography: a report of the American College of Cardiology Foundation Appropriateness Criteria Task Force, American Society of Echocardiography, American College of Emergency Physicians, American Heart Association, American Society of Nuclear Cardiology, Society for Cardiovascular Angiography and Interventions, Society of Cardiovascular Computed Tomography, and Society for Cardiovascular Magnetic Resonance endorsed by the Heart Rhythm Society and the Society of Critical Care Medicine. J Am Coll Cardiol 51:1127–1147
16. Hendel RC, Patel MR, Kramer CM et al, American College of Cardiology Foundation Quality Strategic Directions Committee Appropriateness Criteria Working Group, American College of Radiology, Society of Cardiovascular Computed Tomography, Society for Cardiovascular Magnetic Resonance, American Society of Nuclear Cardiology, North American Society for Cardiac Imaging, Society for Cardiovascular Angiography and Interventions, Society of Interventional Radiology (2006) ACCF/ACR/SCCT/SCMR/ASNC/NASCI/SCAI/SIR 2006 appropriateness criteria for cardiac computed tomography and cardiac magnetic resonance imaging: a report of the American College of Cardiology Foundation Quality Strategic Directions Committee Appropriateness Criteria Working Group, American College of Radiology, Society of Cardiovascular Computed Tomography, Society for Cardiovascular Magnetic Resonance, American Society of Nuclear Cardiology, North American Society for Cardiac Imaging, Society for Cardiovascular Angiography and Interventions, and Society of Interventional Radiology. J Am Coll Cardiol 48:1475-97
17. Gibbons RJ, Abrams J, Chatterjee K et al, American College of Cardiology, American Heart Association Task Force on practice guidelines (Committee on the Management of Patients With Chronic Stable Angina) (2003) ACC/AHA 2002 guideline update

for the management of patients with chronic stable angina–summary article: a report of the American College of Cardiology/American Heart Association Task Force on practice guidelines (Committee on the Management of Patients With Chronic Stable Angina). J Am Coll Cardiol 41:159–168
18. Fraker TD Jr, Fihn SD, 2002 Chronic Stable Angina Writing Committee, American College of Cardiology, American Heart Association, Gibbons RJ, Abrams J, Chatterjee K et al (2007) 2007 chronic angina focused update of the ACC/AHA 2002 guidelines for the management of patients with chronic stable angina: a report of the American College of Cardiology/American Heart Association Task Force on Practice Guidelines Writing Group to develop the focused update of the 2002 guidelines for the management of patients with chronic stable angina. J Am Coll Cardiol 50:2264-2274
19. Wenger NK (2012) 2011 ACCF/AHA focused update of the guidelines for the management of patients with unstable Angina/Non-ST-elevation myocardial infarction (updating the 2007 guideline): highlights for the clinician. Clin Cardiol 35:3–8
20. Eggers KM, Kempf T, Venge P, Wallentin L, Wollert KC, Lindahl B (2010) Improving long-term risk prediction in patients with acute chest pain: the global registry of acute coronary events (GRACE) risk score is enhanced by selected nonnecrosis biomarkers. Am Heart J 160:88–94
21. Priest VL, Scuffham PA, Hachamovitch R, Marwick TH (2011) Cost-effectiveness of coronary computed tomography and cardiac stress imaging in the emergency department: a decision analytic model comparing diagnostic strategies for chest pain in patients at low risk of acute coronary syndromes. JACC Cardiovasc Imaging 4:549–556
22. Ferket BS, Genders TS, Colkesen EB, Visser JJ, Spronk S, Steyerberg EW, Hunink MG (2011) Systematic review of guidelines on imaging of asymptomatic coronary artery disease. J Am Coll Cardiol 57:1591–1600